DOT/FAA/TCTT/25-12

Federal Aviation Administration
William J. Hughes Technical Center
Aviation Research Division
Atlantic City International Airport
New Jersey 08405

Point Cloud Failure Criterion for Impact Modeling of Composite Structures

April 2025

Technical Thesis

The research described in this report was funded by the FAA as part of its mission to improve aircraft safety. The views and opinions expressed are those of the author alone and do not necessarily represent the views of the FAA. The FAA assumes no liability for the contents or use thereof. The FAA has not edited or modified the contents of the report in any manner.

U.S. Department of Transportation
Federal Aviation Administration

NOTICE

This document is disseminated under the sponsorship of the U.S. Department of Transportation in the interest of information exchange. The U.S. Government assumes no liability for the contents or use thereof. The U.S. Government does not endorse products or manufacturers. Trade or manufacturers' names appear herein solely because they are considered essential to the objective of this report. The findings and conclusions in this report are those of the author(s) and do not necessarily represent the views of the funding agency. This document does not constitute FAA policy. Consult the FAA sponsoring organization listed on the Technical Documentation page as to its use.

This report is available at the Federal Aviation Administration William J. Hughes Technical Center's Full-Text Technical Reports page: actlibrary.tc.faa.gov in Adobe Acrobat portable document format (PDF).

Technical Report Documentation Page

Form DOT F 1700.7 (8-72) Reproduction of completed page authorized

1. Report No.	2. Government Accession No.	3. Recipient's Catalog No.
DOT/FAA/TCTT/25-12		

4. Title and Subtitle	5. Report Date
Point Cloud Failure Criterion for Impact Modeling of Composite Structures	April 2025
	6. Performing Organization Code

7. Author(s)	8. Performing Organization Report No.
Ashutosh Maurya	

9. Performing Organization Name and Address	10. Work Unit No. (TRAIS)
Arizona State University PO Box 876011 Tempe, AZ 852876011	11. Contract or Grant No. 692M152340002

12. Sponsoring Agency Name and Address	13. Type of Report and Period Covered
692M152340002	Technical Thesis
	14. Sponsoring Agency Code AIR-600

15. Supplementary Notes

The FAA William J. Hughes Technical Center Aviation Research Division COR was Daniel Cordasco.

16. Abstract

An orthotropic elasto-plastic damage material model (OEPDMM) suitable for impact analysis of composite materials has been developed through a joint research project funded by the Federal Aviation Administration (FAA) and the National Aeronautics and Space Administration (NASA). The developed material model has been implemented into LS-DYNA®, a commercial finite element program. The material model is comprised of deformation, damage and failure sub-models. The deformation sub-model captures rate- and temperature-dependent elastic and inelastic behavior through a viscoelastic-plastic formulation. The damage sub-model accounts for reductions in elastic stiffness, while the failure sub-model predicts complete loss of load-carrying capacity, leading to element erosion. The primary objective of this dissertation is to improve the failure prediction sub-model. Traditional failure theories using analytical expressions to predict failure either in the composite or its constituents have not proven to be reliable. To overcome the predictability conundrum, a multi-scale modeling scheme based on a combination of virtual and laboratory testing is used to generate the failure surface as point cloud data points in the stress/strain space. At the microscale, the constituent components of the composite are used in modeling a representative volume element (RVE) that is subjected to multi-axial state of stress until the first failure in the RVE is detected. These discrete points are used in the developed Point Cloud Failure Criterion (PCFC). The secondary objectives of the dissertation are to enhance OEPDMM capabilities - (a) develop a new deformation sub-model, the Simplified Material Model that can be used for modeling materials exhibiting little or no elasto-plastic behavior, and (b) develop a framework for obtaining traction-separation law using inverse analysis for modeling delamination in laminated composites. Five validation tests were conducted to assess the accuracy, efficiency and versatility of available capabilities of OEPDMM. The findings from this research establish a robust foundation for future advancements in constitutive modeling of composite materials, with ongoing efforts directed toward extending PCFC to thick-shell and solid finite elements, incorporating rate and temperature-dependent failure surface, and incorporating mesh regularization techniques to further improve computational efficiency and accuracy in high-fidelity finite element simulations.

17. Key Words	18. Distribution Statement
Composite, Impact, Dynamic models, Failure, Plasticity, Orthotropic, Simulation, Finite element method, Carbon fiber, Resin, LS-DYNA, MAT_213	This document is available to the U.S. public through the National Technical Information Service (NTIS), Springfield, Virginia 22161. This document is also available from the Federal Aviation Administration William J. Hughes Technical Center at actlibrary.tc.faa.gov.

19. Security Classif. (of this report)	20. Security Classif. (of this page)	21. No. of Pages	22. Price
Unclassified	Unclassified		

Point Cloud Failure Criterion for Impact Modeling of Composite Structures

by

Ashutosh Maurya

A Dissertation
Presented in Partial Fulfillment
of the Requirements for the Degree
Doctor of Philosophy

Approved March 2025 by the
Graduate Supervisory Committee:

Subramaniam Rajan, Chair
Narayanan Neithalath
Barzin Mobasher
Christian Hoover
Ravi Kiran
Daniel Cordasco

ARIZONA STATE UNIVERSITY

May 2025

ABSTRACT

An orthotropic elasto-plastic damage material model (OEPDMM) suitable for impact analysis of composite materials has been developed through a joint research project funded by the Federal Aviation Administration (FAA) and the National Aeronautics and Space Administration (NASA). The developed material model has been implemented into LS-DYNA®, a commercial finite element program. The material model is comprised of deformation, damage and failure sub-models. The deformation sub-model captures rate- and temperature-dependent elastic and inelastic behavior through a viscoelastic-plastic formulation. The damage sub-model accounts for reductions in elastic stiffness, while the failure sub-model predicts complete loss of load-carrying capacity, leading to element erosion. The primary objective of this dissertation is to improve the failure prediction sub-model. Traditional failure theories using analytical expressions to predict failure either in the composite or its constituents have not proven to be reliable. To overcome the predictability conundrum, a multi-scale modeling scheme based on a combination of virtual and laboratory testing is used to generate the failure surface as point cloud data points in the stress/strain space. At the microscale, the constituent components of the composite are used in modeling a representative volume element (RVE) that is subjected to multi-axial state of stress until the first failure in the RVE is detected. These discrete points are used in the developed Point Cloud Failure Criterion (PCFC). The secondary objectives of the dissertation are to enhance OEPDMM capabilities - (a) develop a new deformation sub-model, the Simplified Material Model that can be used for modeling materials exhibiting little or no elasto-plastic behavior, and (b) develop a framework for

obtaining traction-separation law using inverse analysis for modeling delamination in laminated composites. Five validation tests were conducted to assess the accuracy, efficiency and versatility of available capabilities of OEPDMM. The findings from this research establish a robust foundation for future advancements in constitutive modeling of composite materials, with ongoing efforts directed toward extending PCFC to thick-shell and solid finite elements, incorporating rate and temperature-dependent failure surface, and incorporating mesh regularization techniques to further improve computational efficiency and accuracy in high-fidelity finite element simulations.

DEDICATION

This work is dedicated to my family and friends.

ACKNOWLEDGMENTS

I am greatly indebted to my thesis supervisor, Dr. Rajan for his invaluable mentorship and guidance throughout my doctoral journey at Arizona State University. I would like to thank my committee members, Dr. Narayanan Neithalath, Dr. Barzin Mobasher, Dr. Christian Hoover, Dr. Ravi Kiran, and Dr. Daniel Cordasco for their guidance and support.

I extend my heartfelt thanks to my friends, colleagues, and mentors at ASU. A special note of appreciation goes to Dr. Loukham Shyamsunder (IIT Tirupati), Dr. Bilal Khaled (Tesla), and Gunther Blankenhorn (ANSYS) for their collaboration in developing the material presented in this dissertation. I am also grateful to Dr. Robert Goldberg and Dr. Michael Pereira from NASA-GRC, Dr. Kelly Carney, and Paul DuBois for their invaluable feedback which greatly contributed to refining this work. I am also grateful to Jeff Long (ASU) for his assistance with the experimental components of this research and to the technical support team at ASU's high-performance computing facility for ensuring the efficient execution of computationally intensive models.

I sincerely acknowledge the financial support from the Federal Aviation Administration (FAA) without which this work would not have been possible. This research was supported by FAA Grant #17-G-005, "Enhancing the Capabilities of MAT213 for Impact Analysis," and FAA Grant #692M152340002, "Composite Material Modeling Enhancements to MAT_213 for Impact Analysis," under the supervision of Dr. Dan Cordasco, Technical Monitor.

I also want to acknowledge my friends and colleagues at ASU, including Dr. Avinaya Tripathi, Sahil Surehali, Dharanidharan Arumugam, Surajit Dey, Devansh Patel,

Mohammed Raihan, Thilak Rajendran Senthil, Sateesh Pechetti, Howard Chen, Seetha Pavan Tanneru, Sayee Srikarah Volaity, Pranav Acharya, Shubham Agrawal, and Oluwadamilare Adesina, for their support, and encouragement throughout this journey.

I am profoundly grateful to all my teachers, whose guidance and blessings have led me to this stage in my academic journey.

Finally, I extend my deepest appreciation to my family and friends for their unwavering love and support throughout my life.

TABLE OF CONTENTS

Page

LIST OF TABLES

Table Page

Table Page

Table Page

LIST OF FIGURES

Figure Page

Figure Page

Figure Page

Figure Page

Figure Page

Figure Page

Figure Page

Figure Page

Figure Page

LIST OF SYMBOLS

Symbols	Nomenclature
1-2-3 or a-b-c	Principal material directions
C	Orthotropic elastic stiffness matrix
c^d	Effective damage parameter
σ	Stress in the true space
σ^{eff}	Stress in the effective stress space
ε_f	Erosion strain
$\dot{\varepsilon}$	Total strain rate
$\dot{\varepsilon}^p$	Plastic strain rate
Δt	Time step
d_{ij}^{kl}	Damage parameter
E_{ii}	Elastic modulus in i^{th} direction
$f(\sigma)$	Yield function
F_i *or* F_{ij}	Yield function coefficients
f^{fail}	Failure parameter
G_{ij}	Shear modulus in i-j plane
h	Plastic potential function
H_{ij}	Flow rule coefficients
L_2^j	Distance of j^{th} point on failure surface from centroid of failure points
L_2^{FEA}	Distance of stress/strain Gauss point from centroid of failure surface
L_2^{PCD}	Average distance of neighborhood points from centroid of failure points
k	Number of nearest neighborhood points
M	Damage tensor matrix
v_{ij}	Poisson's Ratio
β	Reduction factor
n_{PC}	Number of point cloud failure data points
s	Scaling parameter in neural network method
v_i^j	j^{th} stress/strain component of i^{th} point on failure points
$\left(v^j\right)_c$	Centroid of j^{th} stress/strain component
v_j^m	Max absolute stress/strain of j^{th} stress/strain component

$\left(v_i^j\right)^t$	Transformed j^{th} stress/strain component of i^{th} point on failure points
v_{ij}	Transformed and normalized j^{th} stress/strain component of i^{th} point on failure points
w_N	Weight of N^{th} neighborhood point in simplified approximate nearest neighborhood method.

LIST OF ABBREVIATIONS

Abbreviations	Descriptions
4PBT	4-Point Bend Test
AD	Average Distance
AM	Additively Manufactured
ANN	Approximate Nearest Neighbor
BFS	Back-Face Signature
CDM	Continuum Damage Mechanics
CTOD	Crack Tip Opening Displacement
CZE	Cohesive Zone Element
CZM	Cohesive Zone Modeling
CTPD	Composite Tabulated Plasticity Damage
DIC	Digital Image Correlation
DCB	Double Cantilever Beam
ENF	End-Notched Flexure
FEA	Finite Element Analysis
F-NN	Feed-forward Neural Network
FPCD	Failure Point Cloud Data
FRPC	Fiber Reinforced Polymer Composites
GTFC	Generalized Tabulated Failure Criterion
IDW	Inverse Distance Weightage
ME	Multi-Element
OEPDMM	Orthotropic Elasto-Plastic Damage Material Model
OONM	Object-Oriented Numerical Methods
NN	Neural Network
PCFC	Point Cloud Failure Criterion
PFC	Puck Failure Criterion
PMD	Principal Material Direction
PMP	Principal Material Plane
PPRD	Post Peak Residual Damage
QS-RT	Quasi-Static and Room Temperature
RMSE	Root Mean Squared Error
RUC	Repeating Unit Cell
RVE	Representative Volume Element
RSM	Response Surface Methodology
SANN	Simplified Approximate Nearest Neighbor
SDM	Stress Degradation Model
SE	Single Element
SEM	Scanning Electron Microscopy
SGD	Surface Generated Data

SMM	Simplified Material Model
SPVCT	Stacked Ply Validation Compression Test
SPVTT	Stacked Ply Validation Tension Test
TSL	Traction Separation Law
TWFC	Tsai-Wu Failure Criterion
UCTWF	Uniaxial Compression Test with Fiber
UDC	Unidirectional Composite
UHPC	Ultra-High-Performance Concrete
UT	Ultrasonic Testing
V&V	Verification and Validation
VEVP	Visco-Elastic-Visco-Plastic
WWFE	World-Wide Failure Exercises

LIST OF TERMS ASSOCIATED WITH MAT_213 AND MULTISCALE MODELING

Terms	Definitions
Damage	Reduction in the stiffness of a material. Damage is used to model unloading and reloading.
Effective stress	Stress in undamaged material state.
Erosion	Deletion of an element from FE simulation.
Failure	State of a finite element when there is no more load carrying capacity, i.e., when stress drops to a very tiny fraction of the peak value.
Gage Section	Representative Volume Element section used for stress and strain extraction post-analysis.
Homogenized Property	Effective macroscopic property of the constituents of a composite in the RVE
Model curve	The *Model Curve* is a representative stress-strain curve for each experiment obtained by averaging the average stress value from all replicates for a given strain value. This curve is used in FE analyses.
Onset of Failure	Instance when the failure criterion condition is satisfied in a finite element.
Orthotropic Plasticity	Ability of material to undergo permanent deformation under the applied loads. The initiation of plasticity in CTPD is dictated by converting the classical Tsai-Wu failure criterion to a quadratic, orthotropic yield function.
Repeating Unit Cell (RUC)	A smallest repeating building block used to describe the microstructure of a composite material.
Representative Volume Element (RVE)	A set of RUCs with statistically significant volume that contains all the microstructural information needed to represent material behavior at a larger scale.
Residual Strength	The remaining strength in the material in the presence of damage.
True stress	Stress in damaged material state.

CHAPTER 1

INTRODUCTION

Composite materials have garnered significant attention in structural engineering due to their superior strength-to-weight ratios and customizable mechanical properties. These materials are widely used in aerospace, automotive, and other structural engineering applications. However, their complex heterogeneous nature, arising from the combination of fibers and matrix materials, presents significant challenges for accurate modeling and simulation. These materials are notoriously difficult to characterize via laboratory tests as well as model via numerical methods such as finite element methods. However, their use is increasing at a very rapid rate due to all the advantages that composite materials provide over other structural materials e.g., high strength to weight ratio, strength and stiffness, design flexibility, thermal and electric performance etc. These benefits have led to the redesign of structures for lightweight and durable solutions, driving widespread adoption in the aerospace industry.

The increasing adoption of composite materials in jet engine fan blades and containment structures has significantly enhanced engine performance, efficiency, and safety. Traditional metal alloys, such as titanium and aluminum, while strong and durable, impose weight penalties that limit fuel efficiency and design flexibility. In contrast, carbon fiber-reinforced polymers (CFRP) and hybrid composites offer superior strength-to-weight ratios, improved fatigue resistance, and greater damage tolerance, making them ideal for next-generation aircraft engines (GE Aerospace, 2015). The transition to composite fan blades, as seen in engines like the GE90 and GEnx, has enabled larger fan diameters and

reduced fuel consumption without compromising structural integrity (Upadhyay and Sinha, 2018). Additionally, composite-based containment structures provide critical impact resistance during fan blade-out events, ensuring passenger safety by preventing debris from breaching the engine nacelle (GE Aerospace, 2005). As the demand for more efficient and lightweight propulsion systems grows, understanding the behavior of composite materials under operational and extreme conditions becomes increasingly vital.

The characterization and modeling challenges have been recognized as legitimate investigation issues for researchers. For example, a NASA-commissioned report presents a detailed roadmap for integrated, multiscale modeling and simulation of materials and systems (X. Liu et al., 2018). The report was developed using input from over 450 contributors who identified not only the critical technical and cultural challenges/gaps facing the multiscale modeling community but also nine core technical work areas (Key Elements). The goal is to work towards maturation of these Key Elements to create a collaborative digital environment (i.e., tools, resources, practices, and people) necessary to efficiently, cost-effectively, and accurately design, manufacture, and certify future aerospace systems in the year 2040. Two of the nine key elements in the report deal with models and methodologies, and with multiscale measurement and characterization tools and methods. The length scale spans about 15 orders of magnitude (from pico/femto to macro) and 23 orders of magnitude in time (10^{-15} to 10^{9} s). The finite element method, the numerical tool discussed in this thesis, covers a fraction of this length-time domain shown in the report.

Building an accurate predictive numerical model for composite structural systems has been challenging because of the complicated behavior of the material system. Amongst several key components in building an end-to-end predictive modeling framework for composites, the five key areas are models to reliably predict deformation, damage, onset of failure, post-onset-of-failure, and erosion behaviors (Maurya and Rajan, 2024).

The deformation model captures the rate- and temperature-dependent elastic and inelastic behavior using a visco-elastic-plastic formulation (Hoffarth et al., 2017). The damage model accounts for the reduction in elastic stiffness and stresses along the principal material directions (Khaled et al., 2019a; Shyamsunder et al., 2021). The onset of failure model detects when the failure criterion condition is satisfied (Shyamsunder et al., 2020a, 2021), marking the point at which the material can no longer sustain additional load. The post-onset of failure model gradually reduces element stress, allowing load redistribution around failed elements, a critical step for preventing numerical instability during analysis (Shyamsunder et al., 2022b). Finally, the erosion model removes severely damaged elements from the finite element simulation to account for complete material failure (Shyamsunder et al., 2021). Together, these components form a robust framework for accurately predicting the behavior of composite structures under various conditions.

1.1 Background and Prior Art

Fiber reinforced polymer matrix composites are being used more and more in the aerospace and automotive industries. Because of this, accurate material models are needed to simulate how these materials deform, undergo damage, and fail. LS-DYNA (LS-DYNA®, 2022a)

is a commercially available transient dynamic finite-element code that is widely used in the aerospace industry. It has several material models that can be used to analyze composites. For example, MAT_22 is an orthotropic linear elastic material with limited capability to simulate the nonlinear shear response and the ratio of stress to strength to predict fiber and matrix failure with linear unloading. MAT_54/55 is an enhanced version of MAT_22 by allowing the reduction of the elastic constants which are selected based on the failure mode. MAT_55 uses the Tsai-Wu failure criterion for matrix failure mode, with the fiber failure modes the same as MAT_22. MAT_58 uses a continuum damage model for the initiation and accumulation of damage. Material stress strain curves are determined by user specified point wise properties - failure stress, failure strain etc. MAT_161/ MAT_162 uses a stress-to-strength ratio approach to specify the beginning of either fiber- or matrix-based failure then appropriate failure mode-based damage functions are used to compute the reduction in elastic moduli in each of the coordinate directions. MAT_117/MAT_118 are used for modeling elastic responses of composites using shell elements. These material models are based on standard composite lay-up theory, and are used for the computation of extensional, bending and coupling stiffness components. The only difference between MAT_117 and MAT_118 is that MAT_117 gives stiffness coefficients in the material coordinate system and MAT_118 gives the stiffness coefficients in the element coordinate system. Separate damage accumulation and modulus reduction functions based on the failure mode are used. The MAT_261 damage and failure model has separate models for different types of failure: fiber tension, fiber kinking, matrix tensile, and matrix compressive. Each of the failure criteria also has different functional

forms. MAT_262 uses an energy approach to generate damage functions in various coordinate directions within the context of a continuum damage mechanics formulation (LS-DYNA®, 2022b). A detailed comparison of the various composite constitutive models shows that the currently available models need improvements especially for modeling impact and crush problems (Shyamsunder et al., 2021, 2020b).

Even though all the material models discussed so far have been used to model impact response of polymer composites with some success, there are still ways in which their ability to predict can be improved. In general, the existing material models used in LS-DYNA assume that the nonlinear response of the composite is caused by either damage mechanisms or deformation mechanisms, e.g., plasticity. An improved model, on the other hand, should be able to simulate actual material behavior in which material nonlinearity is caused by a combination of deformation and damage mechanisms. Most of the existing material models that are currently used for composite impact analysis take inputs as point-wise characteristics, e.g., elastic modulus of elasticity, Poisson's ratio, etc., or a specified failure stress or failure strain. These assumptions lead to curve-fitting approximations of the material's stress-strain curves. This methodology results in either models with few parameters that are only a rough approximation of the actual stress-strain curve, or models with many parameters that require numerous difficult tests to determine their values or are obtained via numerical calibration. An improved approach would be to use data from a well-defined set of experiments in a tabulated form. In addition, many of the existing models are only suitable for use with two-dimensional thin shell elements which cannot capture the thorough-thickness response which may be significant in impact applications.

Therefore, it would be advantageous to have a three-dimensional formulation that is compatible with solid elements, in addition to a shell element formulation (Goldberg et al., 2016).

To address the needs of accurate modeling of composites, an orthotropic elasto-plastic damage material model has been developed at ASU through a joint research project funded by the Federal Aviation Administration (FAA) and the National Aeronautics and Space Administration (NASA). The developed material model has been implemented into LS-DYNA as COMPOSITE_TABULATED_PLASTICITY_DAMAGE (MAT_213) (Goldberg et al., 2016; Hoffarth et al., 2016a; Shyamsunder et al., 2020b). The terms OEPDMM and MAT_213 are used interchangeably. However, one should note that the OEPDMM theory can be implemented in any computer program.

1.2 Modeling of Structural Composites

Modeling structural composites is crucial for predicting their mechanical behavior, failure mechanisms, and overall performance under various loading conditions. Due to their heterogeneous and anisotropic nature, capturing their behavior accurately is inherently challenging. The main aspects of composite modeling include deformation, damage, and failure. Deformation is particularly complex due to the material's directional properties requiring models that account for both elastic and nonlinear behaviors. Damage often begins with matrix cracking and fiber-matrix de-bonding and is commonly modeled using techniques such as Continuum Damage Mechanics (CDM) and cohesive zone modeling (CZM). Failure occurs when the material loses its load-carrying capacity, and predicting it

is difficult due to the interaction of multiple damage mechanisms under multiaxial loading. While progress has been made in understanding deformation and damage, accurately predicting failure remains a significant challenge.

Accurately predicting composite failure, particularly in the context of the crush and impact loadings, is a huge challenge. For example, composites fail in compression in a variety of ways – fiber crushing, splitting, elastic micro-buckling, matrix failure and plastic micro-buckling, buckle delamination, shear-band formation, etc. There are other modes of failure involving fracture of the material that is brought about by fiber breakage, fiber micro-buckling, fiber pullout, matrix cracking, delamination, de-bonding, or any combination of these mechanisms.

1.2.1 Failure Modeling of Composite

Due to the heterogeneous and anisotropic nature of composite materials, failure prediction of structural composites has always been a challenging task. The current version of MAT_213 supports three failure theories: Generalized Tabulated Failure Criterion (GTFC), Puck Failure Criterion (PFC), and Tsai-Wu Failure Criterion (TWFC). The implementation of PFC and GTFC within MAT_213 has been presented in earlier work at ASU along with the validation tests carried out at quasi-static and room temperature (QSRT) (Shyamsunder et al., 2021, 2020b) and at high strain rate conditions (Shyamsunder et al., 2022a, 2022b). Despite its strengths, some limitations are discussed in aspects of modelling damage and failure for the composites.

1. The majority of failure models comprise a significant number of parameters related to failure, and acquiring these values from experiments can be challenging. For example PFC requires at least 15 failure related parameters (Shyamsunder et al., 2020a). To establish accurate numerical predictions, these parameter values are determined through a calibration process of the models to obtain valid numerical response.
2. To account for the post-failure behavior and ensure numerical stability, every stress-strain curve obtained from principal material direction/plane testing must be extended to include a post-failure regime. This extension is necessary even when the composite exhibits a brittle and sudden failure. Including the post-failure behavior is vital because it allows for a numerically stable solution as a finite element cannot be instantly eroded (deleted) once the failure criterion is met. Obtaining the post-failure regime from experiments is challenging and hence, post-peak data may be artificially added to the experimentally obtained pre-peak data (Shyamsunder et al., 2022b).
3. Both PFC and GTFC are failure criteria that depend on the element size which means the erosion of elements is sensitive to the mesh size (Shyamsunder, 2020).
4. It is generally accepted by researchers that the damage and failure of composite systems are influenced by the composite architecture and the constituent materials, and these aspects are not fully considered in any of the failure criteria (Talreja, 2016). As a result, these limitations hinder the proper correlation of macro-behavior with micro-behavior. Composite failure criteria are significantly more complex

compared to those used for materials like metals, necessitating the use of expensive multi-scale modeling approaches to develop more accurate predictive models (Shyamsunder, 2020; Shyamsunder et al., 2020b).

Over the last few decades, many failure prediction models have been developed by numerous researchers around the globe. Structural composites exhibit various failure modes based on loading direction, state of stress, and manufacturing defects. For example (Figure 1.1), the failure modes in fiber-reinforced polymeric composites (FRPC) include (a) fiber failure modes such as fiber breakage in longitudinal tension and localized fiber micro-buckling in longitudinal compression, (b) matrix and inter-laminar tension failure which are examples of matrix cracking, (c) matrix and inter-laminar compression failure, and (d) fiber-matrix shear-out failure which is cause of cracking or debonding in the fiber-matrix interface (Pinho et al., 2006; Zhang et al., 2016). To explore failure in distinct components of composites, researchers have investigated composite failure at multiple scales encompassing microscale, mesoscale, and macroscale levels (Figure 1.2). While examining FRPC, the microscale level focuses on the failure mechanisms within each individual fiber and the matrix phase surrounding the fibers. The mesoscale level examines failure homogeneity at the lamina level which is larger than the fiber size. On a larger scale, the macroscale model examines failure homogeneity in laminates which involves various stacking arrangements of laminae (Christensen, 2008; Gao et al., 2017; Nasirov et al., 2020).

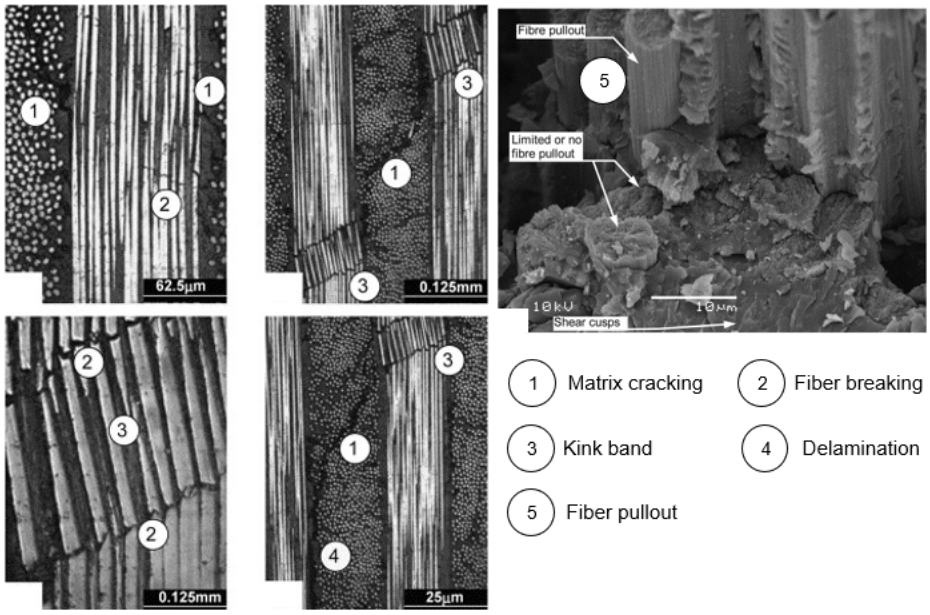

Figure 1.1: Scanning Electron Microscopy (SEM) Micrographs of Different Failure Modes (Pinho et al., 2006).

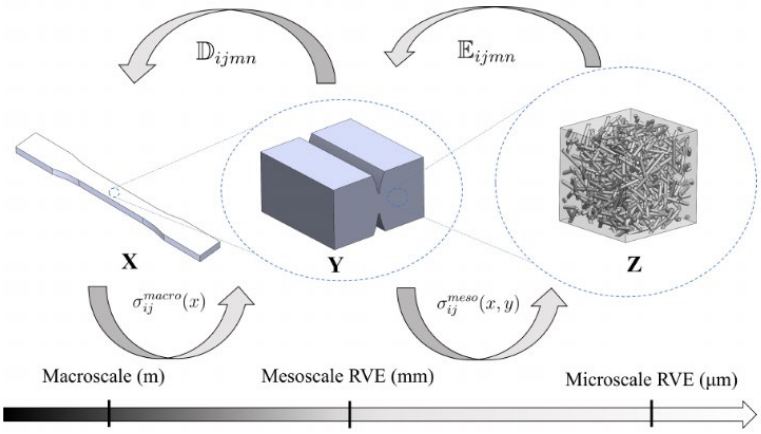

Figure 1.2: Macroscale, Mesoscale and Microscale Domains, and Three-Scale Hierarchy (Nasirov et al., 2020).

To fully utilize the mechanical properties of newly developed composites, accurate and trustworthy failure criteria are required. Over the last three decades to evaluate the state of the art in this area, World-Wide Failure Exercises (WWFE) have been organized where

participants have used benchmark experimental data to validate their theories (Hinton et al., 2004). The first World-Wide Failure Exercise (WWFE-I, 1996 - 2004) focused on response of fiber-reinforced polymer composites under in-plane biaxial loading in absence of stress concentrations. The failure theories considered include interactive failure theories, physically based failure criteria, damage mechanics, industrial and standard design code approaches as well as commercial software vendors and developers (Hinton et al., 2004). The predictions from theories were compared to experimental results as presented in (Hinton et al., 2004). The second World-Wide Failure Exercise (WWFE-II, 2007 - 2013) focused on the response of laminated fiber-reinforced composites under three-dimensional stress condition (Hinton and Kaddour, 2012). Twelve groups took part and ranking of the participating theories were made. There were few models which worked at micromechanical scale (Carrere et al., 2012; Huang et al., 2012) and rest were at meso-mechanical or macro-mechanical scales. The advantage of micro-mechanical model over meso-mechanical or macro-mechanical model is that it becomes "easy to determine the stresses in the constituent materials and to identify failure modes". In comparing various theories and experiments it was noted that "The designers, wishing to use the models benchmarked in WWFE-II, can only expect a few theories to give acceptable correlation (within 50%) with test data for 75% of the test cases used" (Kaddour and Hinton, 2013). The third world-wide failure exercise (WWFE-III, 2013-unknown end date) (Kaddour et al., 2013) focuses on modeling sub-critical damage under in-plane loading, especially continuum damage mechanics (CDM) and fracture mechanics approaches. From the three exercises, (Kaddour and Hinton, 2018) noted that "…none of the theories was capable of

predicting all the strength and deformation of the lamina and laminates within ±10% of the measured data".

A list of the more popular failure theories is presented next (Shyamsunder et al., 2020b). The purpose of listing these theories is not to present a detailed summary, as those can be found in other publications, but to illustrate the fact that there are numerous competing models where the failure definitions are extremely varied. It should be noted that the first three theories have been implemented in commercial finite element codes. The rest have been implemented into in-house codes written in a variety of languages (FORTRAN, MathCad, Visual Basic, Matlab etc.).

Tsai-Ha's Theory (Huang et al., 2013, 2012): The model is based on 3D laminate theory and is tied to the use of commercial finite element programs (MD NASTRAN and ABAQUS) via user-supplied subroutines. The failure model is based on micromechanics of failure (MMF) and considers failure in the fiber, matrix, and the fiber-matrix interface. A progressive damage model is used for the matrix. Thermal stresses are also considered in the model.

Pinho's Theory (Pinho et al., 2013, 2012): The model is implemented in a finite element program. The underlying constitutive model is tailored to capture the nonlinear behavior of unidirectional composites. A nonlinear response is considered in shear, and in the transverse and through-thickness directions. Matrix failure, fiber kinking and fiber tensile failure are handled separately. Fracture energy is used with each failure mode.

Puck's Theory (Deuschle and Puck, 2013; Matthias Deuschle and Kröplin, 2012): The model is implemented in ABAQUS via a user-supplied subroutine and in MAT_213 LS-

DYNA. The failure criteria for fiber fracture and inter-fiber fracture of unidirectional fiber-reinforced polymer composites are suitably modified forms of the Coulomb-Mohr theory of fracture.

Huang's Theory (Huang and Zhou, 2013; Zhou and Huang, 2012): The model is based on 3D laminate theory and the Bridging Model. The Bridging Model, a micromechanical theory, is modified and applied to laminates. Using the constituent properties as the material data, the model can predict the elastic-plastic behavior of a unidirectional (UD) composite and compute the stresses in the constituent materials. Final failure of the laminate takes place when fiber failure occurs, or the resin has failed in compression. The lamina is assumed to fail if any of its constituents fail, and subsequently the stiffness of the resin is reduced.

Carrere's Theory (Carrere et al., 2013, 2012): This is a multi-scale Micromechanical-based Hybrid Mesoscopic (MHM) progressive failure model. The model considers the effect of microdamage on the ply strength parameters. This involves the determination of microdamage in the UD ply using a damage law which is based on continuum damage mechanics. Nonlinear behavior is taken care of by a thermo-viscoelastic constitutive law. The failure criterion at the ply level depends on the effective strength which is a function of the microdamage and considers fiber-fracture (FF) and inter-fiber fracture (IFF) as modes of failure. The model distinguishes between tension and compression failures. The failure in each mode is then followed by the degradation of the failed ply based on a damage law.

Bogetti's Theory (Bogetti et al., 2013, 2012): A laminate theory is used to compute the effective laminate stress-strain response. Nonlinear behavior as well as progressive ply failure are accounted for in the model. The failure theory is based on computing and using the maximum 3D strain. The ply strains are used in nine modes of failure that are connected to strain values in the principal material directions. This is the only model that showed all the failure envelopes to be closed in WWFE-II.

Cuntze's Theory (Cuntze, 2013, 2012): The model assumes that the composite at the ply level is transversely isotropic. The failure model is based on the author's Failure Mode Concept and considers five modes of failure – two FF modes and three IFF modes. Furthermore, the interaction of all the modes is considered using a probabilistic based series spring model where the interaction exponent is obtained by curve fitting of experimental data.

Wolfe's Theory (Doudican et al., 2013; Zand et al., 2012): The model assumes that each lamina is an inelastic homogenous orthotropic material. Failure is based on a strain-energy formulation that incorporates the effects of in-plane thermal residual stresses accumulated during the curing of composite laminates and considers the failure of matrix and fiber separately. The failure criterion is described by the ratio of strain energy acquired to the strain energy at failure. The stiffness of the lamina is reduced once the failure criterion in the lamina is satisfied. It should be noted that the test cases which have been used in exercising the eight failure models listed above for WWFE-II, involve only static loading scenarios.

What can be garnered from the WWFE publications is that several failure theories for FRPC have been developed from physical and phenomenological points of view. Failure theories can be classified mainly in three categories: (1) limit or non-interactive failure criteria, (2) interactive failure criteria, and (3) partially interactive or failure mode based failure criteria (Chen et al., 2019; Daniel, 2007; De Luca et al., 2017; Gupta et al., 2022; Pai et al., 2023; Talreja, 2016; Tsai and Melo, 2016; Wang and Duong, 2016). Limit or non-interactive criteria include maximum stress criteria and maximum strain criteria which have shown poor predictions in the case of multiaxial loading. Interactive failure criteria like Tsai-Wu (Tsai and Wu, 1971) was developed to address the limitation of non-interactive failure criteria by allowing interaction between different stress and material strength components with a quadratic function. Several other popular and well-known interactive quadratic failure criteria are available and proposed by Tsai-Hill (Tsai, 1965), Azzi-Tsai (Azzi and Tsai, 1965), Hoffman (Hoffman, 1967), and Chamis (Chamis, 1969). To ensure a good fit of the failure surface to the experimental results, these failure criteria can be expressed in terms of the general Tsai-Wu failure criterion by varying the coefficients. The aforementioned interactive failure criteria have some drawbacks. For example, these criteria do not consider the composite's microstructure in the failure predictions but do consider homogenized properties obtained from experiments to make predictions at the laminae level (macroscale). These criteria don't consider the different failure modes that can be used to account for various damage mechanisms. Another point that should be noted while using quadratic failure criteria is that the predicted failure strength under a biaxial tensile stress state depends on compressive strengths or vice versa

which is physically unacceptable. Partially interactive or failure mode based failure criteria includes Hashin-Rotem criteria (Hashin and Rotem, 1973), Hashin's criteria (Hashin, 1980), Puck failure criteria (Puck and Schürmann, 2002) etc. Both Hashin-Rotem and Hashin's failure criteria include two failure modes, one associated with fiber failure and the other with matrix failure, distinguishing between tension and compression. PFC has also two different failure or fracture modes: fiber fracture (FF) and inter-fiber fracture (IFF) (matrix cracking). PFC differs from those proposed by Hashin in the matrix cracking mode. PFC has three different matrix cracking modes, differing in the angle between the fracture plane and the lamina, as well as in the type of load which causes the fracture. The failure model is an action-plane based model for transversely isotropic UD fiber reinforced composite lamina (Shyamsunder et al., 2021, 2020a). It should be noted that both Tsai-Wu and Puck failure surfaces are open in biaxial compression of $\sigma_2 - \sigma_3$ plane, implying that the Tsai-Wu and Puck failure models make an unreal assumption that the composite does not fail under biaxial compression (Katusele, 2021).

To describe the failure surface, all classical failure models use mathematical functions that assume a particular shape of the failure surface. For example, two-dimensional failure surface of Tsai-Wu in $\sigma_1 - \sigma_2$ plane is elliptical due to the quadratic nature of the equation defining the failure surface. In reality, the failure surfaces of actual composites often do not exhibit this simple shape (Goldberg et al., 2018). Many actual failure surfaces cannot be easily defined by a mathematical function of the stresses. Alternatively, complex failure surfaces for advanced materials can be successfully defined

using tabulated approaches based on experimental data. With the tabulated approach, failure surfaces can be defined experimentally, using any available failure model, or by combining experimental and numerically obtained "virtual" data. To take the advantage of tabulated approach, a stress-based generalized tabulated failure criterion (GTFC) was implemented in cylindrical coordinate system (r,θ) where r defines the magnitude of the failure surface and θ defines the relative location of the point on the failure surface in stress space (Goldberg et al., 2018). In general, the stress-based failure criteria predict only peak stresses and do not define post-peak behavior. Some recent efforts have shown that the failure behaviors depend not only on the failure onset predicted by the failure criteria, but also on the subsequent fracture propagation processes which is necessary for an impact analysis (Shyamsunder et al., 2022b; Sun et al., 2019). To predict post-peak behavior, a strain based GTFC is preferable (Shyamsunder et al., 2021).

Several studies have been conducted in the past where challenges in conducting and modeling the impact events are discussed (Polla et al., 2023; Shyamsunder et al., 2022b, 2022a). The accuracy of impact modeling requires temperature and strain rate dependent failure models. Most of the failure criteria are based on quasi-static and room temperature condition. A strain rate dependent engineering failure criterion was proposed based on a carbon/epoxy composite material that was characterized over a wide range of strain rates. It was found that both the moduli and strengths varied linearly with the logarithm of strain rate (Daniel et al., 2011). In this process, a failure criterion developed based on multiscale technique was modified to include the strain rate effect. Modified

failure criterion was validated with QS-RT and Charpy impact test along with the numerical model (Kwon and Panick, 2020).

To overcome most of the deficiencies listed previously, a multi-scale modeling approach is necessary. A new failure criterion hereafter referred to as the Point Cloud Failure Criterion (PCFC) (Katusele, 2021; Rajan et al., 2021) is currently in the development and implementation stage, and is the focus of this dissertation. The failure surface for PCFC is generated by experiments and multiscale modeling of a polymeric unidirectional composites (Harrington et al., 2017; Katusele, 2021; Khaled et al., 2021; Parakhiya, 2020).

1.2.2 Multiscale Modeling Framework (Maurya and Rajan, 2024)

Accurate prediction of failure of composite materials and structures for various system has been a difficult task because of the complexity of the failure micro-mechanisms. In absence of accurate models to predict the failure strength of composites, the burden of testing is huge to demonstrate safety in composite structures whose integrity depends on human lives. For instance, certification of an airframe structure requires testing of 10,000 material specimens in addition to testing of individual parts and structures up to and including entire tails, wing boxes, and fuselages (LLorca et al., 2011). However, both the failure criteria themselves and the experimental program used to evaluate them have certain limitations. Throughout the experimental program, one of the most common challenges encountered is the complexity of conducting combined stress state tests and accurately identifying initial failure stresses, damage propagation, and failure modes.

However, recent advances in multiscale simulations, along with more powerful computers and better modeling tools, are rapidly changing this scenario. The multiscale modeling strategy starts with the in-situ measurement of the matrix and interface mechanical properties to build up a framework of the numerical simulations which consider the relevant failure mechanisms at different length scales. The bottom-up approach is being developed to model composite materials and structures at various scales (Figure 1.3). This approach begins with the lowest level, using test coupons, and progresses to higher levels, including details, subcomponent, and component tests. The goal is to validate the accuracy and effectiveness of the analysis methods employed at each level. Moreover, the test coupons can be further classified and refined into different scales (Figure 1.2) based on the available information about the microstructure of the components. In the first, the ply properties are predicted using computational micromechanics based on the thermomechanical characteristics of the constituents (fiber, matrix, and interfaces), as well as the volume fraction and spatial distribution of the fibers within a single ply. A new reconstruction method based on SEM images in conjunction with genetic algorithm was used to create realistic microstructural models of a carbon fiber-reinforced polymeric composites CFRPC with desired volume fraction, size distribution, and spatial arrangement of embedded fibers (Ahmadian et al., 2017). Subsequently, computational meso-mechanics is used to determine the homogenized behavior of laminates starting from the homogenized ply properties, information about the laminate lay-up, and inter-ply behavior. Finally, the response of structural components until fracture is determined using these results within the computational macro-mechanics framework (LLorca et al., 2011).

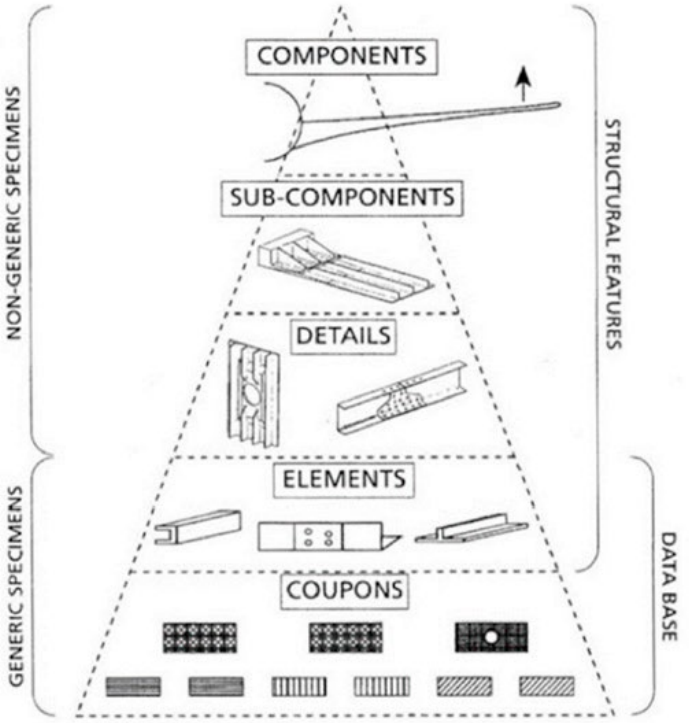

Figure 1.3: Schematic Diagram of Building Block Approach (FAA, 2018).

An examination of various approaches shows that several decisions need to be made to maintain a balance between accuracy, efficiency, and robustness in the generation of the constitutive model.

1. Is the goal of multiscale models to generate a framework for carrying out virtual testing of various composite systems to create input for finite element analysis?
2. At what length scale should multiscale modeling be conducted?
3. How should the RVE be generated? How should the RVE behavior be homogenized? Are deformation, damage and failure captured for use in a homogenized constitutive model?
4. How does the size of the RVE and the mesh density influence the results?

5. How can the generated data be used in a finite element analysis, e.g., are there multiple options available to measure if the computed state of stress or strain at a point in the FE model is inside or just outside the failure surface?
6. How should the developed approach be verified and validated?

State-of-the-art research that provides answers to some of these questions can be divided into two major categories – multi-scale modeling where the focus is on generating high-fidelity RVEs, and linking the behavior of RVEs to failure prediction. Amongst hundreds of publications, summary findings from the ones connected with the current work are discussed below.

Totry and his co-researchers (Totry et al., 2008a) show how the failure locus of unidirectional fiber reinforced composite can be constructed using computational micromechanics. Circular fibers are placed randomly in an RVE to model a unidirectional composite. The 2D RVE was subjected to transverse compression and longitudinal shear. In a follow-up paper (Totry et al., 2008b), a 3D RVE was constructed and used to model a unidirectional C/PEEK composite with similar loading. The generated failure locus showed excellent match when compared to Hashin (Hashin, 1980), Puck (Puck and Schürmann, 2002) and LaRC03(Davila et al., 2005) failure criteria when a strong interface between the fiber and the matrix was considered, while with weak interface, the failure criteria overestimated strength in the shear dominated region.

In (Herráez et al., 2016) the effect of the shape of the fiber cross-section such as circular, lobular, polygonal, and elliptical, are investigated to find the transverse strength

of unidirectional fiber composites. Two-dimensional RVEs containing uniform and random dispersions of 50% of these differently shaped fibers in a polymer matrix are modeled using periodic boundary conditions. A large enough RVE was used to ensure simulation results were size independent in a statistical sense, without exceeding computational resources. Results indicated that circular fibers exhibited the best homogenized behavior.

(Bouaoune et al., 2016) conducted a comparison between random and periodic microstructures that had similar fiber and matrix volume fractions. The difference in macroscopic elastic properties between random and periodic microstructure samples was approximately 1% at most. However, they caution that periodic RVEs are likely to miss predicting local behavior such as significant increase in both bulk and shear stresses brought about by regions where fibers are positioned very close to each other.

In (Z. Liu et al., 2018) details of a recently developed RVE package in LS-DYNA (LS-DYNA®, 2022a) are presented. The package offers two types of boundary conditions – periodic boundary conditions and displacement boundary conditions. They show that if the RVE is large enough, both types of boundary conditions yield similar results. 2D and 3D RVEs are used to illustrate how the package can be used to compute homogenized properties for inclusions embedded in the matrix and carbon fiber reinforced woven composite.

(Sun et al., 2018) use a modified conventional RVE (fiber and matrix with zero-thickness interface) to include an interphase region between the fiber and matrix to enhance the accuracy of the simulation outcomes. The thickness of the interphase region was

estimated using the transmission electron microscopy (TEM) technique, while the interphase material properties were characterized using molecular dynamics simulation and an analytical gradient model. In a follow up paper (Sun et al., 2019), failure data was generated by conducting in-plane and out-of-plane biaxial testing while accounting for the initial misalignment of fibers in the modified RVE and evaluated against existing classical failure criteria, including Puck, Tsai-Wu, Hashin failure, and others. The study revealed that classical failure criteria yielded different results compared to computational micromechanical models, specifically in the shear dominated region, when examining the combined transverse compression and in-plane shear, as well as the combined transverse compression and out-of-plane shear.

In (Katusele, 2021) a micromechanical model that generates limited failure surface of a unidirectional composite (T800/F3900) through in-plane and out-of-plane biaxial tests is presented. The generated failure surface was compared to classical failure theories, including Tsai-Wu and Puck. It was concluded that both Tsai-Wu and Puck failure surfaces are open in biaxial compression in the $\sigma_2 - \sigma_3$ plane, implying that these failure models make an unrealistic assumption about the strength of the composite.

Finally, in a more recent work (Balasubramani et al., 2022) investigate the influence of size and shape of 3D RVEs on homogenized effective properties and localized damage onset. They conclude that the properties obtained from both square and hexagonal representative volume elements (RVEs) converge when the RVEs contain more than 11 fibers.

While there is some consensus amongst these research efforts – classical failure theories have severe shortcomings, micromechanical model using RVEs is an effective way to study damage and failure of composites not afforded with laboratory testing with multi-axial state of stress, and sufficiently large RVEs provide reasonably accurate stress and strain predictions aided by inverse analysis/model calibration, a comprehensive framework that answers the six questions posed earlier and provides a path forward for modeling composite structures is missing.

1.2.3 Cohesive Zone Modeling of Composite (Maurya et al., 2024c)

Composite structures sustain significant internal damage when subjected to impact and crush loads. This internal damage is primarily the result of delamination caused by high normal, large tangential stresses, and stress concentrations generated by impact loads. This causes the interfaces of the laminate to de-bond. Delamination significantly reduces the structure's stiffness and strength. Moreover, it cannot be visually inspected because it occurs in the inter-laminar layers. Understanding the mechanisms of delamination in composite laminates is therefore essential for preventing catastrophic structural failure. Therefore, in recent decades, a significant amount of focus has been placed on the development of models to predict delamination. There are three different modes in delamination, including mode I or opening mode, mode II or shearing mode, and mode III or tearing mode. Among these damage modes, mode I, mode II and mixed mode (derived from combination of mode I and mode II) are the most commonly occurring delamination modes in laminated composite. Various numerical modeling techniques like Virtual Crack

Closing Technique (VCCT), Extended Finite Element Method, Multiscale Reduced Order Modeling (ROM), Random Lattice Method (RLM), and Cohesive Zone Modeling (CZM) can be used for modeling delamination. L. F.Alessandro Fascetti discusses each one of these methods, highlighting their salient features, advantages, challenges and applications in detail.

The Virtual Crack Closing Technique (VCCT) is based on the assumption that the energy released during delamination propagation equals the work required to close the crack back to its original position (Krueger, 2002; Turon et al., 2007). Similarly, the Extended Finite Element Method (XFEM) methods were specifically developed to overcome limitations of the classical FEM approach in the treatment of discontinuities such as cracks or material boundaries (Fascetti et al., 2021). Other techniques such as Multiscale Reduced Order Modeling (ROM) use a two-step process. In the first step, Representative Volume Elements (RVEs) are used at the micro-scale to model the constituent components of the composite and a singular domain constituted by cohesive bands. In the next step, a reduced order model is developed that extracts the relevant information from the RVE and carries out the computations at the macroscale in an efficient manner (Oliver et al., 2017). Random Lattice Method (RLM) leverages the duality of Delaunay and Voronoi tessellations of the computational domain to construct dense networks of 1-D elements that simulate interactions between material points within the domain (Fascetti et al., 2021). Cohesive Zone Modeling (CZM) and Tie-break Contact (TBC) techniques offer the simplest, yet the most powerful way delamination can be incorporated in finite element models. A comprehensive review of these techniques can be found in (Fascetti et al., 2021).

Recently, a new method called inter-laminar matrix stress modification method, has been offered as an alternative to the techniques discussed before. Prediction of delamination in a hybrid laminate made of steel sheet and carbon fiber reinforced plastic (CFRP) plate has been achieved by the researchers by modifying the stresses of an inter-laminar matrix layer in between the sheet and the plate. The normal and shear stresses of the matrix layer are modified with two coefficients which are determined by the critical displacements corresponding to the peak loads applied to the double cantilever beam (DCB) and end-notched flexure (ENF) tests on the hybrid laminate (Zhou et al., 2023; Zhou and Huang, 2022).

In a CZM model, a traction-separation law (TSL) is used to define the relationship between stress and relative displacements at the integration points of cohesive zone elements (CZE). In most common approaches, three parameters are used to define the behavior - peak traction, $\sigma_{\max}$, critical energy release rate, G_C, also known as fracture toughness representing the area under the curve, and the initial, undamaged linear region stiffness, k (Azevedo et al., 2015; Dourado et al., 2012; Jensen et al., 2019; Shanmugam et al., 2013). Similarly, in a TBC model, adjacent laminae are tied together, i.e., one node from each lamina is placed at the same location so that the two laminae are in contact. If the shear failure strength or the normal failure strength value is reached at the point of contact, the contact is broken resulting in two separate surfaces that are presented from penetrating each other using surface-to-surface contact detection algorithms (Dogan et al., 2012).

The consensus is that amongst all these approaches, the two that are attractive because of their low computational cost, high accuracy, and the ease with which they can be implemented in a computer program (LS-DYNA) are Cohesive Zone Modeling (CZM) and Tie-Break Contact.

1.3 Research Objectives

The deformation, damage, and failure modeling theory used in this work has been previously verified and validated through a combination of actual and virtual experimental data (Goldberg et al., 2016; Hoffarth et al., 2016a, 2017; Shyamsunder et al., 2020b, 2021). The specific research objectives of this dissertation are as follows:

1. Develop multiscale modeling of unidirectional carbon fiber-reinforced composites, i.e., Toray's T800/F3900 UDC. Subject these models to uniaxial and multiaxial loading conditions to determine the stress/strain state when the first element in the RVE would satisfy the failure criterion for the material and erode. Generate sufficient number of these points so as to have a sufficiently dense point cloud data approximating the failure surface.
2. Enhance the capabilities of MAT_213 by implementing a new failure model, the Point Cloud Failure Criterion that uses the generated point cloud data from (1).
3. Develop a new deformation sub-model, the Simplified Material Model (SMM), that can be used for modeling materials exhibiting little or no elasto-plastic behavior
4. Develop a traction-separation law for unidirectional carbon fiber-reinforced composites using inverse analysis.

5. Verify and validate the enhanced capabilities using statically loaded structural test data from Arizona State University (ASU) and impact test results from NASA Glenn Research Center (NASA-GRC). Reduce the number of material parameters that cannot be determined experimentally and hence, need to be calibrated, to as small a number as possible.
6. Demonstrate the versatility of MAT_213 across diverse material systems beyond traditional aerospace and automotive composites.

Chapter 2 outlines existing and new capabilities of MAT_213 and the experimental procedures needed to construct the input cards for all material models required for composite simulation.

Chapter 3 discusses multiscale material modeling to generate the point cloud data for PCFC.

Chapter 4 introduces the implementation of a new failure criterion, termed the Point Cloud Failure Criterion (PCFC).

In Chapter 5 presents the verification and validation tests for the developed models and capabilities.

Finally, Chapter 6 concludes the dissertation by discussing potential improvements to the material model for future work.

Equation Chapter (Next) Section 1

CHAPTER 2

MATERIAL MODEL AND GENERATION OF MATERIAL DATA

2.1 Material Model for Capturing Orthotropic, Visco-Elastic-Visco-Plastic Behavior

MAT_213 has three different sub-models - deformation, damage and failure as shown in Figure 2.1. The first sub-model, deformation is used to capture the rate and/or temperature dependent elastic and inelastic behavior via a visco-elastic-visco-plastic formulation (Hoffarth et al., 2017; Shyamsunder et al., 2022a). The second sub-model, damage is used to determine the reduction in the elastic stiffness and stresses of principal material directions (PMD) when loading and unloading take place. The damage sub-model supports both uncoupled and coupled damage parameters. Uncoupled damage signifies that damage is induced in a principal material direction (PMD) or principal material plane (PMP) and the elastic stiffness is reduced in the same PMD or PMP. On the other hand, coupled damage indicates that when damage is induced in a PMD or PMP, the elastic stiffness is reduced in a different PMD or PMP (Khaled et al., 2019a). The third sub-model, failure, is used to predict when there is no more load carrying capacity in a finite element and erosion of the element from the finite element model takes place.

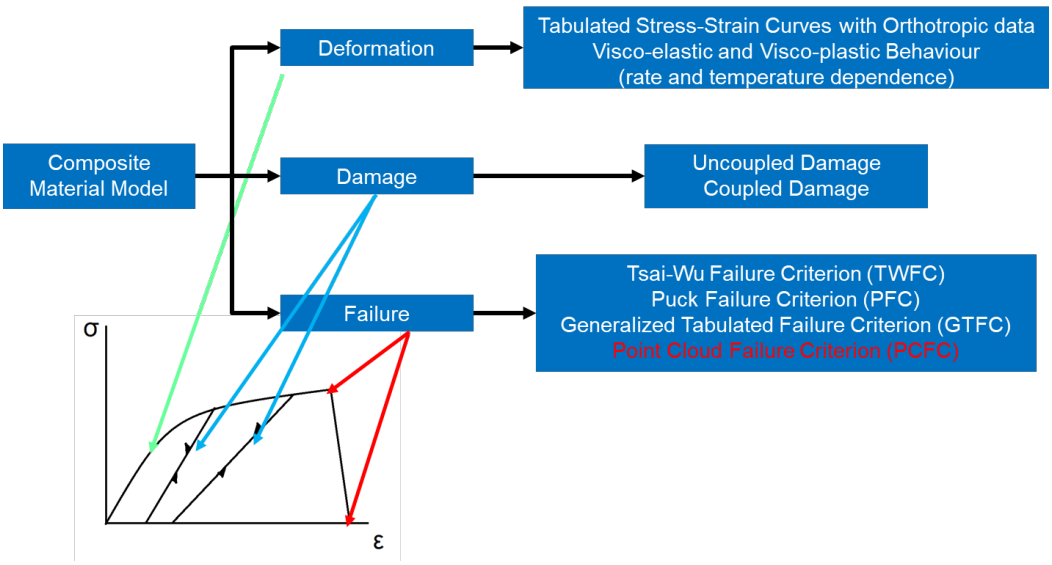

Figure 2.1: Components of OEPDMM Constitutive Model.

2.1.1 QS-RT Deformation Model

The elasto-plastic deformation in the model is based on a general orthotropic constitutive relationship

$$\sigma_{n+1} = \sigma_n + C\Delta t : \left(\dot{\varepsilon} - \dot{\varepsilon}^p\right) \tag{1.1}$$

where C is the orthotropic elastic stiffness matrix, Δt is the time step, $\dot{\varepsilon}$ is the total strain rate and $\dot{\varepsilon}^p$ is the plastic strain rate. The elastic stiffness matrix is written in terms of the compliance matrix as

$$\mathbf{C}=\mathbf{S}^{-1}=\begin{bmatrix} \frac{1}{E_{11}} & -\frac{v_{21}}{E_{22}} & -\frac{v_{31}}{E_{33}} & 0 & 0 & 0 \\ & \frac{1}{E_{22}} & -\frac{v_{32}}{E_{33}} & 0 & 0 & 0 \\ & & \frac{1}{E_{33}} & 0 & 0 & 0 \\ & & & \frac{1}{G_{23}} & 0 & 0 \\ & Sym & & & \frac{1}{G_{31}} & 0 \\ & & & & & \frac{1}{G_{12}} \end{bmatrix}^{-1} \tag{1.2}$$

The elastic moduli values to be used for Eqn. (2.2) are computed internally by MAT_213 using initial yield stress and the specified initial yield strain. The initiation and evolution of plasticity in deformation model is dictated by a general quadratic three-dimensional orthotropic yield function given by the Tsai-Wu failure model as shown in Eqn. (2.3) (Tsai and Wu, 1971).

$$\begin{aligned} f(\sigma)=a+\begin{pmatrix} F_1 & F_2 & F_3 & 0 & 0 & 0 \end{pmatrix}\begin{bmatrix} \sigma_{11} \\ \sigma_{22} \\ \sigma_{33} \\ \sigma_{12} \\ \sigma_{23} \\ \sigma_{13} \end{bmatrix} \\ +\begin{bmatrix} \sigma_{11} \\ \sigma_{22} \\ \sigma_{33} \\ \sigma_{12} \\ \sigma_{23} \\ \sigma_{13} \end{bmatrix}^{T}\begin{bmatrix} F_{11} & F_{12} & F_{13} & 0 & 0 & 0 \\ F_{12} & F_{22} & F_{23} & 0 & 0 & 0 \\ F_{13} & F_{23} & F_{33} & 0 & 0 & 0 \\ 0 & 0 & 0 & F_{44} & 0 & 0 \\ 0 & 0 & 0 & 0 & F_{55} & 0 \\ 0 & 0 & 0 & 0 & 0 & F_{66} \end{bmatrix}\begin{bmatrix} \sigma_{11} \\ \sigma_{22} \\ \sigma_{33} \\ \sigma_{12} \\ \sigma_{23} \\ \sigma_{13} \end{bmatrix} \end{aligned} \tag{1.3}$$

where $a=-1$, the $1-2-3$ subscripts refer to the principal material directions, and σ_{ij} represents the current yield stresses and the F_{ii} terms are the yield function coefficients and are computed based on the current yield stress values in the various coordinate directions as shown

$$
\begin{aligned}
F_1 &= \frac{1}{\hat{\sigma}_{11}^T} - \frac{1}{\hat{\sigma}_{11}^C} \qquad & F_{11} &= \frac{1}{\hat{\sigma}_{11}^T \hat{\sigma}_{11}^C} \qquad & F_{44} &= \frac{1}{\hat{\sigma}_{12}^2} \\
F_2 &= \frac{1}{\hat{\sigma}_{22}^T} - \frac{1}{\hat{\sigma}_{22}^C} \qquad & F_{22} &= \frac{1}{\hat{\sigma}_{22}^T \hat{\sigma}_{22}^C} \qquad & F_{55} &= \frac{1}{\hat{\sigma}_{23}^2} \\
F_3 &= \frac{1}{\hat{\sigma}_{33}^T} - \frac{1}{\hat{\sigma}_{33}^C} \qquad & F_{33} &= \frac{1}{\hat{\sigma}_{33}^T \hat{\sigma}_{33}^C} \qquad & F_{66} &= \frac{1}{\hat{\sigma}_{13}^2} \\
F_{12} &= \frac{2}{\left(\sigma_{12}^{45}\right)^2} - \frac{F_1+F_2}{\sigma_{12}^{45}} - \frac{1}{2}\left(F_{11}+F_{22}+F_{44}\right) \\
F_{23} &= \frac{2}{\left(\sigma_{23}^{45}\right)^2} - \frac{F_2+F_3}{\sigma_{23}^{45}} - \frac{1}{2}\left(F_{22}+F_{33}+F_{55}\right) \\
F_{13} &= \frac{2}{\left(\sigma_{13}^{45}\right)^2} - \frac{F_1+F_3}{\sigma_{13}^{45}} - \frac{1}{2}\left(F_{11}+F_{33}+F_{66}\right)
\end{aligned}
\tag{1.4}
$$

The yield stresses in the various coordinate directions are obtained from the input twelve sets of tabulated curves consisting of stress-strain curves in tension in the $1, 2$ and 3 directions, in compression in the $1, 2$ and 3 directions, tensorial shear stress-strain in the shear $1-2, 2-3$ and $1-3$ planes, and off-axis stress-strain curves in $1-2, 2-3$ and $1-3$ planes. If the material exhibits rate and/or temperature dependency, the twelve input curves can be defined for as many sets of different strain-rate and temperature combinations as required. These stress-strain curves can be obtained experimentally (Khaled et al., 2018) or by virtual testing (Harrington et al., 2017). The yield stresses need to be such that the

yield surface is convex at any point of time so that a converging solution is obtained (Hoffarth et al., 2016b). If for any reason, the yield surface is not convex, then convexity is enforced by modifying the off-axis yield function coefficients as

$$\begin{aligned} F_{12} &= -\frac{1}{2}\sqrt{F_{11}F_{22}} \\ F_{23} &= -\frac{1}{2}\sqrt{F_{22}F_{33}} \\ F_{13} &= -\frac{1}{2}\sqrt{F_{11}F_{33}} \end{aligned} \tag{1.5}$$

A non-associative flow rule is used to define the evolution of the plastic strain components, with the plastic potential for the flow rule calculated as

$$h = \sqrt{\begin{aligned} &H_{11}\sigma_{11}^2 + H_{22}\sigma_{22}^2 + H_{33}\sigma_{33}^2 + 2H_{12}\sigma_{11}\sigma_{22} + 2H_{23}\sigma_{22}\sigma_{33} + \\ &2H_{31}\sigma_{33}\sigma_{11} + H_{44}\sigma_{12}^2 + H_{55}\sigma_{23}^2 + H_{66}\sigma_{13}^2 \end{aligned}} \tag{1.6}$$

where H_{ij} are flow rule coefficients that depend on the average value of various plastic Poisson's ratios. Experimental data are used to calculate the flow rule coefficients as follows.

1. First, the unidirectional test results from the PMDs are used to calculate six of the coefficients. For example, Eqn. (2.7) shows how the simplified plastic potential function along with the relationship $\dot{\boldsymbol{\varepsilon}}^p = \dot{\lambda}\frac{\partial h}{\partial \boldsymbol{\sigma}}$, can be used to compute the plastic Poisson's ratios, ν_{ij}^p as,

$$
\begin{array}{lll}
\sigma_{11} \neq 0 & \sigma_{22} \neq 0 & \sigma_{33} \neq 0 \\
\nu_{12}^{p} = -\dfrac{\dot{\varepsilon}_{22}^{p}}{\dot{\varepsilon}_{11}^{p}} = -\dfrac{H_{12}}{H_{11}} & \nu_{21}^{p} = -\dfrac{\dot{\varepsilon}_{11}^{p}}{\dot{\varepsilon}_{22}^{p}} = -\dfrac{H_{12}}{H_{22}} & \nu_{32}^{p} = -\dfrac{\dot{\varepsilon}_{22}^{p}}{\dot{\varepsilon}_{33}^{p}} = -\dfrac{H_{23}}{H_{33}} \\
\nu_{13}^{p} = -\dfrac{\dot{\varepsilon}_{33}^{p}}{\dot{\varepsilon}_{11}^{p}} = -\dfrac{H_{13}}{H_{11}} & \nu_{23}^{p} = -\dfrac{\dot{\varepsilon}_{33}^{p}}{\dot{\varepsilon}_{22}^{p}} = -\dfrac{H_{23}}{H_{22}} & \nu_{31}^{p} = -\dfrac{\dot{\varepsilon}_{11}^{p}}{\dot{\varepsilon}_{33}^{p}} = -\dfrac{H_{13}}{H_{33}}
\end{array}
\tag{1.7}
$$

where, $\dot{\varepsilon}_{ij}^{p}$ are the plastic strain-rate components.

2. Second, since Eqn. (2.7) shows that the flow rule coefficients are not linearly independent. One of the flow rule coefficients is assumed – normally a value for the flow rule coefficient corresponding to the direction with the most plasticity is assumed, after which Eqn. (2.7) is used to compute the values of the remaining coefficients. The stress-strain curve in this direction is denoted as the master curve.
3. Third, the final three terms, H_{44}, H_{55} and H_{66}, are computed by fitting the shear curves with the master curve in the effective stress versus effective plastic strain space.

2.1.2 Damage Model

Damage in fiber reinforced-polymer matrix composites (FRP) is typically a phenomenon observed at the microscale which manifests itself as a degradation of macroscopic properties. Typically, damage does not result in a complete loss of load carrying capacity in the composite. Rather, it results in a reduction of load-carrying properties as the effective load transfer mechanisms are altered (Khaled, 2019; Khaled et al., 2019b). The damage model is based on the effective and true stress which are related through a fourth order damage tensor, M as shown below

$$\sigma = M : \sigma^{eff} \tag{1.8}$$

where σ is the Cauchy stress in the true space and σ^{eff} represents stress in the effective stress space. The true stress space refers to the stress that would be measured directly from an experiment whereas the effective stress space is in reference to the equivalent undamaged material. The damage sub-model controls both the pre-peak (loading and unloading), and the post-peak behavior of a finite element with peak denoting the instant when the primary stress component reaches a maximum value in a uniaxial test. M is a diagonal matrix shown as

$$M = \begin{bmatrix} M_{11} & 0 & 0 & 0 & 0 & 0 \\ 0 & M_{22} & 0 & 0 & 0 & 0 \\ 0 & 0 & M_{33} & 0 & 0 & 0 \\ 0 & 0 & 0 & M_{44} & 0 & 0 \\ 0 & 0 & 0 & 0 & M_{55} & 0 \\ 0 & 0 & 0 & 0 & 0 & M_{66} \end{bmatrix} \tag{1.9}$$

A diagonal damage tensor is commonly used in composite damage mechanics theories (Matzenmiller et al., 1995; Barbero, 2013), and is desirable for uniaxial load. Uniaxial loading in composite in a particular direction only leads to stiffness reduction in the direction of the load. However, several experimental studies in past (Ogasawara et al., 2005; Salavatian and Smith, 2014) have shown that load in one coordinate direction can lead to stiffness reductions in multiple coordinate directions with complex fiber architectures. Therefore, M is a semi-coupled matrix containing only diagonal element and each diagonal element contains coupled and semi-coupled damage parameter, e.g., $M_{kk} = M_{kk}\left(d_{11}^{kk}, d_{22}^{kk}, d_{33}^{kk}, d_{12}^{kk}, d_{23}^{kk}, d_{13}^{kk}\right)$ where, d_{ij}^{kl} are accounts for damage in the kl

direction due to loading in the ij direction. If the ij and the kl directions are the same, d_{ij}^{kl} is referred to as an uncoupled damage parameter; else, it is referred to as coupled damage parameter. The damage sub-model of MAT_213 is completely driven by the strain-based damage parameters. The directional plastic strains were used to compute the damage parameter $d_{ij}^{kl}\left(\varepsilon_{ij}^{p}\right)$ and used to track damage growth (Hoffarth et al., 2016a; Khaled et al., 2019a). A set of damage parameter versus total strain tabulated curves are given as input which is internally converted into damage parameter versus plastic strain. A total of eighty-four components can be defined which includes both un-coupled and coupled damage terms.

2.1.3 Rate and Temperature Dependent Model

A Visco-Elastic-Visco-Plastic (VEVP) behavior is modeled using a spring-dashpot system, as shown in Figure 2.2, to capture the rate dependency in MAT_213. These computations take place in the effective stress space (Khaled et al., 2018). The total stress is divided into two components (Eqn.(2.10)): equilibrium $\boldsymbol{\sigma}_{n+1}^{e,eff}$ and viscous $\boldsymbol{\sigma}_{n+1}^{v,eff}$, which are used to derive the stresses within the visco-elastic and viscoplastic elements, respectively.

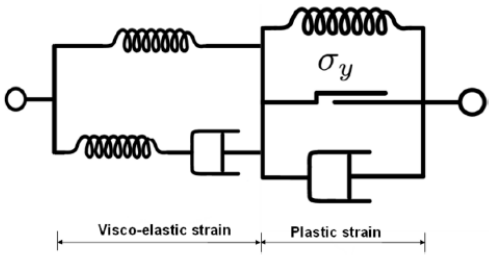

Figure 2.2: Schematic of VEVP Model.

$$\sigma_{n+1}^{t,eff} = \sigma_{n+1}^{e,eff} + \sigma_{n+1}^{v,eff} \tag{1.10}$$

$$\sigma_{n+1}^{e,eff} = \sigma_n^{e,eff} + C_\infty \dot{\varepsilon}_{n+1}^{avg} \Delta t \tag{1.11}$$

$$\sigma_{n+1}^{v,eff} = \sigma_n^{v,eff} \circ \beta + \left[\left(C - C_\infty \right) \circ B \right] \dot{\varepsilon}_{n+1}^{avg} \Delta t \tag{1.12}$$

where $\circ$ denotes Hadamard product between the matrices or vectors. C_∞ is the equilibrium stiffness matrix derived from the moduli corresponding to the quasi-static stress-strain curves while C is the total stiffness matrix generated using the moduli corresponding to the current strain rate. β and B are a vector and a matrix containing among other parameters exponential functions of decay constants (Shyamsunder, 2020).

During high strain rate deformation, the temperature within a material can increase (Farren & Taylor, 1925; Taylor & Quinney, 1934). This occurs because the plastic work done during deformation is converted into heat. This phenomenon is particularly critical in impact scenarios, where high strain rates are involved, leading to a softening of the material around the impact point (Johnston et al., 2017, 2018; Konieczny, 2018). Two different steps were used to capture the temperature dependency into MAT_213.

Step 1: The current temperature is calculated by considering both the reference temperature $\left(T_{n=0} \right)$ and the temperature increase within the material. The temperature rise due to plastic work is described by the following equation:

$$T_{n+1} = T_n + \Delta T \tag{1.13}$$

$$\Delta T = \frac{\beta_t}{c_p \rho} h \Delta \lambda \tag{1.14}$$

where, β_t is the Taylor-Quinney coefficient and c_p is the specific heat. These two parameters are required as input for computing the temperature increase.

Step 2: The total stiffness matrix, C in Eqn. (2.12) is generated using the moduli corresponding to the current strain rate and temperature.

2.1.4 Failure Model

The failure sub-model predicts when there is no further increase in the load-carrying capacity of a finite element, marking the failure onset. Once failure onset is detected, the model triggers a gradual reduction in the element's stiffness and stresses to simulate the progressive degradation of the material, in conjunction with the damage model. This gradual reduction is crucial for accurately capturing load redistribution within the structure while preventing numerical instability. To achieve this, a Stress Degradation Model (SDM) is used as mentioned in (Shyamsunder et al., 2021), which systematically decreases the element's stiffness and stress values over multiple simulation steps, rather than abruptly removing the element. This method helps maintain solution convergence and stability, especially in highly nonlinear simulations, where sudden changes could lead to catastrophic redistribution of loads around the first failed element. Ultimately, when the element's contribution becomes negligible, it is tagged for erosion, meaning it is removed from the finite element model to reflect complete material failure (Shyamsunder et al., 2021).

A summary of the existing failure models in MAT_213 is provided below, with detailed discussions available in (Shyamsunder, 2020; Shyamsunder et al., 2021).

2.1.4.1 Puck's Failure Criterion (PFC)

Puck's failure is an action-plane based model for transversely isotropic UD fiber-reinforced composite lamina (Matthias Deuschle and Kröplin, 2012; Deuschle and Puck, 2013; Shyamsunder et al., 2020a, 2021). Action plane refers to the plane that develops forces to resist the applied force. The theory considers two modes of failure separately - fiber fracture (FF) and inter-fiber fracture (IFF). Failure is dictated by a parameter called stress exposure, which is the ratio of the length of the vectors of the actual stress-state to that of the one corresponding to the failure envelope. Fiber failure is assumed to take place when the stress exposure is greater or equal to one, and is given by equation below

$$f_{EFF} = \frac{\left|\sigma_{\parallel}^{eq}\right|}{R} \tag{1.15}$$

where

$$\sigma_{\parallel}^{eq} = \sigma_{11} - \left(\nu_{\perp\square} - \nu_{\perp\square f} \frac{E_{\square}}{E_{\square f}} m_{\sigma_f} \right) \left(\sigma_2 + \sigma_3 \right)$$

$$R = \begin{cases} +R_{\square}^{t/c} \ for\ \sigma_{\parallel}^{eq} \geq 0 \\ -R_{\square}^{t/c} \ for\ \sigma_{\parallel}^{eq} < 0 \end{cases} \tag{1.16}$$

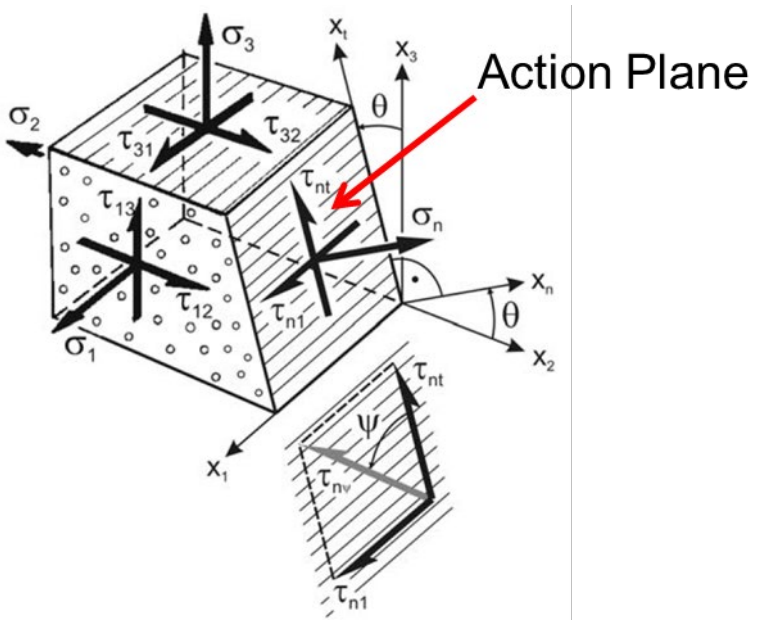

Figure 2.3: Stresses Acting on the Action Plane (Deuschle & Puck, 2012).

The inter fiber fracture is governed by the three stress quantities σ_n, τ_{nt} and τ_{n1} acting on the action plane which is inclined at an angle of θ to the 3-direction represents the section plane. These three stress quantities are derived from the stresses acting along the PMDs as,

$$\sigma_n = \sigma_{22}\cos^2\theta + \sigma_{33}\sin^2\theta + 2\sigma_{23}\sin\theta\cos\theta \tag{1.17}$$

$$\tau_{nt} = -\sigma_{22}\sin\theta\cos\theta + \sigma_{33}\sin\theta\cos\theta + \sigma_{23}\left(\cos^2\theta - \sin^2\theta\right) \tag{1.18}$$

$$\tau_{n1} = \sigma_{13}\sin\theta + \sigma_{12}\cos\theta \tag{1.19}$$

IFF onset is assumed to take place if the stress exposure, f_{EIFF}, is equal to or greater than one using equation below

$$f_{EIFF} = \begin{cases} \sqrt{\left[\left(\frac{1}{R_{\perp}^{At}} - \frac{p_{\perp\psi}^{t}}{R_{\perp\psi}^{A}}\right)\sigma_n(\theta)\right]^2 + \left(\frac{\tau_{nt}(\theta)}{R_{\perp\perp}^{A}}\right)^2 + \left(\frac{\tau_{n1}(\theta)}{R_{\square\perp}^{A}}\right)^2} + \frac{p_{\perp\psi}^{t}}{R_{\perp\psi}^{A}}\sigma_n(\theta) & \sigma_n \geq 0 \\ \sqrt{\left(\frac{\tau_{nt}(\theta)}{R_{\perp\perp}^{A}}\right)^2 + \left(\frac{\tau_{n1}(\theta)}{R_{\square\perp}^{A}}\right)^2 + \left(\frac{p_{\perp\psi}^{c}}{R_{\perp\psi}^{A}}\sigma_n(\theta)\right)^2} + \frac{p_{\perp\psi}^{c}}{R_{\perp\psi}^{A}}\sigma_n(\theta) & \sigma_n < 0 \end{cases} \tag{1.20}$$

where

$$R_{\perp\perp}^{A} = \frac{R_{\perp}^{c}}{2\left(1 + p_{\perp\perp}^{c}\right)} \tag{1.21}$$

$$\left(\frac{p_{\perp\psi}^{t,c}}{R_{\perp\psi}^{A}}\right) = \left(\frac{p_{\perp\perp}^{t,c}}{R_{\perp\perp}^{A}}\right)\cos^2(\psi) + \left(\frac{p_{\perp\square}^{t,c}}{R_{\square\perp}^{A}}\right)\sin^2(\psi) \tag{1.22}$$

$$\cos^2(\psi) = \frac{\tau_{nt}^2}{\tau_{nt}^2 + \tau_{nl}^2} \tag{1.23}$$

Once failure onset $(\varepsilon_0, \sigma_0)$ is detected for any Gauss point in the element, a linear stress degradation model is implemented by computing mode dependent failure strain.

$$\varepsilon_{ij}^{f} = \begin{cases} \varepsilon_{ij}^{0} + \frac{2\Gamma_f}{\sigma_{ij}^{0} L}, for\ ij = 11 \\ \varepsilon_{ij}^{0} + \frac{2\Gamma_I}{\sigma_{ij}^{0} L}, for\ ij = 22, 33 \\ \varepsilon_{ij}^{0} + \frac{2\Gamma_{II}}{\sigma_{ij}^{0} L}, for\ ij = 12, 23, 13 \end{cases} \tag{1.24}$$

where

$\Gamma_f, \Gamma_I, \& \Gamma_{II}$ are fracture energy for fiber mode, inter-fiber mode I and mode II respectively, L is characteristic length of element, computed as cube root of volume of element.

2.1.4.2 Tsai-Wu Failure Criterion (TWFC):

The Tsai-Wu failure criterion is a widely used method for predicting the failure of anisotropic composite materials (Tsai and Wu, 1971) such as fiber-reinforced composites. Unlike traditional isotropic failure criteria, the Tsai-Wu criterion accounts for the directional dependence of material strength, making it particularly suited for composites where properties vary with orientation. The criterion uses a quadratic equation (Eqn. (2.3)) to define a failure envelope in stress space incorporating both the material's tensile and compressive strengths in different directions and the interaction between these stresses.

This failure criterion is implemented with the following checks being carried out at the stress/strain Gauss points in each element.

The failure criterion is satisfied if $f(\sigma) > 0$ where

$$\begin{aligned} f(\sigma) = -1 &+ F_1\sigma_{11,i} + F_2\sigma_{22,i} + F_3\sigma_{33,i} \\ &+ F_{11}\sigma_{11,i}^2 + F_{22}\sigma_{22,i}^2 + F_{33}\sigma_{33,i}^2 \\ &+ F_{44}\sigma_{12,i}^2 + F_{55}\sigma_{23,i}^2 + F_{66}\sigma_{13,i}^2 \\ &+ 2F_{12}\sigma_{11,i}\sigma_{22,i} + 2F_{23}\sigma_{22,i}\sigma_{33,i} + 2F_{13}\sigma_{11,i}\sigma_{33,i} \end{aligned} \tag{1.25}$$

where

$\sigma_{kk,i}; kk = 11, 22, 33, 12, 23, 13$ are stress state of ith Gauss point.

$$
\begin{aligned}
F_1 &= \frac{1}{\hat{\sigma}_{11}^T} - \frac{1}{\hat{\sigma}_{11}^C} \qquad & F_{11} &= \frac{1}{\hat{\sigma}_{11}^T \hat{\sigma}_{11}^C} \qquad & F_{44} &= \frac{1}{\hat{\sigma}_{12}^2} \\
F_2 &= \frac{1}{\hat{\sigma}_{22}^T} - \frac{1}{\hat{\sigma}_{22}^C} & F_{22} &= \frac{1}{\hat{\sigma}_{22}^T \hat{\sigma}_{22}^C} & F_{55} &= \frac{1}{\hat{\sigma}_{23}^2} \\
F_3 &= \frac{1}{\hat{\sigma}_{33}^T} - \frac{1}{\hat{\sigma}_{33}^C} & F_{33} &= \frac{1}{\hat{\sigma}_{33}^T \hat{\sigma}_{33}^C} & F_{66} &= \frac{1}{\hat{\sigma}_{13}^2} \\
F_{12} &= \frac{2}{\left(\hat{\sigma}_{12}^{45}\right)^2} - \frac{F_1 + F_2}{\hat{\sigma}_{12}^{45}} - \frac{1}{2}\left(F_{11} + F_{22} + F_{44}\right) \\
F_{23} &= \frac{2}{\left(\hat{\sigma}_{23}^{45}\right)^2} - \frac{F_2 + F_3}{\hat{\sigma}_{23}^{45}} - \frac{1}{2}\left(F_{22} + F_{33} + F_{55}\right) \\
F_{13} &= \frac{2}{\left(\hat{\sigma}_{31}^{45}\right)^2} - \frac{F_1 + F_3}{\hat{\sigma}_{31}^{45}} - \frac{1}{2}\left(F_{11} + F_{33} + F_{66}\right)
\end{aligned}
\tag{1.26}
$$

where

$\hat{\sigma}_{ij}^{ang}$ are the strength values for different stress components.

Once the onset of failure is detected, a SDM is used to prevent numerical instability. To activate SDM with Tsai-Wu failure criterion, directional residual strengths and erosion strains must be provided as additional inputs.

2.1.4.3 Generalized Tabulated Failure Criterion (GTFC)

GTFC supports two modes of failure – in-plane and out-of-plane modes. The in-plane (IP) failure surface where $\varepsilon_{IP^{FAIL}}^{eq}$ is a function of the failure angle, θ_{IP}, and can take any shape depending on the composite properties. The equivalent strain, ε_{IP}^{eq}, failure angle, θ_{IP}, and the in-plane failure state are computed for each time step and element Gauss point as

$$\varepsilon_{IP}^{eq} = \sqrt{\varepsilon_{11}^2 + \varepsilon_{22}^2 + 2\varepsilon_{12}^2} \tag{1.27}$$

$$\theta_{IP} = \cos^{-1}\left(\frac{\sigma_{22}}{\sqrt{\sigma_{22}^2 + \sigma_{12}^2}}\right) \tag{1.28}$$

$$d_1 = \frac{\varepsilon_{IP}^{eq}}{\varepsilon_{IP^{FAIL}}^{eq}} \tag{1.29}$$

Similarly, the out-of-plane (OOP) failure surface can be constructed with the failure surface expressed in terms of $\varepsilon_{OOP^{FAIL}}^{eq}$ as a function of θ_{OOP} for a given σ_{33} where

$$\varepsilon_{OOP}^{eq} = \sqrt{\varepsilon_{33}^2 + 2\varepsilon_{13}^2 + 2\varepsilon_{23}^2} \tag{1.30}$$

$$\theta_{OOP} = \cos^{-1}\left(\frac{\sigma_{13}}{\sqrt{\sigma_{13}^2 + \sigma_{23}^2}}\right) \tag{1.31}$$

Similarly, the out-of-plane failure state d_2 is computed as

$$d_2 = \frac{\varepsilon_{OOP}^{eq}}{\varepsilon_{OOP^{FAIL}}^{eq}} \tag{1.32}$$

An element is eroded if $d \geq 1$ where

$$d = \begin{cases} \max(d_1, d_2) & if\ n = 0 \\ \sqrt[n]{(d_1)^n + (d_2)^n} & if\ n > 0 \end{cases} \tag{1.33}$$

and n is a user defined interaction parameter that can be used to couple the in-plane state of stress/strain to the out-of-plane state of stress/strain. GTFC requires two sets of tabulated input - the equivalent failure strain and the corresponding failure angle for in-plane $\left(\varepsilon_{IP^{FAIL}}^{eq}, \theta_{IP}\right)$ and the out-of-plane $\left(\varepsilon_{OOP^{FAIL}}^{eq}, \theta_{OOP}\right)$ failure modes.

2.2 Enhancements to the Material Model

2.2.1 Simplified Material Model (SMM)

The full version of MAT_213 includes algorithms for computing visco-elastic and visco-plastic deformations as well as plastic strain-based damage. While these features allow for highly detailed and accurate simulations, they also produce a computationally expensive material model. Additionally, the number of input parameters required for these complex algorithms can pose significant challenges particularly formaterials where there is little or no evidence of plastic deformations.

A simpler and computationally efficient version of MAT_213 has been developed and implemented to handle materials that exhibit purely linear, elastic, orthotropic behavior with tension-compression asymmetry. This simplified version is activated by setting all flow rule coefficients to zero. The model eliminates all plasticity-related computations. This reduction in computational complexity improves simulation speed and efficiency while also making the model more user-friendly by simplifying input requirements.

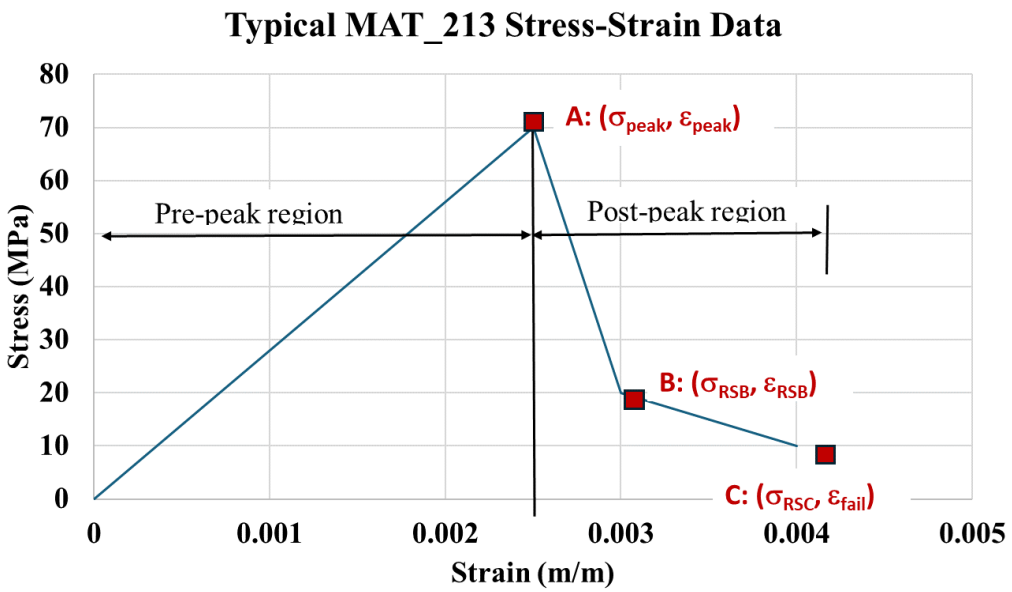

Figure 2.4: Typical Stress-Strain Data for Use in SMM.

A typical SMM stress-strain curve is shown in Figure 2.4. The different key locations in a typical curve are marked in Figure 2.4. Point A represents the peak stress, σ_{peak}. The stress-strain values at this location are used in computing the elastic modulus of elasticity and establish the total stiffness matrix C (Eqn.(2.2)). The post-peak region is divided into two parts – strength degrades to a final residual strength value, σ_{RS} (point B), and the stress is held constant till the failure strain, ε_{fail} (point C) is reached.

During the simulation, stresses are updated using an elastic predictor, ensuring that the material's behavior remains within the elastic regime until this peak stress is reached.

$$\sigma_{n+1} = \sigma_n + C\Delta t : \left(\dot{\varepsilon}_{n+1} - \dot{\varepsilon}_n\right) \tag{1.34}$$

SMM incorporates a semi-coupled damage formulation. Unlike the full version which uses plastic strains to compute the damage parameter, the simplified version utilizes

directional total strains. This change simplifies the damage assessment process while maintaining the needed accuracy. Importantly, all three failure models available in the original MAT_213 can still be activated in the simplified version. This ensures that users retain the flexibility to model different failure mechanisms while benefiting from the reduced complexity and improved computational performance of the simplified model, if appropriate.

2.2.2 Point Cloud Failure Criterion

The Point Cloud Failure Criterion relies on the generated point cloud data for *onset of failure* prediction (Rajan et al., 2021), hereinafter referred to as *failure onset*. Once the points on the failure surface are generated (Figure 2.5), the Approximate Nearest Neighbor (ANN) or neural network methods are used to determine if a given stress or strain tensor computed at a finite element Gauss point is inside or outside the point cloud surface. In general, a set of points p in $d-$ dimensional space is the input to the ANN method. The input data is preprocessed into a data structure such that when given a query (stress or strain tensor computed at a finite element Gauss point), efficient calculations can take place to ascertain whether the query point is inside or outside of the *d*-dimensional point cloud failure surface. Chapter 3 provides a detailed discussion on the generation of failure points using a multiscale modeling framework, while Chapter 4 elaborates on the PCFC framework, followed by problems that are used in its verification and validation steps.

Once failure onset is detected, a stress degradation model (SDM) is implemented to avoid numerical instability. The implemented SDM model is discussed in detail in Section 4.2.

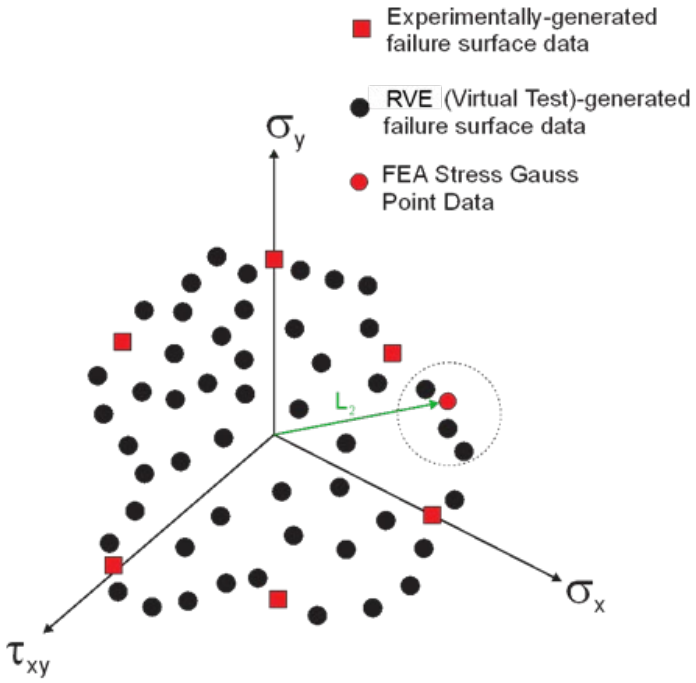

Figure 2.5: A Typical Stress-Based Point Cloud for Thin Shell Element.

2.3 QS-RT Tests to Generate Data for MAT_213

This section covers the generation of material data for different composite systems (Table 2.1) selected to capture a broad spectrum of mechanical behavior and failure characteristics that can be modeled using MAT_213. These systems include two fiber types — one high-stiffness (T800) and one high-toughness (IM7) — paired with either a thermoset or thermoplastic matrix. Additionally, both continuous and discontinuous fiber architectures were tested to assess the influence of fiber arrangement on material response. This diverse selection enables a comprehensive evaluation of how fiber type, matrix composition, and fiber continuity affect failure mechanisms, making the dataset valuable for a wide range of applications.

To accurately model both elastic and plastic deformations, MAT_213 requires twelve stress-strain curve datasets, direction-dependent material constants, and flow rule coefficients as input. These inputs are derived from post-processing results of twelve quasi-static, room-temperature (QS-RT) experiments. These experiments consist of three principal material direction (PMD) tension and compression tests, as well as three principal material plane (PMP) shear and 45° off-axis tests Details of the test equipment and procedures, test results, and photographs of tested specimens highlighting failure modes are documented in publicly available reports (FAA Report, 2019; Holt et al., 2022; Maurya et al., 2023, 2025).

Table 2.1: Characteristic of Four Different Composite Systems.

Composite	**Fiber**	**Matrix**	**Fiber volume fraction (%)**	**Fiber distribution**
T800-F3900 Toray composite	T800	F3900 (Thermoset)	60	Continuous
IM7-8552	IM7	8522 (Thermoset)	57	Continuous
HexPly Unidirectional Composite (HUDC)	IM7	PEKK (Thermoplastic)	57	Continuous
Tuff Short fiber Composite (TSFC)	IM7	PEKK (Thermoplastic)	50	Discontinuous

2.3.1 Tension Tests in the Three Principal Material Directions (1, 2, and 3)

The specimen geometry for both the 1- and 2-direction tension tests was determined according to ASTM D3039 (ASTM D3039, 2014). However, the geometry of 3-direction specimens deviates from ASTM standards as it is difficult to manufacture a sufficiently thick panel. A thick unidirectional panel was manufactured for 3-direction tension

specimen as mentioned in reports (FAA Report, 2019; Maurya et al., 2023, 2025). To ensure accurate specimen placement in the grips, three layers of fiberglass tabs were utilized to create a pocket capable of accommodating sufficiently long specimens (Khaled et al., 2018). Figure 2.6 to Figure 2.8 show the processed stress-strain curves along with the associated *Model Curve*. All three PMDs have primarily linear elastic behavior in tension, but 2-direction has a slight nonlinearity before failure. While the failure in all three directions was brittle, the failure mode in each of the PMDs was distinct. 1-direction specimens have two distinct failure modes: matrix splitting parallel to the fibers, followed by fiber breakage in the gage section. Transverse cracking in the matrix causes inter-fiber failure in 2-direction specimens and inter-laminar failure in 3-direction specimens. The test results for 3-direction specimens show a significant scatter. One possible explanation is the small size of the specimens used in 3-direction tension tests. Smaller specimens may be more susceptible to local defects and variations, resulting in increased scatter in test data.

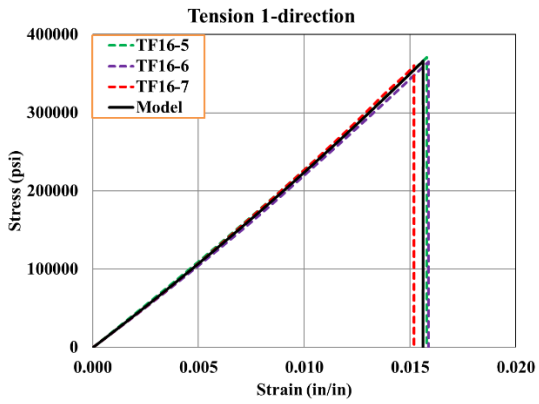

(a)

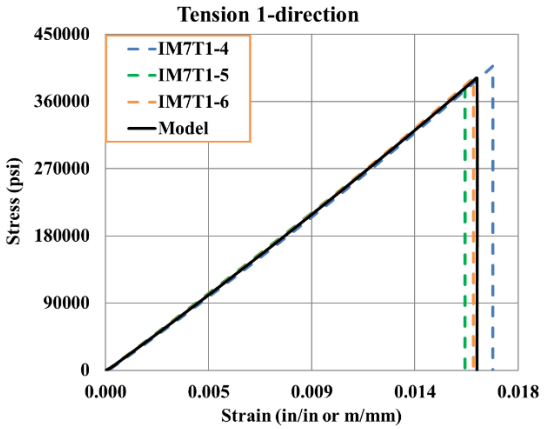

(b)

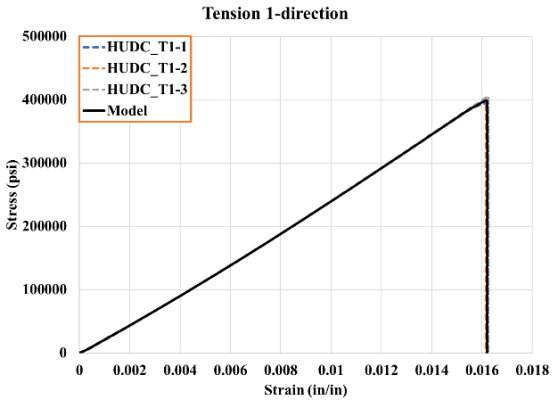

(c)

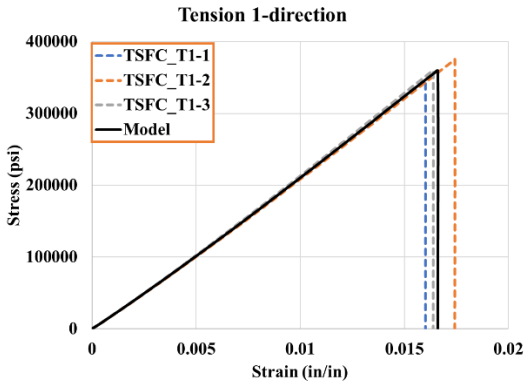

(d)

Figure 2.6: Stress-Strain Curves from 1-Direction Tension Tests - (a) T800-F3900, (b) IM7/8552, (c) HUDC, and (d) TSFC.

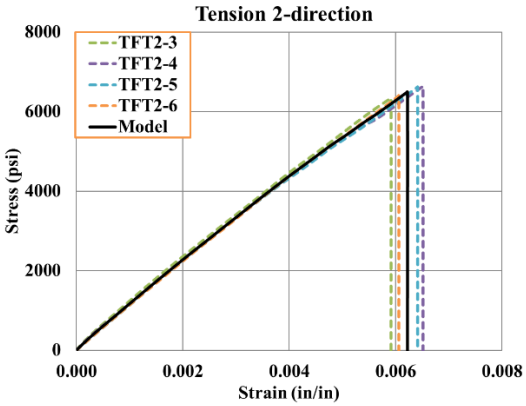

(a)

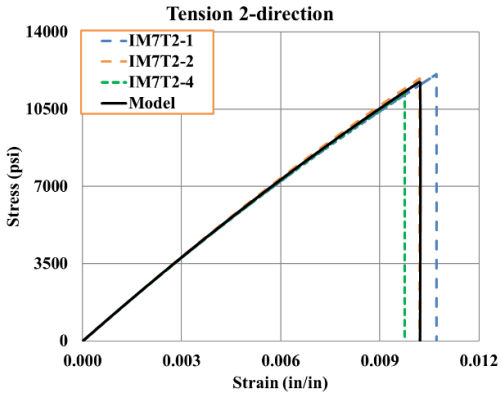

(b)

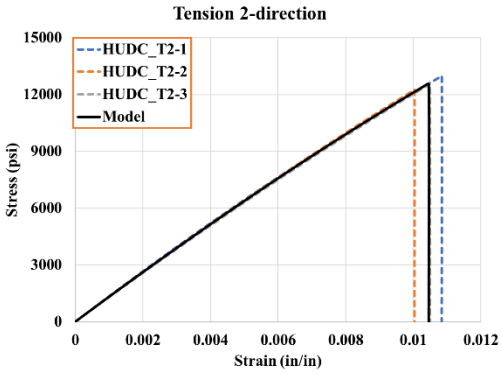

(c)

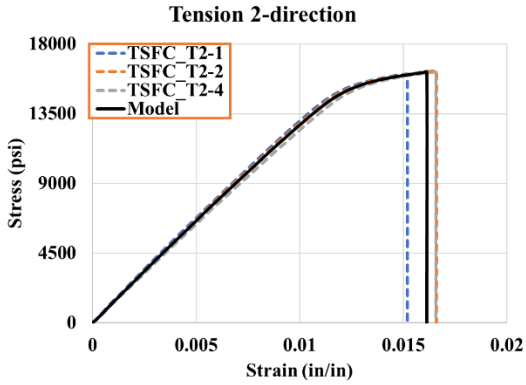

(d)

Figure 2.7: Stress-Strain Curves from 2-Direction Tension Tests - (a) T800-F3900, (b) IM7/8552, (c) HUDC, and (d) TSFC.

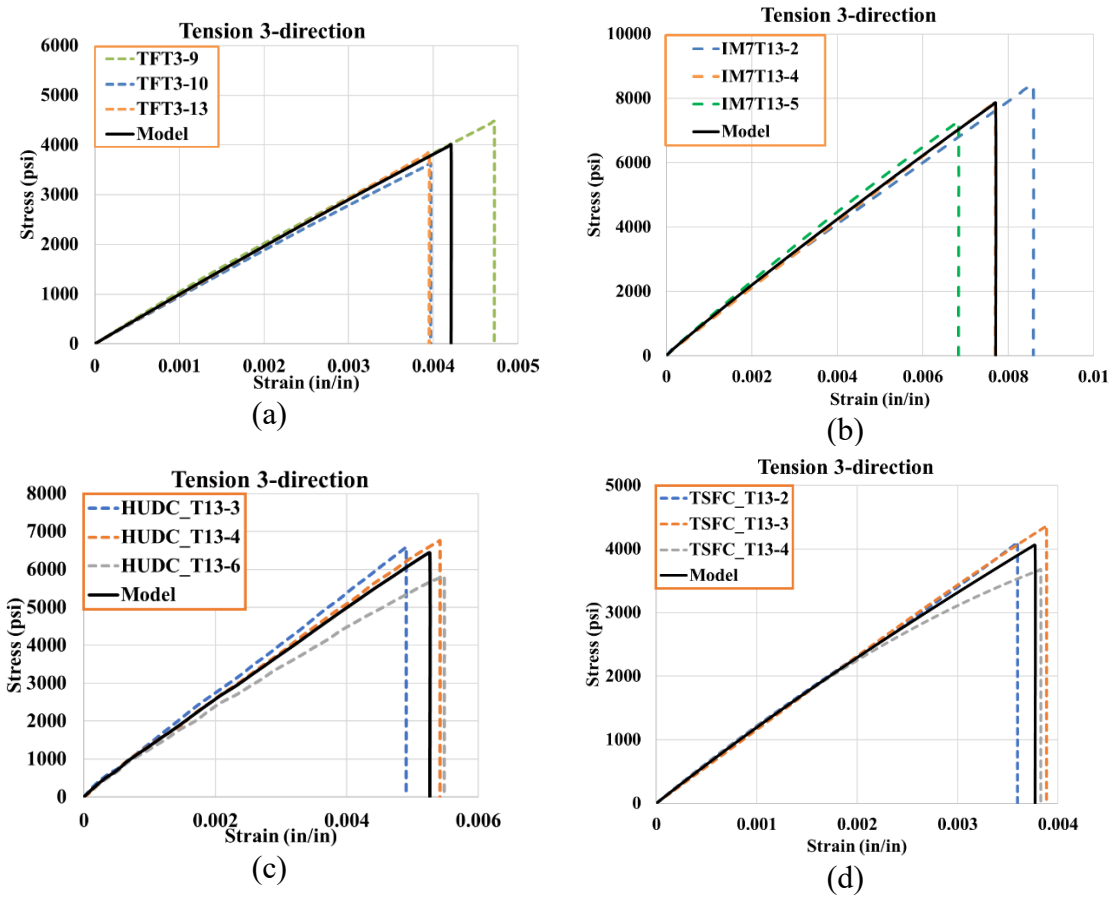

Figure 2.8: Stress-Strain Curves from 3-Direction Tension Tests - (a) T800-F3900, (b) IM7/8552, (c) HUDC, and (d) TSFC.

2.3.2 Compression Tests in the Three Principal Material Directions (1, 2, and 3)

The specimen geometries were determined for both 1- and 2-direction compression tests using ASTM D3410 (ASTM D3410, 2008) and ASTM D6641 (ASTM D6641, 2016) using combined loading compression (CLC) test fixtures. Instead of using the cylindrical specimens that are recommended by ASTM D7291 (ASTM D7291, 2007) for 3-direction compression tests, cube specimens were used since they are easier to machine and prepare for testing. Figure 2.9 to Figure 2.11 show the processed stress-strain curves along with the associated *Model Curve*. 1-direction specimens exhibit linear elastic behavior, whereas 2-

and 3-direction specimens exhibit nonlinear behavior in compression. All three PMDs exhibit distinct failure modes in compression. 1-direction specimens failed due to end crushing followed by matrix splitting parallel to the fibers, 2-direction specimens failed due to transverse cracking in the gage section, and 3-direction specimens failed due to a crack formed between and parallel to the plane of the fibers (2-3 PMP).

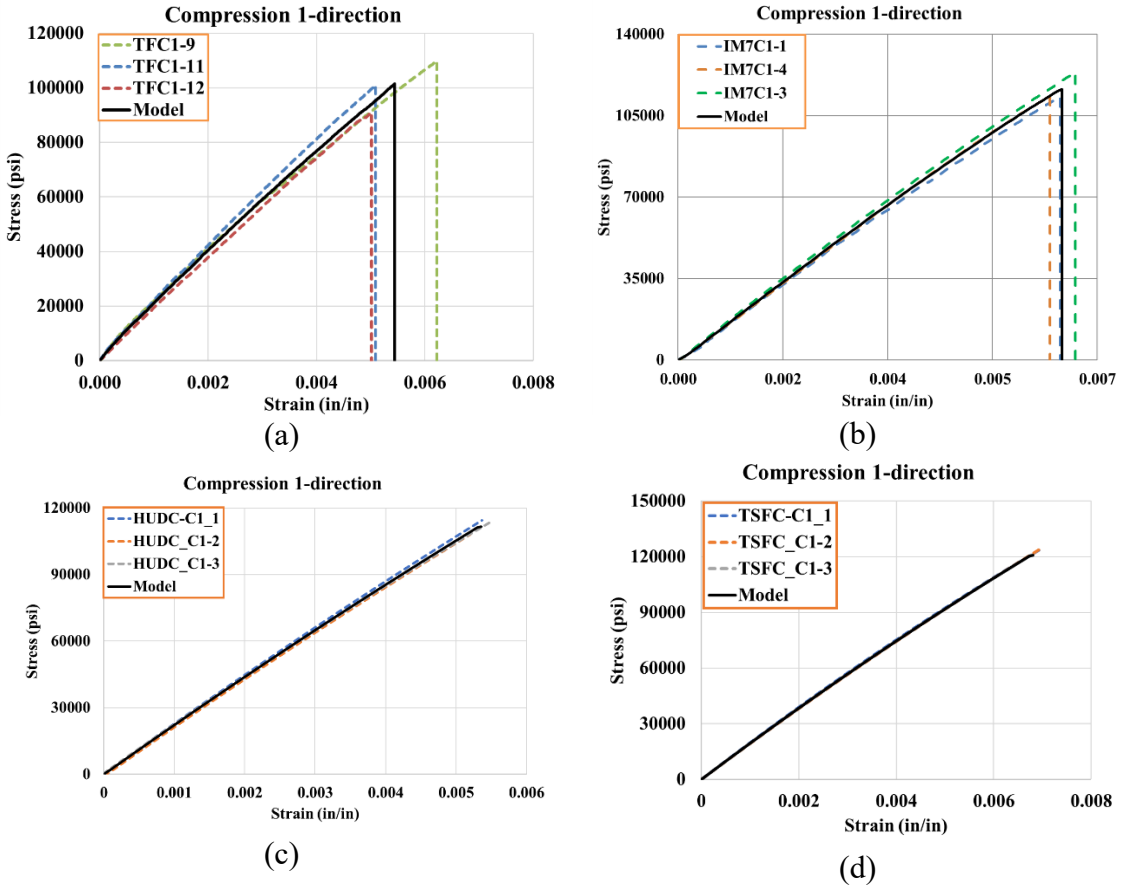

Figure 2.9: Stress-Strain Curves from 1-Direction Compression Tests - (a) T800-F3900, (b) IM7/8552, (c) HUDC, and (d) TSFC.

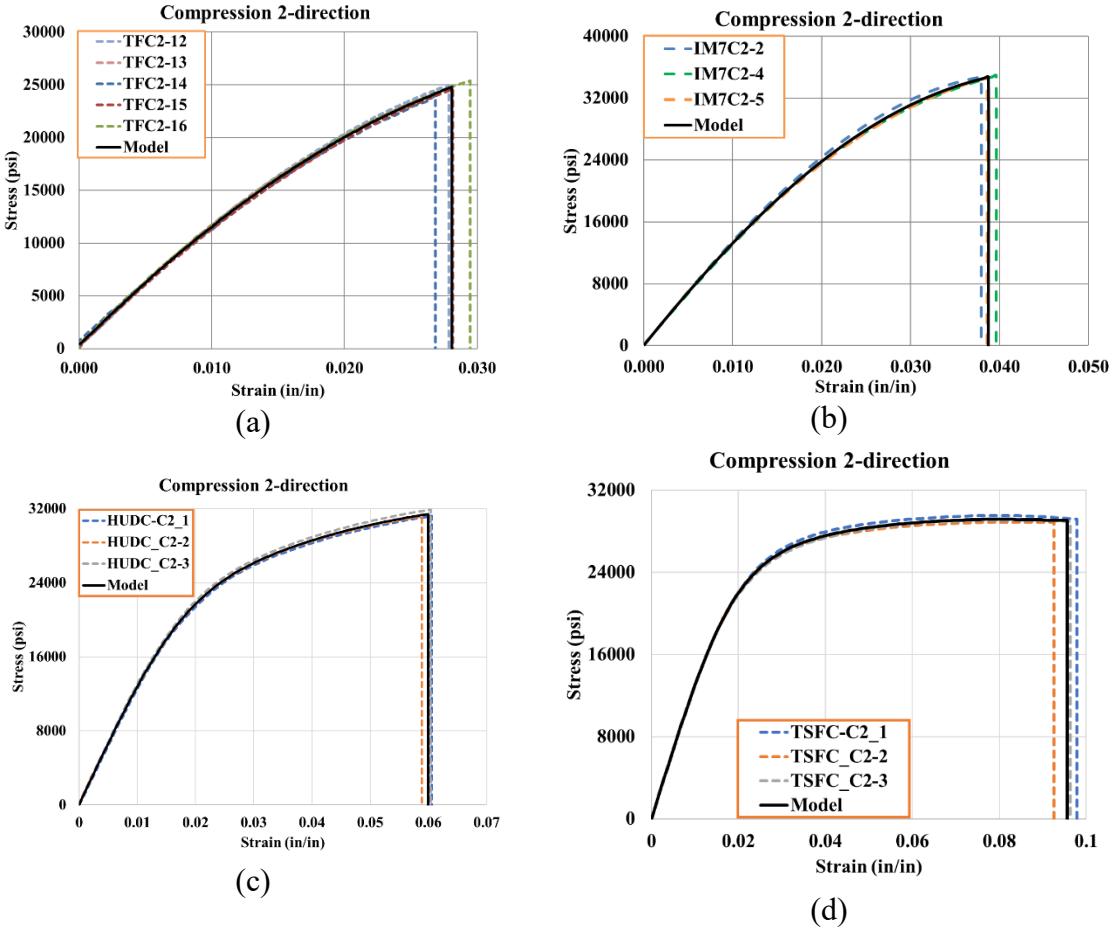

Figure 2.10: Stress-Strain Curves from 2-Direction Compression Tests - (a) T800-F3900, (b) IM7/8552, (c) HUDC, and (d) TSFC.

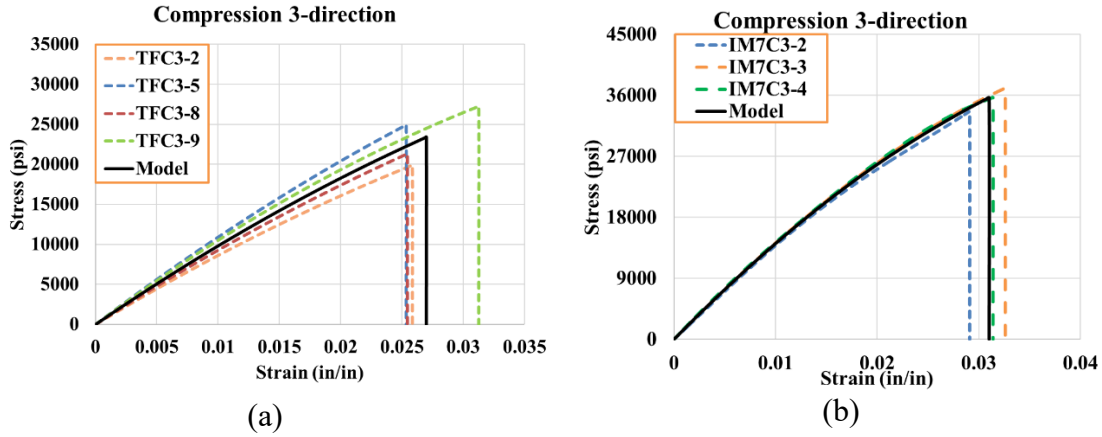

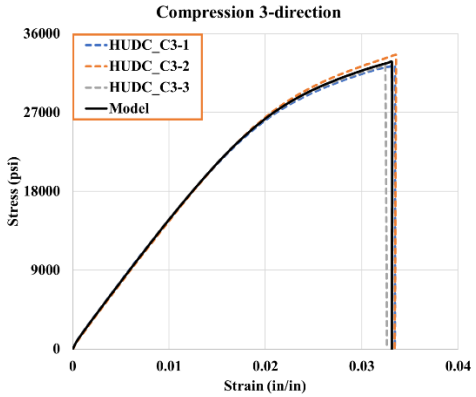

(c)

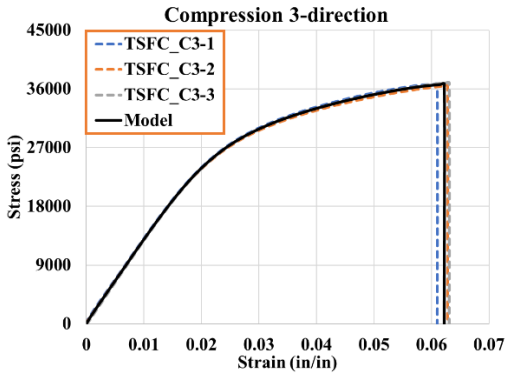

(d)

Figure 2.11: Stress-Strain Curves from 3-Direction Compression Tests - (a) T800-F3900, (b) IM7/8552, (c) HUDC, and (d) TSFC.

2.3.3 Shear Tests in the Three Principal Material Planes (1-2, 2-3, and 1-3)

ASTM D5379 (ASTM D5379, 2012) was used for the specimen geometries and Iosipescu shear test setups. The shear test in the 2-3 plane was carried out all the way until the specimen failed, whereas the tests in the 1-2 and 1-3 planes were stopped when they reached a tensorial shear strain value of 0.025 (excluding T800-F3900) as per ASTM recommendation. Shear specimens for 1-2 and 1-3 PMPs exhibit the same failure modes consistent with ASTM standards. Two major cracks at the notch tips and numerous minor cracks between the notches were initiated by matrix cracks and followed by sudden crack propagation parallel to the fibers. Shear specimens for 2-3 PMP exhibit brittle failure due to matrix crack at notch tip at 45^0. Figure 2.12 to Figure 2.14 show the processed stress-strain curves along with the associated *Model Curve*. Shear test results in 1-2 and 1-3 PMPs exhibit significant nonlinear behavior while shear test in 2-3 PMP exhibits linear elastic behavior.

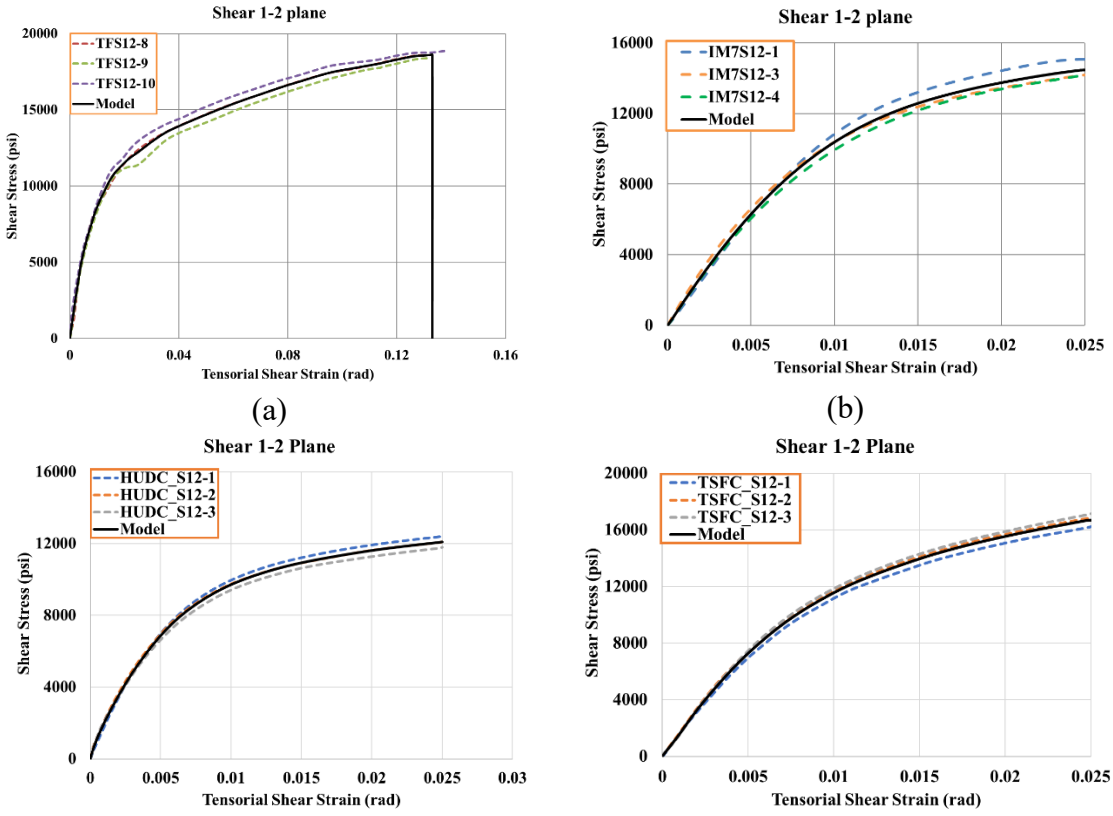

Figure 2.12: Stress-Strain Curves from 1-2 Plane Shear Tests - (a) T800-F3900, (b) IM7/8552, (c) HUDC, and (d) TSFC.

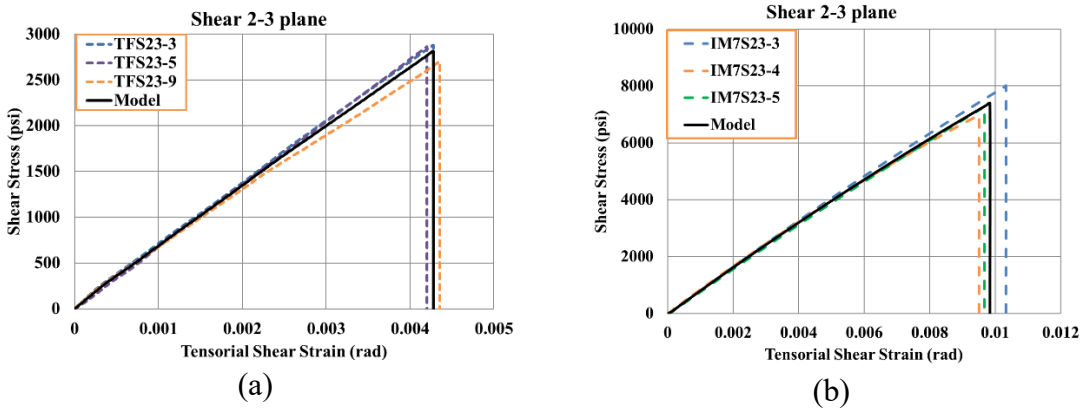

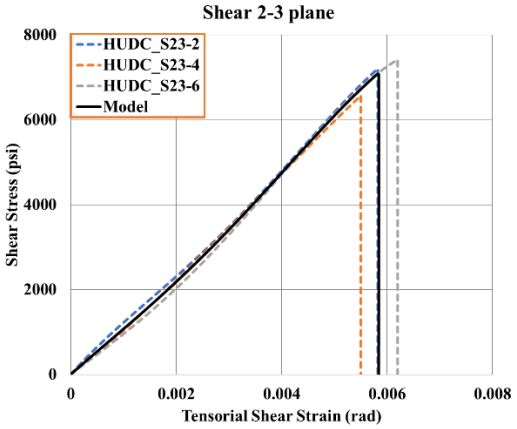

(c)

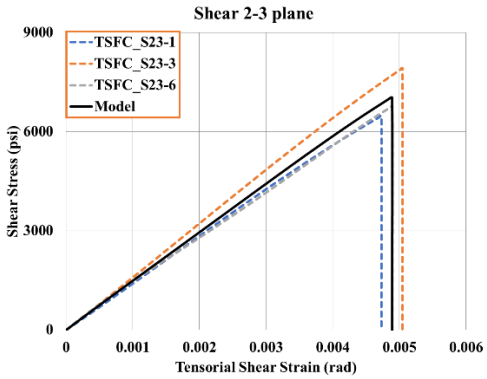

(d)

Figure 2.13: Stress-Strain Curves from 2-3 Plane Shear Tests - (a) T800-F3900, (b) IM7/8552, (c) HUDC, and (d) TSFC.

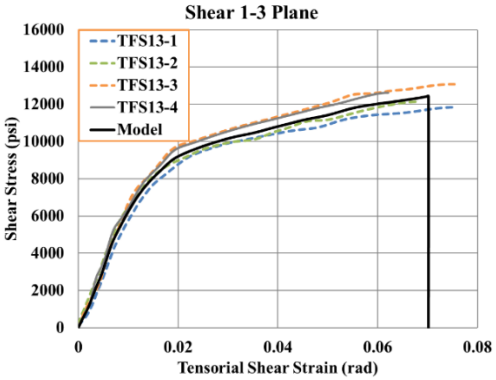

(a)

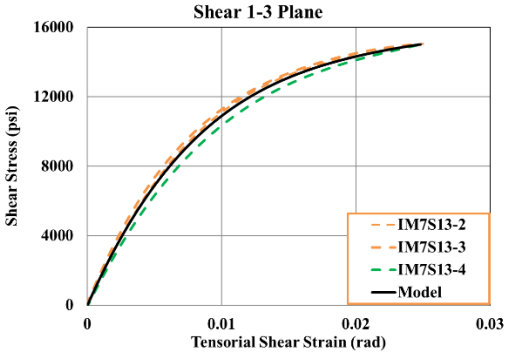

(b)

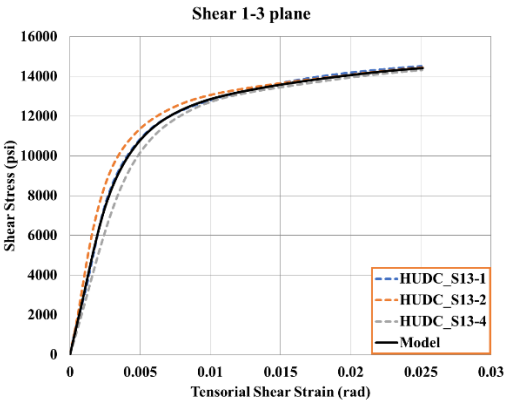

(c)

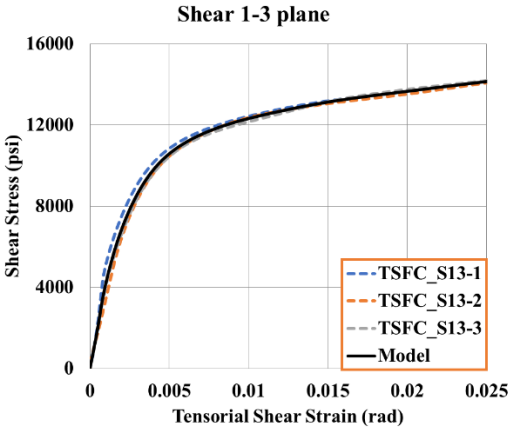

(d)

Figure 2.14: Stress-Strain Curves from 1-3 Plane Shear Tests - (a) T800-F3900, (b) IM7/8552, (c) HUDC, and (d) TSFC.

2.3.4 45^0 Off-axis Tests in the Three Principal Material Planes (1-2, 2-3, and 1-3)

Experiments in the 1-2 plane off-axis were conducted in the same way as 1- and 2-direction tension tests, and experiments in the other two planes were conducted in the same way as 3-direction compression tests (Khaled et al., 2018). Figure 2.15 to Figure 2.17 show the processed stress-strain curves along with the associated *Model Curve*. All three off-axis tests in PMPs exhibit nonlinear behavior. The failures in the 1-2 plane 45^0 off-axis tension tests were consistently inter-fiber due to matrix cracking at 45^0, and the failure in the 2-3 and 1-3 plane 45^0 off-axis compression tests were consistently inter-laminar due to matrix cracking at 45^0. The off-axis tests in the 1-3 plane for HUDC and TSFC were not conducted due to the lack of machined specimens.

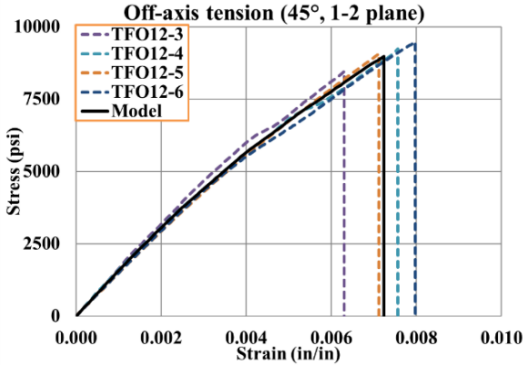

(a)

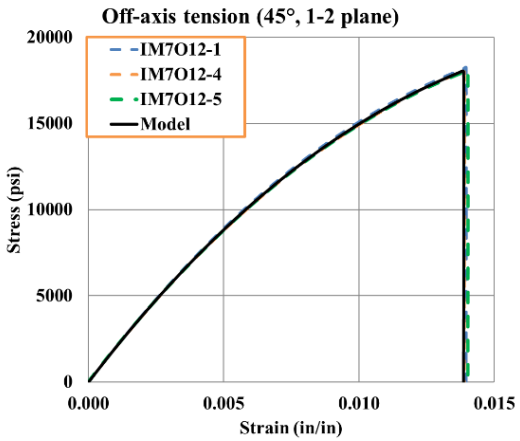

(b)

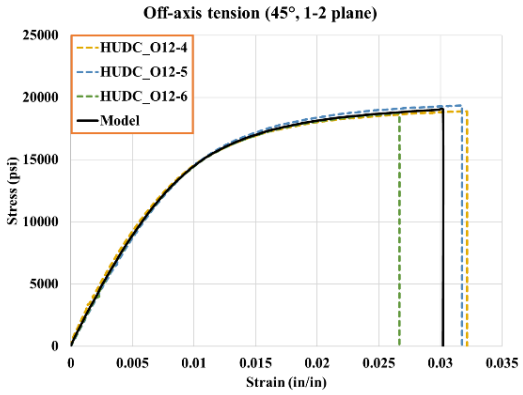

(c)

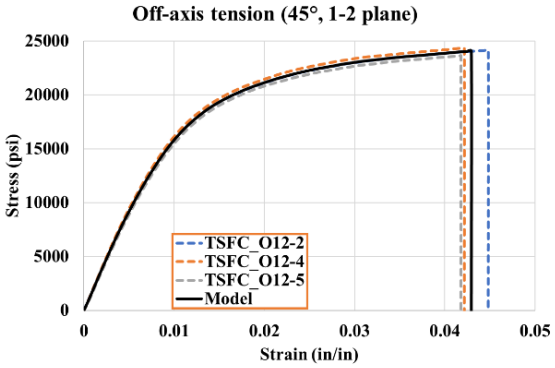

(d)

Figure 2.15: Stress-Strain Curves from 1-2 Plane 45^0 Off-Axis Tests - (a) T800-F3900, (b) IM7/8552, (c) HUDC, and (d) TSFC.

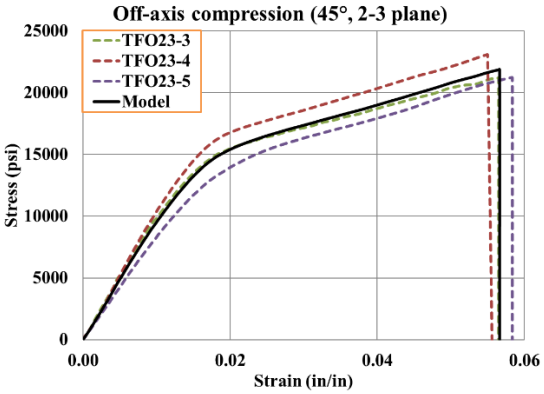

(a)

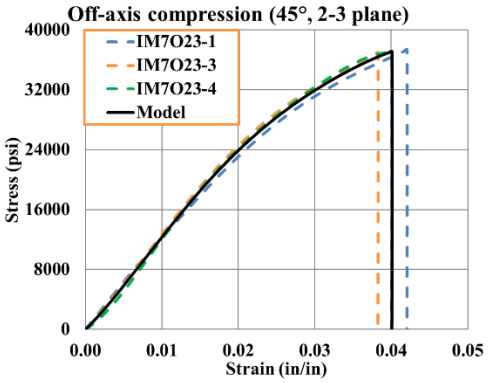

(b)

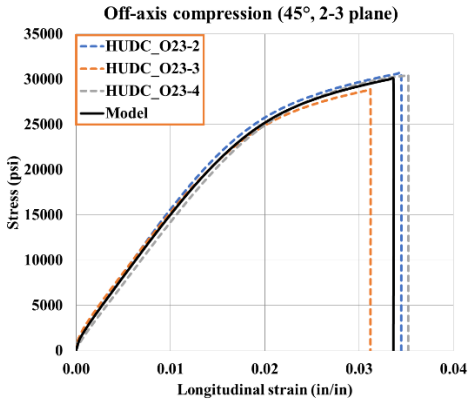

(c)

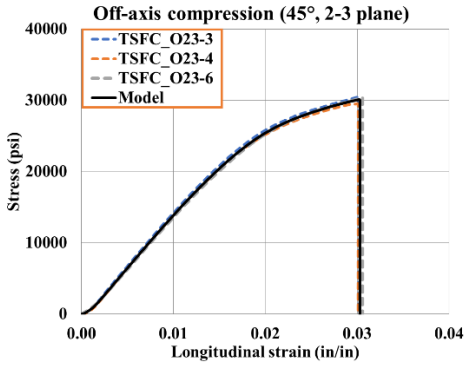

(d)

Figure 2.16: Stress-Strain Curves from 2-3 Plane 45^0 Off-Axis Tests - (a) T800-F3900, (b) IM7/8552, (c) HUDC, and (d) TSFC.

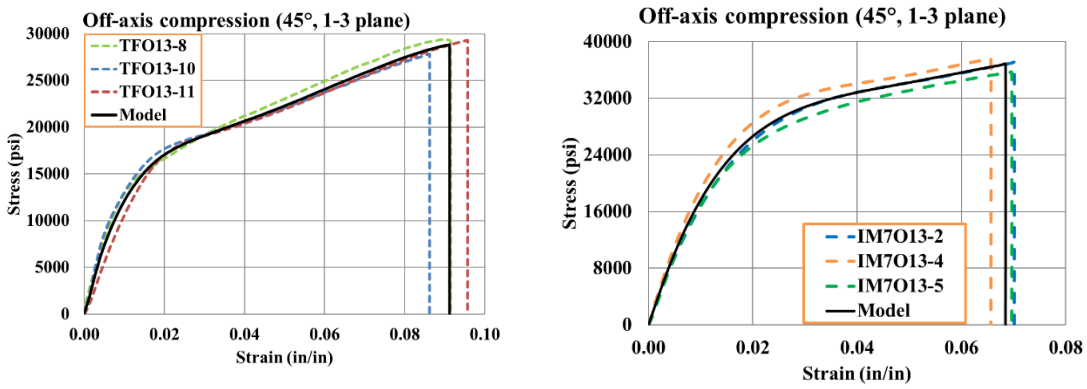

(a) (b)

Figure 2.17: Stress-Strain Curves from 1-3 Plane 45^0 Off-Axis Tests - (a) T800-F3900, and (b) IM7/8552.

2.4 Generation of Traction Separation Law with Inverse Analysis.

The T800-F3900 composite is used in this study to generate fracture properties through inverse analysis, improving upon the method presented in earlier work (Khaled et al., 2019b). The MAT_186 material model incorporates three general irreversible mixed-mode interaction cohesive formulations with an arbitrary normalized traction-separation law. These formulations differ based on the type of effective separation parameter used. The interaction between fracture modes I and II is accounted for, with irreversible conditions enforced through a damage formulation, where the unloading/reloading path returns to the origin (LS-DYNA®, 2022b).

The DCB test is a widely used standard method for evaluating the Mode I inter-laminar fracture properties of composite materials. This study follows ASTM D5528 (ASTM D5528, 2013), which specifies the procedures and requirements for conducting the test. The DCB specimens consist of unidirectional laminated composites with a uniform rectangular cross-section and a predefined crack length at the center, as shown in Figure

2.18 and Table 2.2. Each specimen comprises 24 plies ([0]24). The DCB tests were conducted using (a) an MTS Exceed test frame equipped with a spring-loaded fixture and (b) two-dimensional DIC to monitor displacement fields. To minimize variations in the crack tip among different specimens, a non-precracked (NPC) procedure recommended by ASTM was followed. This involved initially loading the specimen in Mode I until the crack propagated approximately 0.2 in. Once the crack length had been extended by 0.2 in, the specimen was unloaded and reloaded again until the specimens separated into two distinct cantilever pieces.

Similarly, the ENF test is a standard method for evaluating Mode II inter-laminar fracture properties of composite materials. The test followed ASTM D7905 (ASTM D7905, 2014), which outlines the specific procedures and requirements. A displacement-controlled testing protocol was employed, applying a displacement rate of 0.025 in/min at the center of the span. A non-precracked cycle was also conducted for the ENF specimens by loading them until crack propagation was either visually observed or indicated by a drop in the load-displacement curve. Additionally, compliance calibration was performed before the pre-crack cycle, as recommended by ASTM.

Further details on the DCB and ENF test specimens, including machining processes, can be found in an earlier work (Holt et al., 2022).

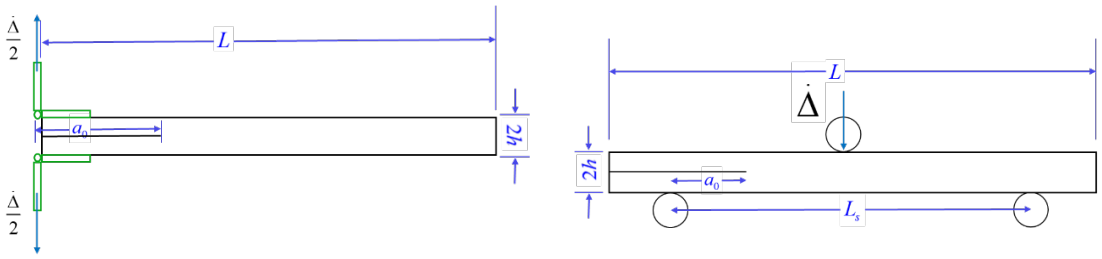

(a) (b)

Figure 2.18: Schematic Diagram of Prepared Specimens - (A) DCB, and (B) ENF.

Table 2.2: Average Dimensions of Three Replicates of Pre-cracked Specimens.

Parameter	DCB	ENF
$a_0\,(in)$	2.8	1.181
$h(in)$	0.094	0.094
$b(in)$	1.0	1.01
$L(in)$	5.0	6.5
$L_S\,(in)$	-	3.941

Figure 2.19 shows the measured load-displacement curves for three replicates, along with the associated *Model Curve*.

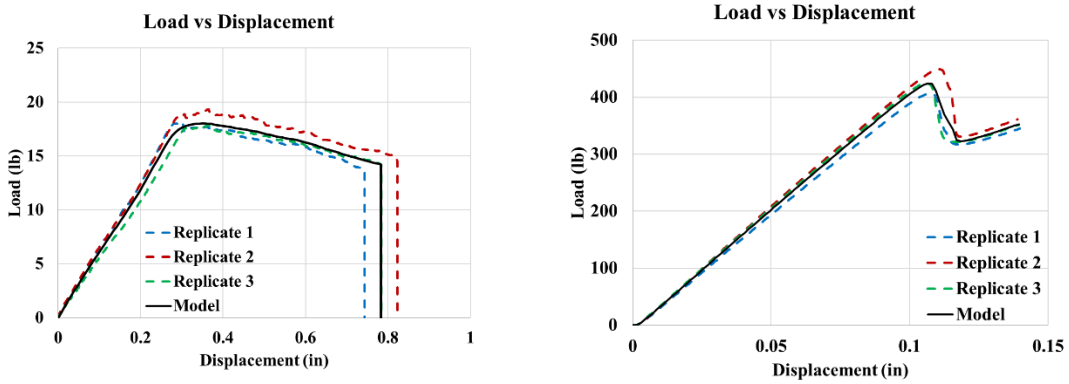

(a) (b)

Figure 2.19: Load versus Displacement Curves - (a) DCB Test, and (b) ENF Test.

In an earlier work (Khaled et al., 2019b), a method to obtain the traction separation laws from DCB and ENF tests for T800/F3900 composites by closely monitoring the crack

propagation during the experiment was presented. The method requires the load-displacement curve and DIC data to obtain Mode I and II fracture properties. The standard compliance method was used to compute the Mode I energy release rate (G_I) which is equivalent to the J integral as

$$G_I = J_1 = \frac{P^2}{2b}\frac{\partial C}{\partial a} \tag{1.35}$$

where $C(a)$ is the compliance of the specimen for crack length a. Compliance was computed as the ratio of displacement to load for a given time instance. DIC data was used to compute the crack tip opening displacement (CTOD, δ_n) which requires drawing several extensometers manually as shown in Figure 2.20.

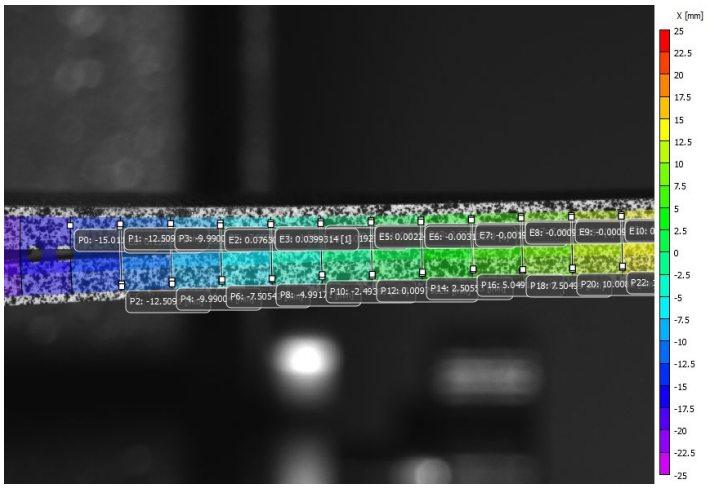

Figure 2.20: Post-Processing of DCB Specimens.

This manual process is not only tedious but presents difficulties to accurately monitor the crack as it propagates through the specimen. There is no assurance that the extracted CTOD values will be accurate and consistent. Traction values are computed by differentiating Eqn. (2.35) with respect to the CTOD (slope of $G-\delta$ plot) as

$$\sigma(\delta) = \frac{\partial J}{\partial \delta} \tag{1.36}$$

As discussed in (Maurya et al., 2024c), the computation of the traction-separation law for the IM7/8552 composite encountered issues due to unreliable CTOD values in both DCB and ENF tests, leading to inconsistencies in the traction-separation law. Furthermore, the computed fracture properties showed a close match with the pre-peak load-displacement curve but did not perform well in the post-peak phase, as evidenced in (Khaled et al., 2019b).

To overcome the difficulties in post-processing DCB and ENF experimental data, an inverse analysis procedure is discussed in (Maurya et al., 2024c) and was used to obtain Mode I and Mode II fracture parameters for T800-F3900 composites. The process flow is shown in Figure 2.21.

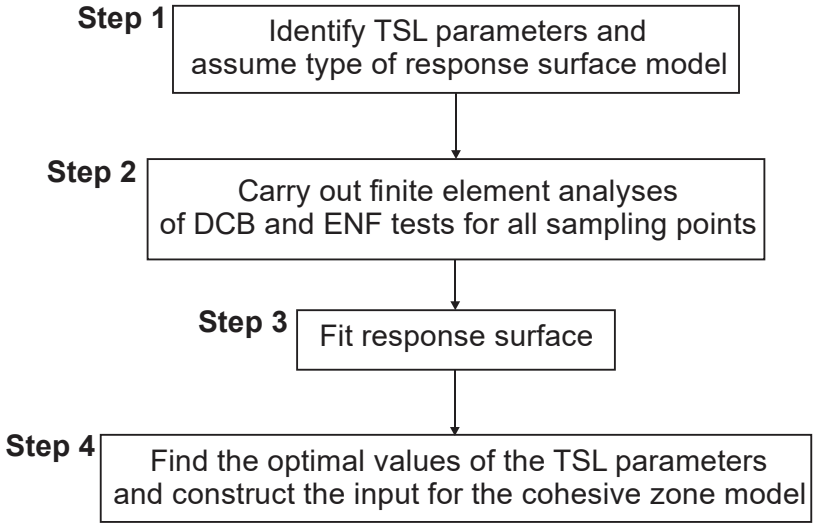

Figure 2.21: Steps Needed to Generate CZE Material Model.

This problem is solved twice – first for the DCB test and then for the ENF test. However, the steps are identical and the processing of just the DCB data is explained next.

2.4.1 Step 1: Inverse Analysis Problem Statement

The inverse analysis problem is posed as

Find

$$\mathbf{x} = \{G_{Ic}, \sigma_{\max}, \delta_0\} \tag{1.37}$$

To minimize

$$f(\mathbf{x}) = \sqrt{\frac{\sum_{i=1}^{m}\left(\left(P_{FEM}\right)_i - \left(P_{EXP}\right)_i\right)^2}{m}} \tag{1.38}$$

where $\left(P_{FEM}\right)_i$ and $\left(P_{EXP}\right)_i$ (see Figure 2.22) are the load values obtained from finite element analysis and from experiment for a known displacement Δ_i, respectively. The parameter m is the number of curve sampling points taken over the entire displacement range such that the root mean squared error (RMSE) can be computed.

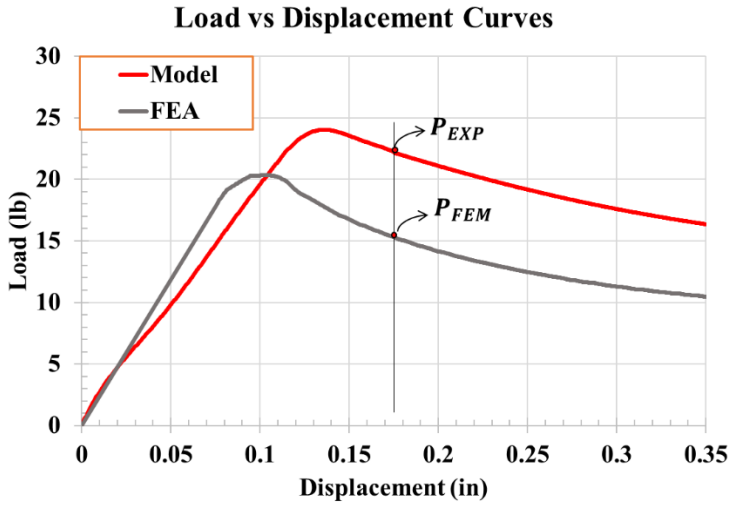

Figure 2.22: Typical Load-Displacement Data from - DCB Experiment, and FE Simulation.

Solving the problem posed by Eqn. (2.37)-(2.38) is computationally expensive as each function evaluation requires a complete finite element analysis. Instead, a surrogate problem can be constructed by replacing the objective function with an approximation that in the current work is taken as a second order polynomial of the form

$$f(\mathbf{x}) = f^{fit}(\mathbf{x}) = c_0 + c_1 x + c_2 y + c_3 z + c_4 x^2 + c_5 y^2 + c_6 z^2 + c_7 xy + c_8 xz + c_9 yz \quad (1.39)$$

where $x \equiv G_c, y \equiv \sigma_{\max}, z \equiv \delta_0$. To find the undetermined constant coefficients $(c_0,...,c_9)$ in the fitting function (Eqn. (2.39)), RMSE is used to match and fit the FE analysis with experimental data. Details of the fitting process are presented in Step 3.

2.4.2 Step 2: Finite Element Analyses

Both DCB and ENF finite element models are constructed and analyzed to mimic the experimental setup as closely as necessary. Based on the convergence and boundary condition analysis done earlier (Khaled et al., 2019b), an element size of 2.54 mm (0.1 in) with an aspect ratio of 1 was chosen for both the DCB and ENF models. To reduce computational time without sacrificing accuracy, the width of the model was reduced to 10% of its original width for DCB and 50% of its original width for ENF model. A single layer of cohesive elements with a thickness of 10^{-5} in was modeled at the center spanning from the initial crack tip to the edge of the composite specimen (highlighted in Figure 2.23). Additionally, the stainless-steel piano hinges (light and dark green colors) for DCB tests and the support (dark green cylinders) and loading fixture (light green) for ENF test were also modeled with 8 node fully integrated hexahedral solid elements. Fully integrated

hexahedral solid elements (ELFORM=2) for composite, solid element with ELFORM=19 for CZE and solid elements with ELFORM=1 for all other parts were used. MAT_213 was used for the composite, MAT_186 for CZE, and MAT_020 for all other parts. For DCB test, nodal velocities (3 in/sec) were applied in the global Y direction along a row of nodes as shown in Figure 2.23(a). All the nodes on the non-hinge end of the specimen (Figure 2.23(a)) were fixed along all three degrees-of-freedom. For the ENF test, the supporting fixtures were fully constrained. Nodes on the loading fixture were permitted to move only in the global Y-direction and a prescribed global Y-velocity of 5 in/sec was applied. Contacts were defined between the support fixtures or loading cell and the composite by using *CONTACT_AUTOMATIC_SURFACE_TO_SURFACE definition in LS DYNA. A quadratic softening TSL for both Modes, as shown in Figure 2.24, was used to generate the model parameters for the cohesive zone model available in MAT_186. A nonlinear softening law was selected to account for the large-scale fiber bridging as a simple linear softening law is insufficient to capture the behavior (Wisnom et al., 2008). TSL has two regions: an initial undamaged linear elastic region, followed by a linear or non-linear damage region. The area under the damage region was assumed to be equal to the area of a parabolic spandrel and 4 parameters were identified for generating the data - G_C, $\sigma_{\max}$, δ_o and δ_f, where G_C is the area under the TSL, $\sigma_{\max}$ is the peak traction, δ_o is the damage initiation crack tip opening displacement (CTOD), and δ_f is the failure CTOD.

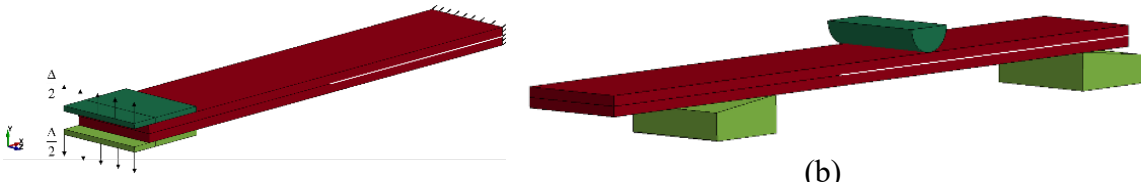

(a) (b)

Figure 2.23: FE Model of the Specimens Showing the Highlighted Line Describing the Location of the Cohesive Elements - (a) DCB, and (b) ENF.

Of the four parameters, the first three are independent parameters while δ_f can be calculated as

$$A_s = G_C - \frac{1}{2}\sigma_{\max}\left(\delta_o\right)$$
$$A_s = \frac{1}{3}\sigma_{\max}\left(\delta_f - \delta_o\right) \tag{1.40}$$
$$\delta_f = \frac{3A_s}{\sigma_{\max}} + \delta_o$$

The load vs displacement curve was extracted from the finite element models. The load values were obtained from the nodal reactions at the support face along the loading direction. Displacement values were obtained by averaging the y-displacements of nodes where nodal velocities were applied.

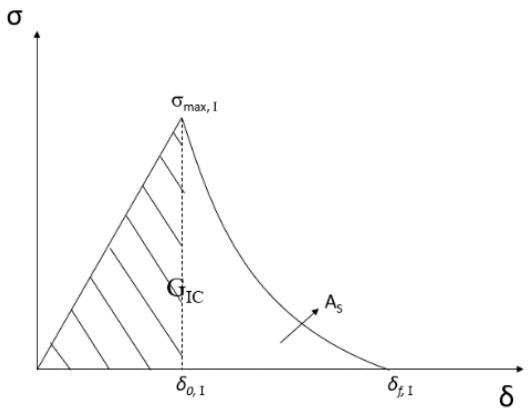

Figure 2.24: Assumed Traction-Separation Law.

2.4.3 Step 3: Response Surface Fit

Response Surface Methodology (RSM) is a collection of statistical and mathematical techniques useful for developing, improving and optimizing processes (Myers and Montgomery, 2002). In other words, RSM is a convenient and robust tool for establishing an approximate relationship between a response variable and a set of predictor variables. As shown in Eqn. (2.39), the fitting function that captures the difference (response variable) between the experimental and FE load-displacement curves is expressed as a function of G_C, $\sigma_{\max}$, and δ_o, the set of predictor variables. To find appropriate lower and upper bounds for each of the three variables, a few preliminary analyses were carried out by arbitrarily selecting the values of the three variables within a relatively small interval based on an earlier work (Khaled et al., 2019b) and computing Eqn. (2.38). Results of these preliminary analyses indicated that a quadratic polynomial was simple and appropriate to use. While there are several approaches to constructing the fitting function, e.g., full factorial, quadratic Koshal, Central Composite Design, *D*-optimal, etc., a full factorial design was chosen as there are only three predictor variables. Hence, a total of 27 RSM sampling points is needed - 3 variables and 3 levels for each variable (Low-Mid-High, or LMH), implying that no more than 27 finite element analyses are needed to generate the fitting data. For DCB Test, δ_o is not a significant parameter (Maurya et al., 2024c); therefore, only two variables with three levels are considered, reducing the required finite element analyses to no more than eight. Any combination variables that yield non-physical

traction separation laws are discarded from finite element analysis and response surface fitting. Table 2.3 shows the LMH values for both the DCB and ENF simulations.

Table 2.3: Values of DCB and ENF Model Parameters Used at RSM Sampling Points.

Parameter	**DCB**			**ENF**		
	Low	**Mid**	**High**	**Low**	**Mid**	**High**
G_C (lb–in/in^2)	2.15	2.75	3.5	10.0	12.0	14.0
$\sigma_{\max}$ (lb/in^2)	1275	2550	3875	2500	5000	10000
δ_o (in)	0.000684			0.00075	0.0015	0.0035

Once the values of $f(\mathbf{x})$ is found for all the RSM sampling points from Eqn. (2.38), the Levenberg-Marquardt Algorithm (LMA) is used to find the unknown coefficients c_0, c_1, c_2, c_3, c_4, c_5, c_6, c_7, c_8, and c_9. Eqn. (2.41) shows the least squared problem solved using LMA where $f_i^{fit}(\mathbf{c})$ is the fitting function (Eqn. (2.39)) and $f_i(x)$ is the error function (Eqn.(2.38)):

Find $\mathbf{c}$ to minimize

$$f(\mathbf{c}) = \sum_{i=1}^{n} \left(f_i^{fit}(\mathbf{c}) - f_i(\mathbf{x}) \right)^2 \tag{1.41}$$

where n is the number of RSM sampling points. The Eigen library (Jacob et al., 2010) was used in the current work to solve this problem.

2.4.4 Step 4: Finding Optimal Values of TSL Parameters

Once the fitting function (Eqn.(2.39)) is obtained, the optimal values of the TSL parameters are found by minimizing the fitting function. Stated mathematically, the optimization problem is:

Find $\mathbf{x} = \{G_C, \sigma_{\max}, \delta_0\}$ to minimize

$$\begin{aligned} f(\mathbf{x}) = {} & c_0 + c_1 G_c + c_2 \sigma_{\max} + c_3 \delta_0 + \\ & c_4 {G_c}^2 + c_5 {\sigma_{\max}}^2 + c_6 {\delta_0}^2 + \\ & c_7 G_c \sigma_{\max} + c_8 G_c \delta_0 + c_9 \sigma_{\max} \delta_0 \end{aligned} \tag{1.42}$$

subject to

$$\begin{aligned} & G_c^{\text{Low}} \le G_c \le G_c^{\text{High}} \\ & \sigma_{\max}^{\text{Low}} \le \sigma_{\max} \le \sigma_{\max}^{\text{High}} \\ & \delta_0^{\text{Low}} \le \delta_0 \le \delta_0^{\text{High}} \\ & \delta_0 < \delta_f \end{aligned} \tag{1.43}$$

The EDO Workbench (Rajan et al., 2023) was used to solve this problem.

Results and Discussions: All load-displacement curves were discretized into 20 curve sampling points, i.e., $m = 20$ in Eqn. (2.38), as this number of sampling points was found to be sufficient to ensure accurate RMSE values. Figure 2.25 shows the load-displacement curves from both FE simulations and experiments.

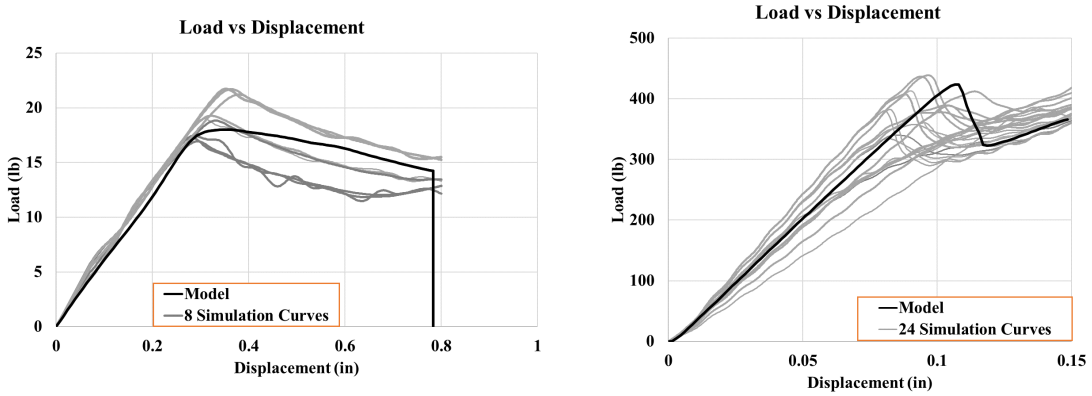

(a) (b)

Figure 2.25: Summary of All Simulations Results and Experimental Data - (a) DCB, and (b) ENF.

The fitting function was obtained for DCB as follows:

$$f^{fit}(c) = 22.05 - 14.33x + 0.000179\,y + 2.4059x^2 + 3.76x^2 - 2.59e-8\,y^2 - 3.27e-6xy \tag{1.44}$$

Finally, the optimal values for the predictor variables were obtained as: $G_{Ic} = 2.974$ and $\sigma_{\max,I} = 2550$. TSL using optimal cohesive parameters were constructed (Figure 2.26(a)) and a final FE simulation was conducted with these optimal values.

Three data points were discarded from the ENF test because the parameters resulted in non-physical traction separation law. Once again using the Eigen library, the fitting function was obtained for ENF as follows:

$$f^{fit}(c) = 306.43 - 34.38x - 0.0129\,y - 11486.7z + 1.741x^2 + 9.643e-7\,y^2 + 1.631e6z^2 + 0.000192xy + 939.95xz - 1.6594\,yz \tag{1.45}$$

Finally, the optimal values for the predictor variables were obtained as: $G_{IIc} = 13.08$, $\sigma_{\max,II} = 5811, \delta_{0,II} = 0.002698$. TSL using the optimal cohesive parameters were constructed (Figure 2.26(b)) and a final FE simulation was conducted with these optimal values. The obtained results from optimal TSL parameters are compared against the best combination and the experimental model curve in Figure 2.27. A good agreement with the experimental results in both pre-peak and post-peak regions is observed for the DCB test. However, better post-peak results are captured by the optimal curve compared to the best curve. For the ENF test, a good agreement with the experimental results in the pre-peak region, but the post-peak region does not show as much load drop as seen in the experiment.

The RMSE for the optimal curve in the DCB test is 0.919 lb per sample point, compared to 1.073 lb for the best curve. For the ENF test, the optimal curve has an RMSE of 12.6 lb per sample point, while the best curve has an RMSE of 17.8 lb per sample point.

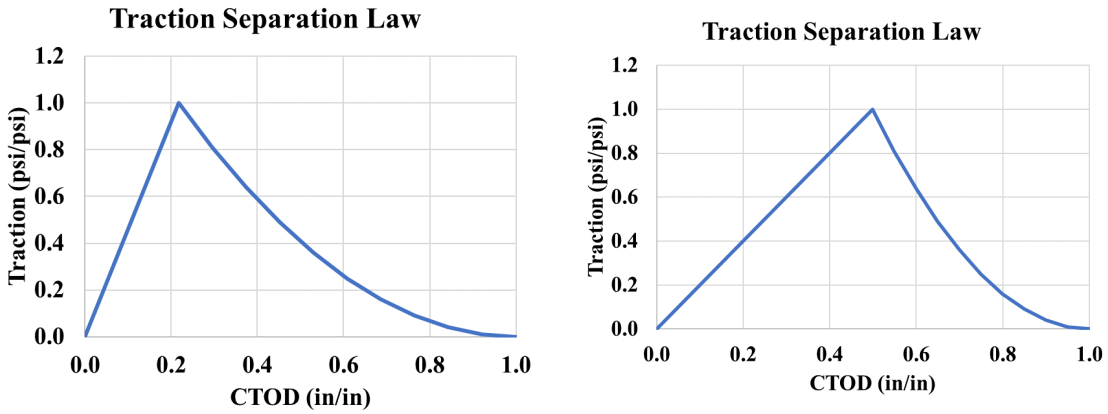

(a) (b)

Figure 2.26: Normalized Traction Separation Law - (a) DCB, and (b) ENF.

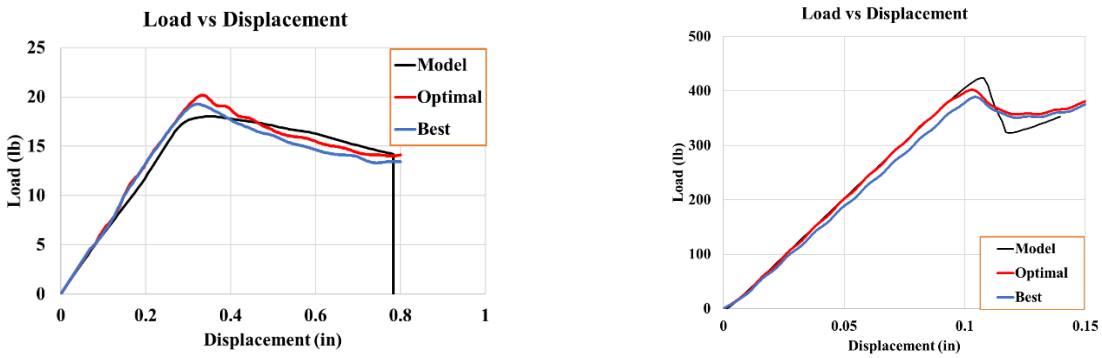

(a) (b)

Figure 2.27: Optimal Load-Displacement Curve Compared with the Best, and Experimental Results - (a) DCB, and (b) ENF.

Equation Chapter (Next) Section 1

CHAPTER 3

MULTI-SCALE MATERIAL MODELING

Many researchers have started exploring the use of multiscale modeling to improve the fidelity of the modeling and simulation of structural systems (Maurya and Rajan, 2024). Figure 3.1 shows components of a multi-scale modeling approach. At the micro-scale, the composite architecture can be represented at the constituent level. Figure 3.1(a) shows a unidirectional composite laminate where the individual plies are visible along with the inter-ply resin-rich zones. Using the dimensions of the fiber and the matrix, and the random distribution of the fibers, detailed FE models can be created. At the next higher level, as shown in Figure 3.1(b), a representative volume element (RVE) is created using several Representative Unit Cells (RUC). The material properties obtained from the constituents of the RVE can then be homogenized and used in component or structural models, i.e., the results from the fiber, matrix, and fiber-matrix interface parts of the model can be homogenized properties to characterize elastic and inelastic properties, damage and failure. The fibers are often represented as elastic orthotropic components, the matrix is typically represented using a nonlinear material model involving one or both of plasticity and damage, and the fiber/matrix interface is represented using the concepts of nonlinear fracture mechanics in the form of cohesive zone modeling (Khaled et al., 2021). This approach has been used by numerous researchers (Totry et al., 2008a, 2008b; Sun et al., 2018, 2019; Katusele, 2021) to derive parts of the failure locus of specific unidirectional composites under different multiaxial stress conditions. Once the homogenized behavior is

computed, they can be used at the structural level to model the behavior of the structure subjected to different types of loading, e.g., impact loading as shown in Figure 3.1(c).

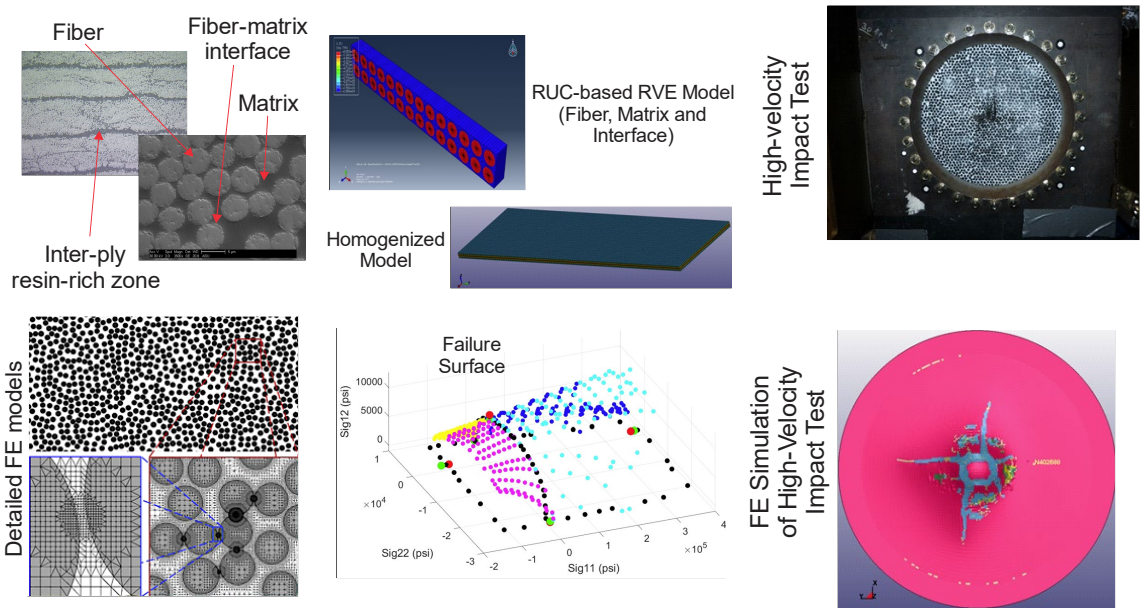

Figure 3.1: Multiscale Modeling - (a) Micro-Scale (Detailed FE (Soghrati, 2021), (b) Meso-Scale, and (c) Macro/Structural-Scale.

To address the deficiencies of existing approaches in predicting damage and failure, a multi-scale modeling framework has been developed and implemented following ASME guidelines for verification and validation shown in Figure 3.2. The overall multiscale modeling framework is shown in Figure 3.3. In the current work, the smallest scale used in the building blocks starts at the mesoscale. There are three components that feed into the final implementation of the constitutive model in a finite element program. The first component is to characterize the constituent materials of the composite (Component 1 in Figure 3.3). For example, in UDC, the constituent parts are the fiber, the matrix, and possibly the fiber-matrix interface. Once the constitutive models for the constituent

materials have been verified and validated, the next step is to build the meso-scale FE model (Component 2 in Figure 3.3). In the current work, Repeating Unit Cells (RUCs) are used to generate a Representative Volume Element (RVE) that is then subjected to multi-axial state of stress that is slowly increased till the onset of failure is detected in any constituent part of the RVE. The onset of failure (hereinafter referred to as failure onset) is the state of the RVE when the first finite element in the RVE meets the constituent material's failure criterion. Simultaneously, the test coupons of the composite are used to generate the meso-scale properties (Component 3 in Figure 3.3). Verification and validation of Component 2 uses information from Component 3, thus ensuring that the mathematical model and the physical model are as consistent as possible (Figure 3.2). Finally, the developed constitutive model can now be implemented in a finite element program (FE Implementation in Figure 3.3) and then subjected to verification and validation tests (V&V in Figure 3.3).

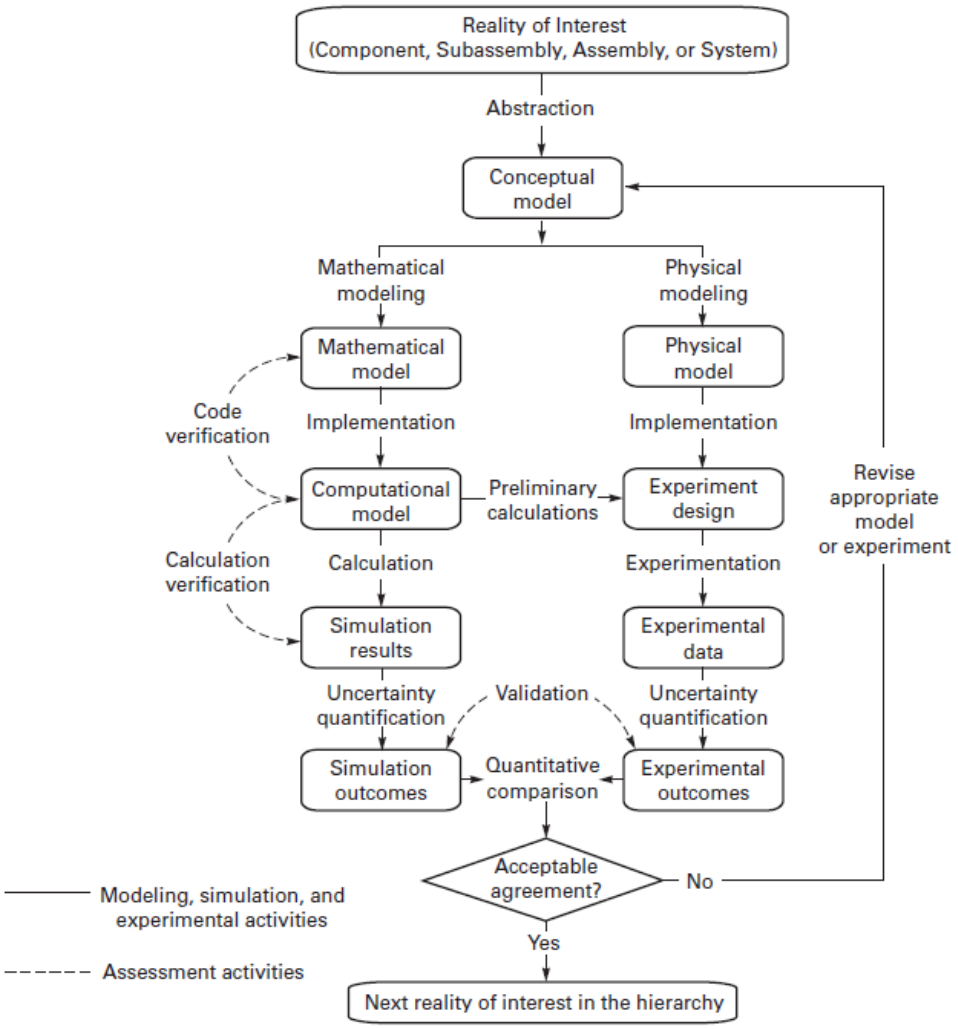

Figure 3.2: ASME V&V Activities, and Products (ASME V&V 10.1, 2012).

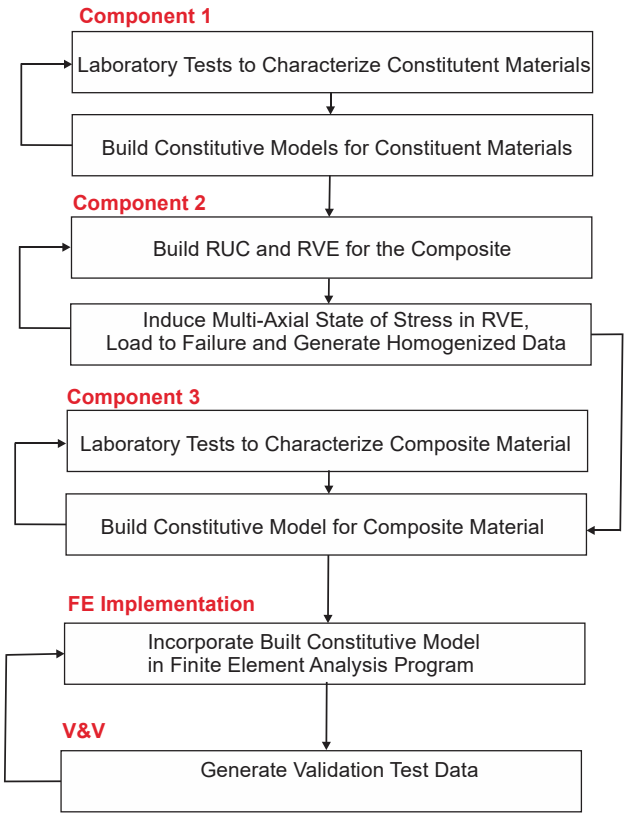

Figure 3.3: Multiscale Modeling Framework

3.1 Fundamental Building Blocks

The T800/F3900 unidirectional composite, a commonly used unidirectional composite material in the aerospace industry, is used in this study to illustrate the use of developed framework. Toray describes T800S as an intermediate modulus, high tensile strength graphite fiber (Toray, 2020). The epoxy resin system F3900 is a toughened epoxy combined with small elastomeric particles to form a compliant interface or interleaf between fiber plies to resist impact damage and delamination (Smith and Dow, 1991). The basic architecture of a continuous unidirectional fiber composite laminate is shown at the top left in Figure 3.4. Table 3.1 shows the manufacturer's reported properties. Since a very

large number of filaments (~24,000) make up yarn, it would be computationally prohibitive to model each individual filament. Instead, using the applicable volume fraction, a meso-scale model is generated by assuming circular-shaped yarns that incorporate the behavior of all the filaments.

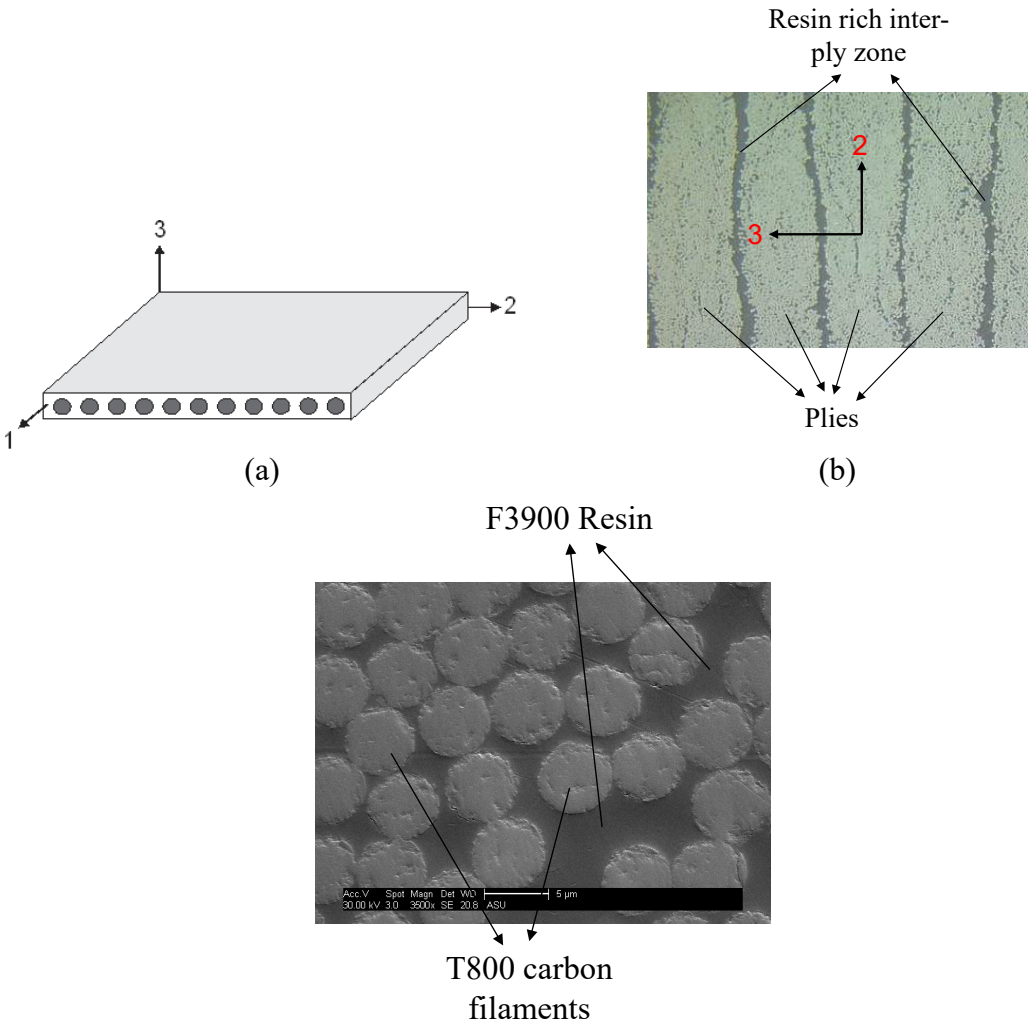

Figure 3.4: T800-F3900 Unidirectional Composite - (a) Principal Material Directions 1-2-3, (b) Optical Microscope Image (200x), and (c) Scanning Electron Microscope Image (3500x) (Holt, 2018).

Table 3.1. T800/F3900 Manufacturer Reported Material Data (Toray, 2020).

Item	Reported Value
Composite Panel	Unidirectional (FAW 191 GSM; RC% Weight 32, Volume 60)
F3900 Resin	Density: 1.22-1.25 g/cc
T800 Fiber	Yarn: 24,000 filaments
	Tensile Strength: 5880 MPa
	Modulus: 294 GPa
	Elongation: 2%
Thickness of a single ply in 16-96 ply flat panels	0.192-0.196 mm

The basic building block, Repeating Unit cell (RUC) is shown in Figure 3.5(a). A square RVE is generated using NxN RUCs as shown in Figure 3.5(b).

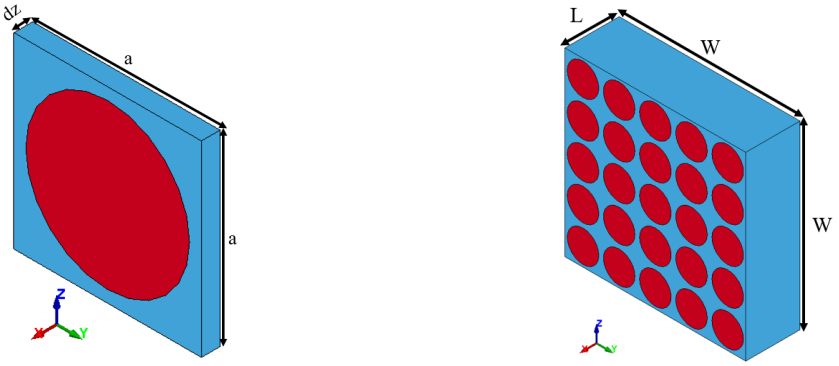

(a) (b)

Figure 3.5: (a) RUC Where Red Color Represents the T800 Fiber and Blue Color Represents the F3900 Matrix, and (b) Typical RVE Formed by a Collection of Regularly Arranged NxN RUCs (N=5).

The dimensions of a typical RUC and RVE are shown in Table 3.2.

Table 3.2. The Dimensions of RUC and RVE.

Parameter	Value
$a\,(in)$	0.007625
$d\,(in)$	0.00666
$dz\,(in)$	0.0007625
$W\,(in)$	Varies
$L\,(in)$	0.01144

Both fiber and matrix in the RVE are modeled using the 8-node reduced integration hexahedral solid elements (ELFORM=1).

3.2 Homogenization

To obtain equivalent material properties that can then be used in a structural model, a homogenization scheme is used (Harrington et al., 2017; Wan et al., 2020) The homogenization is carried out in two steps. First, the average response for each phase is computed by averaging the stress or strain in all the finite elements over the volume of the phase material (i.e., fiber and matrix) in the gage section. Second, the average response for the entire composite is computed from the volumetric average over the volume of the gage section. The two steps are combined as

$$\overline{P}_h = \frac{\sum_{j=1}^{e_t} \left(\frac{\sum_{i=1}^{n_{e_t}} \overline{P}_i V_i}{\sum_{i=1}^{n_{e_t}} V_i} \right)_j V_j}{\sum_{j=1}^{e_t} V_j} \tag{2.1}$$

where

$\overline{P}_h$ is the homogenized response,

$\overline{P}_i$ is the response of the ith element calculated from stresses and strains averaged over the total number of integration points of the element,

e_t is the number of different element types,

n_{e_t} is the number of elements in the jth element type, and

V_i is the volume of the i^{th} element.

3.3 Material Models

3.3.1 Material Model for T800S Fiber

Carbon fibers are assumed to be straight and have a circular cross-section. In this study, a perfect bond is assumed between the fiber and matrix because (a) of the lack of available experimental data to accurately determine the properties required for modeling the interface, and (b) using publicly available data showed that modeling the interface between fiber and matrix using cohesive zone elements did not yield superior results (Parakhiya, 2020). Experimental methods such as the microbond test and the single fiber push-out test are sometimes employed to obtain the interface properties. However, it should be noted that the data from these experiments are often not indicative of *in situ* properties and, in the context of computational modeling, numerical calibration may still be necessary to obtain valid data that can be used in a homogenized model at the continuum/structural scale (Khaled et al., 2021). The carbon fiber is assumed to be linearly elastic and orthotropic (Khaled et al., 2021) but with different tension and compression properties. MAT_213 is used to model fibers. The Generalized Tabulated Failure Criterion (GTFC) (Goldberg et al., 2018; Shyamsunder et al., 2021) is employed for the fiber elements in the gage section as it allows for better control of element erosion by specifying various erosion strains at various stress states and failure angles. The motivation was to obtain fiber failure only in (longitudinal) 1-direction. Therefore, three different states of fiber failure are defined: fiber

fails in 1-direction compression (Katusele, 2021), fiber fails in 1-direction tension (Toray, 2020) and fiber does not fail.

3.3.2 Material Model for F3900 Matrix

F3900 is a highly toughened epoxy resin. Experimental results show the material exhibits significant nonlinear behavior under uniaxial tension, compression, and shear stress loading conditions (Robbins, 2019). Additionally, the behavior under all three conditions varies significantly. Thus, an advanced material model is required to appropriately capture the constitutive behavior. LS-DYNA's MAT_187 provides sufficient freedom to the user to model a wide range of polymer material behavior. Much of the input is in the form of tabulated data which provides a means of more accurately representing the nonlinear and failure behavior than other material models that are largely driven by analytical methodologies. MAT_187 offers erosion of elements based on equivalent plastic strain and this feature was used for matrix elements. The equivalent plastic strain is difficult to measure experimentally since the epoxy does not remain in a state of uniaxial stress in a uniaxial test. The erosion failure strain was obtained through numerical calibration by matching the FE model results with experimentally obtained values (Katusele, 2021; Khaled et al., 2021).

3.4 Selection of RVE

Various characteristics of the RVE are investigated by using boundary conditions that induce a multiaxial stress state that can be increased until first element erosion (FEE) state

is reached. The term erosion is used rather than failure as an explicit FE analysis is carried out where when elements are eroded and removed from the FE model is a function of the constitutive model for the material. A two-step loading method is used using a combination of applied normal stresses followed by prescribed displacements with both functions of time, t. In the first step (Figure 3.6(a)), equal and opposite tractions (normal stresses) are applied on faces marked 1 and 2 and the two opposite faces. The surface tractions, σ_f are increased linearly from $t = 0$ to their final values σ_{final} at $t = t_1$, and then held constant. This loading primarily induces normal stresses in the RVE. At $t = t_1$, equal and opposite prescribed shearing displacements are applied on faces 1 and 2. These displacements are increased from zero to their final value d_{final} at $t = t_2$. There are no constrained nodes in the model as the RVE is in a state of self-equilibrium.

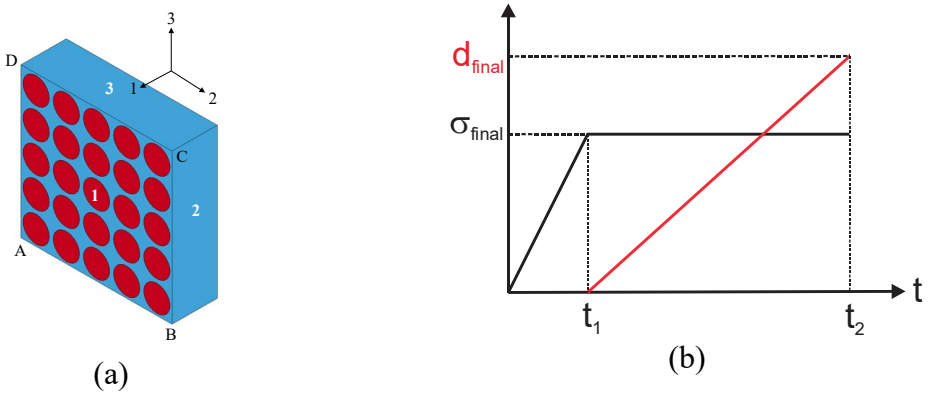

Figure 3.6: Two-Step Loading to Induce Multiaxial Stress State - (a) RVE, and (b) Application of Traction Boundary Conditions and Displacements.

The load curve shown in Figure 3.6(b) can be scaled independently in the 1 and 2-directions thus permitting a variety of load combinations to be applied on the RVE. In the study to generate optimal RVE, multiaxial stress state is obtained by applying compression in the

1-direction, tension in the 2-direction and shear in the 2-1 plane. Since the motivation is to generate the point cloud data for use with thin shell finite elements, homogenized $(\sigma_{11}, \sigma_{22}, \sigma_{12})$ are extracted from the FE model. During this process, the loading is specifically applied only in the 1 and 2 directions in order to generate the desired stress components in the RVE. Consequently, the analysis does not consider loading in the 3-direction. Three parameters are studied – the RVE size, the size of the gage section, and the effect of fiber placement.

Using experimental data from the stress state corresponding to the peak stress state in 1-direction compression and 2-direction tension uniaxial tests, the values of the time and traction parameters were estimated for inducing a typical multi-axial state of stress. For example, $t_1 = 4\ ms, t_2 = 10\ ms,$ with the specified displacements corresponding to 1-2 plane shear test results taken as $d_{final} = 0.0004578\ in$ on Face 1 and $d_{final} = 0.0001728\ in$ on Face 2; the applied surface tractions on the fiber elements in the 1-direction are taken as $\sigma_{final} = -44{,}000\ psi$ and $\sigma_{final} = -640\ psi$ on the matrix elements to induce a stress state in 1-direction equivalent to 25% of 1-direction compressive peak stress; the applied surface traction in the 2-direction is taken as $\sigma_f = 6{,}210\ psi$ on the matrix elements equivalent to 95% of 2-direction tensile peak stress. Figure 3.7(a) shows the applied normal tensile traction in the 1-direction. The traction direction is reversed for compressive loading.

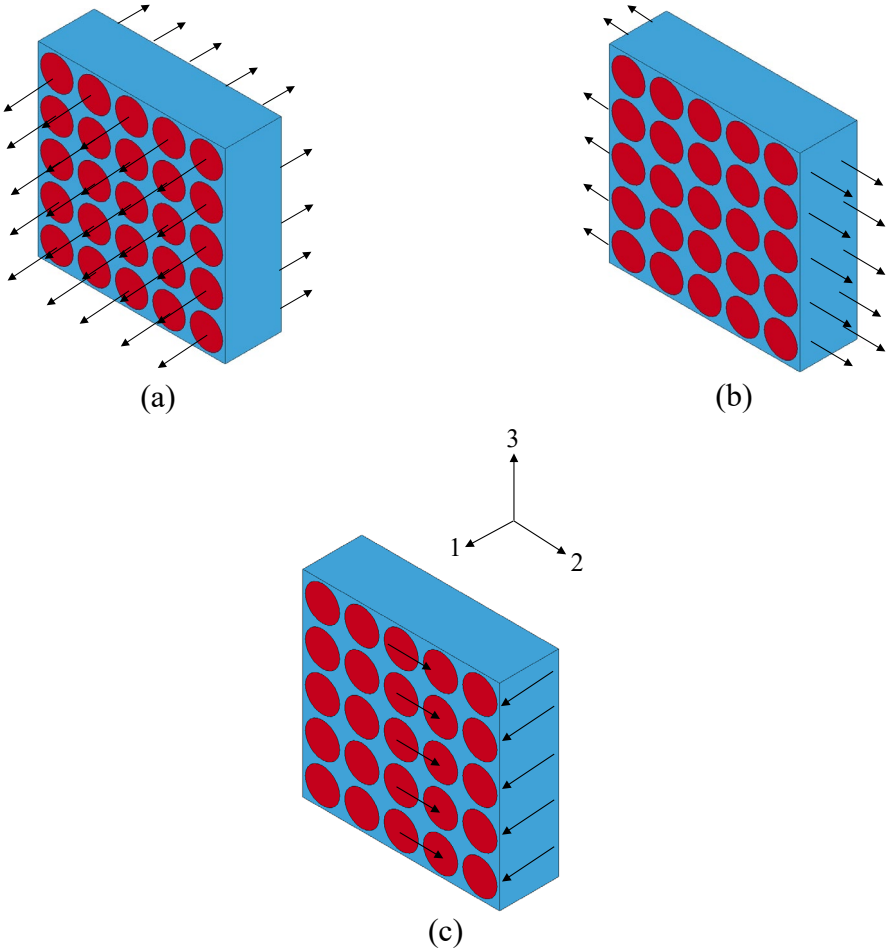

Figure 3.7: Applied Traction and Specified Displacements - (a) 1-Direction Traction Creating Tensile Stresses, (b) 2-Direction Traction Creating Tensile Stresses, and (c) 1-2 Plane Specified Displacements Creating Pure Shear.

To ensure that the FE results from the explicit analyses are acceptable, energy balance checks were carried out. The kinetic energy and hourglass energy were numerically insignificant while the internal energy was numerically equal to the total energy.

3.4.1 Effect of RVE Size

To determine the influence of RVE size as a function of the number of RUCs in the model, three different RVEs are used. Figure 3.8 shows 3x3, 5x5, and 7x7, that mimic 3, 5, and 7

plies, respectively, i.e., W in Figure 3.5(b). The small gage section (Figure 3.8(a)) was used to post-process the results.

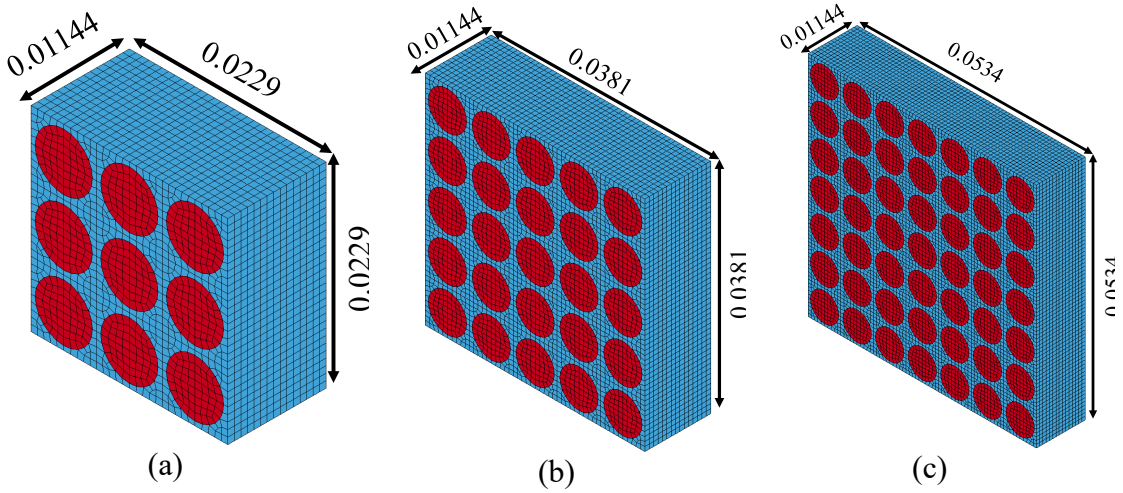

Figure 3.8: Three Different RVEs - (a) 3x3, (b) 5x5, and (c) 7x7. Dimensions in inches.

3.4.2 Size of Gage Section

To be consistent with how laboratory experimental data are analyzed, the homogenization process uses similar criteria used in the experiments when processing Digital Image Correlation (DIC) data (Khaled et al., 2018). The criteria in uniaxial tests are to find a region of uniform state of stress, one that is as large as possible, and one that is free of boundary effects. Since in this study a multiaxial stress state is induced in the elements, to determine the impact of the gage section, three different-sized gage sections as shown in Figure 3.9 are used. They include 1, 4 and 9 fibers in the model and are referred to as small, medium, and large gage sections, respectively.

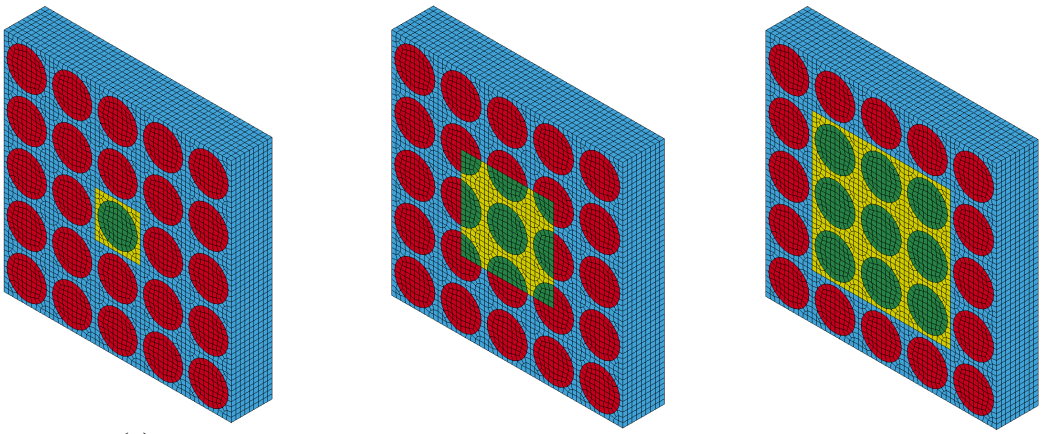

(a) (b) (c)

Figure 3.9: Three Different Gage Sections (in Yellow) - (a) Small, (b) Medium, and (c) Large.

3.4.3 Regular vs Random Fiber Arrangements

Figure 3.10 shows the optical microscopy image of the T800/F3900 composites where nearly circular fibers are randomly placed in the ply. The fiber arrangement at the center of the image is used in generating the FE model. Some of fibers had to be shifted slightly to obtain the required fiber volume fraction as 60 percent, to avoid fibers being placed too close to each other, and to avoid partial fiber geometries within the RVE (Figure 3.11).

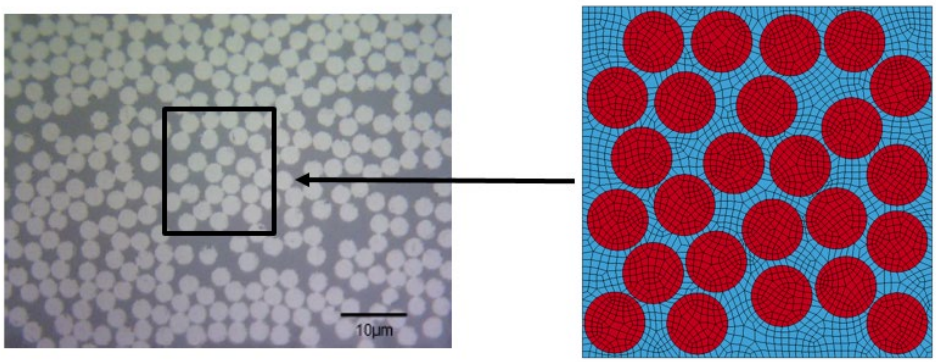

Figure 3.10: Constructing an RVE with Random Distribution of Fibers.

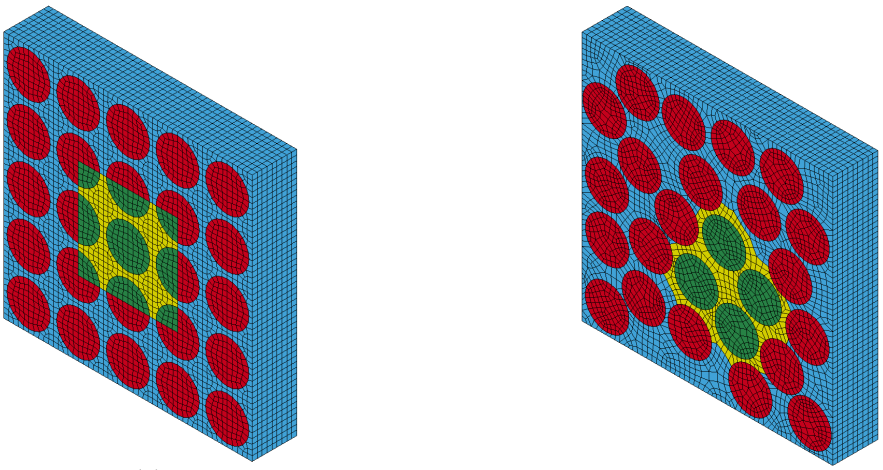

(a) (b)

Figure 3.11: Fiber Arrangements with Gage Section - (a) Regular, and (b) Random. Elements in Green are Fiber Elements and in Yellow Color are Matrix Elements in the Gage Section.

Results and Discussions: The results from the study are shown graphically in Figure 3.12 to Figure 3.15. The following legends are used to denote the different simulations using the following 3-part notation: Type of RVE-Gage Section Size-RVE size [Type of RVE is either Regular (Reg) or Random (Ran), Gage Section is Small (S), Medium (M), Large (L), and RVE Size is 3x3, 5x5, 7x7]. There are six distinct models – Reg-S-3x3, Reg-S-5x5, Reg-S-7x7, Reg-M-5x5, Reg-L-5x5, Ran-M-5x5. In Figure 3.13 to Figure 3.15, the red circle represents the time-stress combination when the first element in the RVE erodes.

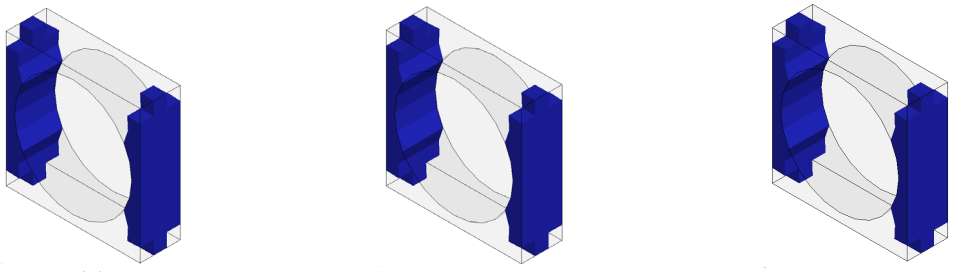

(a) (b) (c)

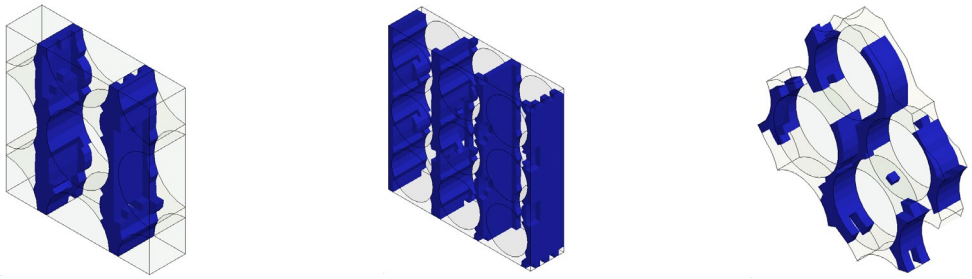

(d) (e) (f)

Figure 3.12: Element Erosion Pattern (Blue Elements) in the Gage Section of the RVEs at $t = 0.01\text{s}$ - (a) Reg-S-3x3, (b) Reg-S-5x5, (c) Reg-S-7x7, (d) Reg-M-5x5, (e) Reg-L-5x5, and (f) Ran-M-5x5.

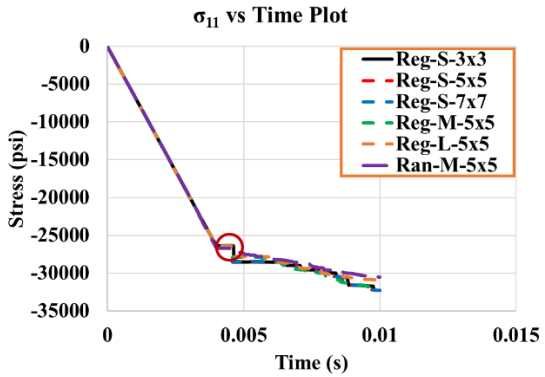

Figure 3.13: σ_{11} versus time.

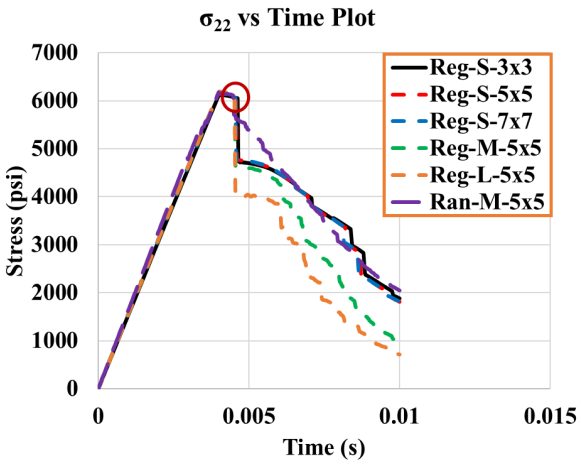

Figure 3.14: σ_{22} versus time.

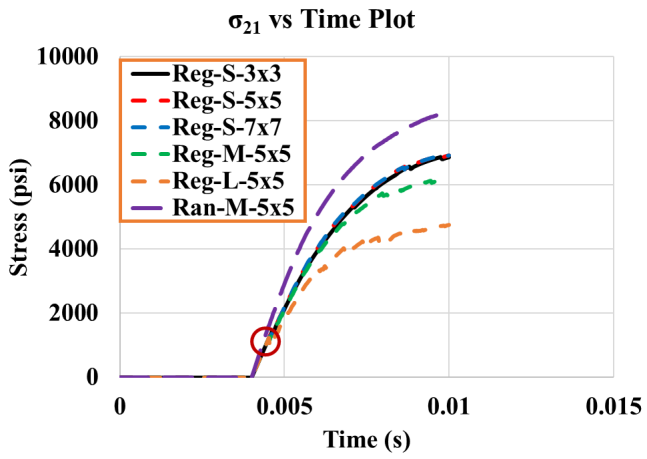

Figure 3.15: σ_{21} versus time.

Figure 3.12 shows the erosion patterns of elements only in the gage section as observed in the six different models at the end of the simulation (t = 0.01 s). Only the matrix elements erode under the applied loading condition with the matrix elements adjacent to the fiber eroding first. In the case of a regular RVE, a symmetrical erosion pattern is observed in the 1-3 plane of the gage section. Figure 3.12(a)-(c) show the same number of eroded elements for different sizes of RVE when the small gage section is used. When comparing regular and random RVEs with the medium gage section (Figure 3.12(d) and (f)), the random RVE model shows a lower number of eroded elements. In a regular RVE with transverse loading, the load is primarily taken up by the matrix elements, whereas in the random RVE, the load is distributed between both fiber and matrix elements depending on the layout of the fibers. While the erosion pattern is different only after FEE, the state of stress at the instant of FEE is the same for all models.

Figure 3.13 to Figure 3.15 show $\sigma_{11}, \sigma_{22}, \sigma_{12}$ versus time plots. These plots are almost identical up until FEE that is independent of the size of the RVE, the size of the gage section, and the fiber arrangement.

Figure 3.13 shows little or no difference in the post-peak region since stress in the 1-direction is predominantly carried by the fibers while only matrix elements actually erode. Consequently, the erosion of matrix elements has a minimal effect in post-peak behavior. However, in Figure 3.14 the post-peak behaviors are not all identical. When considering RVEs of the same gage section size, there is minimal or no variation in the post-peak region because the number of eroded elements remains constant across different RVE sizes. When different gage sections are used in 5x5 RVE, larger gage section shows a more significant drop in the post-peak stress since the number of eroded matrix elements is larger in the gage section. When comparing the effect of random and regular fiber arrangements with medium gage section, the regular RVE shows a higher drop in the post-peak region, primarily due to a higher number of eroded matrix elements in comparison to the random RVE. In Figure 3.15 the shear stress values are initially zero until time $t = t_1 \left(0.004\,\text{sec}\right)$ when shear-inducing loading is applied. Like the scenarios described in Figure 3.13 and Figure 3.14, there is minimal or no variation in the post-peak behavior after FEE across different RVE sizes with the same gage section. There are significant differences observed in the peak stress across different gage sections in a 5x5 RVE. The lowest peak stress is observed with the large gage section, while the highest peak stress is

observed with the small gage section since the number of eroded matrix elements increases with gage size.

Even though the current study does not utilize results from the post-peak region which can be used to derive essential information such as damage-related residual strengths and erosion strains, the future plan is to utilize this information for generating post-peak behavioral data crucial in modeling various impact events (Shyamsunder et al., 2022b).

Based on these findings, the 5x5 RVE with regularly placed fibers and small gage section is taken as the optimal RVE and is used in generating the point cloud data.

3.5 Generating Point Cloud Data

The overarching objective of multiscale modeling is to enable the application of all types of finite elements. However, the scope of the current study is limited to thin shell finite elements. A point cloud surface is generated specifically for thin shell elements, utilizing in-plane (plane stress) failure data. The in-plane tests encompass tension and compression in both longitudinal and transverse directions, in-plane shear, and combinations of these loading scenarios.

Generation of the failure point cloud data (FPCD) involves building a micromechanical model that can be subjected to uniaxial and multiaxial states of stress. Building on prior research (Katusele, 2021; Khaled et al., 2021; Parakhiya, 2020), a similar uniaxial tests were performed with new RUC to validate the results against experiments (Khaled et al., 2018). Following this validation step, multiaxial tests were performed to generate the point cloud data necessary for capturing the composite failure behavior.

To investigate the influence of element size (mesh density), three FE models with varying levels of mesh refinement were constructed and analyzed (as detailed in Table 3.3). The results demonstrated converging behavior across the models, with the fine mesh model yielding results that were most closely aligned with experimental data. However, to strike a balance between computational efficiency and accuracy, the coarse RVE model was adopted for generating the point cloud data. It is worth noting that the generation of element size-dependent point cloud data is outside the scope of this study. Instead, this aspect is earmarked for future work as part of ongoing efforts to refine the modeling framework.

Table 3.3. Coarse, Medium and Fine RVE Finite Element Models.

Parameter	**Coarse**	**Medium**	**Fine**
# Elements	40,500	130,000	279,000
# Nodes	44,816	138,866	294,531
Max. Aspect Ratio	1.82	3.05	2.15
Min. Aspect Ratio	1.05	1.16	1.07
Normalized Wall Clock time	1	3.3	5.0

Considering all the combinations of $\sigma_1 - \sigma_2 - \sigma_{12}$ values, the stress space has 8 octants. However, since the sign of the shear stress σ_{12} does not affect the failure surface, there are effectively only four quadrants of values as shown in Table 3.4. The point cloud data is generated in these quadrants using the 2-step boundary conditions shown earlier in Figure 3.7.

Table 3.4. List of Effective Octants (Quadrants).

Octant/Quadrant number	**($\sigma_1 - \sigma_2 - \sigma_{12}$)**
1	(+, +, +)
2	(-, +, +)
3	(-, -, +)
4	(+, -, +)

3.5.1 Uniaxial Loading Virtual Tests

To evaluate the accuracy and reliability of the developed RUC, a series of in-plane uniaxial tests were conducted. These tests were used to replicate experimental conditions, allowing for direct comparison between the RUC's results and experimental data. Five distinct uniaxial loading scenarios were applied as boundary conditions, as shown in Figure 3.16. These tests included: 1 and 2 direction tension and compression and 1-2 plane shear. The stress-strain data was extracted from the gage section of the RUC model. The extracted data were used to construct stress-strain curves for each of the five tests and then compared with experimental data as shown in Figure 3.17.

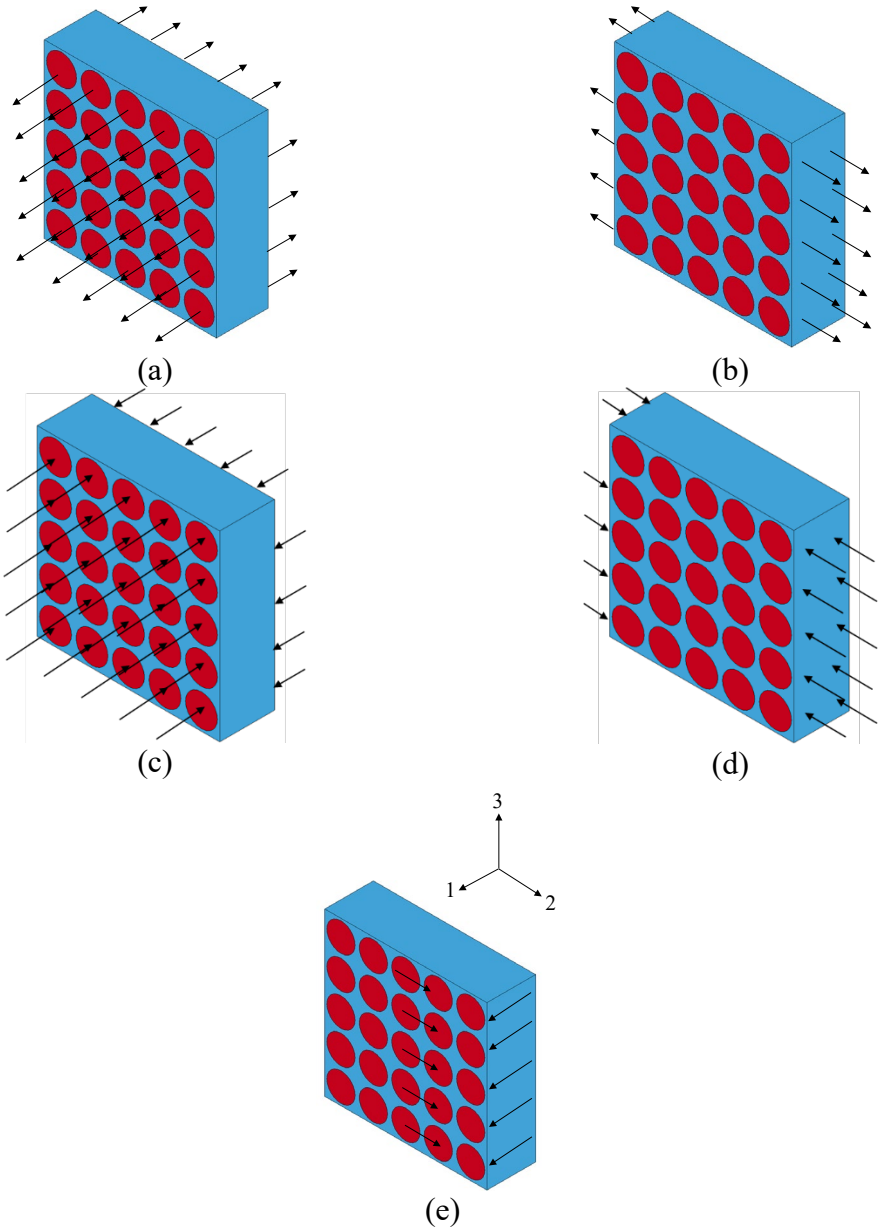

Figure 3.16: Applied Specified Displacements for Uniaxial Tests - (a) 1-Direction Tension, (b) 2-Direction Tension, (c) 1-Direction Compression, (D) 2-Direction Compression, and (e) 1-2 Plane Shear.

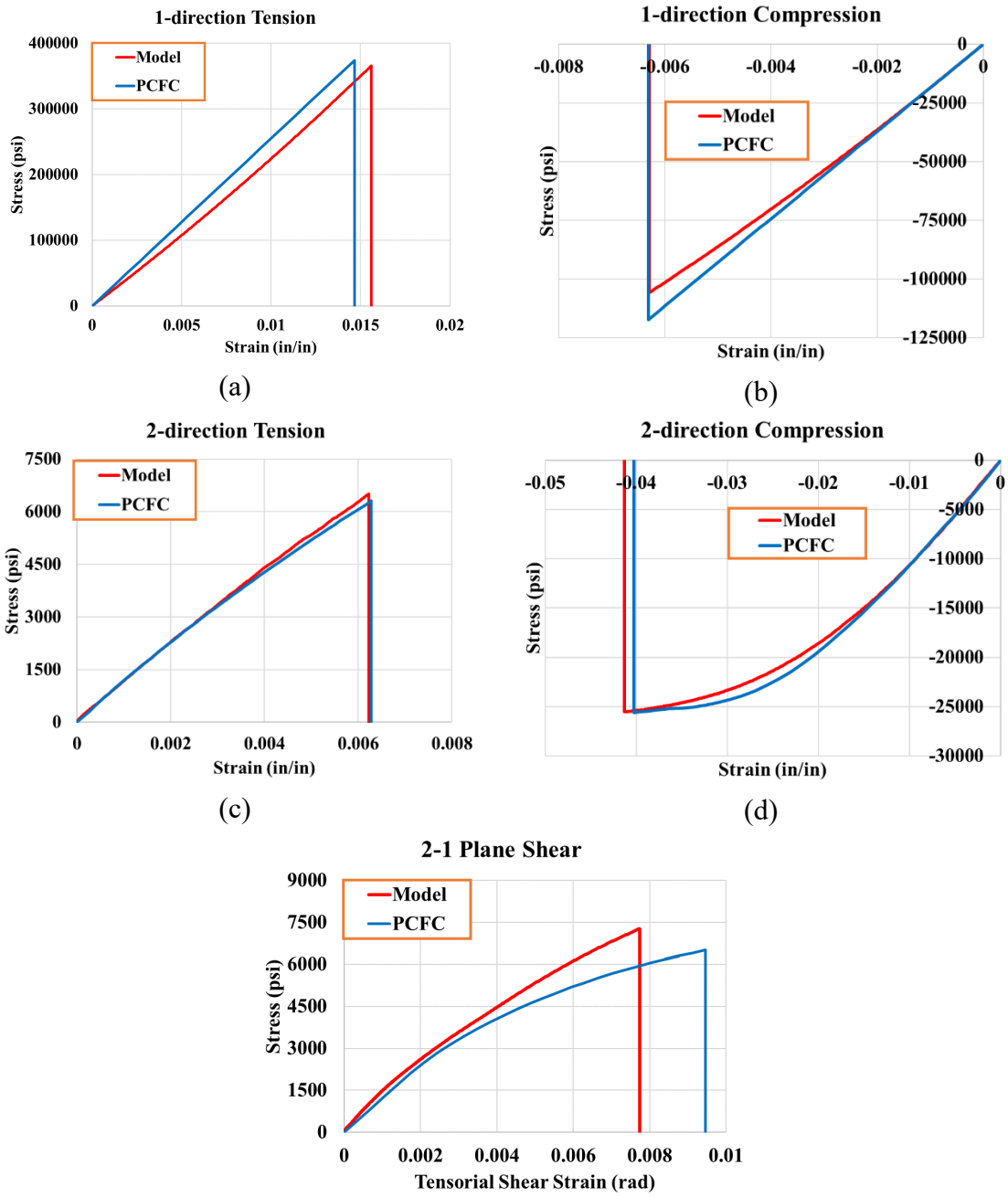

Figure 3.17: Uniaxial Test - (a) 1-Direction Tension, (b) 1-Direction Compression, (c) 2-Direction Tension, (d) 2-Direction Compression, and (e) 2-1 Plane Shear.

Figure 3.17(a)-(e) shows the stress-strain curve from 1-direction and 2-direction tension and compression tests, and shear in the 1-2 plane. The RVE generated results are reasonably close to the experimental data that is the average of at least three replicates. The modulus of the 1-direction tension test from RVE model is higher than the corresponding value from experiment. One possible reason is that the fibers likely straighten (due to initial slack) in the experiment whereas fibers in the RVE model are assumed to be straight with no initial slack. The 2-1 plane shear stress-strain curve from FE is close to the experiment up to 0.004 strain beyond which the experimental data shows higher peak stress and lower ultimate strain. This discrepancy is likely due to the difference in specimen geometry: the experiment utilized an Iosipescu specimen, whereas a rectangular specimen was used in the FE analysis. A total of 5 FPCD points is computed and validated using these virtual tests.

3.5.2 Multiaxial Loading Virtual Tests

To generate a sufficiently large number of FPCD points, several hundred RVE models need to be created, analyzed and post-processed. Each octant was uniformly discretized into 100 points in $\sigma_1 - \sigma_2$ plane and surface traction scale factors for each point were calculated (Figure 3.6(b)). The scale factor ranged from 0 to 1, with 0 indicating no stress value in RVE and 1 corresponding to the applied largest normal traction values in the RVE.

Figure 3.18 shows the generated point cloud data. A few of the points are compared to uniaxial test results from experiments and from FE models (Katusele, 2021) and show excellent agreement. The generated point cloud data covers the space that lies within the

strength values obtained from uniaxial tests. About 10% of the data points are located near the edges (defined as the state of stress where one or more components numerically dominate all other components), i.e., data points are located near the edges where σ_{11} component is dominant in all four effective octants. Specifically, the applied normal traction values in range from $567,000\,psi$ to $630,000\,psi$ on fiber element in 1-direction tension, $-198,000\,psi$ to $-220,000\,psi$ on fiber elements in 1-direction compression, $5670\,psi$ to $6300\,psi$ on matrix element in 1-direction tension or $-2880\,psi$ to $-3200\,psi$ on matrix elements in 1-direction compression resulted in erosion of fiber or matrix elements before applying the specified displacement for shear loading. There are two clearly distinguishable types of failure regions. The vast majority of the failure stress space is associated with matrix failure while fiber-matrix failure region is localized at the ends where the longitudinal (1-direction) stress values are very high.

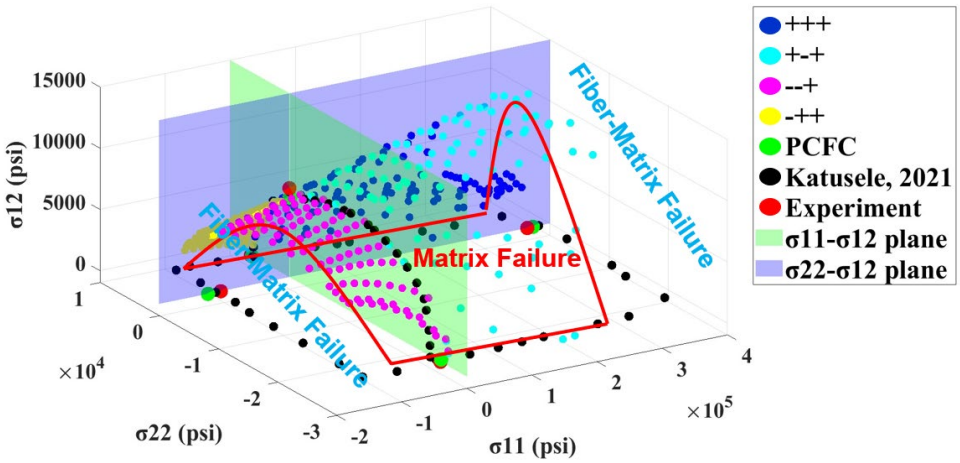

Figure 3.18: Point Cloud Data.

A total of 424 points were generated as point cloud failure data as shown in Table 3.5 where compressive stresses are denoted as negative values.

Table 3.5. List of Effective Octants (Quadrants).

Octant number	**# of Points**	**(Min) - (Max) σ_1 (psi)**	**(Min) - (Max) σ_2 (psi)**	**(Min) - (Max) σ_{12} (psi)**
1	117	(33) – (357665)	(31) – (5905)	(900) – (9892)
2	87	(-118747) – (0)	(258) – (6136)	(969) – (6392)
3	124	(-118678) – (0)	(-26845) – (-56)	(1237) – (8093)
4	96	(5) – (356196)	(-26162) – (-11)	(8) – (12641)

Equation Chapter (Next) Section 1

CHAPTER 4

POINT CLOUD FAILURE CRITERION

The Point Cloud Failure Criterion is based on the use of the generated FPCD presented in the previous chapter. This chapter explores various prediction methods used with PCFC, underlying theories, data structures, implementation strategies, and the verification and validation of the developed procedures.

4.1 Prediction Methods

Three prediction methods that build a model using the generated FPCD and then use the model to answer if a given state of stress or strain is inside or outside the failure envelope, are discussed.

4.1.1 Approximate Nearest Neighbor (ANN) Method (Maurya et al., 2024a)

The approximate nearest neighbor problem involves finding the nearest neighbor given a query point (Maurya et al., 2024a; Maurya and Rajan, 2024). The main reason why this problem is of importance is because checking whether the current state of stress or strain is inside or outside the failure envelope is an important part of finite element analysis. In other words, once the points on the failure surface are generated, the approximate nearest neighbor methods can be used to determine *k*-nearest neighbors from which it can be ascertained if a given stress or strain tensor computed at a finite element stress Gauss point is inside or outside the failure surface.

Given the general Minkowski norm of order *r*, the distance of the failure point from the origin, L_r is given by

$$L_r = \left(\sqrt{\sum_{i=1}^{d} \left| v_i^j \right|^r} \right) \tag{3.1}$$

where,

d is the dimension of the space (in the current work, $d = 3$ such that $\boldsymbol{\sigma} = \{\sigma_1, \sigma_2, \sigma_{12}\}$)

v is the vector position of each point in the d-dimensional space representing σ or ε.

With $r = 2,$ the Euclidean distance is computed, and this distance is used in the current work. Determination of whether the stress point is inside or outside the failure envelope is made as follows. Let

$$f^{fail} = L_2^{FEA} - \left(\left(L_2^{PCD} \right)_{avg} - \beta \sigma_{range} \right) \tag{3.2}$$

where L_2^{FEA} is the computed distance using the stress components obtained from finite element analysis, L_2^{PCD} is the distance of a point in the point cloud data, $\sigma_{range} = \max\left\{ \left(\sigma_1^{\max} - \sigma_1^{\min} \right), \left(\sigma_2^{\max} - \sigma_2^{\min} \right), \left(\sigma_{12}^{\max} - \sigma_{12}^{\min} \right) \right\}$, and $\beta^L \le \beta \le \beta^U$, is a reduction factor that moves the failure surface towards the origin and can be thought of as a safety factor. The onset of failure is predicted if

$$f^{fail} \ge 0 \tag{3.3}$$

and no failure is predicted if

$$f^{fail} < 0 \tag{3.4}$$

4.1.1.1 ANN Implementation (Maurya and Rajan, 2024)

The ANN method used in this study is based on the standard *k-d* tree search algorithm that has been enhanced to use incremental distance calculation and implemented in the ANN library (Mount, 2010). Since the dimensionality of the underlying data is small and the points are not clustered, the standard search option in ANN library is used.

The overall approach can be divided into two steps. The first step concerns development of the ANN data structure.

Step 1.1: Once FPCD is read and stored, the centroid of the failure surface is computed as

$$\left(v^j\right)_c = \frac{\sum_{i=1}^{n_{PC}} v_i^j}{n_{PC}}, j = 1,..,3 \tag{3.5}$$

Step 1.2: Each point on the failure surface is translated as

$$\left(v_i^j\right)^t = \left(v_i^j\right) - \left(v^j\right)_c, i = 1,..,n_{PC}, j = 1,..,3 \tag{3.6}$$

Step 1.3: The translated failure surface is then normalized by using the absolute maximum value of each stress component as

$$v_{ij} = \frac{\left(v_i^j\right)^t}{v_j^m}, i = 1,..,n_{PC}, j = 1,..,3 \tag{3.7}$$

where v_j^m is the absolute maximum value for jth component of the failure surface. The process of translating and scaling the (stress/strain) component values have the following

advantages. First, all values are between $[-1,1]$. This is relevant since unidirectional composites are typically very strong in the 1-direction and much weaker in the 2, 3 directions. Second, this makes the number of points per octant nearly equal, thus facilitating an effective search.

Step 1.4: Finally, the *k-d*-tree construction takes place. First, a skeleton tree is built. Next, the bounding box for all the points is computed. Finally, the tree is built using an appropriate splitting routine.

The second part deals with using the constructed data structure to evaluate if a given stress state $\boldsymbol{\sigma}^{FEA} = \{\sigma_1, \sigma_2, \sigma_{12}\}^{FEA}$ is inside or outside the failure surface.

Step 2.1: The query point $\boldsymbol{\sigma}^{FEA} = \{\sigma_1, \sigma_2, \sigma_{12}\}^{FEA}$ are translated and scaled using Eqns. (4.6) -(4.7).

Step 2.2: The query point is then used by the search algorithm that requires in addition to the point, the number of nearest neighbor points (k) and the error bound, ε. The search algorithm returns the indices of the *k*-nearest points and their distances from the query point.

Step 2.3: The average Euclidean distance of the *k*-neighborhood points is computed as

$$L_2^{PCD} = \frac{\sum_{N=1}^{k} L_2^N}{k} \tag{3.8}$$

and is used in Eqn. (4.2). If $f^{fail} \geq 0$, the query point is tagged as having satisfied the failure onset criterion.

4.1.1.2 Simplified ANN (SANN) (Maurya and Rajan, 2024)

The Simplified ANN method has been developed to specifically handle low dimensionality point space ($d = 3, 4, \text{ and } 6$) for use with FPCD in the context of finite element simulations. The overall approach can be divided into two steps. The first step deals with the development of the SANN data structure.

Step 1.1 to 1.3: Same as ANN's Step 1.1 to 1.3.

Step 1.4: Compute the distance of each point from the origin as

$$L_2^i = \sqrt{\sum_{j=1}^{d} (v_{ij})^2}, i = 1, .., n_{PC} \tag{3.9}$$

In addition, store the octant number and distance. The data structure is made up of – an index that points to the location in the user-specified FPCD input, octant number, and distance.

Step 1.5: Sort the data so that all the data points for an octant are stored together in ascending order of octant number. This sorted list makes it possible to efficiently search through only the data points for one octant when search is initiated in Step 2.

The second step deals with using the constructed data structure to evaluate if a given stress state $\boldsymbol{\sigma}^{FEA} = \{\sigma_1, \sigma_2, \sigma_{12}\}^{FEA}$ is inside or outside the failure surface.

Step 2.1: The query point $\boldsymbol{\sigma}^{FEA} = \{\sigma_1, \sigma_2, \sigma_{12}\}^{FEA}$ is translated and scaled using Eqns. (4.6) -(4.7) and the Euclidean distance is computed as

$$\left(L_2^i\right)^{FEA} = \sqrt{\sum_{j=1}^{3} (v_{ij})^2} = \sqrt{\sum_{j=1}^{3} (\sigma_{ij})^2} \tag{3.10}$$

Step 2.2: Using $\boldsymbol{\sigma}^{FEA} = \{\sigma_1, \sigma_2, \sigma_{12}\}^{FEA}$ the octant number is obtained, and a search is initiated so that the nearest *k*-neighbors can be found from the data structure created in Step 1.5.

Step 2.3: The average Euclidean distance of the *k*-neighborhood points is computed using two methods: (1) the Uniform Weightage (UW) method where each *k*-neighborhood point is assigned equal weight representing the average distance (AD) of the neighborhood points, and (2) the Inverse Distance Weightage (IDW) method where points closer to the target location are given higher weight compared to those farther away.

$$L_2^{PCD} = \frac{\sum_{N=1}^{k} w_N L_2^N}{\sum_{N=1}^{k} w_N}$$

$$where \tag{3.11}$$

$$w_N = \begin{cases} 1 & for\ AD \\ \dfrac{1}{(d_N)^p} & for\ IDW \end{cases}$$

where, d_N is the distance between query point and neighbor point and p is a power parameter (typically 1 for inverse distance and 2 for inverse squared distance).

L_2^{PCD} is used in Eqn. (4.2). If $f^{fail} \geq 0$, the query point is tagged as having satisfied the failure onset criterion.

4.1.2 Neural Network (Maurya et al., 2024a)

In the neural network approach, the failure onset for a given stress state is predicted in two steps. In the first step, a Feed-forward Neural Network (F-NN) that maps the failure surface using point cloud stress data is configured. The prediction about whether a specified stress state falls inside or outside of this mapped failure surface is predicted in the second step. It should be noted that F-NN is constructed only once for a given composite. As with the previous methods, the second step of the process is used in the finite element analysis with each new query point.

Step 1: Building an F-NN to map the failure surface.

A F-NN model is constructed to predict σ_{12} that lies on the failure surface $\left(\hat{\sigma}_{12,f}\right)$ for a given combination of σ_{11} and σ_{22}. The construction of the F-NN model includes configuration and training of the network that best approximates the failure surface. Configuring a neural network involves determining the architecture, including the number of fully connected layers, the number of neurons in each layer, and the choice of activation function for each neuron in every layer. Training the network involves optimizing the trainable parameters (weights and biases) to minimize prediction errors. Finding the optimal neural network configuration requires training networks with different architectures and comparing their prediction performance. To train and configure the F-NN, the first two stress components σ_{11} and σ_{22} are used as input features, while the third stress component $\left(\hat{\sigma}_{12,f}\right)$ is generated as the output variable. The input and output values

were scaled using a scaling vector $\mathbf{s} = \left\{ s^1, s^2, s^3 \right\}$ to prevent exploding weights and improve convergence stability prior to the training as

$$v_{ij} = \left(s^j \right) \left(v_i^j \right), i = 1,..,n_{PC}, j = 1,..,3 \tag{3.12}$$

The scaled dataset is then split 80/20 into training and testing sets. The training set is used to tune the network weights and biases by minimizing the network loss using backpropagation with the Adaptive Moment Estimation (ADAM) optimizer (Kingma and Ba, 2014). The unseen testing set is then used to evaluate the model generalization capability.

$$loss = 1/n \sum_1^n (\hat{y}_i - y_i)^2 + \lambda \sum_1^m w_i^2 \tag{3.13}$$

where, $\hat{y}_i$ and y_i are the predicted and true outputs respectively, w_i is a weight parameter, n is the number of data instances used in the training, and m is the number of relevant weight parameters.

The network loss is calculated using the expression in Eqn. (4.13), which consists of two terms. The first loss term is called data loss and is defined as the mean squared error between the predicted output and the true output, which are $\hat{\sigma}_{12,f}$ and $\sigma_{12,f}$ respectively. The data loss term drives the model learning from the data. The second term is the L2 (ridge) regularization loss optionally added to penalize the higher magnitudes of squared weights and thus obtain less complex models that generalize well for all data. L2 regularization is selected over L1 regularization in this work because the input feature sets are small as they contain only 2 features that contribute equally to prediction. The regularization coefficient

λ controls model complexity and tradeoffs between under fitting and overfitting. Higher λ values lead to under fitting, while lower values risk overfitting.

Step 2: Prediction of the failure condition of a stress state.

In this step, the queried stress states are evaluated as being inside or outside the failure surface. The following steps describe this process.

Step 2.1: The first two components of query point $\sigma^{FEA} = \{\sigma_{11}, \sigma_{22}, \sigma_{12}\}^{FEA}$ are scaled using Eqn. (4.12).

Step 2.2 $\hat{\sigma}'_{12,f}$ is then computed by feedforwarding σ'_{11} and σ'_{22} based on the expressions shown in Eqn. (4.14).

$$\begin{aligned} z_j^l &= w_{jk}^l a_k^{l-1} + b_j^l z_j^l \\ a_j^l &= \phi(z_j^l) \end{aligned} \tag{3.14}$$

where l is the layer number, j is the neuron number in the l^{th} layer. w and b are weights and biases associated with the l^{th} layer. z and a are net inputs and activation values of l^{th} layer. ϕ is an activation function, i.e., ReLU or TanH. There is no activation for the zeroth layer as they are the input (σ'_{11} and σ'_{22}) to the F-NN and the output of the activation function of the neuron in the last layer is the output value ($\hat{\sigma}'_{12,f}$).

Step 2.3: $\hat{\sigma}_{12,f}$ is obtained by $\hat{\sigma}'_{12,f}$ rescaling and compared σ_{12} with as follows to predict the onset of failure:

$$\begin{aligned} &If\ \sigma_{12} \le \beta\hat{\sigma}_{12,f} :\ No\ onset\ of\ failure \\ &If\ \sigma_{12} > \beta\hat{\sigma}_{12,f} : Onset\ of\ failure \end{aligned} \tag{3.15}$$

4.2 Implementation in Computer Programs (Maurya et al., 2024a)

Implementation of the methods in two computer programs is discussed.

Standalone Program: Algorithms for all three methods were coded in a single computer program, SAPCFC, written in C++. The entire system is implemented using Microsoft Visual Studio 2022 running on a workstation with 64-bit Windows 10 Enterprise. The program architecture is shown in Figure 4.1. The main class, CPCFC, controls the program flow. The Object-Oriented Numerical Methods (OONM) library (Rajan, 2021) provides the data structures and methods such as vector and matrix classes, an input file parser, a pseudo-random number generator, an interface to Windows API to obtain memory usage, and wall clock/CPU timings, etc.

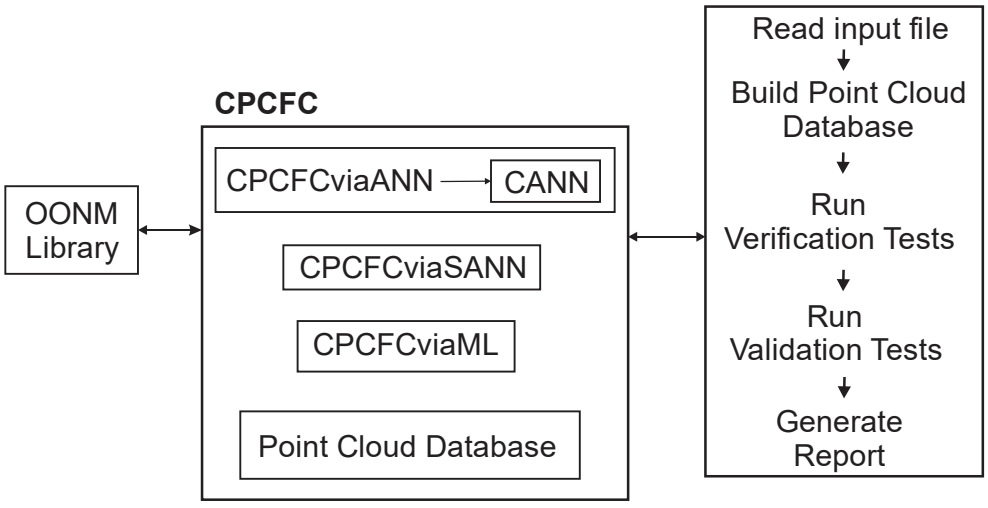

Figure 4.1: SAPCFC Program Architecture, and Flow.

The classes that implement the three methods, CPCFCviaANN, CPCFCviaSANN, and CPCFCviaML, are used in the main class. They have access to the point cloud database once the input file is read and the database is created. Command line arguments are used to run either verification tests or validation tests or both. At the end of the execution, a

report is generated. Results from the report for the verification and validation tests are used in Sections 4.1 and 4.2.

LS-DYNA: Only two methods are coded into MAT_213 as the task of converting the ANN C++ code to FORTRAN was determined to require substantial effort. The overall program architecture is shown in Figure 4.2.

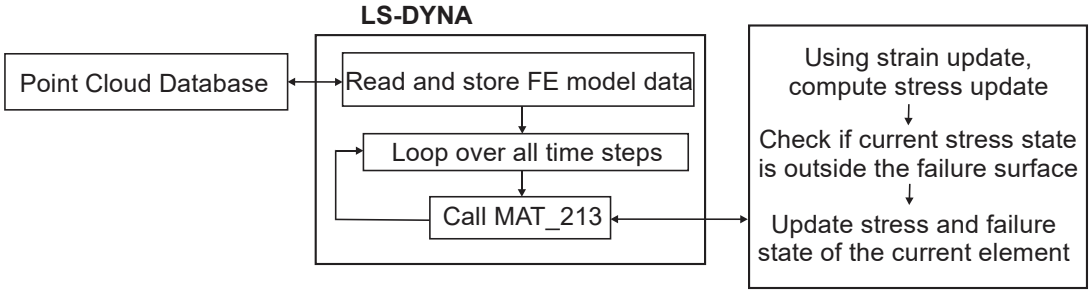

Figure 4.2: MAT_213 Program Architecture, and Flow in LS-DYNA.

Once failure onset is detected, a stress degradation model is implemented to avoid numerical instability. In an explicit FE analysis, eroding an element that satisfies the failure criterion is likely to cause a large redistribution of loads around the eroded element leading to extremely distorted elements and a drastic reduction in the stable time step (Shyamsunder et al., 2022b). Therefore, the state of stress in an element where failure onset is detected needs to be reduced gradually. A Stress Degradation Model (SDM) is implemented as shown Figure 4.3(a). The term true stress refers to the stress state in a damaged state, whereas the effective stress refers to the stress state in an undamaged state. The effective stress is held constant in the post-peak region, but the true stress is gradually reduced. The gradual degradation of stress (see Figure 4.3(a)) is linked to the corresponding effective damage parameter (c^d) shown in Figure 4.3(b). At failure onset, let $\sigma_{eff,0}, \sigma_0$ and

ε_0 represent the effective stress, true stress, and true strain values, respectively. Parameter c_0^d is an effective damage parameter at failure onset, that has a zero value in the absence of pre-peak damage. The true stress value reduces from σ_0 by increasing the effective damage parameter from c_0^d to a larger value at increasing strain values that range from $\varepsilon_0 - \varepsilon_1 - \varepsilon_f$ as shown in Eqns. (4.16)-(4.17). The final reduced strength (called residual strength) of the material is computed as $\left(\sigma_f\right)_i = \left(\sigma_{eff,0}\right)_i \left(1 - c_i^d\right), i = 1,2,4,5,7$, and is maintained at a constant value from ε_1 to ε_f till the element is eroded at the erosion strain value, ε_f.

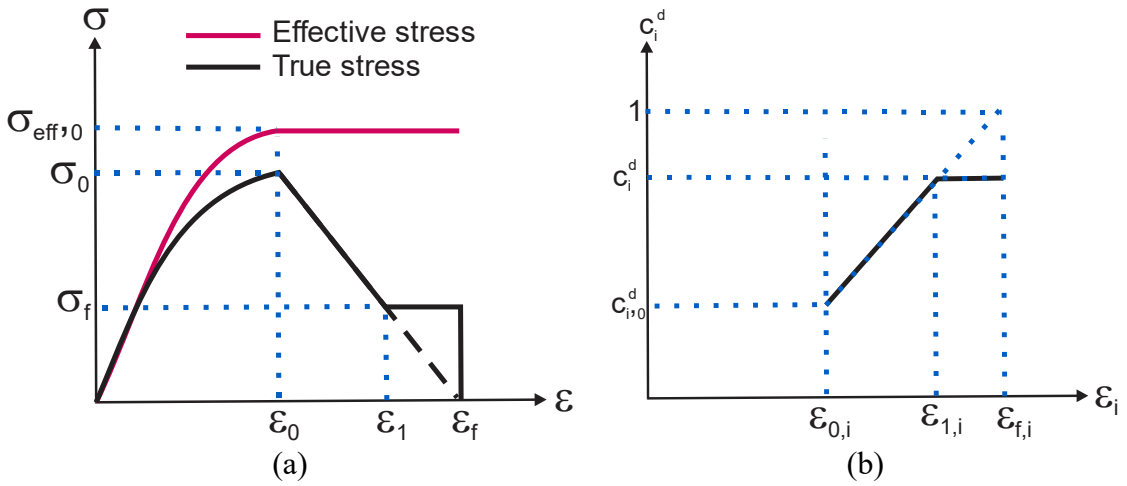

Figure 4.3: Typical - (a) Stress vs Strain Response, and (b) Effective Damage Parameter vs Strain.

Step 1: If failure onset has taken place, compute the c^d as follows

$$c_t^d = c_{t-1}^d + \Delta c_t^d \tag{3.16}$$

where

$$\Delta c_t^d = \begin{cases} 0 & \varepsilon_t < \varepsilon_0 \\ 1 + (1 - c_{t-1}^d)\dfrac{\varepsilon_t - \varepsilon_{t-1}}{\varepsilon_f - \varepsilon_{t-1}} & \varepsilon_0 < \varepsilon_t \le \varepsilon_1 \end{cases} \tag{3.17}$$

If $c_t^d > c_i^d$, then $c_t^d = c_i^d$.

Step 2: If the element is not in the failure state, compute the c^d as follows

$$\begin{aligned}
c_1^d &= 1 - \left\{\left(1 - d_{11_T}^{11_T}\right)\left(1 - d_{11_C}^{11_T}\right)\left(1 - d_{22_T}^{11_T}\right)\left(1 - d_{22_C}^{11_T}\right)\left(1 - d_{12}^{11_T}\right)\right\} \\
c_2^d &= 1 - \left\{\left(1 - d_{11_T}^{22_T}\right)\left(1 - d_{11_C}^{22_T}\right)\left(1 - d_{22_T}^{22_T}\right)\left(1 - d_{22_C}^{22_T}\right)\left(1 - d_{12}^{22_T}\right)\right\} \\
c_4^d &= 1 - \left\{\left(1 - d_{11_T}^{11_C}\right)\left(1 - d_{11_C}^{11_C}\right)\left(1 - d_{22_T}^{11_C}\right)\left(1 - d_{22_C}^{11_C}\right)\left(1 - d_{12}^{11_C}\right)\right\} \\
c_5^d &= 1 - \left\{\left(1 - d_{11_T}^{22_C}\right)\left(1 - d_{11_C}^{22_C}\right)\left(1 - d_{22_T}^{22_C}\right)\left(1 - d_{22_C}^{22_C}\right)\left(1 - d_{12}^{22_C}\right)\right\} \\
c_7^d &= 1 - \left\{\left(1 - d_{11_T}^{12}\right)\left(1 - d_{11_C}^{12}\right)\left(1 - d_{22_T}^{12}\right)\left(1 - d_{22_C}^{12}\right)\left(1 - d_{12}^{12}\right)\right\}
\end{aligned} \tag{3.18}$$

where c_1^d is effective damage parameter in 1-direction tension,

c_2^d is effective damage parameter in 2-direction tension,

c_4^d is effective damage parameter in 1-direction compression,

c_5^d is effective damage parameter in 2-direction compression,

c_7^d is effective damage parameter in 1-2 plane shear, and

d_{ij}^{kl} indicates damage in direction ij and the reduction of stiffness in direction kl and is obtained from the damage curve based on computed effective plastic strain. Details of this process can be found in a previous publication (Shyamsunder et al., 2021).

Step 3: If the current point is in failure state, the element is eroded from finite element model if

$$\varepsilon^{eq} = \sqrt{\varepsilon_{11}^2 + \varepsilon_{22}^2 + 2\varepsilon_{12}^2} > \varepsilon_{IP}^f \tag{3.19}$$

where ε_{IP}^f is the in-plane erosion strain (a user input).

4.3 Standalone Program Tests and Results (Maurya et al., 2024a)

Multiple sets of verification and validation tests were conducted. The first set of tests is conducted by generating the point cloud data using the Tsai-Wu Failure Criterion (TWFC data). Since this failure criterion is a smooth, differential function, a smooth point cloud failure surface is generated. The second set of tests is conducted with point cloud data constructed with virtual testing as described in Section 3 (PCFC data). The Standalone program is used with two sets of tests involving all three predictive methods.

In both test datasets, the points on the point cloud failure surface, $\boldsymbol{\sigma}$ were scaled by a strength factor, SF that in this part of the study is varied as $0.5 \le SF \le 1.1$. If $SF < 1$, the point is shifted inside the failure surface, otherwise it is moved outside. In other words, the test data points are created as $\sigma_i^{test} = SF_i \sigma_i, i = 1,...,n_t$ with f_i created using a pseudo-random number generator with n_t being the total number of test data points. The primary objective of these tests is to gage how the developed algorithm would work in an actual FE analysis (third test) where the stresses in an element would increase to approach the failure surface from inside the failure envelope. The result generated for each test data point belongs to one of three categories: Correct Prediction, False Positive, and False Negative.

Correct Prediction: A prediction is counted as being correct if the prediction matches the data, i.e., failure prediction for test data points on or outside the failure surface $(SF \geq 1)$, and no failure prediction otherwise $(SF < 1)$.

False Positive: A false positive is the test case where the test data is classified as being outside the failure envelope, but the test data point is, in fact, inside the failure surface.

False Negative: A false negative is the test case where the test data point is classified as being inside the failure envelope, but the test data point is, in fact, outside the failure surface.

Accuracy: Defined as $\frac{\#\text{ of Correct Predictions}}{n_t} \times 100.$

All three methods require tuning values of method-related parameters. The tuning methodology is explained next.

ANN and SANN Modeling: The accuracy of these two methods is affected by two parameters – *k*, the number of nearest neighbors (see Eqns. (4.8) and (4.11)), the reduction factor, β (see Eqn. (4.2)) and power parameter p (see Eqn. (4.11)). Testing with small and large, smooth, and noisy data indicated that $k = 3$, $\beta = 0.003$ and $p = 2$ provided the best combination that balanced accuracy and compute time.

Neural Network Modeling: The point-cloud datasets TWFC and PCFC form two distinct failure-onset surfaces. The point-cloud data of TWFC has a smooth surface since it is generated from a closed-form expression. In contrast, the point-cloud data for the PCFC is not smooth since it comes from a finite set of finite element analyses (see Figure 3.18). The

TWFC dataset is also 6 times larger in size compared to the PCFC dataset (2527 vs. 415 data points). Due to these reasons, the final feedforward neural network (F-NN) configurations for each dataset were explored separately. Finding the final configurations for each dataset involved exploring various configurations by varying the number of fully connected layers, number of neurons in each layer, and activation functions like Rectified Linear Unit (ReLU), Hyperbolic Tangent (Tanh), and Exponential Linear Unit (ELU). The optimal configurations were selected based on the prediction performance, considering not only the training data but also the testing data unseen during training. To simplify the configuration process, only networks that start with the 2^q (where q is an integer) number of neurons in the first hidden layer and halve over subsequent hidden layers were explored. Ultimately, two top-performing configurations, one leaner than the other, were chosen for each dataset for further investigation of their classification accuracy and computational efficiency. The F-NN with larger network parameters is denoted as 'deep', while the one with smaller network parameters is termed 'shallow' in the current work.

For both datasets, the best estimates of the scaling parameters (Eqn. (4.12)) were found to be $\mathbf{s} = \left\{10^{-5}, 10^{-4}, 10^{-4}\right\}$. Through parametric analysis, optimal L2 regularization coefficients (λ) of 10^{-4} and 10^{-5} were chosen for the FNNs trained on TWFC and PCFC (deep model) data, respectively. No regularization was applied for the PCFC shallow model since failure onset surface is more complex and using L2 regularization resulted in an under fit model with poor prediction performance. Figure 4.4 illustrates the deep F-NN

trained on PCFC data, comprising five hidden layers with 2,977 total trained network parameters.

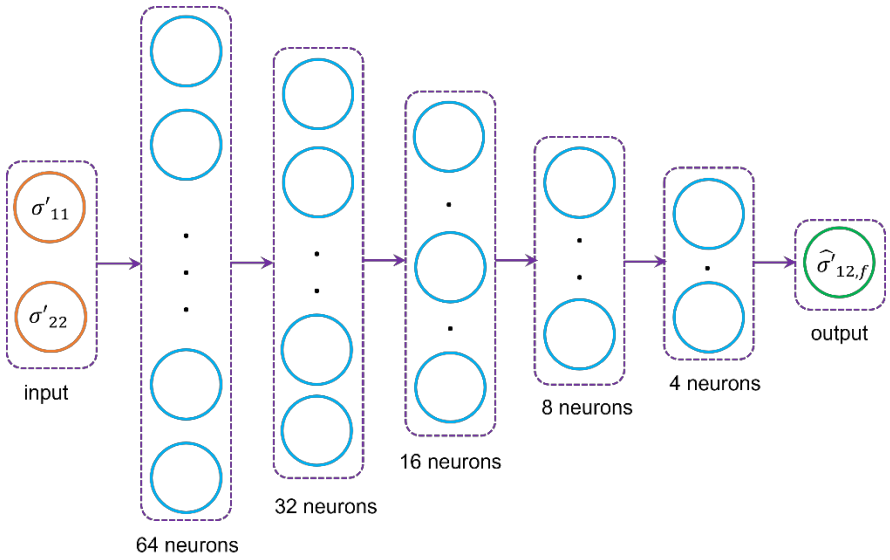

Figure 4.4: Network Architecture of the Deep F-NN Trained on PCFC Point Cloud Dataset.

Table 4.1: Network Configuration and Training Details of the F-NN Used in the Analysis.

Network Details	**PCFC**		**Tsai-Wu**	
	Deep	**Shallow**	**Deep**	**Shallow**
No. of data instances	415	415	2527	2527
No. of hidden layers	5	4	5	4
No. of neurons in the first layer	64	32	32	16
No. of trainable network parameters	2977	801	809	233
Activation function for hidden layers	ReLU†	ReLU†	ReLU†	ReLU†
Regularization Coefficient	10^{-5}	-	10^{-4}	10^{-4}
Mean Squared Error	0.00651	0.00667	0.00221	0.00247
Mean Absolute Error	0.03168	0.03761	0.01292	0.01739

† ReLU – Rectified Linear activation function

Deep neural network models of both datasets perform marginally better at predicting failure onset surface than shallow models (Table 4.1). However, the marginal performance gains of deeper models come at a steep computational expense. Since the number of matrix-vector operations required for prediction scales directly with the parameter count, deep networks are significantly less efficient in terms of run time, which negates the benefits of their slightly improved predictive accuracy. Additionally, incorporating the NN model in finite element analysis for failure onset prediction requires storing the neural network parameters and creates an additional computational head compared to ANN and SANN methods. However, the computational expense of neural networks can be reduced by 'pruning' - removing parameters that do not significantly impact model predictions. Many pruning techniques exist, including removing neurons, synapses, or entire layers during or after training (Vadera and Ameen, 2020). As pruning may adversely affect performance, selecting an appropriate technique is essential. In the current work, a pruning strategy that operates on the trained neural network and removes synapses (neural connections) that are redundant to the network prediction is devised. The synapses are considered redundant if the neurons associated with them have nearly zero activation values for any possible input. While a hard constraint like this tends to prune fewer synapses, providing less computational improvement, the approach is effective for sparse networks, and the deeper networks that avoid overfitting tend to be sparse. The approach also simplifies implementation for networks with ReLU activation functions, as shown in Eq. 21, without sacrificing desired prediction accuracy:

$$\sum_{i=1}^{m}\left|w_{ir}^{l}\right| \le 10^{-6}$$
$$b_{r}^{l} \le 10^{-6} \tag{3.20}$$

where w_{ir}^{l} is the weight value corresponding to the synapse connecting i^{th} neuron in the preceding layer (l^{-}) and the redundant r^{th} neuron in the l^{th} layer, and b_{r}^{l} is the bias value of r^{th} neuron in the l^{th} layer, and m is the number of neurons in the l^{-th} layer.

Overall, the employed pruning strategy, illustrated in Figure 4.5, provides an efficient way to improve the computational performance of deep neural networks while retaining acceptable predictive performance.

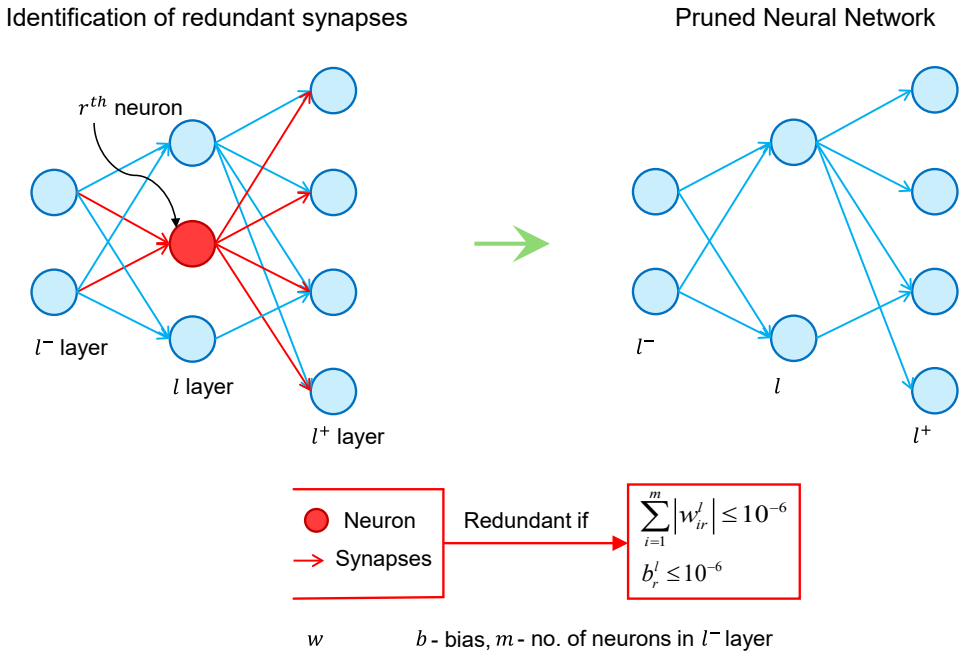

Figure 4.5: Pruning Strategy Employed in the Study.

With this pruning strategy, the number of neural network parameters of the deep model trained on PCFC data was reduced from 2,977 in the original model to 355 in the pruned

version. Interestingly, this 75% decrease in network size resulted in the pruned deep model containing less than half the network parameters of the shallow model that has 801 parameters. The pruned version of the deep model is more efficient than the shallow model while retaining the prediction accuracy of the deep model. Table 4.2 compares the architectural details and number of trainable parameters for the pruned deep (NN-DP) model, the original deep (NN-D) and the shallow (NN-S) models. Finally, it should be noted that the safety factor (β) of 0.02 was used for all the F-NN models.

Table 4.2: Comparison of Network Architecture of Pruned Network with Unpruned Deep and Shallow.

Layers	**No. of neurons**			**No. of trainable parameters**		
	NN-D	**NN-S**	**NN-DP**	**NN-D**	**NN-S**	**NN-DP**
Input	2	2	2	-	-	-
hidden1	64	32	23	192	96	69
hidden2	32	16	7	2080	528	168
hidden3	16	8	7	528	136	56
hidden4	8	4	5	136	36	40
hidden5/output	4	1	3	36	5	18
output	1	-	1	5	-	4
No of Trainable Network Parameters				2977	801	355

The computer runs were made on a Windows 10 64-bit system running on a Dell Precision T5610 workstation with Intel Xeon CPU E5-2637 and 64 GB RAM. The timings shown in Sections 4.1.1 and 4.1.2 are the average of 5 runs.

4.3.1 Verification and Validation Test Cases using Tsai-Wu Failure Criterion (TWFC)

Using the laboratory test results (Khaled et al., 2018), the TWFC was computed for various combinations of $\{\sigma_1, \sigma_2, \tau_{12}\}$ resulting in a discretized representation of the failure surface as shown in Figure 4.6. A total of 2527 points were generated, i.e., $n_{PC} = 2527$.

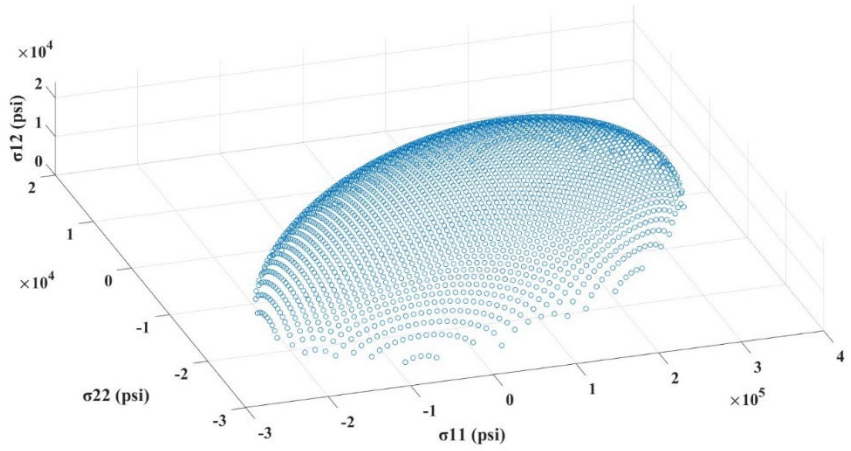

Figure 4.6: Point Cloud Data Generated Using the Tsai-Wu Failure Criterion.

Verification Tests: Twenty percent of the total number of point cloud data points were randomly selected to form the verification test pool, i.e., $n_t = 0.2 n_{PC} = 0.2(2527) = 505$. These data points were then used in the verification tests by varying $0.003 \le \beta \le 0.01$ for the ANN and SANN tests (AD and IDW), and by varying $0.01 \le \beta \le 0.07$ for NN tests. The results are not presented here, but as expected, the accuracy increases for all the methods as the reduction factor, β, increases.

Validation Tests: Fifty percent of the total number of point cloud data points were randomly selected to form the validation test pool while n_{PC} strength factor values were randomly

created between $SF^{lower} \le SF \le SF^{upper}$, i.e., $n_t = \left(0.5 n_{PC}\right)\left(n_{PC}\right) = 0.5(2527)^2 \approx 3{,}191{,}601$. The results for the three methods are shown in Table 4.3.

Table 4.3: Tsai-Wu Failure Data: Performance of the Three Methods ($0.5 \le s \le 1.1$ with $n_t = 3{,}191{,}601$).

Method	**Correct**	**False Positive**	**False Negative**	**Accuracy (%)**	**Wall Clock Time (s)**
ANN	3114988	75997	616	97.8	11
SANN (AD)	3142376	44952	4273	98.5	17
SANN (IDW)	3157176	34332	93	98.9	17
NN-S	3123347	65389	2865	98.1	1
NN-D	3137576	52803	1222	98.3	3

In order to better understand how the methods work when the test (query) points are close or far from the failure surface, the strength factors were divided into three bands: $0.5 \le SF \le 0.8$ such the test points would be placed well inside the failure surface, $0.8 \le SF \le 0.95$ such that the points moved closer to the failure surface but were still inside, and finally $0.95 \le SF \le 1.1$ with the test points close to being both inside and outside the failure surface. The results from these test cases are shown in Table 4.4 to Table 4.6.

Table 4.4: Tsai-Wu Failure Data: Performance of the Three Methods ($0.5 \le SF \le 0.8$ with $n_t = 3,191,601$).

Method	Correct	False Positive	False Negative	Accuracy (%)	Wall Clock Time (s)
ANN	3181387	10214	0	99.7	16
SANN (AD)	3191601	0	0	100	16
SANN (IDW)	3191601	0	0	100	16
NN-S	3191601	0	0	100	1
NN-D	3191601	0	0	100	3

Table 4.5: Tsai-Wu Failure Data: Performance of the Three Methods ($0.8 \le SF \le 0.95$ with $n_t = 3,191,601$).

Method	Correct	False Positive	False Negative	Accuracy (%)	Wall Clock Time (s)
ANN	3146518	45083	0	98.6	8
SANN (AD)	3191392	209	0	100.0	17
SANN (IDW)	3191583	18	0	100	16
NN-S	3191601	0	0	100	1
NN-D	3191601	0	0	100	3

Table 4.6: Tsai-Wu Failure Data: Performance of the Three Methods ($0.95 \le SF \le 1.1$ with $n_t = 3,191,601$).

Method	Correct	False Positive	False Negative	Accuracy (%)	Wall Clock Time (s)
ANN	2983593	205837	2171	93.5	5
SANN (AD)	3020395	157452	13754	94.6	17
SANN (IDW)	3080906	110310	385	96.5	18
NN-S	2927470	254799	9332	91.7	1
NN-D	2981350	206365	3886	93.4	3

Performance Analysis: Both SANN methods show the excellent predictive capabilities in all cases with SANN IDW being superior to SANN AD because IDW uses an inverse squared distance weighting which accounts for the spatial proximity of neighboring points,

while SANN (AD) treats all neighboring points equally leading to lower accuracy. The wall clock time is same for both SANN methods but higher than other methods as most of the wall clock time was used by SANN methods to find the nearest query point as it uses simple brute force method (Iwamura et al., 2013). The NN method exhibits predictive capabilities similar to those of SANN but operates faster. The shallow and deep neural networks model the failure surface as a decision surface that delineates the stress states that will induce failure from the stress states that do not. Hence, classification of a stress state in to one or the other category is easy when the stress state is away from the failure surface in the case of neural networks. On the other hand, ANN methods shows slightly less accurate results. This reduced accuracy stems from the ANN's sensitivity to data dimensionality and the relative position of the queried stress state in relation to nearby point cloud data points. Despite a $k = 3$ value works well in this study; it is not possible to eliminate the model's tendency to learn some noise as the prediction solely depends on the neighboring 3 data points. However, none of the methods predicted false negatives when the query points are well within the failure surface. This is as per the general expectation as the models are trained on the point cloud data that lies on the failure surface.

The accuracy of all three methods decreases and is nearly equal when the query points are close to the failure surface $\left(0.95 \leq SF \leq 1.1\right)$. The accuracy of the method when the stress states approach the failure surface depends on the propensity of the model to overfit the data particularly in this case as Tsai-Wu has a smooth failure surface. When implemented in lieu of a failure model, false negatives and false positives lead to bolder

and conservative designs, respectively. In an engineering standpoint, false negatives are more harmful when compared to false positives as the model does not capture fracture when the failure has already happened. The false negative to the false positive ratio ranged between 1-3.7% which is very low. The false negative rate decreased for the deep neural network as the simulated failure surface (decision surface) is much smoother when compared to its shallow counterpart (note the increase in the number of parameters, hidden layers and neurons in Table 4.1).

The NN-S method has the largest number of false negatives, followed by the SANN, NN-D, and ANN methods. Finally, as expected, the wall clock times for the NN methods appear to be nearly independent of the location of the query point. The ANN method takes considerably less time as the query points move closer to the failure surface whereas the SANN method's compute time is independent of the location of the query point.

4.3.2 Validation Using Virtual Testing Created Point Cloud Data

Using the virtual testing procedure discussed in Section 2, the point cloud data was computed for various combinations of $\{\sigma_1, \sigma_2, \tau_{12}\}$ as shown in Figure 3.18. A total of 415 points were generated, i.e., $n_{PC} = 415.$ Once again, fifty percent of the total number of point cloud data points were randomly selected to form the validation test pool while $1000 n_{PC}$ strength factor values were randomly created between $SF^{lower} \leq SF \leq SF^{upper}$, i.e.,

$n_t = \left(0.5n_{PC}\right)\left(1000n_{PC}\right) = 0.5(415)(415000) \approx 85,905,000$. The results for the three methods are shown in Table 4.7 to Table 4.10.

Table 4.7: Point Cloud Failure Data: Performance of the Three Methods ($0.5 \le SF \le 1.1$ with $n_t = 85,905,000$).

Method	Correct	False Positive	False Negative	Accuracy (%)	Wall Clock Time (s)
ANN	77563383	7243941	1097676	90.29	105
SANN (AD)	81901979	2879914	1123107	95.34	88
SANN (IDW)	83729175	2024657	151168	97.47	91
NN-S	83417499	1862552	624949	97.10	69
NN-D	83588529	1066046	1250425	97.30	213
NN-DP	83588529	1066046	1250425	97.30	42

Table 4.8: Point Cloud Failure Data: Performance of the Three Methods ($0.5 \le SF \le 0.8$ with $n_t = 85,905,000$).

Method	Correct	False Positive	False Negative	Accuracy (%)	Wall Clock Time (s)
ANN	83098571	2806429	0	96.70	132
SANN (AD)	85637158	267842	0	99.68	89
SANN (IDW)	85668305	236695	0	99.72	89
NN-S	85905000	0	0	100.0	70
NN-D	85877917	27083	0	99.97	207
NN-DP	85877917	27083	0	99.97	41

Table 4.9: Point Cloud Failure Data: Performance of the Three Methods ($0.8 \le SF \le 0.95$ with $n_t = 85,905,000$).

Method	Correct	False Positive	False Negative	Accuracy (%)	Wall Clock Time (s)
ANN	74160828	11744172	0	86.30	84
SANN (AD)	83622364	2282636	0	97.34	87
SANN (IDW)	83119449	2785551	0	96.75	89
NN-S	84834372	1070628	0	98.80	71
NN-D	84740306	1164694	0	98.60	218
NN-DP	84740306	1164694	0	98.60	45

Table 4.10: Point Cloud Failure Data: Performance of the Three Methods ($0.95 \le SF \le 1.1$ with $n_t = 85,905,000$).

Method	Correct	False Positive	False Negative	Accuracy (%)	Wall Clock Time (s)
ANN	69840395	11657907	4406698	81.30	63
SANN (AD)	72759051	8637896	4508053	84.70	88
SANN (IDW)	80348759	4948529	607712	93.53	88
NN-S	76382372	6912139	2610489	88.9	71
NN-D	77832405	3051528	5021067	90.60	212
NN-DP	77832405	3051528	5021067	90.60	43

Performance Analysis: Like the earlier example, the NN methods and SANN (IDW) show excellent predictive capabilities when the query points are well inside the failure surface, $\left(0.5 \le SF \le 0.8\right)$ while the ANN and SANN (AD) methods show less accurate results without any false negative predictions for the same reasons previously discussed. The SANN (IDW) method improves the predictive capability compared to SANN (AD) because IDW uses an inverse squared distance weighting which accounts for the spatial proximity of neighboring points, while SANN (AD) treats all neighboring points equally leading to lower accuracy.

When the query points are close to the failure surface $\left(0.95 \le SF \le 1.1\right)$, the accuracy of all three methods decreases. However, the SANN (IDW) method remains the most accurate, while the NN methods minimize false positive predictions. Among the methods, SANN (AD) has the highest number of false negatives, followed by NN-D, NN-DP, ANN, NN-S, and SANN (IDW). The ratio of false negatives to false positives is significantly higher in this case because the point cloud data extracted from the RVE analysis lacks the smoothness of the Tsai-Wu failure surface. The superior performance of the pruned deep neural network can be attributed to the removal of data transformations within the neural network that do not adversely affect the prediction accuracy. This reduces the number of tunable parameters in the training phases and lowers the number of operations during implementation without sacrificing accuracy. For this reason, the NN-DP method shows the best accuracy and computational effort amongst all the methods.

Figure 4.7 shows the error map of three methods- SANN (AD), SANN (IDW) and SANN (NN) for the query point with strength factor $0.5 \le SF \le 1.1$. To plot error map, the σ_1 and σ_2 plane $\left(\sigma'_1 \& \sigma'_2 \text{ translated plane}\right)$ are divided into 30×15 stress buckets. For each bucket, the number of correct predictions and false predictions is determined, and the percentage of false predictions in each stress bucket is plotted as the error. The overall error percentages for the methods are as follows: SANN (AD): 4.66%, SANN (IDW): 2.53%, and SANN (NN): 2.70%. The corresponding accuracy values, calculated as 100−error, match those presented in Table 4.7. Notably, the stress buckets exhibiting higher error rates are predominantly located in the $+\sigma'_1$ direction, particularly in the $+\sigma'_1 \ \& \ -\sigma'_2$ quadrant.

This occurs because the number of failure points (52) in this region is smaller compared to other quadrants $(114, 144 \& 105)$, contributing to increased prediction errors. To improve this, a uniform distribution of failure points in the $\sigma_1 \& \sigma_2$ directions should be achieved. The current approach generates point cloud data through quadrant-wise $n \times n$ discretization in the $\sigma_1 \& \sigma_2$ planes. This method leads to a non-uniform distribution of failure points due to asymmetry in material strength along these directions.

To ensure a uniform distribution of failure points, data generation should use a stress increment-based discretization of the $\sigma_1 \& \sigma_2$ planes. Additionally, refining the stress increments will increase the density of failure points, enhancing the resolution and improving prediction accuracy.

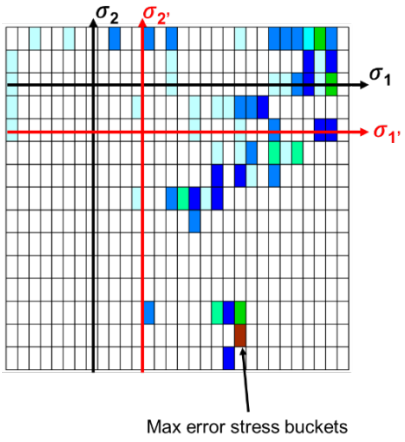

(a)

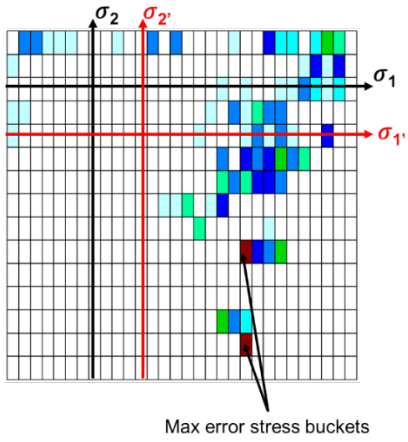

(b)

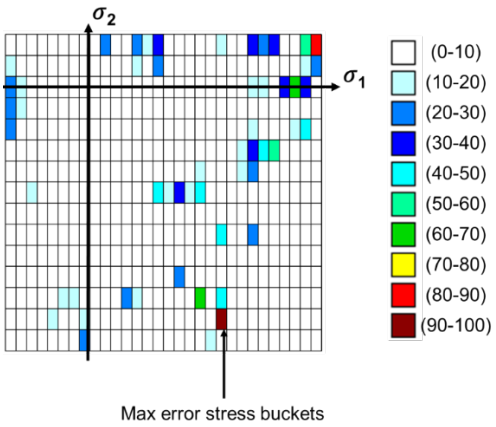

(c)

Figure 4.7: Error map for $0.5 \leq SF \leq 1.1$ – (a) SANN (AD), (b) SANN (IDW), and (c) NN.

CHAPTER 5

VERIFICATION AND VALIDATION OF FAILURE MODEL

Verification and validation (V&V) are critical components in the development of any material model. Verification ensures that the implementation of the model has been performed correctly and adheres to its theoretical foundations. This step often begins with straightforward tests, such as single-element simulations, to identify and address any potential issues in the implementation. On the other hand, validation evaluates the accuracy, fidelity, and reliability of the developed material model by comparing its predictions against experimental data or well-established benchmarks. Together, these processes provide confidence in the robustness and applicability of the material model.

The V&V processes discussed in this section focus on a specific carbon/epoxy unidirectional composite material, T800/F3900, manufactured by Toray Carbon Fibers America (Toray, 2020). While extensive details about the verification and validation of existing deformation, damage, and failure models can be found in previous works (Hoffarth, 2016; Hoffarth et al., 2017; Khaled et al., 2019a, 2018; Shyamsunder et al., 2021, 2020a), this chapter highlights a subset of test cases to demonstrate the application of the V&V framework. These selected examples serve to illustrate the process in detail and discuss the results achieved with the Point Cloud Failure Criterion (PCFC) and Simplified Material Model (SMM). Only simplified ANN (SANN) and Neural Network (NN) methods are currently available within the MAT_213 framework.

5.1 Verification Tests

Verification tests are conducted using the T800S/F3900 composite material to evaluate the implementation of the Point Cloud Failure Criterion (PCFC). Verification was carried out using both SANN (AD and IDW) and NN techniques. The material properties of the T800S/F3900 composite used in the verification process were derived from coupon-level experimental testing. These properties, essential for setting up the verification tests, are summarized in Table 5.1.

Initial verification tests used single-element finite element (FE) models. These models consisted of a single quadrilateral element with dimensions of 1 inch by 1 inch. This approach allows for a controlled environment to identify and resolve potential discrepancies between theoretical predictions and numerical implementation. Subsequently, multi-element verification tests were conducted to simulate more complex scenarios. In these cases, the FE models were developed using the same geometry as those used in experimental setups (Khaled et al., 2018).

Table 5.1: Material Properties.

Property	Value (Tensile)	Value (Compressive)
1-direction modulus (E_{11}, psi)	23.5 x10^6	18.7 x 10^6
2-direction modulus (E_{22}, psi)	1.07 x10^6	1.12 x10^6
3-direction modulus (E_{33}, psi)	9.66 x10^5 (6.6 GPa)	1.04 x10^6
1-2 plane shear modulus (G_{12}, psi)	5.80 x10^5	
2-3 plane shear modulus (G_{23}, psi)	3.26 x10^5	
1-3 plane shear modulus (G_{13}, psi)	3.48 x10^5	
Poisson's ratio (ν_{12})	0.317	0.342
Poisson's ratio (ν_{23})	0.484	0.728
Poisson's ratio (ν_{13})	0.655	0.578
Poisson's ratio (ν_{21})	0.0168	0.0207
Poisson's ratio (ν_{32})	0.439	0.676
Poisson's ratio (ν_{31})	0.027	0.032
Density (ρ, slugs/in^3)	1.457 x 10^{-4}	

5.1.1 Single Element Verification

Five single-element verification tests were conducted using thin shell elements (ELFORM 16) in LS-DYNA, with two integration points (NIP) through the thickness. The schematic of the single-element model is illustrated in Figure 5.1. Red arrows indicate the translational displacements that are restrained. Black arrows represent the velocity applied to a specific node in the designated direction, simulating the loading conditions. Additionally, the principal material directions, labeled as 1, 2, and 3, are cmarked in the schematic diagrams to illustrate the orientation of the composite material in the simulation.

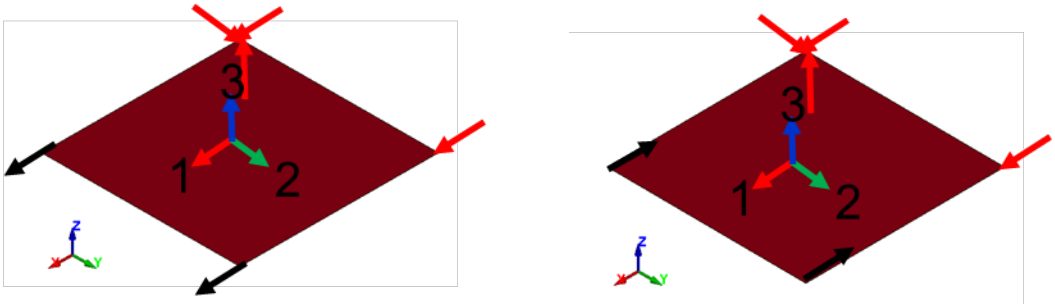

(a) (b)

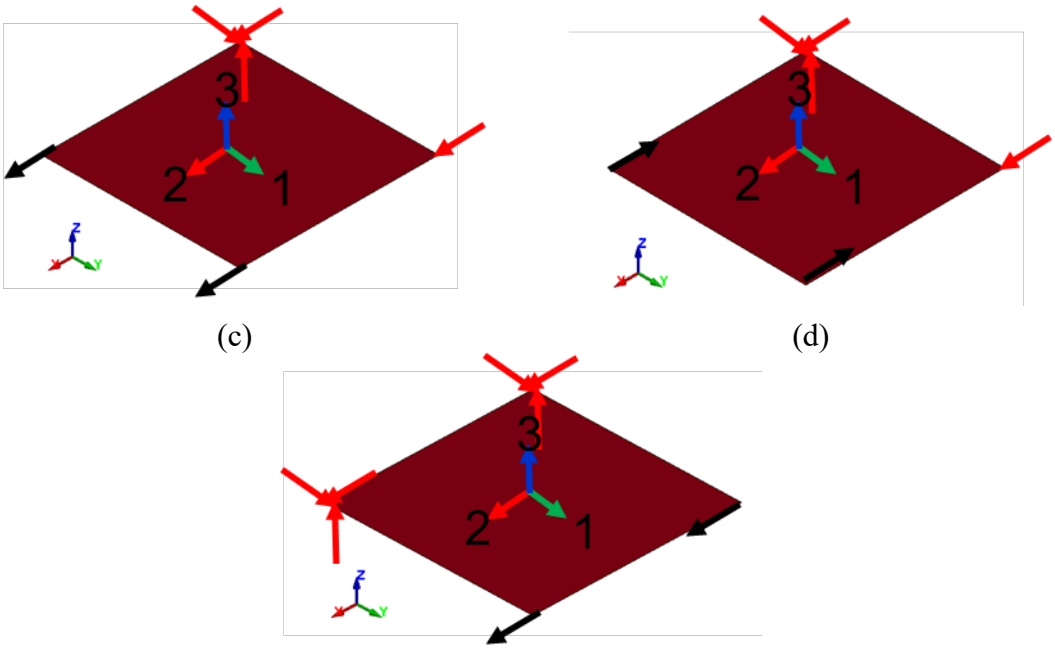

(c) (d)

(e)

Figure 5.1: Schematic Diagram of Single Element Verification Tests - (a) 1-Direction Tension, (b) 1-Direction Compression, (c) 2-Direction Tension, (d) 2-Direction Compression, and (e) 2-1 Plane Shear.

A velocity of 1.0 in/s is applied to the nodes in the single-element verification tests. This value is significantly higher than the displacement rate of 10^{-4} in/s used in the corresponding experiments (Khaled et al., 2018). The higher displacement rate in the simulation is chosen to expedite the computational process while ensuring that the results remain unaffected by the increased loading rate.

The results from the single-element verification tests are summarized in Table 5.2. The predicted strength values from these tests closely match those obtained in PCFC uniaxial tests, demonstrating the consistency and reliability of the implemented material model in reproducing expected behaviors.

Table 5.2: Single Element Verification Results (Values in psi).

Test	Single element verification results			PCFC uniaxial tests
	SANN (AD)	SANN (IDW)	NN	
T1	369871	373974	366656	373954
T2	6492	6307	6258	6307
C1	-145587	-124997	-124717	-125110
C2	-26549	-25694	-26112	-25617
S21	6517	6178	6367	6515

5.1.2 Multi-Element Verification

Multi-element verification tests were conducted to replicate the uniaxial stress conditions induced in composite specimens during QS-RT experiments. A total of five tests were performed. For each simulation, only the gage section of the experimental geometry was modeled to focus on the critical region of interest.

Figure 5.2 shows the schematic of the multi-element models. All simulations utilized 4-noded thin shell elements to represent the composite material. Translational displacements were restrained using either pin or roller supports. Black arrows indicate the applied velocity at specific nodes representing the loading conditions. The principal material directions are labeled as 1 and 2.

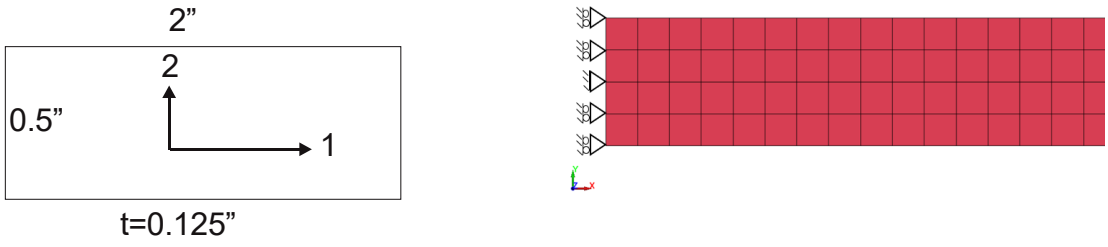

(a)

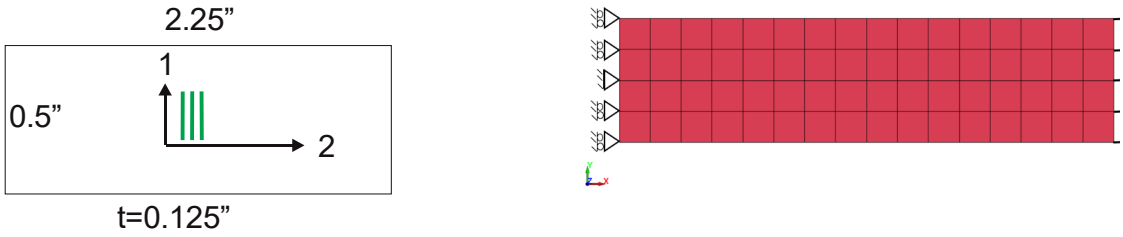

(b)

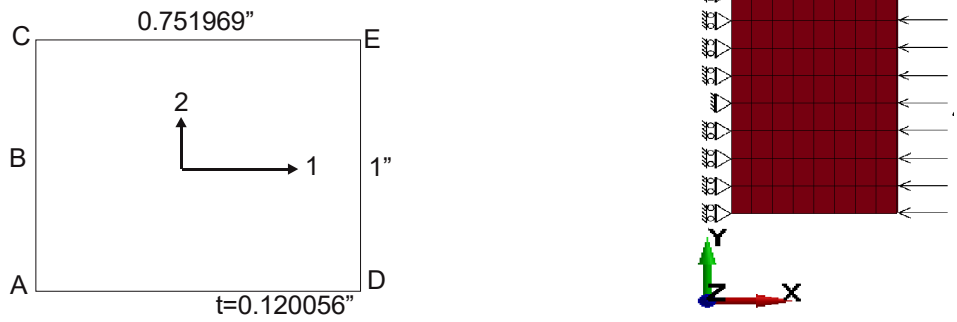

(c)

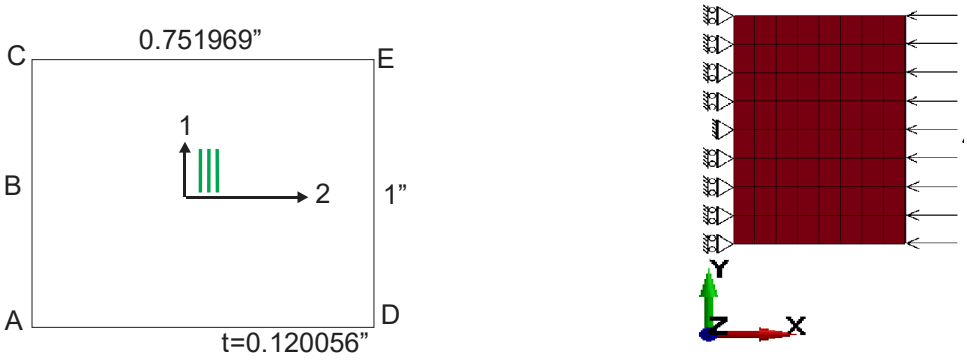

(d)

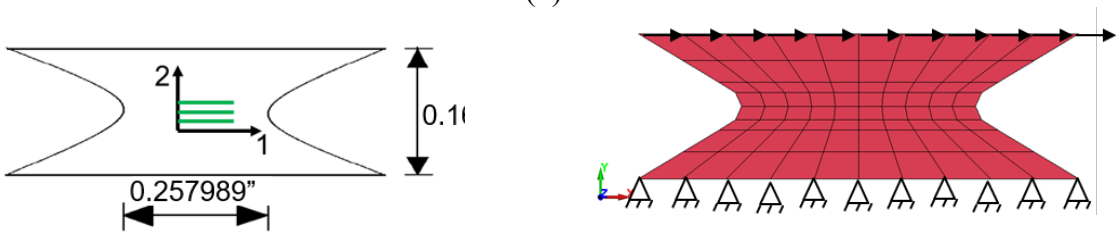

(e)

Figure 5.2: Schematic Diagram of Multi-Element Verification Tests - (a) 1-Direction Tension, (b) 2-Direction Tension, (c) 1-Direction Compression, (d) 2-Direction Compression, and (e) 2-1 Plane Shear.

The results of the multi-element verification tests are presented in Table 5.3. The predicted strength values from these simulations show excellent agreement with those obtained in PCFC uniaxial tests.

Table 5.3: Multi-element Verification Test Results (Values in psi).

Test	**Multi-element verification results**			**PCFC uniaxial tests**
	SANN (AD)	**SANN (IDW)**	**NN**	
T1	369444	373974	366656	373954
T2	6495	6305	6251	6307
C1	-144822	-124980	-124650	-125110
C2	-26541	-25690	-26110	-25617
S21	6507	6150	6340	6515

5.2 Validation Tests

Five validation tests are discussed in this section with each test designed to assess the accuracy and applicability of the material models across a range of loading, material, and FE modeling scenarios. The validation tests include:

1. Stacked-ply validation tests.
2. Impact tests.
3. 3D-printed Aluminum Alloys.
4. A Framework for Soft Body Armor Design.
5. Modeling of mechanical behavior of 3D-printed concrete.

The first two validation tests focus on comparing the predictive capabilities of different failure criteria within MAT_213. The subsequent three tests highlight the versatility of the material model, showcasing their application across diverse material systems beyond traditional aerospace structural composites.

The first three tests use MAT_213 with plasticity-based deformation and damage calculations. In contrast, the last two tests use SMM, a simplified version of MAT_213 that excludes plasticity for deformation and damage calculations and instead use elastic predictors.

Each validation test is discussed in detail focusing on the modeling methodology, key findings, and correlation between simulation and experimental results. Collectively, these tests are designed to validate the versatility and reliability of the material models across a diverse range of applications.

Three validity checks are conducted to ensure the accuracy and reliability of the finite element modeling:

- *Convergence Analysis:* This check verifies that the simulation results stabilize as the mesh is refined. By progressively reducing the element size, convergence analysis ensures that the solution approaches a consistent value, minimizing numerical errors.
- *Energy Checks:* To verify the consistency and physical realism of the results, energy checks are conducted during post-processing. This involves ensuring that the total energy balance (including internal, kinetic, and external energies) remains stable and follows expected trends (Table 5.4) throughout the analysis. Energy inconsistencies may indicate issues such as numerical instability, poor element quality, or improper boundary conditions.

Table 5.4: Energy Checks (AWG_LS-DYNA, 2013).

Description	Acceptable Limit
Max. Internal Energy Ratio (internal energy/ total energy)	< 1.0
Max. Kinetic Energy Ratio (kinetic energy/ total energy)	< 0.05
Max. Hourglass Energy Ratio (hourglass energy/ total energy)	< 0.05
Max. Sliding Energy Ratio (sliding energy/ total energy)	< 0.10

- *Comparison with Experimental Data:* The numerical results are compared with experimental observations to validate the model's accuracy in predicting real-world behavior. This step is crucial for assessing the model's ability to capture key response characteristics such as stress distribution, deformation patterns, and failure modes.

All simulations mentioned in the validation test section were performed on two computing platforms as follows:

- *Platform 1 (FAA Cluster):* Each compute node has Dell R630 system with Intel E5-2690 V4@2.6 GHz, 2 × 14 cores and 256 GB RAM.
- *Platform 2 (Sol Cluster):* Every compute node has 2x64 cores AMD EPYC 7713 @ 2.0 GHz, 1024 GB RAM per node.

5.2.1 Evaluating Failure Criteria in MAT_213

Two different validation tests are used. The first test is a quasi-static loading test while the second test is an impact test. In modeling both the tests, MAT_213 was used for the composite panel and cohesive zone elements were modeled with MAT_138. The five input curves shown in Figure 3.17(a)-(e) are used as MAT_213 stress-strain input. Data from DCB and ENF tests were used for the CZE elements (Khaled et al., 2019b).

To compare different failure criteria available in MAT_213, the validation tests were performed using thin shell elements with (a) Generalized Tabulated Failure Criterion (GTFC), Tsai-Wu Failure Criterion (TWFC), and Point Cloud Failure Criterion (PCFC). For all three failure models, the input stress-strain curves are identical in the pre-peak region. The post-peak input curves are different as the inputs required in this region are failure model dependent. GTFC uses a strain-based failure onset criterion and uses damage curves in the post-peak region (Figure 4.3(b)). In contrast, TWFC and PCFC use stress-based failure onset criteria with a linear stress degradation model that is activated using residual strength $\left(1-c_i^d\right)$ and ε_f as input as shown in Figure 4.3. All three failure criteria use element strain as the element erosion criterion.

While most of the input data for MAT_213 are obtained from experiments (six distinct in-plane stress-strain curves: tension and compression in the 1 and 2 directions, shear, and off-axis curves in the 1-2 plane), the post-peak data need to be estimated. These parameters are associated with post-peak damage and erosion behavior. In general, there are six calibration parameters: $\left(c_1^d, c_2^d, c_4^d, c_5^d, c_7^d, \varepsilon_{IP}^f\right)$. However, the following assumptions are used to reduce the number of tunable parameters to two.

1. The in-plane damage values corresponding to residual strengths for tension $\left(c_1^d \,\&\, c_2^d\right)$ and shear $\left(c_7^d\right)$ were assumed to be equal, i.e., $\left(c_1^d = c_2^d = c_7^d\right)$. All the compression residual strength values were set equal to their respective peak valuess in the stress-strain input curves $\left(c_4^d = c_5^d = 0.0\right)$. In compression, failure is typically governed by fiber microbuckling, kinking, or matrix shear failure, rather than

catastrophic fiber breakage as seen in tension. Since the fibers are assumed to remain largely intact after localized buckling or kinking, the material is considered to retain significant load-carrying capacity. Consequently, it is assumed that the compressive post-peak behavior is unaffected by damage.

2. The in-plane erosion strain, ε_{IP}^{f} is a user input rather than a value derived from experiments.

5.2.1.1 Stacked-ply Validation test (Maurya and Rajan, 2024)

The developed failure criterion is validated using stacked-ply tests involving 8-ply panel of T800/F3900 specimens with a $[0/90/+45/-45]_S$ layup. Details of the specimens are shown in Figure 5.3. The grey regions show where fiberglass tabs were glued to the specimen. The tabs prevent the specimens from crushing when the specimens are inserted and held in the fixtures. The white center region is the gage section that was speckled for gathering Digital Image Correlation (DIC) data. More details are available in an earlier publication (Shyamsunder et al., 2021).

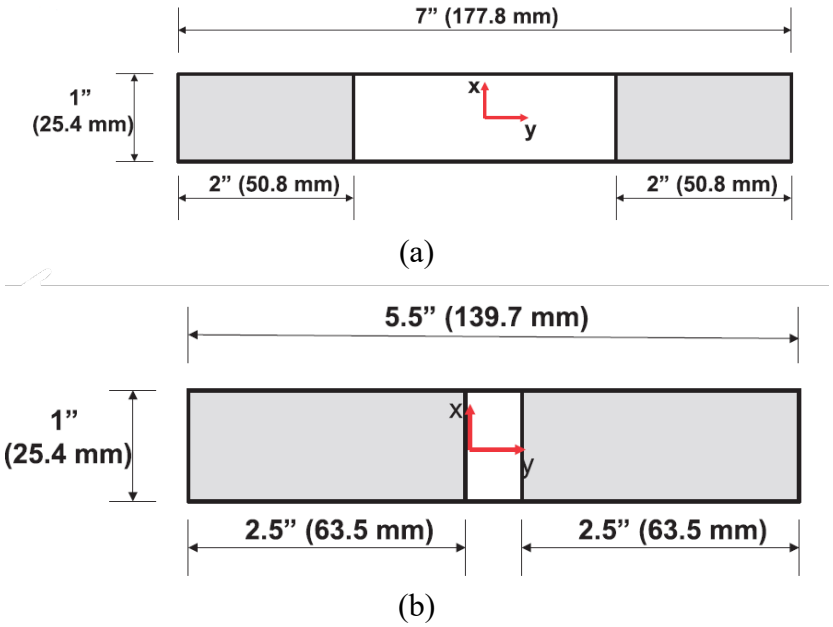

Figure 5.3: Schematic Diagrams for Stack Ply Validation Test - (a) Tension (SPVTT), and (b) Compression (SPVCT).

FE Model: Only the gage section was modeled using 4-noded thin shell elements with ELFORM=16. There are eight elements through thickness corresponding to the eight plies in the experimental specimen. Cohesive zone elements (CZE) were used between two layers of composites with 8 node hexahedral solid elements (ELFORM=20).

Material Data: The composite panels were modeled using MAT_213, with three failure criteria activated: the Generalized Tabulated Failure Criterion (GTFC), the Tsai-Wu Failure Criterion (TWFC), and the Point Cloud Failure Criterion (PCFC). For the PCFC approach only SANN was used for both tests. Only quasi-static and room temperature (QS-RT) curves are used as input. The post peak curve is obtained by calibration to match simulation results with the experimental results. Cohesive zone elements were modeled with MAT_138. Table 5.5 shows the input parameters for MAT_213.

Table 5.5: MAT_213 Input Parameters.

Failure Model	Residual Strength	Erosion strain
GTFC	10% with damage (except no damage in compression curves)	SPVCT: 0.0085 SPVTT: 0.05
TWFC	10% (except no damage in compression curves)	SPVCT: 0.02 SPVTT: 0.04
PCFC (SANN-AD)		

Results and Discussions: The load versus time graph is used to compare FE and experimental results for both models – SPVCT (Figure 5.4) and SPVTT (Figure 5.6). Nodal reactions at the support face along the loading direction were added to obtain the load value. Figure 5.5 and Figure 5.7 show the eroded elements in different colors for each layer.

SPVCT Results: The load-displacement response from the FE model closely matches the experiment result. With all three failure criteria, the peak load is approximately 8% less than the experimental value. After 150 seconds, the force value is constant for the TWFC and PCFC models while the GTFC model shows oscillating behavior due to the initiation of 2-direction damage in the 0-degree ply at $t = 150\,\text{sec}$. Notably, 2-direction damage in the 0-degree ply was observed with PCFC before the loss of load capacity. In the experiment, the damage initiation starts at the center of the 0-degree plies and progresses to one end of the 90 degree and +/- 45-degree plies as the load increases. The PCFC failure prediction is the closest to the failure pattern seen in the experiment (Figure 5.5(a)). The elements in the 0-degree ply erode at the center, followed by other layers eroding at one end of the model (Figure 5.5(b)). Most of the elements in TWFC model erode at one end of the model (Figure 5.5(c)). In the GTFC model (Figure 5.5(d)), elements in the 90- and +45-degree layers were eroded at the center and most of the elements at one end eroded from all the layers.

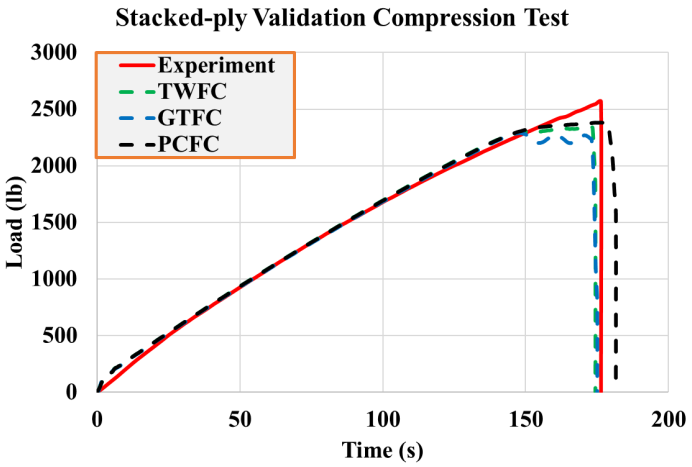

Figure 5.4: SPVCT Load vs Time Plot.

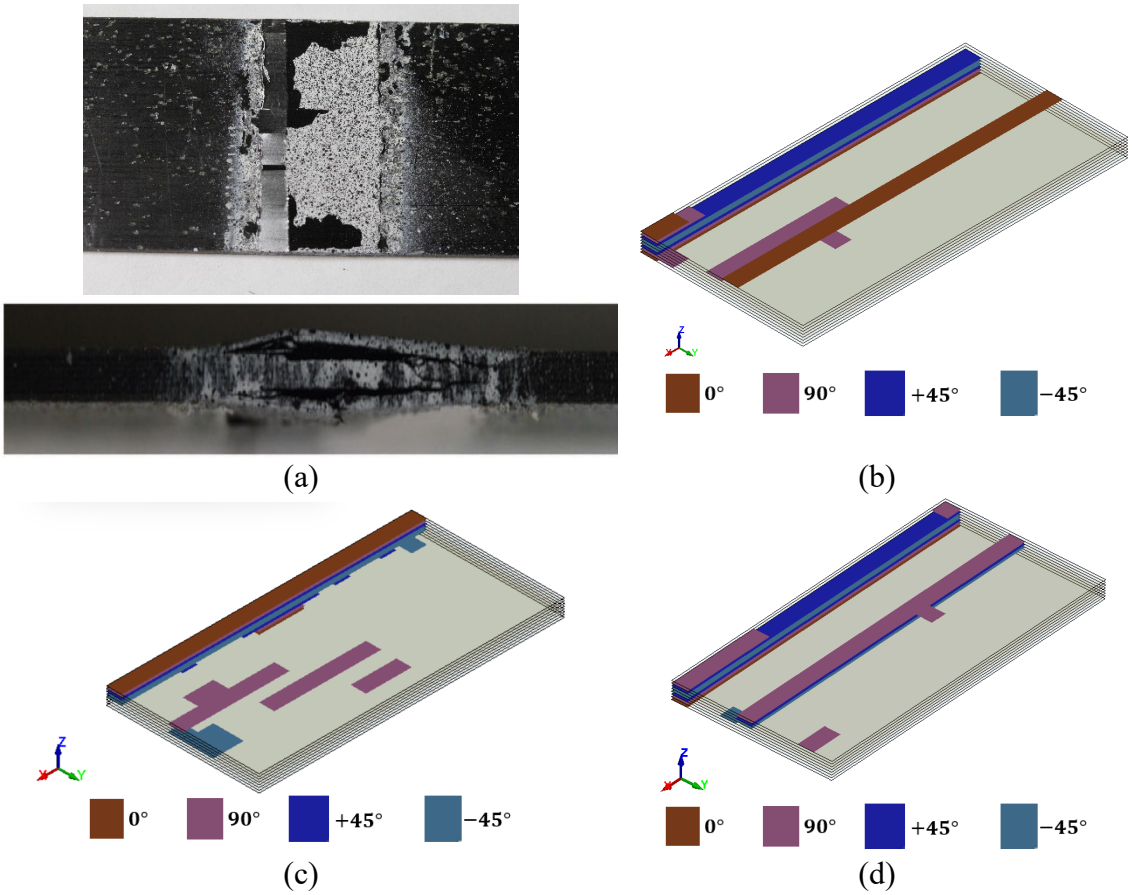

Figure 5.5: Failure Pattern for SPVCT - (a) Experiment, (b) PCFC (SANN-AD), (c) TWFC, and (d) GTFC.

SPVTT Results: The FE response shows slightly stiffer behavior compared to the experimental result. The peak load predicted by TWFC, GTFC and PCFC are all very close to experimental results. In the experiment, the specimen failed at the center. The best model is the PCFC model (Figure 5.7(b)) where most of the eroded elements are at the center of the model. Both the TWFC and GTFC models comparatively smaller number of eroded elements with; element erosion in the TWFC model occurs at one end (Figure 5.7(c)), and in the GTFC model, element erosion occurs at the two ends of the specimen (Figure 5.7(d)). While all the three models predict the peak load within ±10% of the experimental value, the PCFC model predicts a failure pattern that is comparatively closer to the tested specimen.

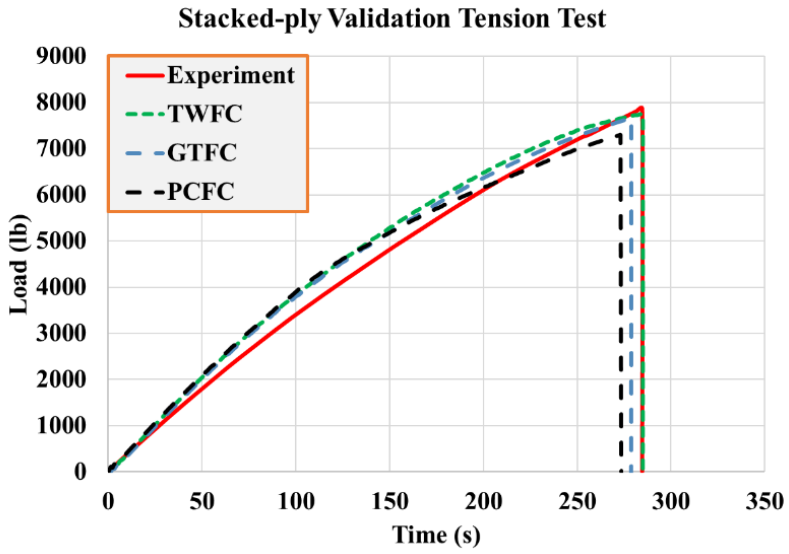

Figure 5.6: SPVTT Load vs Time Plot.

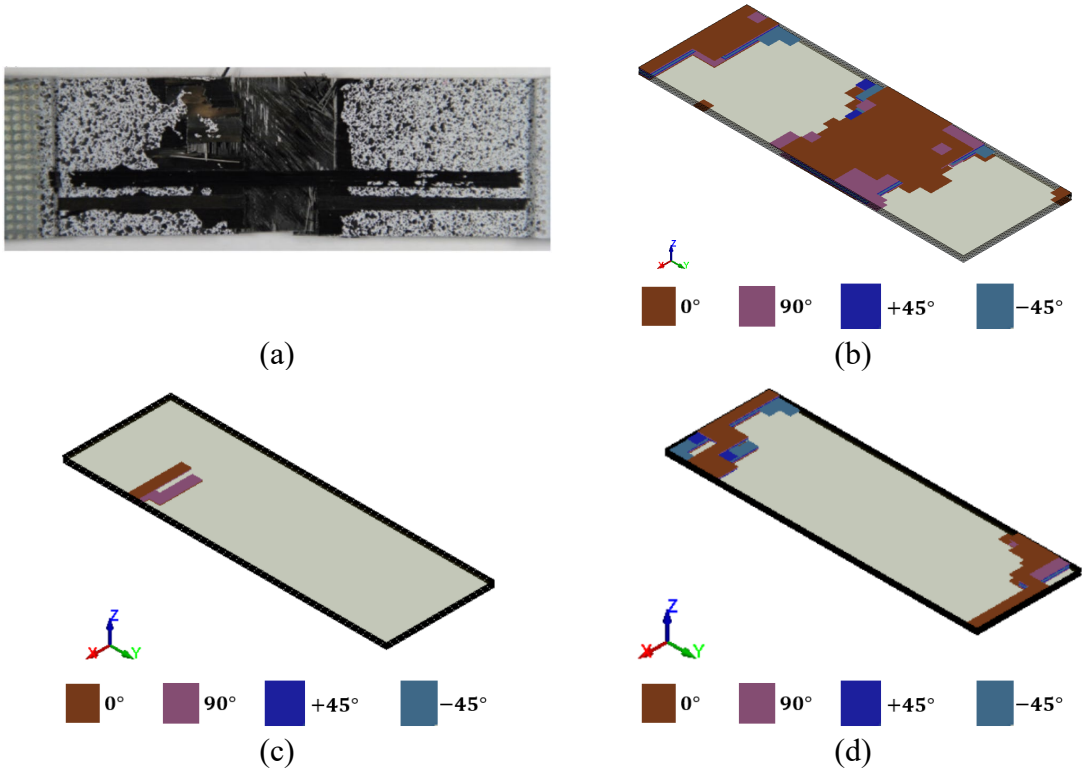

Figure 5.7: Failure Pattern for SPVTT - (a) Experiment, (b) PCFC, (c) TWFC, and (d) GTFC.

Table 5.6 presents a summary of the runtime comparison for all stacked-ply tests.

Table 5.6: Run Time Comparison for Stacked-ply Tests.

Model	**FTYPE**	**# of Elements**	**Computing Platform (# Nodes)**	**Wall-Clock Time Min:Sec**
Compression	GTFC	1600 Shell + 1400 CZE	Platform 1 (4)	1:17
	TWFC			1:30
	PCFC (SANN-AD)			1:36
Tension	GTFC	2400 Shell + 2100 CZE		13:41
	TWFC			8:14
	PCFC (SANN-AD)			8:42

5.2.1.2 Impact Tests (Maurya et al., 2024a; Maurya and Rajan, 2024)

A series of impact tests were conducted at the NASA Glenn Research Center Impact Dynamics Laboratory using a single stage gas gun shown in Figure 5.8. The test utilizes a cup-shaped aluminum 2024 projectile with a complex radiused nose and a mass of 1.77 oz (50 g) as per ASTM D8101. A cross-section of the projectile is shown in Figure 5.9. The specimen (12 in x 12 in flat panel, 16-ply [(0/90/45/-45)2]s layup) is clamped with 28 bolts between two thick metal plates with a 10-inch (25.4 cm) diameter circular aperture, as shown in Figure 5.10. The ASTM standard is designed for measuring the response of composite materials under free-flight impact conditions when impacted in a normal direction. Two pairs of high-speed cameras were used to capture digital image correlation (DIC) images from the speckled composite panel both on the impacted side and backside of the panel. The DIC data was analyzed to obtain full-field displacements and surface strains.

Figure 5.8: Single Stage Gas Gun Set-Up at NASA-Glenn Research Center.

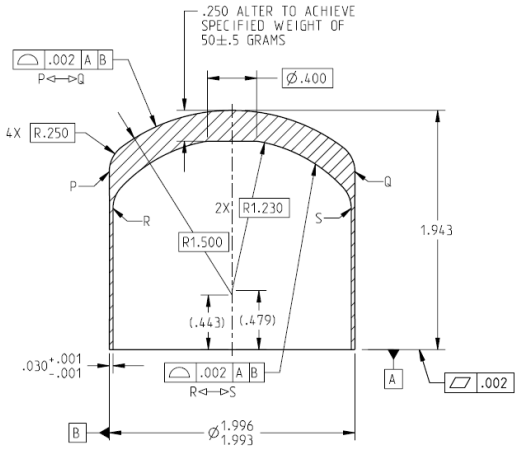

Figure 5.9: Cross Section of Standard Projectile ASTM D8101 (Dimensions in inches).

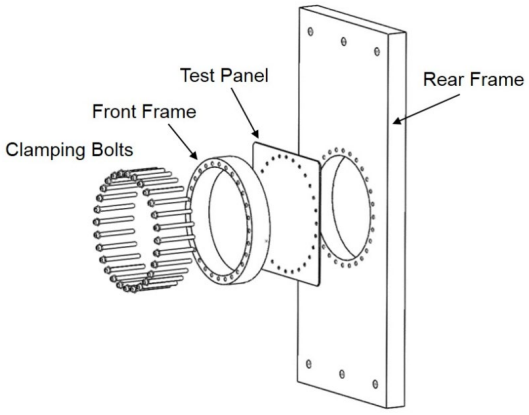

Figure 5.10: Schematic of Fixturing for Test Method ASTM D8101.

In addition, two pairs of cameras were placed in front of and behind the panel to measure the projectile velocity and orientation before and after impact using photogrammetry software. Further details can be found in an earlier publications (Shyamsunder et al., 2022b, 2022a). Three of those impact tests were selected as validation tests covering a wide range of impact velocities – from low velocity (LVG906) to much higher velocities (LVG1074 and LVG1075) that straddle the ballistic limit. Table 5.7 summarizes the test data. A negative final velocity implies that the projectile rebounded and did not penetrate the panel.

Table 5.7: Impact Test Details.

Test	**Lay-up Details**	**Projectile**		**Projectile**
		Impact Velocity, ft/s (m/s)	**Final Recorded Velocity, ft/s (m/s)**	
LVG906	Unidirectional	27.4 (8.35)	-18.1 (5.52)	Contained
LVG1075	$\left[\left(0/90/45/-45\right)_2\right]_S$	385.0 (117.3)	-46.4 (14.1)	Contained
LVG1074	$\left[\left(0/90/45/-45\right)_2\right]_S$	417.0 (127.1)	25.4 (7.74)	Uncontained

FE Model: The structural model consists only of the composite panel and the projectile. Figure 5.11 shows details of the 16 layers in the panel, the 28 bolt holes, and the projectile. A matching layer of cohesive zone elements (CZE) are placed between two plies. 185,536 4-noded fully integrated thin shell elements (ELFORM=16) are used to model the composite panel, 173,940 8-noded hexahedral solid elements (ELFORM=20) form the CZE elements while there are 17,040 solid elements in the projectile. To replicate the test setup, the nodes on the circumference of the bolt holes were restrained in-plane, while the nodes at location of the bolt hole clamps at the top and bottom layers were restrained in the out-of-plane direction. During the LVG906 impact test, the bullet's point of impact was 0.7 inches (1.8 cm) below the center of the panel, while the point-of-impact of the projectile is precisely at the center for LVG1075 and LVG1074 impact tests.

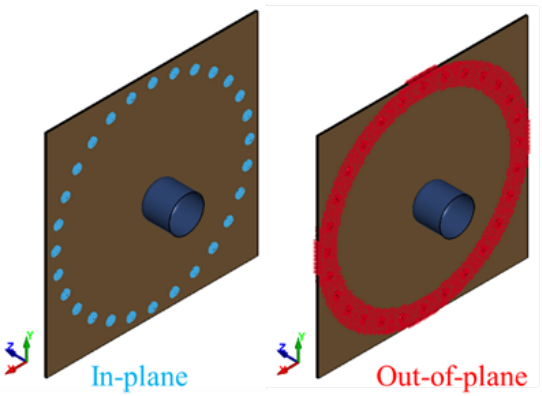

(a)

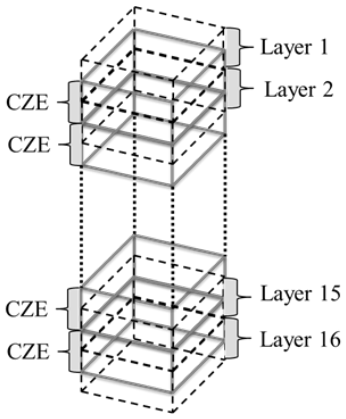

(b)

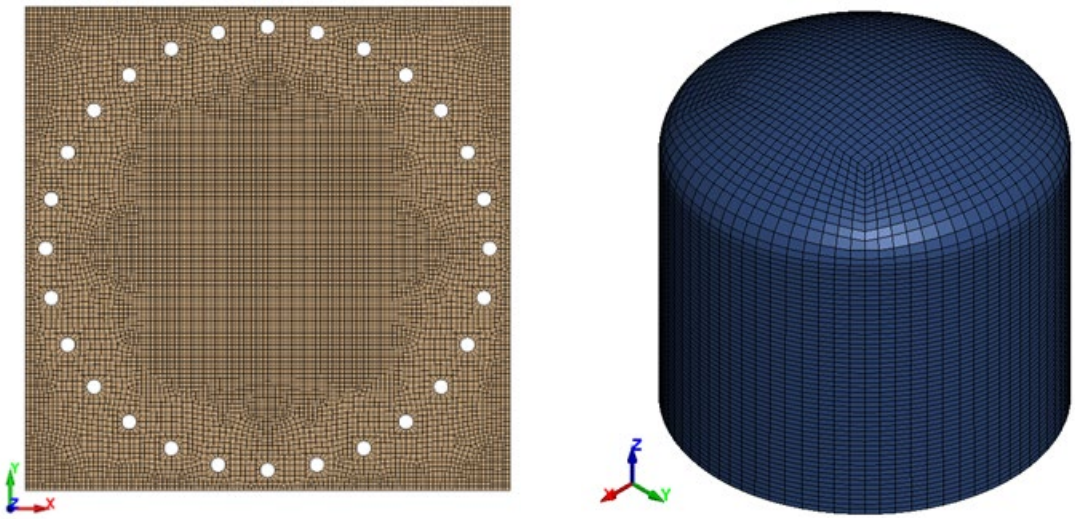

(c) (d)

Figure 5.11: FE Model Details - (a) Panel, Projectile, and In-Plane and Out-Of-Plane Fixity Conditions, (b) Close-Up of Typical Inter-Ply Regions Showing CZE Elements (Layer 1 is the Strike Face), Mesh Layout in (c) the Panel (12033 Nodes And 11596 Shell Elements with a Thickness of 0.007625" Per Layer), and (d) The Projectile (22566 Nodes and 17040 Solid Elements).

Material Data: The composite panels were modeled using MAT_213, with three failure criteria activated: the Generalized Tabulated Failure Criterion (GTFC), the Tsai-Wu Failure Criterion (TWFC), and the Point Cloud Failure Criterion (PCFC). For the PCFC approach, the Neural Network (NN) method was used exclusively for the LVG1074 impact test, while the Simplified ANN (SANN) method was used for all three LVG tests. The projectile is modeled using MAT_024 incorporating strain-rate dependent elastoplastic behavior with the data obtained from publicly available data (Nicholas, 1980). Table 5.8 shows the input parameters for MAT_213 that control post-peak behavior.

Table 5.8: MAT_213 Input Parameters.

Failure Model	Residual strength	Erosion strain
GTFC	6.5% (T1, T2, S12) 100% (C1, C2)	$\varepsilon_{IP}^{f} = 0.8$
PCFC (SANN - AD & NN (only with LVG1074))	6.5% (T1, T2, S12) 100% (C1, C2)	$\varepsilon_{IP}^{f} = 0.65$
PCFC (SANN - IDW (only with LVG1074)	7.05% (T1, T2, S12) 100% (C1, C2)	$\varepsilon_{IP}^{f} = 0.65$
TWFC	10% (T1, T2, S12) 100% (C1, C2)	$\varepsilon_{IP}^{f} = 0.09$

Results and Discussions: The validation test was completed by simulating the models – LVG906, LVG1074 and LVG1075 with material data shown in Table 5.8.

LVG906: The results of this low-velocity impact model are presented in Figure 5.12. The GTFC and PCFC models over predict the peak displacement value at center while displacement predictions of TWFC model at the center are close to the experimental values with a small phase discrepancy. The edge displacement predictions agree with the experimental values from 0 to 0.75 ms. The GTFC and PCFC models predict the final rebound velocity closer to the experiment, while the TWFC model overestimates the final rebound velocity.

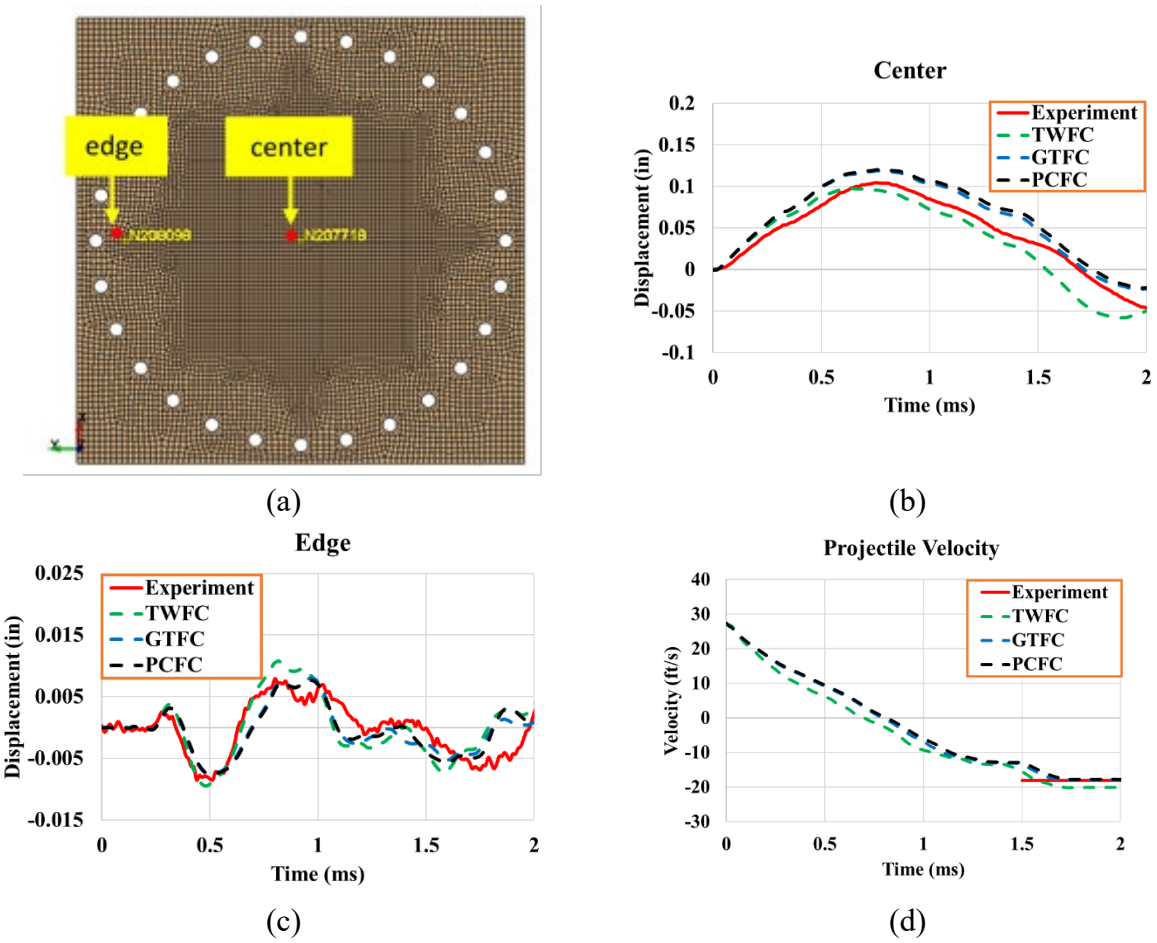

Figure 5.12: LVG906 Results - (a) Points on the Panel Backside Where Out-of-Plane Displacements Were Monitored, (b) Out-of-Plane Displacements at Center, (c) Out-of-Plane Displacements at Edge, and (d) Projectile Velocity.

LVG1075: This is a contained test where the projectile velocity is slightly below threshold penetration velocity. The results are shown in Figure 5.13. The first positive peak at Point 2 is very well captured by the GTFC model while it is under predicted by the TWFC model and over-predicted by the PCFC model. The GTFC and PCFC models do not predict any negative peak, whereas TWFC predicts a negative peak with noticeable out-of-phase displacements. The displacement at Point 3, which is significantly smaller than displacement at Point 2, exhibits a varied pattern. Initially, the simulation predictions are

close to the experimental results but are quite different for the rest of the simulation. Finally, the PCFC and GTFC models closely predict the final rebound velocity while TWFC model overpredicts the final velocity.

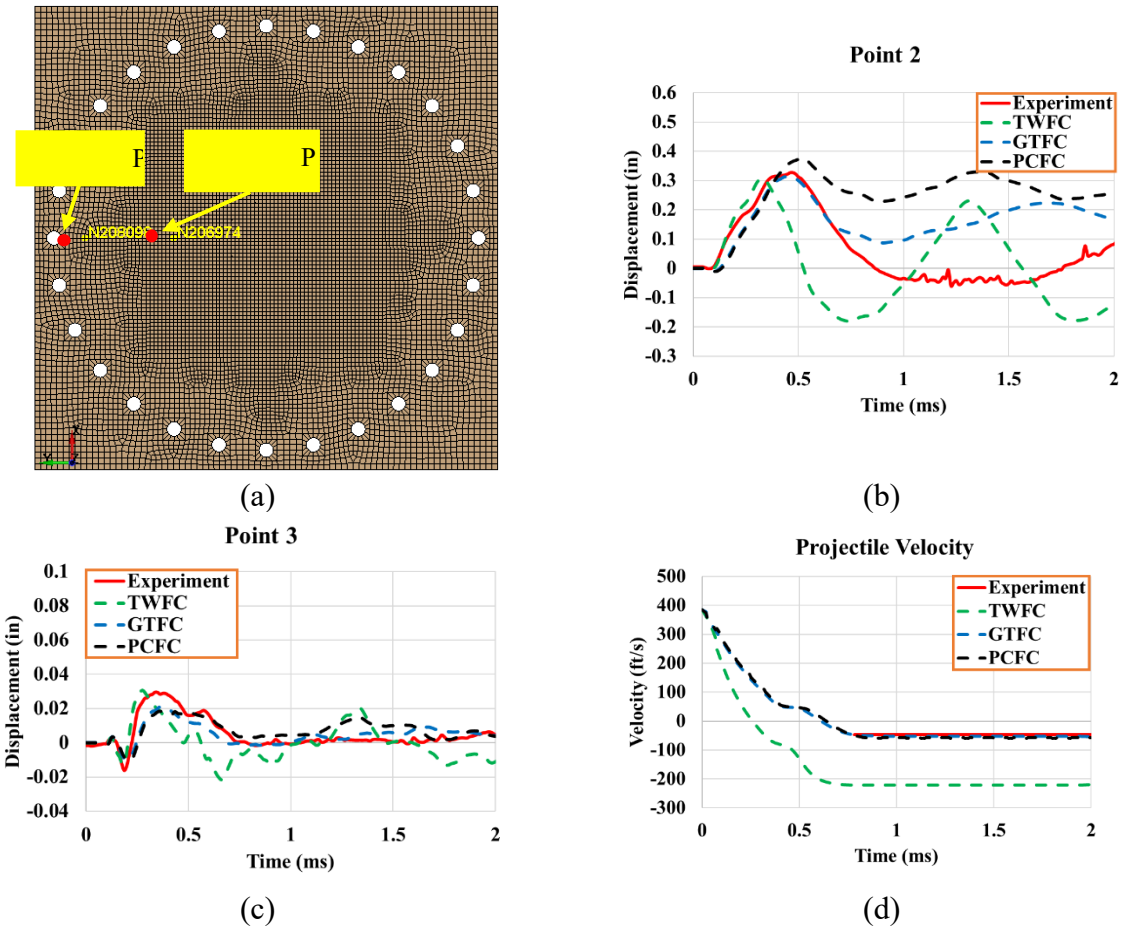

Figure 5.13: LVG1075 Results - (a) Points on the Panel Backside Where Out-of-Plane Displacements Were Monitored, (b) Out-of-Plane Displacements at Point 2, (c) Out-of-Plane Displacements at Point 3, and (d) Projectile Velocity.

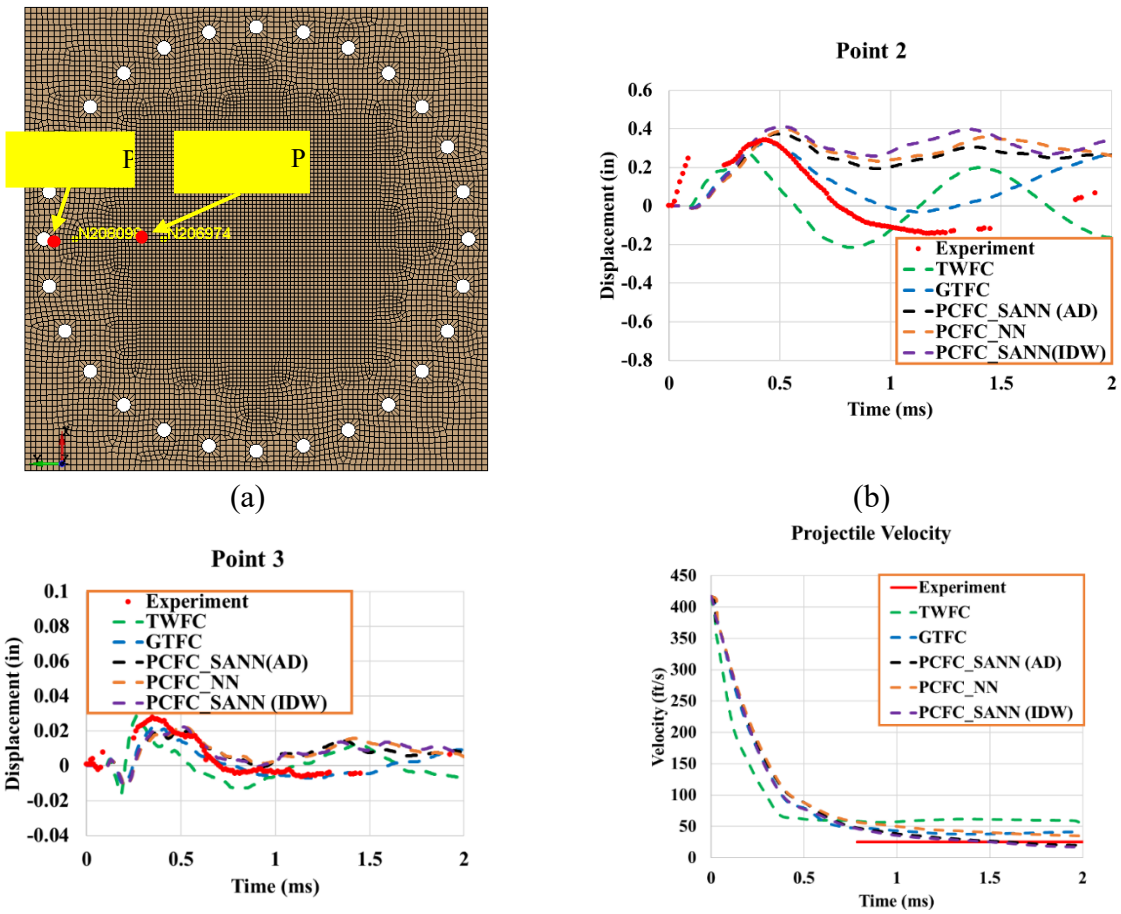

Figure 5.14: LVG1074 Results - (a) Points on the Panel Backside Where Out-of-Plane Displacements Were Monitored, (b) Out-of-Plane Displacements at Point 2, (c) Out-of-Plane Displacements at Point 3, and (d) Projectile Velocity.

LVG1074: This is an uncontained test where the final velocity is slightly more than the threshold penetration velocity. The results are shown in Figure 5.14. The experimental (DIC) displacement plots are discontinuous due to data loss. Like the LVG1075 model, the first positive peak displacement at Point 2 is under-predicted with the TWFC model, over-predicted with both PCFC methods compared to the GTFC predictions. All three PCFC methods do not show any negative peak, while the GTFC model shows a very small negative peak, and the TWFC model predicts a negative peak with noticeable out-of-phase

displacements. The significantly smaller displacement at Point 3 is predicted well by the three models at the first positive and first negative peaks, but notably diverges from experimental values for the remainder of the simulation. The final (exit) velocity in the PCFC_SANN model is the closest to the experimental value, while PCFC_NN, GTFC and TWFC models overestimate the velocity.

The simulation results versus experimental results are summarized in Table 5.9.

Table 5.9: Summary of the Simulation (FE) versus Experimental Data (Exp).

LVG Model (Failure Model)	**Impact Velocity, V_{IMP} (ft/s)**	**Final Velocity, V_f (ft/s)**		**Normalized Absorbed Energy** $\left(\frac{\frac{1}{2}mV_{IMP}^2 - \frac{1}{2}mV_f^2}{\frac{1}{2}mV_{IMP}^2}\right)$		
		Exp	**FE**	**Exp (%)**	**FE (%)**	**Diff. (%) (FE – Exp)**
906 (TWFC)	27.4	-18.4	-20.1	54.9	46.2	-8.7
906 (GTFC)	27.4	-18.4	-17.8	54.9	57.8	2.9
906 (PCFC (SANN-AD))	27.4	-18.4	-17.8	54.9	57.8	2.9
1075 (TWFC)	385	-46.4	-220.8	98.5	67.1	-31.4
1075 (GTFC)	385	-46.4	-54.3	98.5	98.0	-0.5
1075 (PCFC (SANN-AD))	385	-46.4	-59.0	98.5	97.6	-0.9
1074 (TWFC)	417	+25.4	52.2	99.6	98.4	-1.2
1074 (GTFC)	417	+25.4	37.5	99.6	99.2	-0.4
1074 (PCFC (SANN-AD))	417	+25.4	20.0	99.6	99.8	0.14
1074 (PCFC (SANN-IDW))	417	+25.4	17.1	99.6	99.8	0.2
1074 (PCFC-NN)	471	+25.4	35.2	99.6	99.3	-0.3

Overall Observations: The first positive peak out-of-plane displacement at the center/point 2 has been predicted reasonably well by all three failure models. With reference to LVG1074 and LVG1075, the TWFC models were able to predict both positive and negative peaks quite accurately. However, the displacement values were out-of-phase after the first positive peak. On the other hand, the GTFC and PCFC models were unable to predict negative peak displacements. The predictions of the peak out-of-plane displacement at edge/Point 3 appear to show poor predictions. However, these magnitudes are significantly lower compared to the displacements at center/Point 2. The exit/rebound

projectile velocities of the projectile obtained from the FE simulations are reasonably close to the experimental data. As shown in Table 5.9, the difference involved in the prediction of the energy absorbed is within 3% of the experimental value except for the LVG906 model and TWFC models.

The post-impact crack patterns on the back side of the panels are qualitatively compared for LVG1075 and LVG1074 tests in Figure 5.15 and Figure 5.16, respectively when the projectile reaches a constant final velocity, corresponding to 0.8 ms for LVG1075 and 0.6 ms for LVG1074. All three failure models show significant damage at the center. Figure 5.15(a) and Figure 5.16(a) show localized damage at the point of impact with cracks from the center to the outer edge of the panel in the LVG1074 test. For the LVG1075 test, the TWFC model shows no clear hole at the center with some element erosion, whereas the GTFC and PCFC models both predict a clear hole at center. The hole is larger in the GTFC model and smaller in the PCFC model. For the LVG1074 test, all three failure models predict a clear hole at the center of the panel. The TWFC model predicts holes closely matching the projectile dimensions with no visible cracks. In contrast, the PCFC models show smaller central holes at the center and much longer surface cracks compared to GTFC models.

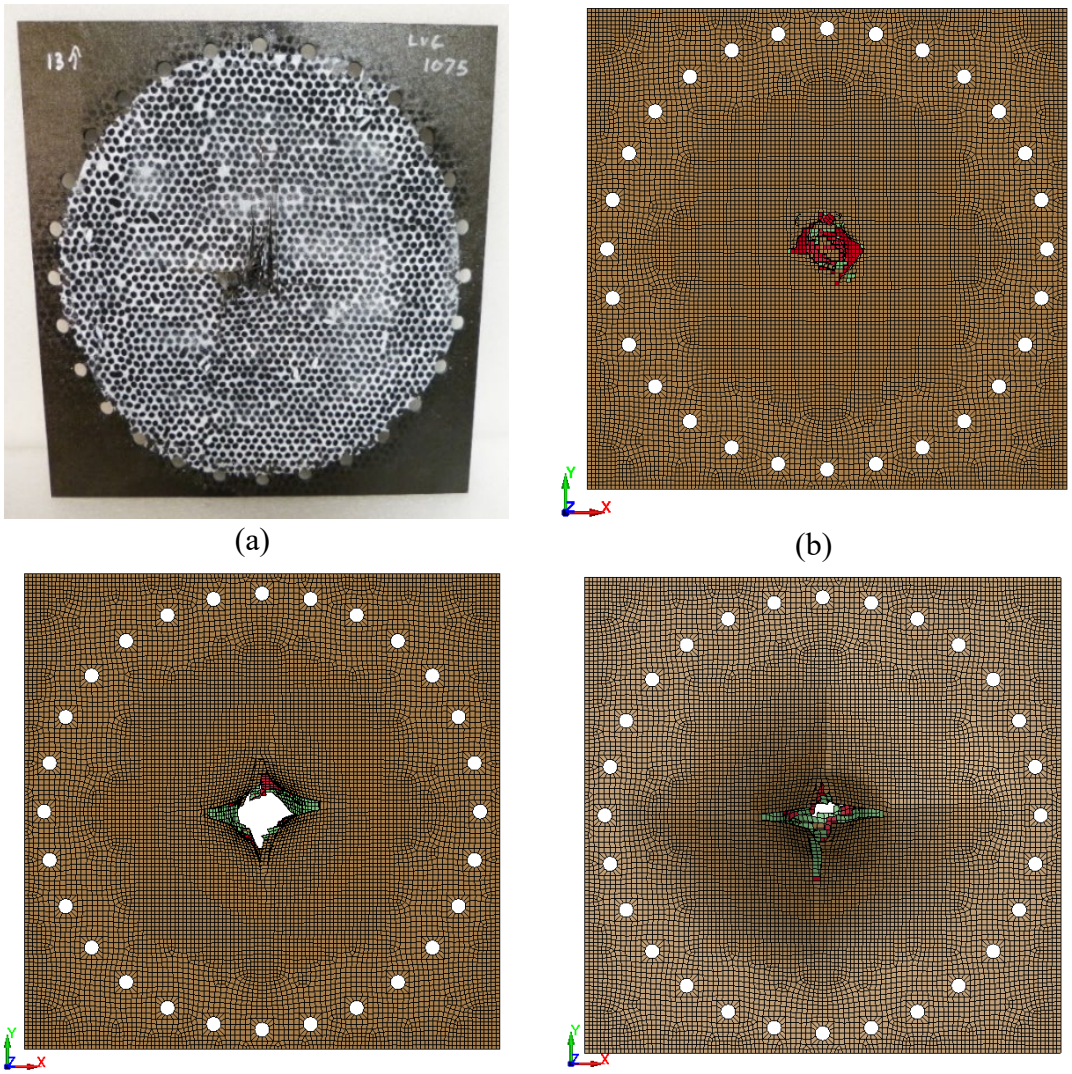

Figure 5.15: LVG1075 Crack Pattern at Time $t = 0.8ms$ - (a) Experiment, (b) TWFC, (c) GTFC, and (d) PCFC.

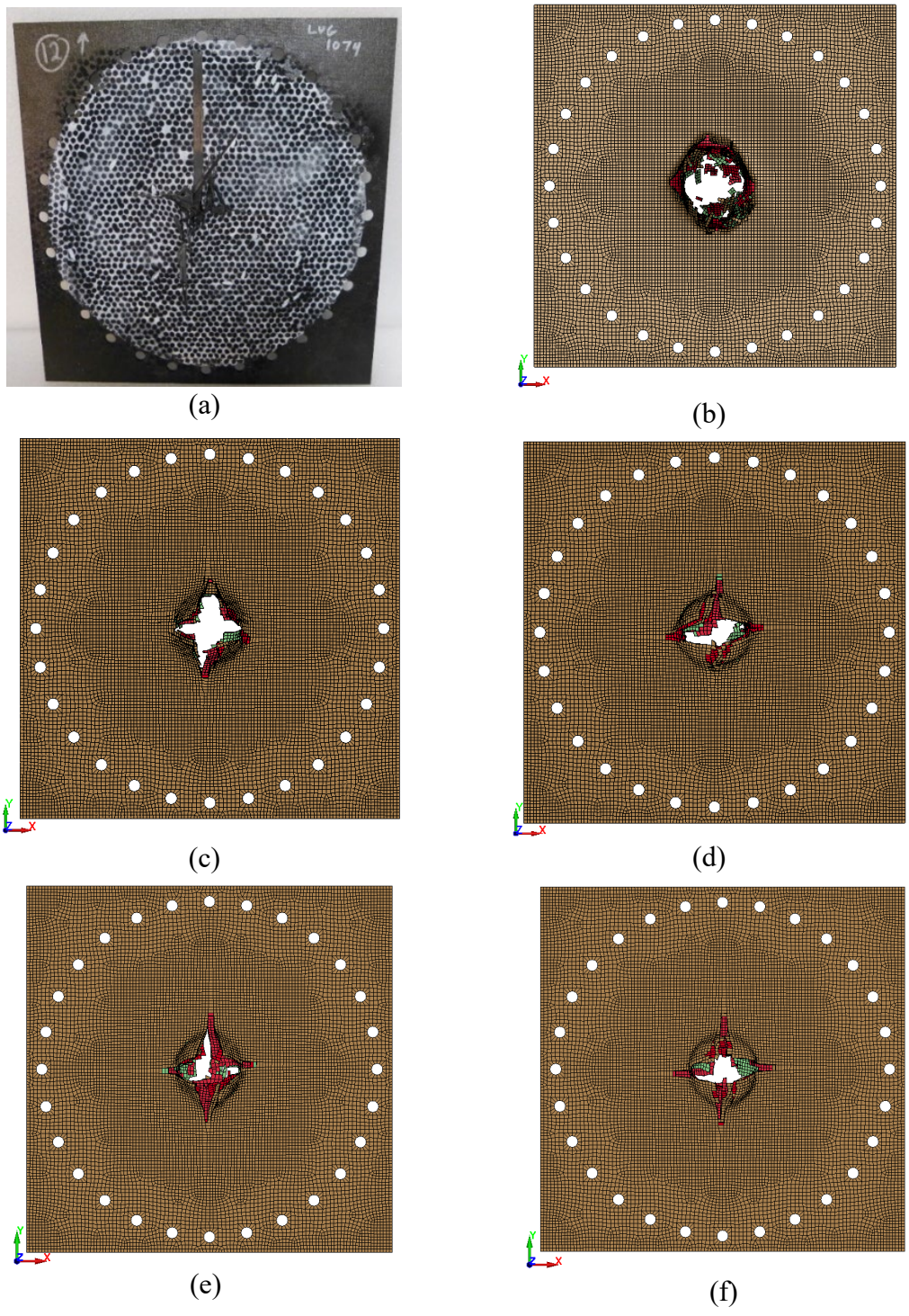

Figure 5.16: LVG1074 Crack Pattern at Time $t = 0.6ms$ - (a) Experiment, (b) TWFC, (c) GTFC, (d) PCFC_SANN (AD), (e) PCFC_SANN (IDW), and (f) PCFC_NN.

The delamination patterns for LVG1075 and LVG1074 are shown in Figure 5.17 and Figure 5.18, respectively. Delamination in FE simulation is measured by the number of eroded CZE elements whereas Ultrasonic Testing (UT) scans of the panel yielded the experimental images. The black regions at the center of the UT scan image (Figure 5.17(a) and Figure 5.18(a)) do not represent a through hole. Instead, the black color is due to loss of data caused by a combination of small through cracks and severe damage (Shyamsunder et al., 2022b). The grey area represents the delamination region. The TWFC model shows a diagonal delamination pattern at the point of impact like the delamination observed in the UT scan. On the other hand, the GTFC and PCFC models show delamination in both vertical and horizontal directions. The PCFC models exhibit less delamination indicating a stiffer composite panel compared to the other models.

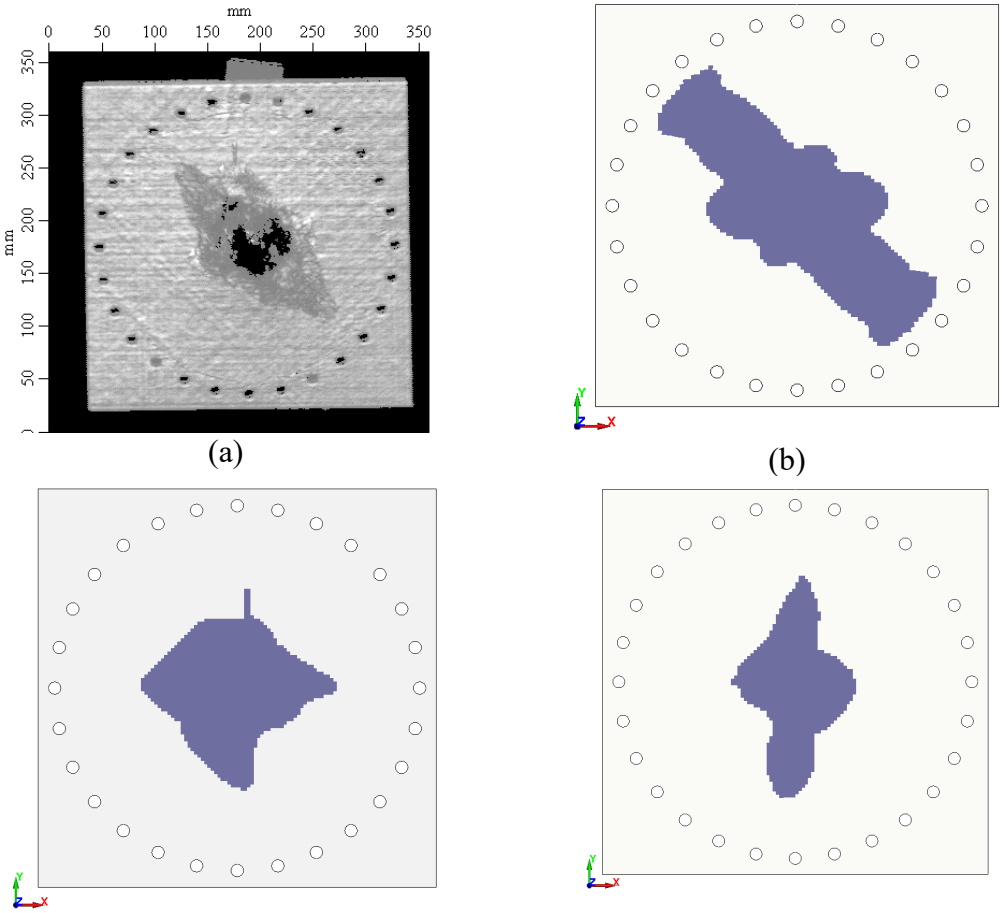

Figure 5.17: LVG1075 Delamination Pattern at Time $t = 2ms$ - (a) Experiment, (b) TWFC, (c) GTFC, and (d) PCFC.

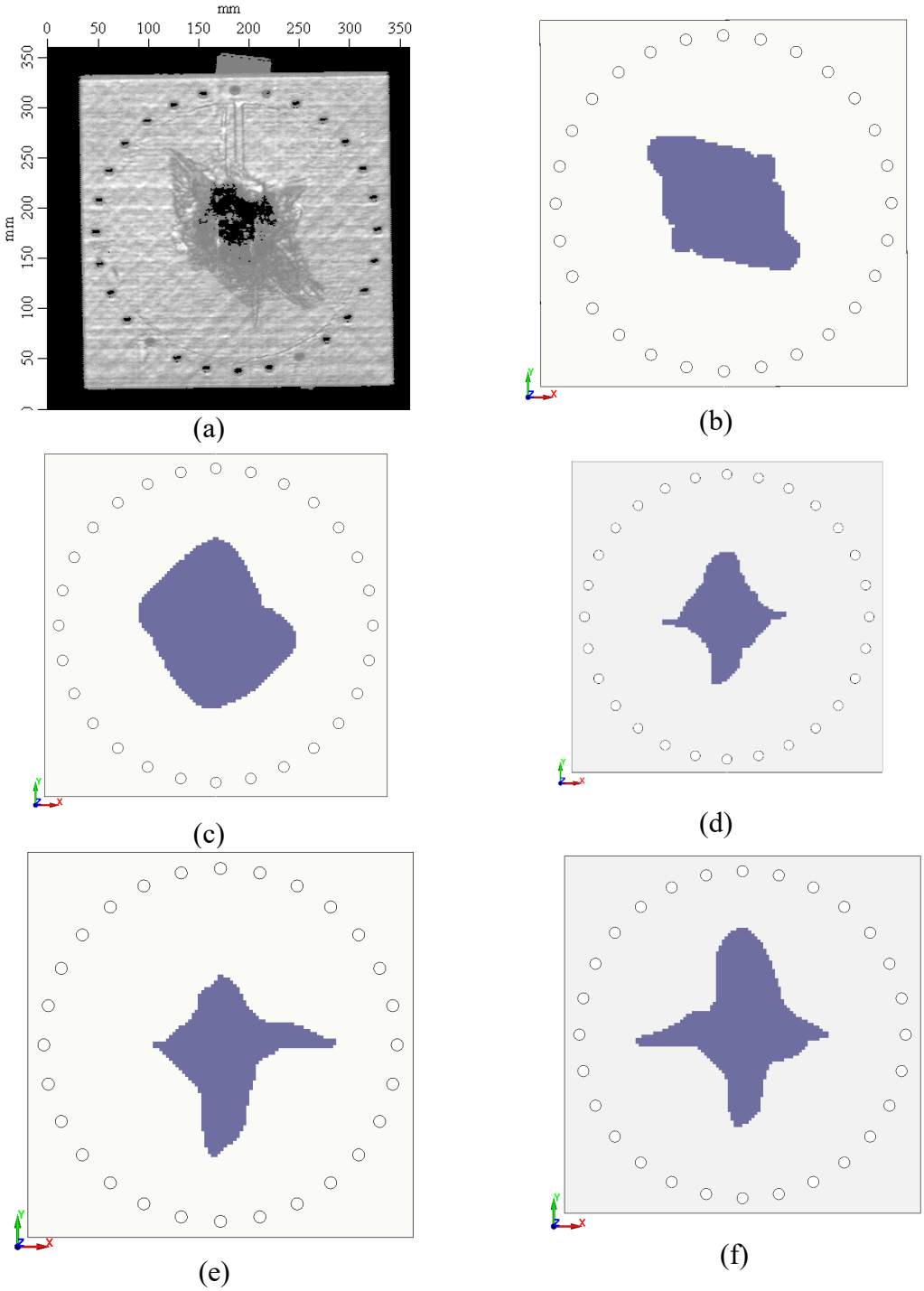

Figure 5.18: LVG1074 Delamination Pattern at Time $t = 2ms$ - (a) Experiment, (b) TWFC, (c) GTFC, (d) PCFC_SANN (AD), (e) PCFC_SANN (IDW), and (f) PCFC_NN.

When six distinct output metrics (displacements at center and edge of the panels, projectile final velocity, absorbed energy, crack pattern, and delamination) are used to assess the reliability of the three failure models, overall, PCFC_SANN and PCFC_NN models demonstrate better accuracy in predicting the final velocity of the projectile, absorbed energy, and crack/damage pattern compared to the other two failure models. Table 5.10 presents a summary of the runtime comparison for all impact tests.

Table 5.10: Run Time Comparison for Impact Tests.

LVG Model	**FTYPE**	**# of Elements**	**Computing Platform (# Nodes)**	**Wall-Clock Time Hour:Min**
906	GTFC	185536 Shell + 17040 Solid + 173940 CZE	Platform 1 (4)	2:22
906	TWFC		Platform 1 (4)	1:18
906	PCFC (SANN-AD)		Platform 1 (4)	2:44
1075	GTFC		Platform 1 (4)	1:58
1075	TWFC		Platform 1 (4)	1:36
1075	PCFC (SANN-AD)		Platform 1 (4)	2:44
1074	GTFC		Platform 1 (4)	1:59
1074	TWFC		Platform 1 (4)	1:34
1074	PCFC (SANN-AD)		Platform 1 (4)	3:52
1074	PCFC (SANN-IDW)		Platform 2 (1)	3:37
1074	PCFC (SANN-NN)		Platform 1 (4)	3:36

5.2.2 3D-printed Additively Manufactured Aluminum Alloys (Mauersberger et al., 2024)

Additively manufactured (AM) materials play an important role in designing lightweight structures especially in the aerospace industry. Despite their growing adoption, a comprehensive understanding of their unique mechanical properties remains limited. This study addresses the gap by presenting a methodology to characterize the material properties of two AM aluminum alloys: Al2139 and AlSi10Mg through macro-mechanical experimental investigations. The study focuses on capturing two critical behaviors of AM materials:

1. A distinct yield point with softening and re-hardening as with Al2139, and
2. Directionally dependent plastification that cannot be classified as isotropic or kinematic hardening as with AlSi10Mg.

Three validation tests were conducted to analyze the mechanical behavior of the two alloys. The first test was a 2-direction tension test using Al2139 material. The second and third tests were 2- and 3-direction tension tests, respectively, using AlSi10Mg material.

FE Model: The specimen geometries are shown in Figure 5.19. Eight-noded hexahedral solid elements (ELFORM=1) were used. Details of the finite element model are presented in Figure 5.20. The boundary conditions are shown in Figure 5.20(c) and (d). To replicate the experimental setup, the nodes along the circumference of both specimen edges were constrained in the X and Z directions. Nodal velocities were applied to one edge of the specimen while the opposite edge was restrained in the Y direction. The black arrows in Figure 5.20(c) indicate the direction of the applied velocity. The gage section, shown in Figure 5.20(d), was used to extract the stress-strain results.

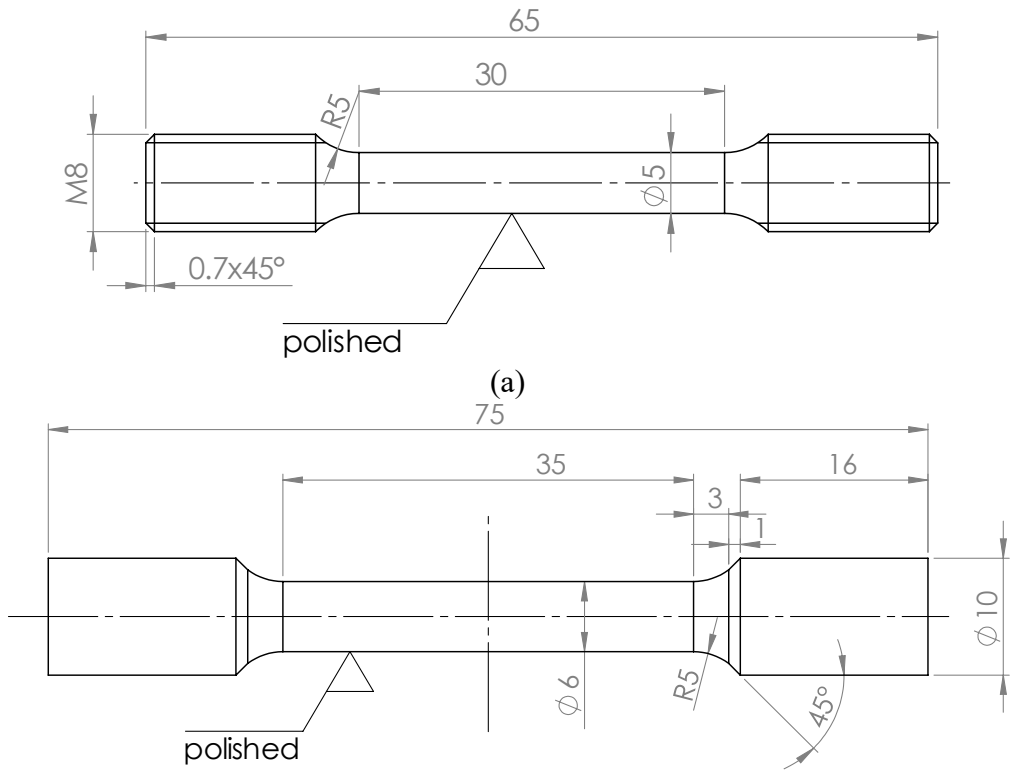

Figure 5.19: Geometries of Tensile Test Specimens According to DIN EN ISO 6892-1 - (a) Al2139, and (b) AlSi10Mg.

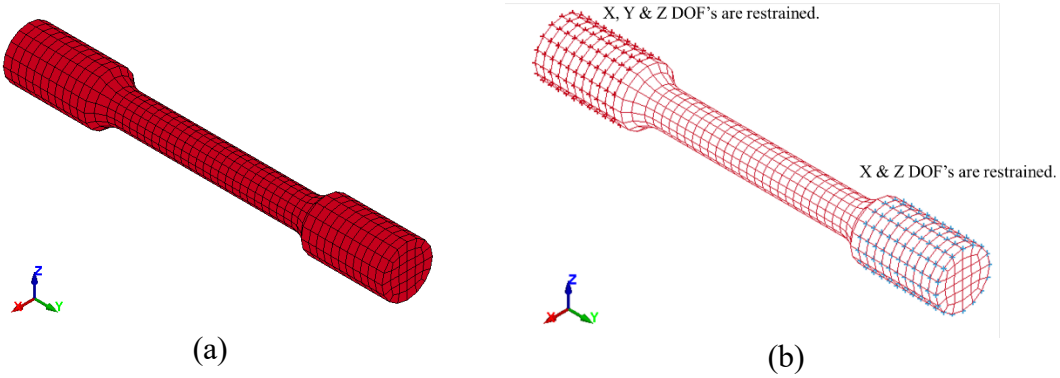

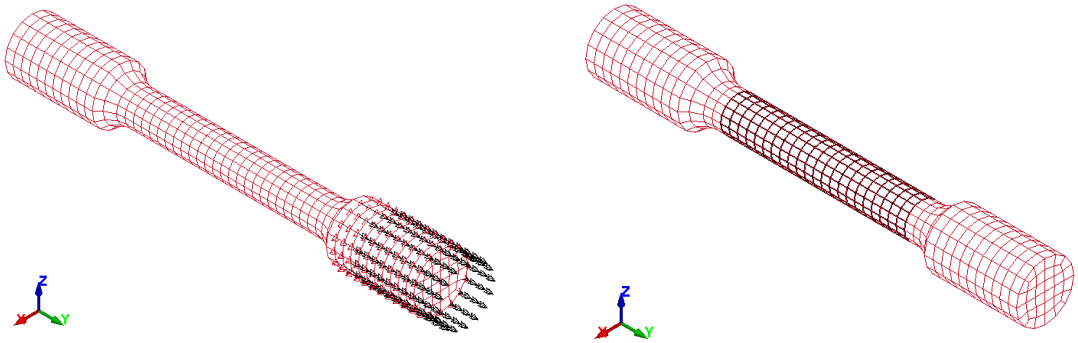

(c) (d)

Figure 5.20: Typical Tension Test Model - (a) FE Mesh, (b) Boundary Conditions, (c) Loading Condition (Velocity), and (d) Gage Section (Highlighted Elements).

Material Data: MAT_213 was used to model both Al2139 and AlSi10Mg alloys, by activating deformation and failure models with the Generalized Tabulated Failure Criterion (GTFC) for element erosion. Tension tests in all three principal material directions provided data to build material cards. Figure 5.21 shows the *Model Curve*. Details to generate the input parameter from these tension tests can be found in a recent work (Mauersberger et al., 2024). Table 5.11 shows the calibrated equivalent failure strains.

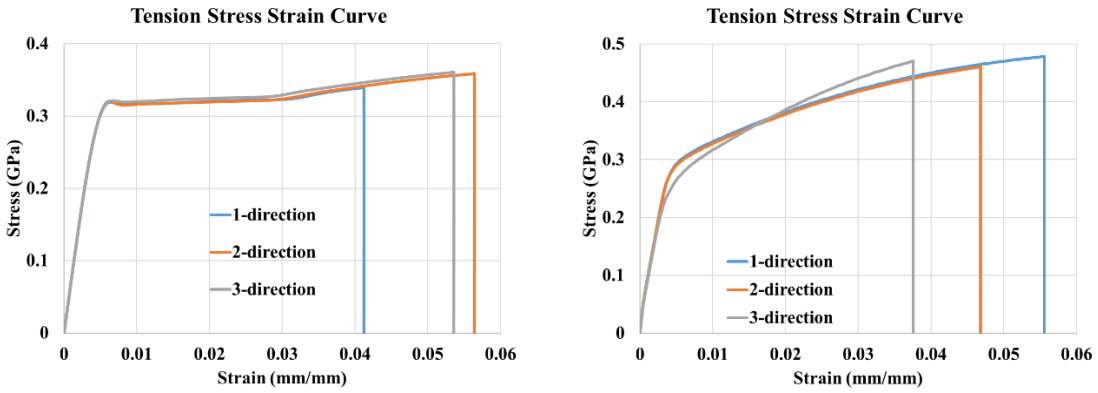

(a) (b)

Figure 5.21: Tension Stress-Strain Curves for As-Built Material - (a) Al2139, and (b) AlSi10Mg.

Table 5.11: MAT_213 Element Erosion Parameters.

Material	**Equivalent failure strain** $\left(\varepsilon_{12}^{f} = \varepsilon_{3}^{f}\right)$
Al2139	0.13
AlSi10Mg (y, z)	(0.086, 0.061)

Results and Discussions: The results from the simulations are presented and analyzed.

Al2139 Material: Figure 5.22 provides a comparison between the load-displacement and stress-strain curves obtained from the FE analysis and the corresponding experimental results. The load-displacement and stress-strain behavior can be broadly divided into two regions: the linear elastic region, and the plastic region where a long softening plateau is followed by a re-hardening plateau before the test article fractures.

Figure 5.22(a) shows the load-displacement curve where the FE model provides reasonably accurate predictions in the linear elastic region when compared to the three experimental replicates (ZP8_Y, ZP10_Y, ZP12_Y). The FE model predicts a higher initial stiffness that is likely due to the initial slippage of the test article in the grip. The first peak load prediction is close with the load drop-off in the FE model closely matching the experimental results followed by a long plateau. Subsequently, the load increases in the re-hardening region with the final FE peak load being slightly higher than the experimental data.

Figure 5.22(b) presents the stress-strain curve. The FE model predicts the same modulus as the experiment in the elastic region though with a slightly lower peak stress. In the plastic region, the FE model underestimates the stresses in both softening region and re-hardening region. It should be noted that stress wave propagation was observed in the

FE model in the plastic region. A low-pass filter was used to smoothen the stress-strain response with peak stress values approximately 5% lower than the experimental data.

Figure 5.23(a) shows the specimen prior to failure with the erosion parameter highlighted. The erosion parameter is used to identify regions within the model that are approaching failure. Red indicates the maximum value as 1.0 representing elements prone to erosion, while blue corresponds to the minimum value as 0.0. As the loading increases, elements in the red color will likely be eroded from the analysis simulating the progression of material failure. Figure 5.23(b) shows the resultant fracture surface of the Al2139 material. The fracture of an experimentally tested Al2139 specimen is shown in Figure 5.24 for comparison where the fracture surface is slightly inclined possibly due to the varying microstructure of the material which is not part of the simulation model.

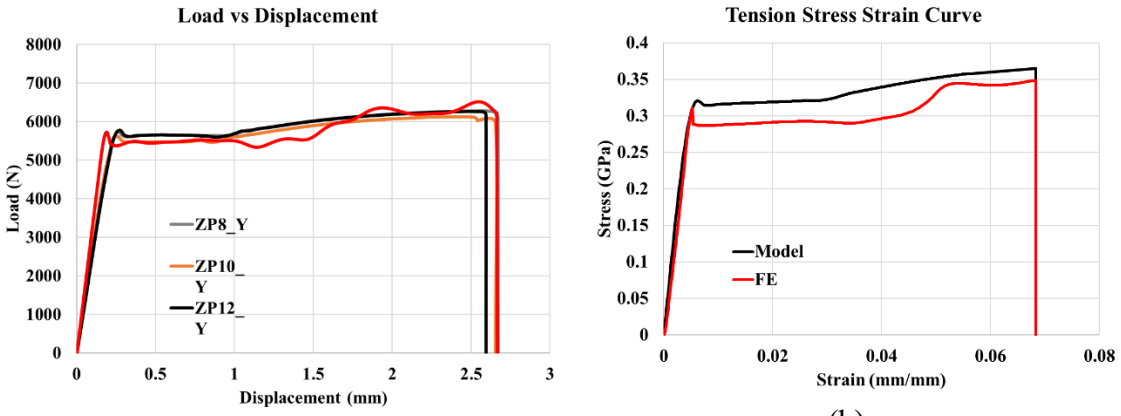

(a) (b)

Figure 5.22: Validation Test Results with Al2139 Material - (a) Load vs Displacement, and (b) Stress vs Strain.

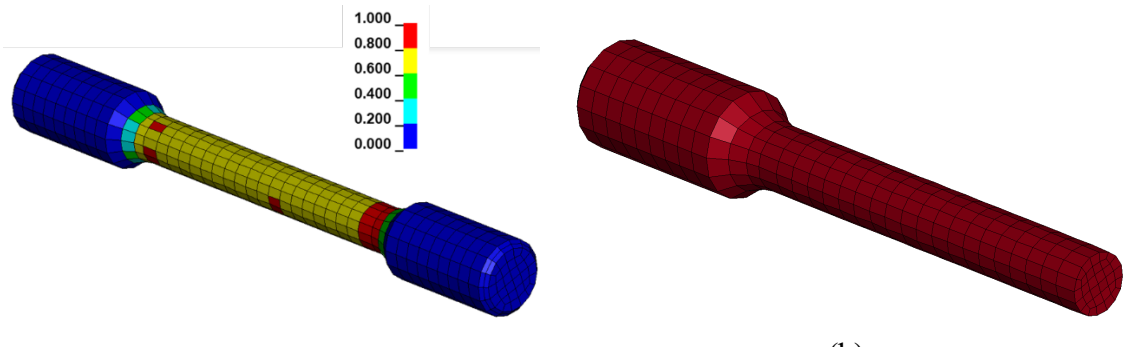

(a) (b)

Figure 5.23: Failure Pattern for Al2139 Material - (a) Specimen Before Failure Showing Erosion Parameter d , and (b) Fracture Surface.

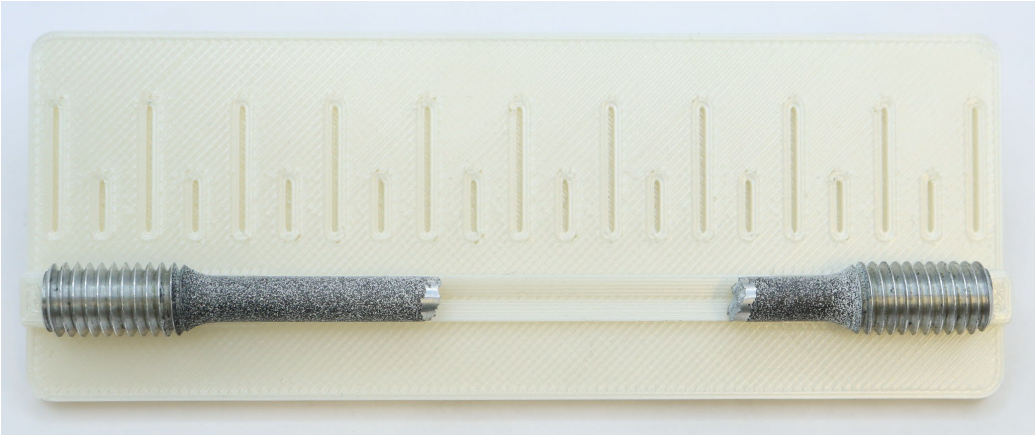

Figure 5.24: Failure Pattern for Real Specimens from Al2139 Material (ZP12_Y).

AlSi10Mg Material: Figure 5.25 compares the load-displacement and stress-strain curves for the 2 and 3-direction tension tests with AlSi10Mg material. Like the Al2139 model, the load-displacement and stress-strain behavior of AlSi10Mg can also be divided into a linear elastic region and a plastic region. However, unlike Al2139, the plastic region of AlSi10Mg exhibits only a hardening plateau which makes the use of MAT_213 attractive for modeling this material.

2-direction test: In the linear elastic region, the FE model predicts similar stiffness for AlSi10Mg as observed in the experiment though it slightly under predicts the peak load. In

the plastic region, the FE model predicts an ultimate peak load that is about 6% lower than the average experimental value. The total energy absorbed during deformation, derived from the area under the load-displacement curve, is underestimated by about 7% in the FE simulation compared to the experiment. The stress-strain curve shows that the FE model predicts a similar modulus and peak stress in the elastic region. The stress in the plastic region is underestimated with the ultimate stress value that is about 5% lower than the experimental value.

3-direction test: Similar to the 2-direction test, the FE model predicts slightly lower stiffness than observed experimentally. In the plastic region, the model predicts an ultimate peak load that is approximately 10% below the average experimental value. The total energy absorbed is about 14% lower in the FE simulation compared to experimental results. The stress-strain curve shows that while the FE model accurately predicts the modulus and peak stress in the elastic region, it underestimates the stress in the plastic region, with the ultimate stress about 9% lower than the experimental results.

Figure 5.26(a) displays the specimen just before failure with the erosion parameter d highlighted and the fractured surface from the FE model. Three distinct regions with the maximum d values are clearly visible, indicating areas of localized stress concentration within the model. Similarly, Figure 5.26(b) presents the specimen just before failure for z-direction specimen with the erosion parameter highlighted.

Figure 5.27 presents the fracture of a real AlSi10Mg specimen. The fracture surface is not planar as in the simulation but exhibits a zig-zag pattern. Differences may be explained by the microstructure of the material which is not part of the simulation model.

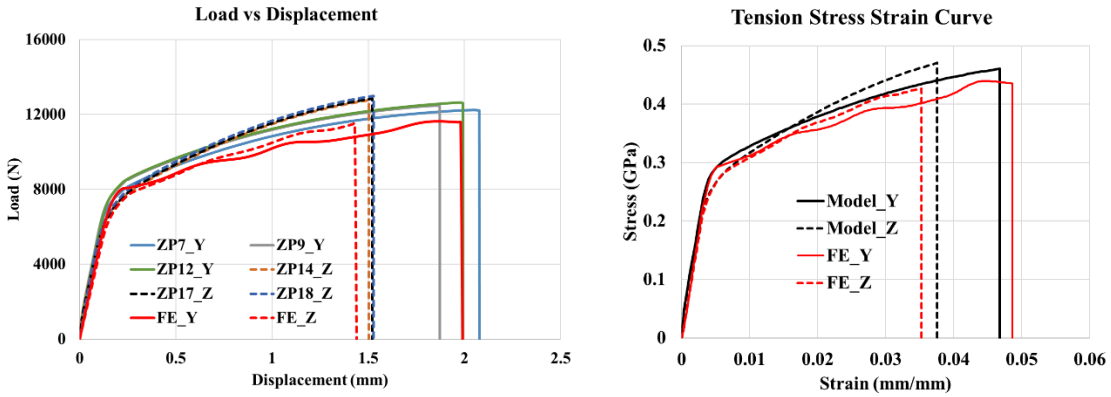

(a) (b)

Figure 5.25: Validation Test Results with AlSi10Mg Material - (a) Load vs Displacement, and (b) Stress vs Strain.

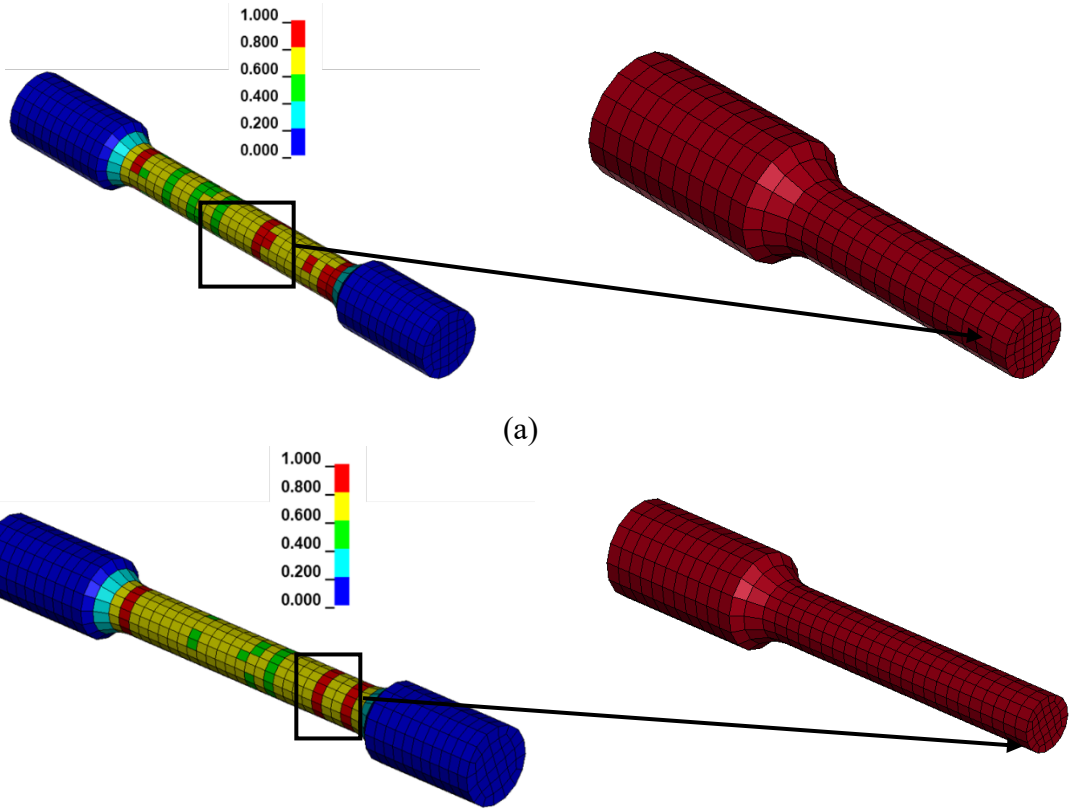

(a)

(b)

Figure 5.26: Failure Pattern for AlSi10Mg Material with Erosion Parameter d, and Fracture Surface - (a) Y-Direction, and (b) Z-Direction.

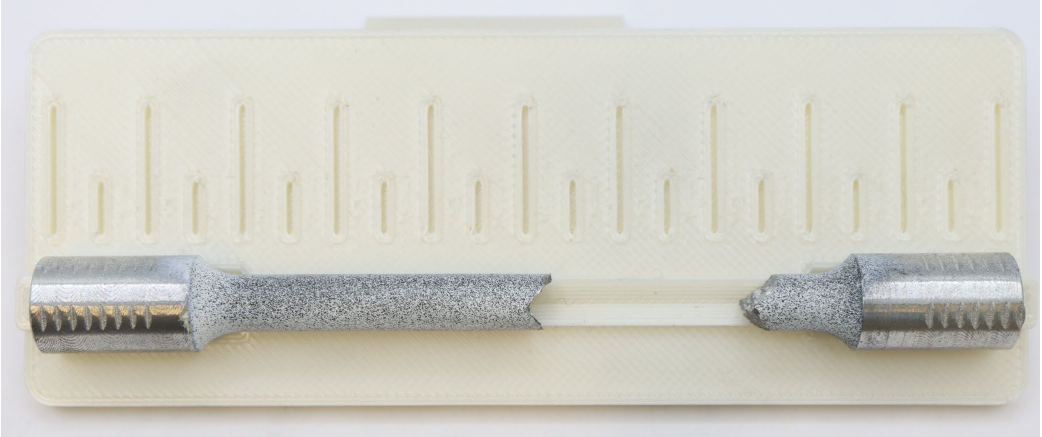

Figure 5.27: Failure Pattern for Real Specimens from Alsi10mg Material (ZP9_Y).

Table 5.12 to Table 5.14 present a summary of the finite element (FE) results for the two materials.

Table 5.12: Summary of the Simulation (FE) versus Experimental Results (Exp) for Al2139.

Parameter	**Experiment (Average)**	**FE**	Diff=$\frac{\text{Exp-FE}}{\text{Exp}}$ **(%)**
Stiffness (load-displacement) (N/mm)	26164	33142	-26.7
First peak (load-displacement) (N)	5707	5718	-0.2
Ultimate Peak (load-displacement) (N)	6072	6208	-2.2
Area under load-displacement curve (N-mm)	14880	14952	-0.5
First peak stress (stress-strain) (GPa)	0.321	0.311	3.2
Ultimate peak stress (stress-strain) (GPa)	0.365	0.348	-4.7

Table 5.13: Summary of the Simulation (FE) versus Experimental Results (Exp) for AlSi10Mg (y-direction).

Parameter	**Experiment (Average)**	**FE**	**Diff= $\frac{\text{Exp-FE}}{\text{Exp}}$ (%)**
Stiffness (load-displacement) (N/mm)	51280	47902	6.6
First peak (load-displacement) (N)	7838	8078	-3.1
Ultimate Peak (load-displacement) (N)	12426	11580	6.8
Area under load-displacement curve (N-mm)	20567	19001	7.6
First peak stress (stress-strain) (GPa)	0.268	0.268	0.0
Ultimate peak stress (stress-strain) (GPa)	0.365	0.348	-4.7

For all the metrics used to validate the FE model, a vast majority of the FE model results are within 10% of the experimental data. It should be noted that only one experimental test data (tension tests in the PMDs) was used to generate the MAT_213 input with all other input curves estimated analytically.

Table 5.14: Summary of the Simulation (FE) versus Experimental Results (Exp) for AlSi10Mg (z-direction).

Parameter	**Experiment (Average)**	**FE**	**Diff= $\frac{\text{Exp-FE}}{\text{Exp}}$ (%)**
Stiffness (load-displacement) (N/mm)	49378	44450	10.0
First peak (load-displacement) (N)	7280	7151	1.8
Ultimate Peak (load-displacement) (N)	12858	11503	10.5
Area under load-displacement curve (N-mm)	15135	12926	14.6
First peak stress (stress-strain) (GPa)	0.248	0.248	0.0
Ultimate peak stress (stress-strain) (GPa)	0.47	0.427	9.3

5.2.3 A Framework for Soft Body Armor Design (Maurya et al., 2024b)

The design of soft body armor for law enforcement involves balancing conflicting requirements of cost, thickness, and weight. Traditional trial-and-error methods may achieve certification standards but rarely yield optimal solutions addressing all three competing factors. However, advancements in experimental techniques and numerical modeling have opened new possibilities to design current and future design work.

This section builds upon an earlier work (Pittie et al., 2023) where experimental methods, machine learning, and FE analysis were combined to create a predictive numerical model for soft armor design. In this study the newly developed constitutive material model, the SMM, is used to model the shoot pack. By integrating solid finite elements, the model replicates behavior observed in laboratory ballistics tests with minimal numerical calibration. Material parameters that cannot be directly measured in experiments are tuned using regression analysis to enhance the model's predictive capabilities. Additional details of the methodology and results are provided in the following publications (Maurya et al., 2024b; Pechetti, 2024).

FE Model: Figure 5.28 shows the 14SS FE model consisting of (a) the shoot pack composite layers, (b) Plastilina clay block, (c) elastic straps to hold the shoot pack against the clay backing, and (d) 44-magnum bullet that is the projectile impacting against the shoot pack. In a laboratory ballistics test, the entire assembly is placed inside a wooden box and placed vertically before the shots(s) are fired. However, to reduce the FE execution time, a smaller number of layers is used in the FE model, i.e., the 28-layer shoot pack is modeled using 14 FE layers.

The shoot pack details are shown in Figure 5.29. S1-S3 are the approximate locations of the three shots. For this study, only the first shot (S1) is modeled and analyzed in detail. 1-2 shows the principal material directions used in the FE analysis. The layer next to the clay block is designated Layer 1 while the rest of the layers that are stacked upon each other are numbered in numerically increasing order such that the strike face is numbered Layer 14. In the current study, perimeter stitching (dashed line) is not a part of the FE model. Eight-noded hexahedral solid elements (ELFORM=-1) were used for shoot pack material. The straps are modeled using ELFORM = -16 which is a fully integrated shell element modified with three integration points through the thickness for higher accuracy. The bullet and the clay are modeled using ELFORM = 1 which is a reduced integration formulation for solid elements.

Material Data: The orthotropic behavior of shoot pack material necessitated the use of MAT_213 for modeling. Table 5.15 lists all the required input material parameters and their sources. Most in-plane parameters were obtained through laboratory experiments while the remaining in-plane and out-of-plane parameters were determined via numerical calibration and regression analysis (Maurya et al., 2024b; Pechetti, 2024).

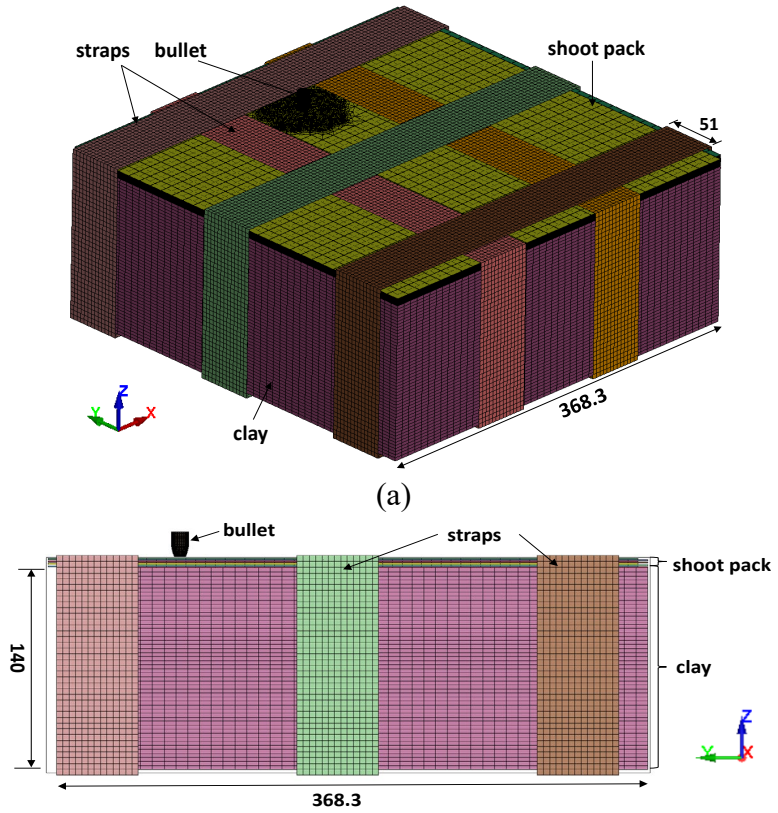

Figure 5.28: Geometric Assembly of 14-Layer FE Model - (a) Isometric View, and (b) Elevation. All Dimensions are in mm.

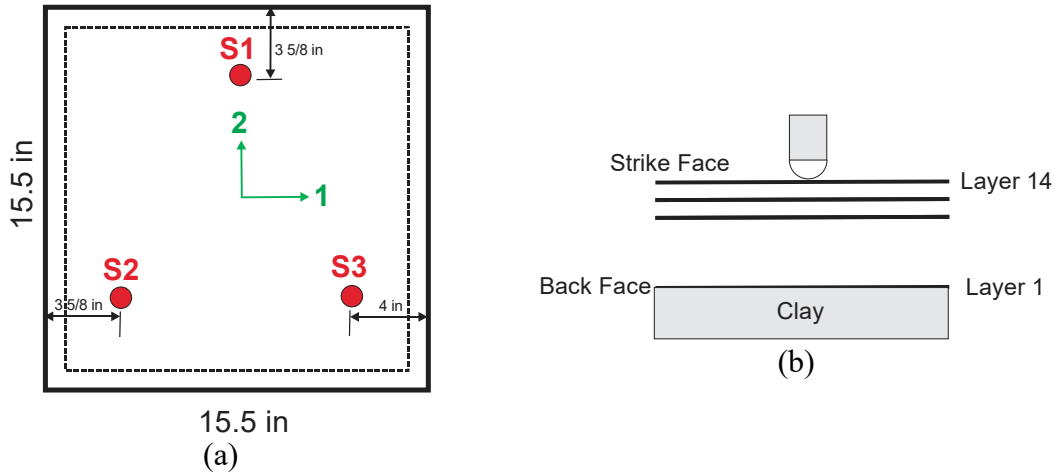

Figure 5.29: Schematic Diagram of the Shoot Pack Showing Overall Dimensions and Locations of the Three Shots as Well as How the 14 Layers are Designated - (a) Plan View, and (b) Elevation View.

The backing clay material was modeled with MAT_015 (Johnson-Cook) along with an equation-of-state (EOS) to account for strain rate and temperature softening effects. The bullet was modeled using MAT_098 (Simplified Johnson-Cook Model), with material parameters sourced from published data (Varmint Al's Engineering Page, 2023). The effective plastic strain at failure was the sole calibrated parameter to ensure that the bullet's mushrooming effect would be replicated in the FE model. The straps were modeled using *MAT_ELASTIC.

Table 5.15: List of Shoot Pack Material Parameters.

Parameter	**Remarks**	**Value(s) (Source)**[1]
$(E_1)^t$	Tensile Young's modulus in 1-direction	$35\ GPa$ (Lab)
$(E_2)^t$	Tensile Young's modulus in 2-direction	$35\ GPa$ (Lab)
ν_{12}	Poisson's ratio in 1-2 plane	0.03 (Lab)
$(E_3)^t$	Tensile Young's modulus in 3-direction	$35\ GPa$ (Est)
ν_{23}	Poisson's ratio in 2-3 plane	0.03 (Est)
ν_{13}	Poisson's ratio in 1-3 plane	0.03 (Est)
$(E_1)^c$	Compressive Young's modulus in 1-direction	$35\ GPa$ (Est)
$(E_2)^c$	Compressive Young's modulus in 2-direction	$35\ GPa$ (Est)
$(E_3)^c$	Compressive Young's modulus in 3-direction	$35\ GPa$ (Est)
$\left(\sigma_1^{peak}\right)^t$	Peak tensile stress in 1-direction	$0.7\ GPa$ (Lab)
$\left(\sigma_2^{peak}\right)^t$	Peak tensile stress in 2-direction	$0.7\ GPa$ (Lab)
$\left(\sigma_{RS}\right)_1^t$	Tensile residual strength in 1-direction	$0.7\ GPa$ (Est)
$\left(\sigma_{RS}\right)_2^t$	Tensile residual strength in 2-direction	$0.035\ GPa$ (Est)

[1] Lab denotes experimental value obtained from laboratory tests and range established the lower and upper bounds for a more comprehensive study using regression analysis.

$\left(\sigma_1^{peak}\right)^c$	Peak compressive stress in 1-direction	0.035 GPa (Est)
$\left(\sigma_2^{peak}\right)^c$	Peak compressive stress in 2-direction	0.035 GPa (Est)
$\left(\sigma_{RS}\right)_1^c$	Compressive residual strength in 1-direction	0.035 GPa (Est)
$\left(\sigma_{RS}\right)_2^c$	Compressive residual strength in 2-direction	0.035 GPa (Est)
τ_{12}^{peak}	Peak shear stress in 1-2 plane	0.001 GPa (Lab)
$\left(\tau_{12}\right)_{RS}$	Shear residual strength in 1-2 plane	0.00005 GPa (Est)
$\left(\sigma_3^{peak}\right)^t$	Peak tensile stress in 3-direction	1.0 GPa (Est)
$\left(\sigma_3^{peak}\right)^c$	Peak compressive stress in 3-direction	1.0 GPa (Est)
$\left(\sigma_{RS}\right)_3^t$	Tensile residual strength in 3-direction	1.0 GPa (Est)
$\left(\sigma_{RS}\right)_3^c$	Compressive residual strength in 3-direction	1.0 GPa (Est)
τ_{23}^{peak}	Peak shear stress in 2-3 plane	0.125 GPa (Est)
τ_{13}^{peak}	Peak shear stress in 1-3 plane	0.125 GPa (Est)
$\left(\tau_{13}\right)_{RS}$	Shear residual strength in 1-3 plane	0.125 GPa (Est)
$\left(\tau_{23}\right)_{RS}$	Shear residual strength in 2-3 plane	0.125 GPa (Est)
ε_{IP}^{eq}	Equivalent failure strain for in-plane mode	1.5 (Est)
ε_{OOP}^{eq}	Equivalent failure strain for out-of-plane mode	1.5 (Est)

Results: Two key metrics from ballistic testing are used to assess the accuracy of the finite element (FE) model:

1. Back-Face Signature (BFS): The deformation on the back side of the shoot pack.
2. Number of Penetrated Layers: The count of layers fully penetrated on the strike face side.

Table 5.16 compares the results from the FE models with the ballistic test data. The predicted number of penetrated layers (12) closely matches the observed value (11). Similarly, the BFS value predicted by the FE model (40.1 mm) aligns well with the experimental measurement (41.4 mm).

Figure 5.30 shows the final state of the shoot pack after the simulation. The strike face layer displays a hole consistent with punch shear closely resembling the physical damage observed in ballistics tests.

Table 5.16: Comparison between Ballistics Test and FE Model

Source	**BFS (mm)**	**No. of Penetrated Layers**
Ballistics Test: Shot 1	41.4	11
FE Model	40.1	12

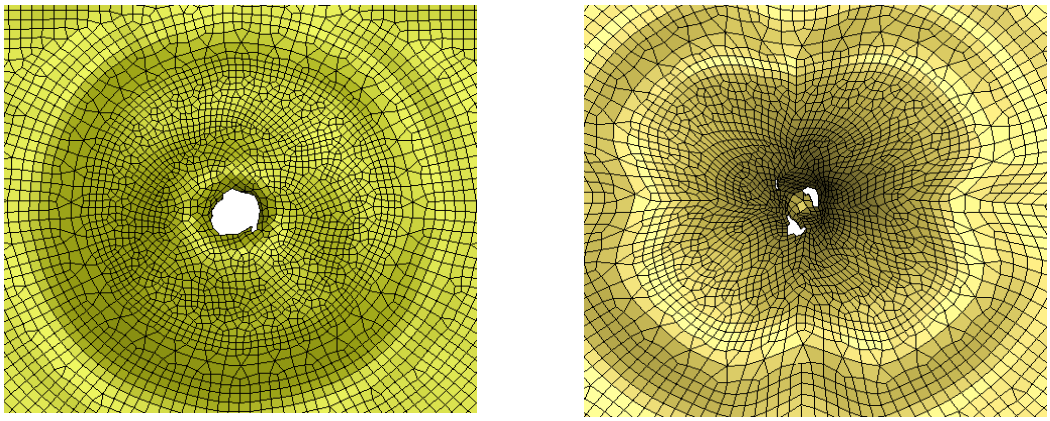

(a) (b)

Figure 5.30: FE Model Results Showing the Final State of the Shoot Pack - (a) Strike Face (Layer 14), and (b) Last Penetrated Layer (Layer 9).

5.2.4 Modeling of Mechanical Behavior of 3D-printed Concrete (Tripathi et al., 2024a)

Traditionally, concrete construction has relied on mold and formworks, prioritizing ease of casting over the efficient use of materials for optimal structural performance. However, the emergence of additive manufacturing in concrete construction has revolutionized the field bringing significant changes. Formwork-free construction offers unprecedented architectural, structural, and functional flexibility, enabling designers and builders to create more efficient and innovative structural systems.

Unlike traditional methods, 3D printing of concrete involves a layer-by-layer deposition of a time-dependent material, introducing unique challenges such as interlayer bonding and curing dynamics that do not arise in mold-cast structures. These complexities, coupled with a limited understanding of the behavior of printed materials, contribute to inherent unpredictability in their performance. Addressing this knowledge gap necessitates the development of refined analytical and design methods tailored specifically for 3D-printed concrete structures, ensuring their reliability and broader applicability in modern construction. Recent work (Tripathi et al., 2024a) focuses on developing a constitutive material model capable of capturing both isotropic and orthotropic behaviors of 3D-printed concrete structures, with and without steel fiber reinforcement. This model integrates laboratory test data to accurately simulate the mechanical properties and structural performance of these advanced materials, bridging critical knowledge gaps and advancing the practical application of 3D-printed concrete in construction.

This section discusses the modeling and analysis of four-point bend tests (4PBT) conducted on ultra-high-performance concrete (UHPC) reinforced with steel fibers. The test specimens were designed with a layer width (LW) of 20 mm and a layer height (LH) of 10 mm (Figure 5.31). A critical aspect of these tests is the alignment of steel fibers predominantly along the print direction, a characteristic intrinsic to the 3D printing process (Tripathi, 2024). This fiber alignment significantly influences the mechanical behavior of the material, enhancing its strength and stiffness along the printed direction. As a result, the UHPC reinforced with steel fibers exhibits orthotropic behavior, with distinct material properties in the principal directions (Figure 5.32).

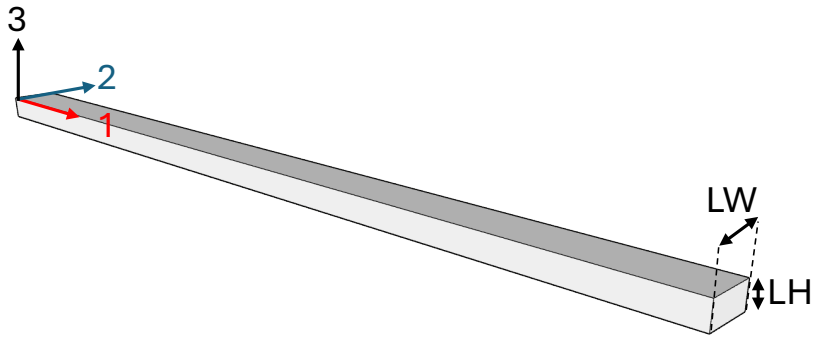

Figure 5.31: Representative Single Filament and Representation of Coordinate Axes; Layer Height (LH), the Layer Width (Tripathi et al., 2024b).

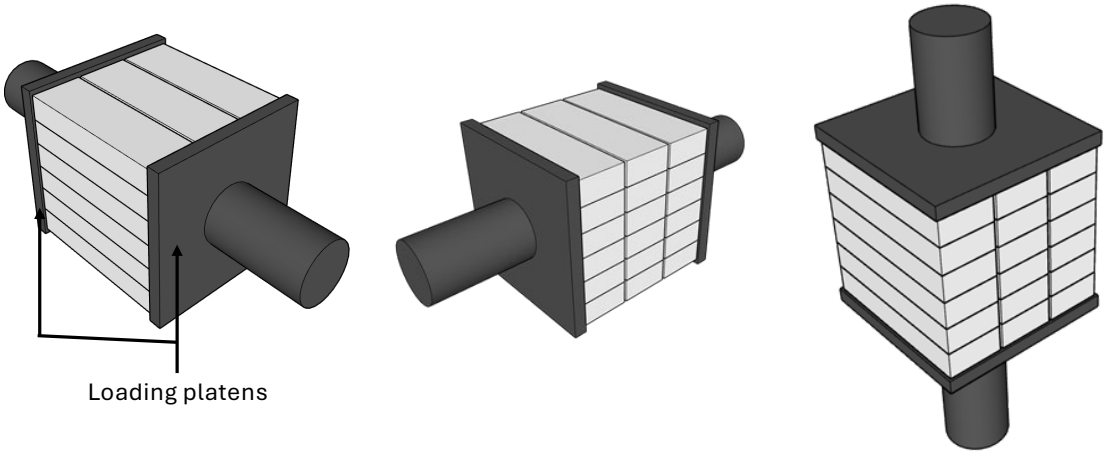

(a) (b) (c)

Figure 5.32: Principal Material Directions - (a) Direction-1 (D1), (b) Direction-2 (D2), and (c) Direction-3 (D3) (Tripathi et al., 2024b).

UHPC Behavior in 4PBT: Figure 5.33 shows typical load vs central deflection plots from 4PBTs conducted on UHPC specimens with and without fibers (Tripathi, 2024). UHPC without fibers exhibits brittle failure upon reaching the cracking load, characterized by a linear elastic response (Zone I), similar to conventional concrete under 4PBT. In contrast, UHPC with steel fibers shows a more complex response, including hardening and softening behavior after the initial linear elastic region. The hardening phase represents flexural hardening, not tensile hardening, occurring after the tensile cracking load is reached. During this phase (Zone II), the load is sustained by mechanisms involving load redistribution at the bottommost steel fibers. The fibers enable the material to carry increasing loads (hardening behavior) until a peak stress (ultimate load) is reached.

Following this, a softening behavior is observed (Zone III), attributed to mechanisms such as failure of fibers, fiber pull-out, and fiber/matrix de-bonding (ACI, 2018). The inclusion of fibers significantly enhances the material's ability to absorb

additional deformation energy making it far more ductile compared to conventional concrete or UHPC without fibers.

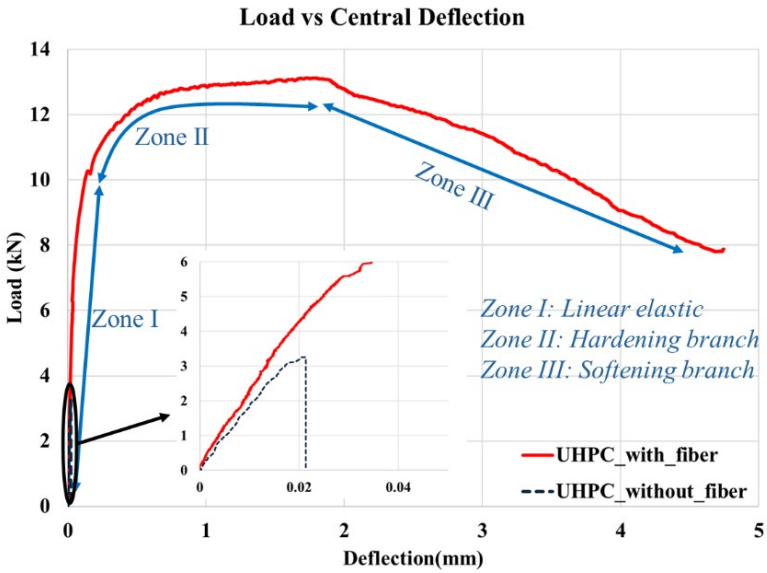

Figure 5.33: Load vs Central Deflection of UHPC with and Without Fiber (Tripathi, 2024).

FE Model: A four-point bend test (4PBT) was simulated for beams with dimensions of 60 × 60 × 300 mm and a span of 240 mm closely replicating the setup of the corresponding experimental tests. To optimize computational efficiency, a quarter-symmetric model was utilized for the analysis, as shown in Figure 5.34(a). Symmetry boundary conditions were applied along the y-z and x-z planes to represent the full geometry with reduced computational effort, as shown in Figure 5.34(b). To replicate the experimental boundary conditions, the translational degree of freedom was restrained in the z-direction at the bottom surface. Loading was applied via nodal displacements at the designated locations, consistent with the experimental setup. These conditions ensured that the simulation accurately mimicked the physical test.

To address potential oscillations in the load-displacement curve, a lower TSSFAC value was combined with a mass scaling technique. This approach was implemented by activating a negative DT2MS parameter in the LS-DYNA time step control card. The mass scaling method works by artificially increasing the mass of elements with time steps smaller than a specified threshold. This adjustment enables a larger critical time step, thereby reducing computation time while maintaining stability in the numerical model.

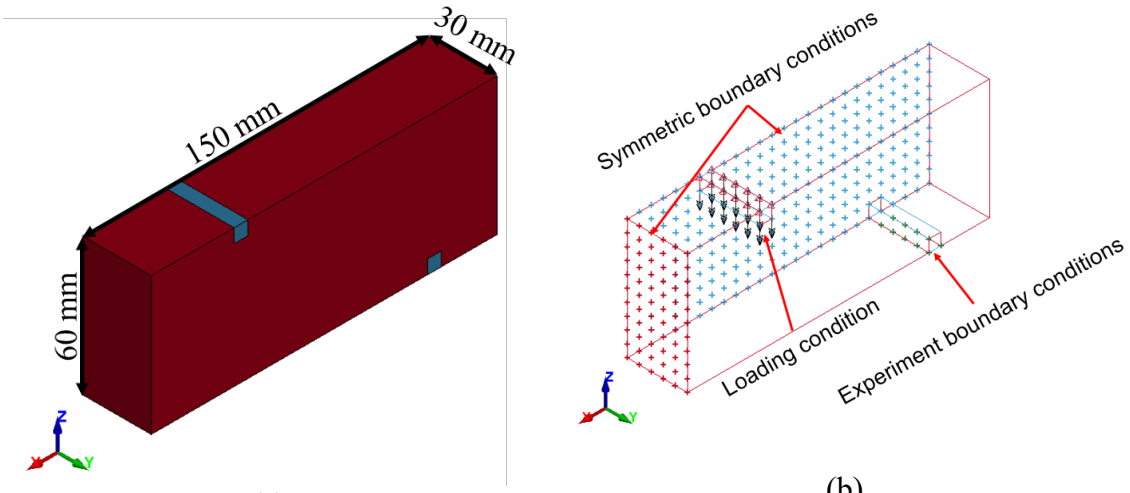

(a) (b)

Figure 5.34: (a) FE Model, and (b) Boundary Conditions.

Material Data: UHPC with steel fibers exhibit orthotropic behavior and tension-compression asymmetry, necessitating an appropriate model for accurate representation. For this study, the Simplified Material Model (SMM) of MAT_213 was used. The UHPC test data has a long flexural softening region, where the load-displacement curves terminated due to large deformations rather than complete specimen failure. Consequently, only the deformation and damage modeling capabilities of MAT_213 were activated. The majority of input parameters for MAT_213, such as elastic moduli, shear moduli, Poisson's

ratios, and peak compressive and tensile stresses, were derived directly from the following experimental data:

1. Uniaxial Compression Test with Fiber (UCTWF)
2. 4-Point Bend Test (4PBT)

However, certain parameters, particularly those controlling post-peak damage were calibrated. Table 5.17 summarizes all the parameter values used in the model, along with their sources, categorizing them as experimentally determined, or calibrated.

Table 5.17: List of MAT_213 Parameters to Define Printed Filaments.

Parameter	Remarks	4PBTSF (Source)
ρ	Mass density (kg/m^3)	2616
E_1	Young's modulus in 1-direction (GPa)	45 (UCTWF)
E_2	Young's modulus in 2-direction (GPa)	40 (UCTWF)
E_3	Young's modulus in 3-direction (GPa)	40 (UCTWF)
ν_{12}	Poisson's ratio in 1-2 plane	0.18 (UCTWF)
ν_{23}	Poisson's ratio in 2-3 plane	0.18 (UCTWF)
ν_{31}	Poisson's ratio in 1-3 plane	0.2 (UCTWF)
$\left(\sigma_1^{peak}\right)^t$	Peak tensile stress in 1-direction (MPa)	Calibrated
$\left(\sigma_2^{peak}\right)^t$	Peak tensile stress in 2-direction (MPa)	3.67 (4PBT)
$\left(\sigma_3^{peak}\right)^t$	Peak tensile stress in 3-direction (MPa)	3.67 (4PBT)
$\left(\sigma_1\right)_{RS}^t$	Tensile residual strength in 1-direction (MPa)	Calibrated
$\left(\sigma_2\right)_{RS}^t$	Tensile residual strength in 2-direction (MPa)	3.67 (4PBT)
$\left(\sigma_3\right)_{RS}^t$	Tensile residual strength in 3-direction (MPa)	3.67 (4PBT)
$\left(\sigma_1^{peak}\right)^c$	Peak compressive stress in 1-direction (MPa)	121 (UCTWF)
$\left(\sigma_2^{peak}\right)^c$	Peak compressive stress in 2-direction (MPa)	121 (UCTWF)
$\left(\sigma_3^{peak}\right)^c$	Peak compressive stress in 3-direction (MPa)	121 (UCTWF)
$\left(\sigma_1\right)_{RS}^c$	Compressive residual strength in 1-direction	121 (UCTWF)

	(MPa)	
$(\sigma_2)_{RS}^c$	Compressive residual strength in 2-direction (MPa)	121 (UCTWF)
$(\sigma_3)_{RS}^c$	Compressive residual strength in 3-direction (MPa)	121 (UCTWF)
τ_{12}^{peak}	Peak shear stress in 1-2 plane (MPa)	$1.45(\sigma_1^{peak})^t$ (Gooch et al., 2023)
τ_{23}^{peak}	Peak shear stress in 2-3 plane (MPa)	$1.45(\sigma_2^{peak})^t$ (Gooch et al., 2023)
τ_{13}^{peak}	Peak shear stress in 1-3 plane (MPa)	$1.45(\sigma_1^{peak})^t$ (Gooch et al., 2023)
$(\tau_{12})_{RS}$	Shear residual strength in 1-2 plane (MPa)	τ_{12}^{peak}
$(\tau_{23})_{RS}$	Shear residual strength in 2-3 plane (MPa)	τ_{23}^{peak}
$(\tau_{13})_{RS}$	Shear residual strength in 1-3 plane (MPa)	τ_{13}^{peak}

Calibration and Results: Figure 5.35 shows the final calibrated stress-strain and damage-strain curves in the D1 direction. Guidance was taken from (ACI, 2018) which provides recommendations for designing with fiber-reinforced concrete. The standard suggests that flexural hardening and softening behaviors can be modeled through tension softening which was incorporated into the tensile stress-strain curve (Figure 5.35) in three distinct regions: a linear elastic zone and two softening zones.

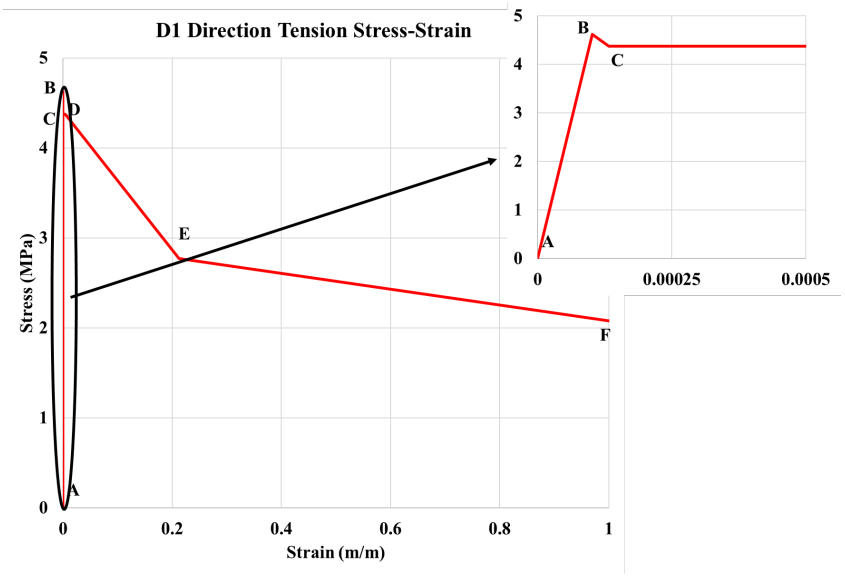

(a)

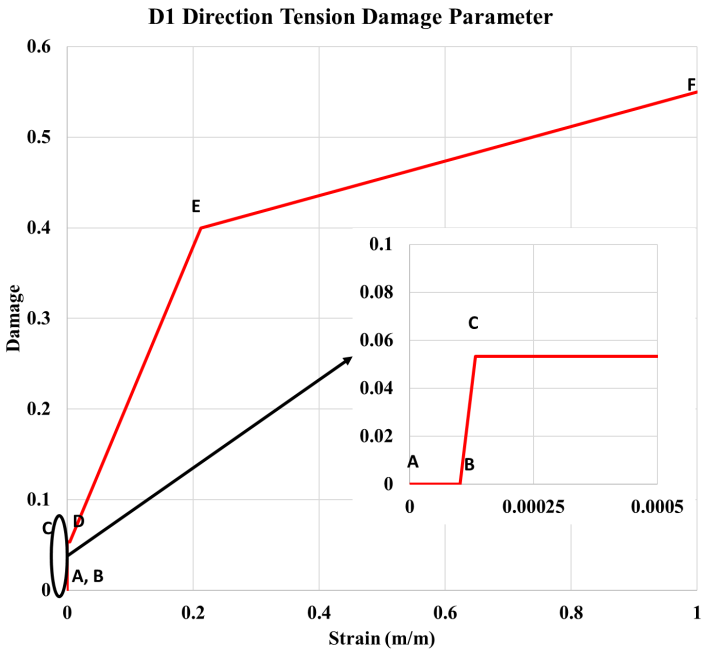

(b)

Figure 5.35: Tension Properties in D1 (Print) Direction - (a) Stress vs Strain, and (b) Damage vs Strain.

Linear Elastic and First Softening Zone: The initial part of the curve (A-B) represents the linear elastic behavior (Zone I) followed by the first softening zone (B-C-D) where tensile

cracking and the hardening branch are observed (Zone II) in the load-displacement response. The parameters for the linear elastic and first softening zones were derived from back-calculations of the 4PBT test results for UHPC with fibers. Initially, this approach resulted in an overestimation of the peak load in the hardening branch. To overcome this, the peak stresses were reduced by 15%, which resulted in a more accurate alignment of the peak load with the experimental data.

Second Softening Zone: The second softening zone (Zone III) was determined through numerical calibration to better match the observed load-deflection response. This bilinear softening curve (D-E-F) was adjusted iteratively until the simulation results matched the experimental softening behavior.

Load-deflection results from the developed FE model are compared with the experimental data in Figure 5.36. The model accurately captures the flexure hardening and softening behavior providing a reliable representation of the UHPC with fiber material's response under flexural loading.

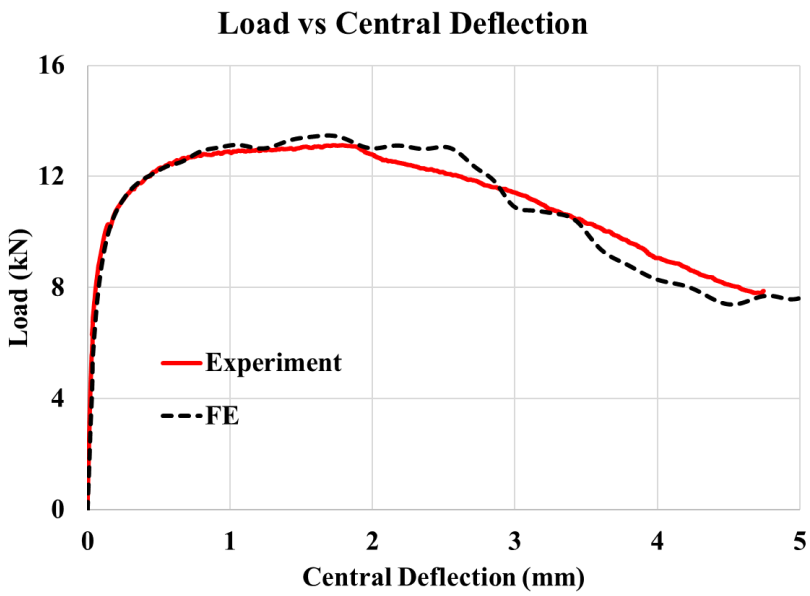

Figure 5.36: Comparison of Load vs Central Deflection.

CHAPTER 6

CONCLUDING REMARKS

The increasing demand for accurate modeling of composite structures under quasi-static and dynamic loading requires more sophisticated material models than the ones currently available in commercial finite element programs. To meet these requirements, the following research objectives were established at the outset of this dissertation.

1. Develop multiscale modeling of unidirectional carbon fiber-reinforced composites, i.e., Toray's T800/F3900 UDC. Subject these models to uniaxial and multiaxial loading conditions to determine the stress/strain state when the first element in the RVE would satisfy the failure criterion for the material and erode. Generate sufficient number of these points so as to have a sufficiently dense point cloud data approximating the failure surface.
2. Enhance the capabilities of MAT_213 by implementing a new failure model, the Point Cloud Failure Criterion that uses the generated point cloud data from (1).
3. Develop a new deformation sub-model, the Simplified Material Model (SMM), that can be used for modeling materials exhibiting little or no elasto-plastic behavior
4. Develop a traction-separation law for unidirectional carbon fiber-reinforced composites using inverse analysis.
5. Verify and validate the enhanced capabilities using statically loaded structural test data from Arizona State University (ASU) and impact test results from NASA Glenn Research Center (NASA-GRC). Reduce the number of material parameters

that cannot be determined experimentally and hence, need to be calibrated, to as small a number as possible.

6. Demonstrate the versatility of MAT_213 across diverse material systems beyond traditional aerospace and automotive composites.

These primary and secondary objectives have been largely met. A summary of the achievements is presented below.

1. A novel failure criterion, the Point Cloud Failure Criterion (PCFC), was developed to improve the modeling of orthotropic structural composites under quasi-static and impact loading. Multi-scale micromechanical modeling and virtual testing were used to construct a discrete failure surface in both stress and strain space. The framework balances computational efficiency with accuracy, providing a robust failure onset prediction methodology. It should be noted that this framework generated point cloud data suitable for use with think shell finite elements.
2. The study also demonstrated that a sufficiently large Representative Volume Element (RVE) enables accurate homogenization of composite behavior under multiaxial stress states. The RVE approach successfully captures deformation, damage, and failure onset through volumetric averaging, offering a viable alternative to experimental multiaxial testing.
3. Two PCFC failure prediction methodologies — Nearest Neighbor and Neural Networks — were developed and compared in terms of efficiency and accuracy. Both approaches yielded promising results, with the inverse distance weightage method Simplified Approximate Nearest Neighbor (SANN-IDW) and a pruned

deep neural network (NN-DP) providing the best balance between accuracy and computational cost.

4. Several validation tests were conducted – stacked-ply specimens with quasi-static loading, and dynamic loading on stacked-ply flat panels with low and high velocity impacts using aluminum impactors.
5. A Simplified Material Model was added as a new deformation sub-model for materials primarily exhibiting only elastic (no plastic) orthotropic behavior with damage and failure. To assess the effectiveness of the implementation, two validation tests were conducted. First, a FE analysis framework was developed for soft body armor systems incorporating thin orthotropic composite shoot pack layers, clay backing, and the bullet. The SMM implementation significantly improved the ability to capture punch shear effects using solid finite elements with the predicted damage and failure very close to the laboratory tests. Second, the developed SMM was used to simulate mechanical behavior under compression and flexural loading of 3D-printed concrete. The model successfully captured the anisotropic nature of printed layers with deformation, damage and failure predictions closely matching experimental results.
6. To demonstrate the versatility of MAT_213, finite element modeling of additively manufactured (AM) aluminum alloys Al2139 and AlSi10Mg was performed. Stress-strain behavior was captured without simplifying assumptions. Validation tests replicated key experimental observations, including softening and re-hardening in Al2139 and directionally dependent plastification in AlSi10Mg. While

overall performance was satisfactory, minor discrepancies in the plastic region were observed, likely due to the limited experimental data used in MAT_213 input parameter development.

7. Lastly, a systematic process was established for characterizing fracture properties of composite materials by integrating experiment and inverse analysis. Experimental test data were analyzed to derive material properties, while inverse analysis was used to determine traction-separation laws for delamination modeling. The developed framework provides a reliable methodology for constructing cohesive zone models focusing on optimizing parameter selection to improve accuracy in damage and failure simulations.

From a design engineer's perspective, the bane of building predictive FE models arises from having to calibrate or tune material parameters that either have no physical significance or are difficult to obtain experimentally. In this study, the validation tests require only two tunable parameters with both parameters in the post-peak part of the material behavior where it is currently difficult to obtain experimental data. The first parameter deals with the residual strength, while the second parameter deals with element erosion criteria.

To further enhance the robustness and applicability of the developed modeling framework, the following follow on work is recommended.

1. Investigating the influence of element size on the generation of point cloud failure data to improve numerical stability and predictive accuracy across varying mesh resolutions.

2. Developing methodologies to extract post-peak damage behavior beyond failure onset, thereby reducing the calibration process and enhancing model robustness.
3. Including strain rate effects improves the predictability of the model, rate-dependent data for the composite will be used to generate rate-dependent failure surface.
4. Extending point cloud failure data to thick-shell and solid finite elements, expanding the applicability of the model to a broader range of structural configurations.
5. Enhancing numerical efficiency by revisiting the overall algorithm, identifying computational bottlenecks, and optimizing implementation strategies to reduce computational time.
6. Extending the framework to support implicit solvers for quasi-static problems where dynamic effects are minimal.

By addressing these areas, the developed constitutive model will continue to evolve into a more versatile and predictive tool for composite materials under a wide range of loading conditions. Future research will focus on further refining these enhancements and expanding the model's applicability to emerging materials and structural systems.

REFERENCES

ACI, 2018. Guide to Design with Fiber-Reinforced Concrete (No. PRC-544.4-18).

Ahmadian, H., Liang, B., Soghrati, S., 2017. An integrated computational framework for simulating the failure response of carbon fiber reinforced polymer composites. Comput Mech 60, 1033–1055. https://doi.org/10.1007/s00466-017-1457-5

ASME V&V 10.1, 2012. An Illustration of the Concepts of Verification and Validation in Computational Solid Mechanics. American Society of Mechanical Engineers.

ASTM D3039, 2014. Test method for tensile properties of polymer matrix composite materials.

ASTM D3410, 2008. Test method for compressive properties of polymer matrix composite materials with unsupported gage section by shear loading.

ASTM D5379, 2012. Test method for shear properties of composite materials by the V-notched beam method.

ASTM D5528, 2013. Standard test method for Mode I interlaminar fracture toughness of unidirectional fiber- reinforced polymer matrix composites.

ASTM D6641, 2016. Compressive Properties of Polymer Matrix Composite Materials Using a Combined Loading Compression (CLC) Test Fixture.

ASTM D7291, 2007. Through-Thickness “Flatwise” Tensile Strength and Elastic Modulus of a Fiber-Reinforced Polymer Matrix Composite Material.

ASTM D7905, 2014. Determination of the Mode II Interlaminar Fracture Toughness of Unidirectional Fiber-Reinforced Polymer Matrix Composites.

AWG_LS-DYNA, 2013. Modeling Guidelines Document Version 13-1.

Azevedo, J.C.S., Campilho, R.D.S.G., da Silva, F.J.G., Faneco, T.M.S., Lopes, R.M., 2015. Cohesive law estimation of adhesive joints in mode II condition. Theoretical and Applied Fracture Mechanics 80, 143–154. https://doi.org/10.1016/j.tafmec.2015.09.007

Azzi, V.D., Tsai, S.W., 1965. Anisotropic strength of composites: Investigation aimed at developing a theory applicable to laminated as well as unidirectional composites, employing simple material properties derived from unidirectional specimens alone. Experimental Mechanics 5, 283–288. https://doi.org/10.1007/BF02326292

Balasubramani, N.K., Zhang, B., Chowdhury, N.T., Mukkavilli, A., Suter, M., Pearce, G.M., 2022. Micro-mechanical analysis on random RVE size and shape in multiscale finite element modelling of unidirectional FRP composites. Composite Structures 282, 115081. https://doi.org/10.1016/j.compstruct.2021.115081

Barbero, E.J., 2013. Finite Element Analysis of Composite Materials Using Ansys®, 2nd ed. CRC Press. https://doi.org/10.1201/b16295

Bogetti, T.A., Staniszewski, J., Burns, B.P., Hoppel, C.P., Gillespie, J.W., Tierney, J., 2013. Predicting the nonlinear response and progressive failure of composite laminates under triaxial loading: Correlation with experimental results. Journal of Composite Materials 47, 793–804. https://doi.org/10.1177/0021998312462616

Bogetti, T.A., Staniszewski, J., Burns, B.P., Hoppel, C.P., Gillespie, J.W., Tierney, J., 2012. Predicting the nonlinear response and progressive failure of composite laminates under tri-axial loading. Journal of Composite Materials 46, 2443–2459. https://doi.org/10.1177/0021998312449889

Bouaoune, L., Brunet, Y., El Moumen, A., Kanit, T., Mazouz, H., 2016. Random versus periodic microstructures for elasticity of fibers reinforced composites. Composites Part B: Engineering 103, 68–73. https://doi.org/10.1016/j.compositesb.2016.08.026

Carrere, N., Laurin, F., Maire, J.-F., 2013. Micromechanical-based hybrid mesoscopic three-dimensional approach for non-linear progressive failure analysis of composite structures—Part B: Comparison with experimental data. Journal of Composite Materials 47, 743–762. https://doi.org/10.1177/0021998312460558

Carrere, N., Laurin, F., Maire, J.-F., 2012. Micromechanical-based hybrid mesoscopic 3D approach for non-linear progressive failure analysis of composite structures. Journal of Composite Materials 46, 2389–2415. https://doi.org/10.1177/0021998312450179

Chamis, C.C., 1969. Failure Criteria for Filamentary Composites, in: Yurenka, S. (Ed.), Composite Materials: Testing and Design. ASTM International, 100 Barr Harbor Drive, PO Box C700, West Conshohocken, PA 19428-2959, pp. 336-336–16. https://doi.org/10.1520/STP49826S

Chen, Y., Zhao, Y., He, C., Ai, S., Lei, H., Tang, L., Fang, D., 2019. Yield and failure theory for unidirectional polymer-matrix composites. Composites Part B: Engineering 164, 612–619. https://doi.org/10.1016/j.compositesb.2019.01.071

Christensen, R., 2008. FAILURE CRITERIA FOR ANISOTROPIC FIBER COMPOSITE MATERIALS.

Cuntze, R., 2013. Comparison between experimental and theoretical results using Cuntze's "failure mode concept" model for composites under triaxial loadings—Part B of the second world-wide failure exercise. Journal of Composite Materials 47, 893–924. https://doi.org/10.1177/0021998312456409

Cuntze, R., 2012. The predictive capability of failure mode concept-based strength conditions for laminates composed of unidirectional laminae under static triaxial stress states. Journal of Composite Materials 46, 2563–2594. https://doi.org/10.1177/0021998312449894

Daniel, I.M., 2007. Failure of Composite Materials. Strain 43, 4–12. https://doi.org/10.1111/j.1475-1305.2007.00302.x

Daniel, I.M., Werner, B.T., Fenner, J.S., 2011. Strain-rate-dependent failure criteria for composites. Composites Science and Technology 71, 357–364. https://doi.org/10.1016/j.compscitech.2010.11.028

Davila, C.G., Camanho, P.P., Rose, C.A., 2005. Failure Criteria for FRP Laminates. Journal of Composite Materials 39, 323–345. https://doi.org/10.1177/0021998305046452

De Luca, A., Caputo, F., Department of Industrial and Information Engineering, University of Campania L. Vanvitelli, Via Roma 29, 81031 Aversa, Italy., 2017. A review on analytical failure criteria for composite materials. AIMS Materials Science 4, 1165–1185. https://doi.org/10.3934/matersci.2017.5.1165

Deuschle, H.M., Puck, A., 2013. Application of the Puck failure theory for fibre-reinforced composites under three-dimensional stress: Comparison with experimental results.

Journal of Composite Materials 47, 827–846. https://doi.org/10.1177/0021998312462158

Dogan, F., Hadavinia, H., Donchev, T., Bhonge, P., 2012. Delamination of impacted composite structures by cohesive zone interface elements and tiebreak contact. Open Engineering 2, 612–626. https://doi.org/10.2478/s13531-012-0018-0

Doudican, B.M., Zand, B., Amaya, P., Butalia, T.S., Wolfe, W.E., Schoeppner, G.A., 2013. Strain energy based failure criterion: Comparison of numerical predictions and experimental observations for symmetric composite laminates subjected to triaxial loading. Journal of Composite Materials 47, 847–866. https://doi.org/10.1177/0021998312462617

Dourado, N., de Moura, M.F.S.F., de Morais, A.B., Pereira, A.B., 2012. Bilinear approximations to the mode II delamination cohesive law using an inverse method. Mechanics of Materials 49, 42–50. https://doi.org/10.1016/j.mechmat.2012.02.004

FAA, 2018. Methodology for Dynamic Seat Certification by Analysis for Use in Parts 23, 25, 27, and 29 Airplanes and Rotorcraft, AC 20-146A.

FAA Report, 2019. Development of a Tabulated Material Model for Composite Material Failure, MAT213 Part 2: Experimental Tests to Characterize the Behavior and Properties of T800-F3900 Toray Composite.

Fascetti, A., Feo, L., Abbaszadeh, H., 2021. A critical review of numerical methods for the simulation of pultruded fiber-reinforced structural elements. Composite Structures 273, 114284. https://doi.org/10.1016/j.compstruct.2021.114284

Gao, J., Liang, B., Zhang, W., Liu, Z., Cheng, P., Bostanabad, R., Cao, J., Chen, W., Liu, W.K., Su, X., Zeng, D., Zhao, J., 2017. Multiscale Modeling of Carbon Fiber Reinforced Polymer (CFRP) for Integrated Computational Materials Engineering Process, in: American Society for Composites 2017. Presented at the American Society for Composites 2017, DEStech Publications, Inc. https://doi.org/10.12783/asc2017/15188

GE Aerospace, 2015. GE's Composite Fan Blade Revolution Turns 20 Years Old. URL https://www.geaerospace.com/news/press-releases/commercial-engines/ges-composite-fan-blade-revolution-turns-20-years-old

GE Aerospace, 2005. New GEnx Engine Advancing Unprecedented Use of Composites in Jet Engines. URL https://www.geaerospace.com/news/press-releases/commercial-engines/new-genx-engine-advancing-unprecedented-use-composites-jet

Goldberg, R.K., Carney, K.S., DuBois, P., Hoffarth, C., Harrington, J., Rajan, S., Blankenhorn, G., 2016. Development of an Orthotropic Elasto-Plastic Generalized Composite Material Model Suitable for Impact Problems. J. Aerosp. Eng. 29, 04015083. https://doi.org/10.1061/(ASCE)AS.1943-5525.0000580

Goldberg, R.K., Carney, K.S., DuBois, P., Hoffarth, C., Khaled, B., Shyamsunder, L., Rajan, S.D., Blankenhorn, G., 2018. Implementation of a tabulated failure model into a generalized composite material model. Journal of Composite Materials 52, 3445–3460. https://doi.org/10.1177/0021998318786778

Gooch, L.J., Masia, M.J., Stewart, M.G., Lam, C.Y., 2023. Statistical assessment of tensile and shear properties of unreinforced clay brick masonry. Construction and Building Materials 386, 131578. https://doi.org/10.1016/j.conbuildmat.2023.131578

Gupta, A., Singh, M., Singh, J., Singh, S., Prakash, C., 2022. A critical review on damage modeling and failure analysis of pin joints in fiber reinforced composite laminates. Polymers and Polymer Composites 30, 096739112210997. https://doi.org/10.1177/09673911221099764

Harrington, J., Hoffarth, C., Rajan, S.D., Goldberg, R.K., Carney, K.S., DuBois, P., Blankenhorn, G., 2017. Using Virtual Tests to Complete the Description of a Three-Dimensional Orthotropic Material. J. Aerosp. Eng. 30, 04017025. https://doi.org/10.1061/(ASCE)AS.1943-5525.0000737

Hashin, Z., 1980. Failure Criteria for Unidirectional Fiber Composites. Journal of Applied Mechanics 47, 329–334. https://doi.org/10.1115/1.3153664

Hashin, Z., Rotem, A., 1973. A Fatigue Failure Criterion for Fiber Reinforced Materials. Journal of Composite Materials 7, 448–464. https://doi.org/10.1177/002199837300700404

Herráez, M., González, C., Lopes, C.S., de Villoria, R.G., LLorca, J., Varela, T., Sánchez, J., 2016. Computational micromechanics evaluation of the effect of fibre shape on the transverse strength of unidirectional composites: An approach to virtual materials design. Composites Part A: Applied Science and Manufacturing 91, 484–492. https://doi.org/10.1016/j.compositesa.2016.02.026

Hinton, M., Kaddour, A., 2012. The background to the Second World-Wide Failure Exercise. Journal of Composite Materials 46, 2283–2294. https://doi.org/10.1177/0021998312449885

Hinton, M.J., Kaddour, A.S., Soden, P.D., 2004. The world-wide failure exercise, in: Failure Criteria in Fibre-Reinforced-Polymer Composites. Elsevier, pp. 2–28. https://doi.org/10.1016/B978-008044475-8/50002-0

Hoffarth, C., 2016. A generalized orthotropic elasto-plastic material model for impact analysis. Arizona State University.

Hoffarth, C., Khaled, B., Shyamsunder, L., Rajan, S., Goldberg, R., Carney, K., DuBois, P., Blankenhorn, G., 2017. Verification and Validation of a Three-Dimensional Orthotropic Plasticity Constitutive Model Using a Unidirectional Composite. Fibers 5, 12. https://doi.org/10.3390/fib5010012

Hoffarth, C., Rajan, S.D., Goldberg, R.K., Revilock, D., Carney, K.S., DuBois, P., Blankenhorn, G., 2016a. Implementation and validation of a three-dimensional plasticity-based deformation model for orthotropic composites. Composites Part A: Applied Science and Manufacturing 91, 336–350. https://doi.org/10.1016/j.compositesa.2016.10.024

Hoffarth, C., Rajan, S.D., Goldberg, R.K., Revilock, D., Carney, K.S., DuBois, P., Blankenhorn, G., 2016b. Implementation and validation of a three-dimensional plasticity-based deformation model for orthotropic composites. Composites Part A: Applied Science and Manufacturing 91, 336–350. https://doi.org/10.1016/j.compositesa.2016.10.024

Hoffman, O., 1967. The Brittle Strength of Orthotropic Materials. Journal of Composite Materials 1, 200–206. https://doi.org/10.1177/002199836700100210

Holt, N., Khaled, B., Shyamsunder, L., Rajan, S., 2022. T800-F3900 Composite Stacked Ply Laminate Testing and Modeling Using MAT_213.

Holt, N.T., 2018. Experimental and Simulation Validation Tests for MAT 213. Arizona State University.

Huang, Y., Jin, C., Ha, S.K., 2013. Strength prediction of triaxially loaded composites using a progressive damage model based on micromechanics of failure. Journal of Composite Materials 47, 777–792. https://doi.org/10.1177/0021998312460261

Huang, Y., Xu, L., Kyu Ha, S., 2012. Prediction of three-dimensional composite laminate response using micromechanics of failure. Journal of Composite Materials 46, 2431–2442. https://doi.org/10.1177/0021998312449888

Huang, Z.-M., Zhou, Y.-X., 2013. Correlation of the bridging model predictions for triaxial failure strengths of composites with experiments. Journal of Composite Materials 47, 697–731. https://doi.org/10.1177/0021998312453864

Iwamura, M., Sato, T., Kise, K., 2013. What is the Most EfficientWay to Select Nearest Neighbor Candidates for Fast Approximate Nearest Neighbor Search?, in: 2013 IEEE International Conference on Computer Vision. Presented at the 2013 IEEE International Conference on Computer Vision (ICCV), IEEE, Sydney, Australia, pp. 3535–3542. https://doi.org/10.1109/ICCV.2013.439

Jacob, B., Guennebaud, G., others [Computer Software], 2010. Eigen v3.

Jensen, S.M., Martos, M.J., Lindgaard, E., Bak, B.L.V., 2019. Inverse parameter identification of n-segmented multilinear cohesive laws using parametric finite element modeling. Composite Structures 225, 111074. https://doi.org/10.1016/j.compstruct.2019.111074

Kaddour, A., Hinton, M., 2013. Maturity of 3D failure criteria for fibre-reinforced composites: Comparison between theories and experiments: Part B of WWFE-II. Journal of Composite Materials 47, 925–966. https://doi.org/10.1177/0021998313478710

Kaddour, A., Hinton, M., Smith, P., Li, S., 2013. The background to the third world-wide failure exercise. Journal of Composite Materials 47, 2417–2426. https://doi.org/10.1177/0021998313499475

Kaddour, A.-S., Hinton, M.J., 2018. 1.23 Failure Criteria for Composites, in: Comprehensive Composite Materials II. Elsevier, pp. 573–600. https://doi.org/10.1016/B978-0-12-803581-8.10354-6

Katusele, D.M., 2021. Generating Point Cloud Failure Surface of Polymeric Unidirectional Composites Using Virtual Tests. Arizona State University.

Khaled, B., 2019. Experimental Characterization and Finite Element Modeling of Composites to Support a Generalized Orthotropic Elasto-Plastic Damage Material Model for Impact Analysis. Arizona State University.

Khaled, B., Shyamsunder, L., Hoffarth, C., Rajan, S.D., Goldberg, R.K., Carney, K.S., DuBois, P., Blankenhorn, G., 2019a. Damage characterization of composites to

support an orthotropic plasticity material model. Journal of Composite Materials 53, 941–967. https://doi.org/10.1177/0021998318793506

Khaled, B., Shyamsunder, L., Hoffarth, C., Rajan, S.D., Goldberg, R.K., Carney, K.S., DuBois, P., Blankenhorn, G., 2018. Experimental characterization of composites to support an orthotropic plasticity material model. Journal of Composite Materials 52, 1847–1872. https://doi.org/10.1177/0021998317733319

Khaled, B., Shyamsunder, L., Holt, N., Hoover, C.G., Rajan, S.D., Blankenhorn, G., 2019b. Enhancing the predictive capabilities of a composite plasticity model using cohesive zone modeling. Composites Part A: Applied Science and Manufacturing 121, 1–17. https://doi.org/10.1016/j.compositesa.2019.03.001

Khaled, B., Shyamsunder, L., Robbins, J., Parakhiya, Y., Rajan, S.D., 2021. Framework for Predicting Failure in Polymeric Unidirectional Composites through Combined Experimental and Computational Mesoscale Modeling Techniques. Fibers 9, 50. https://doi.org/10.3390/fib9080050

Kingma, D.P., Ba, J., 2014. Adam: A Method for Stochastic Optimization. https://doi.org/10.48550/ARXIV.1412.6980

Krueger, R., 2002. The Virtual Crack Closure Technique: History, Approach and Applications.

Kwon, Y.W., Panick, C.J., 2020. Strain rate dependent failure criteria for fibrous composites using multiscale approach. Multiscale and Multidiscip. Model. Exp. and Des. 3, 11–22. https://doi.org/10.1007/s41939-019-00055-0

Liu, X., Furrer, D., Kosters, J., Holmes, J., 2018. Vision 2040: A Roadmap for Integrated, Multiscale Modeling and Simulation of Materials and Systems.

Liu, Z., WU, C., Ren, B., Liu, W., Grimes, R., 2018. Multiscale Simulations of Material with Heterogeneous Structures based in Representative Volume Element Techniques. 15th International LS-DYNA Users Conference.

LLorca, J., González, C., Molina-Aldareguía, J.M., Segurado, J., Seltzer, R., Sket, F., Rodríguez, M., Sádaba, S., Muñoz, R., Canal, L.P., 2011. Multiscale Modeling of Composite Materials: a Roadmap Towards Virtual Testing. Adv. Mater. 23, 5130–5147. https://doi.org/10.1002/adma.201101683

LS-DYNA®, 2022a. KEYWORD USER'S MANUAL VOLUME I.

LS-DYNA®, 2022b. KEYWORD USER'S MANUAL VOLUME II Material Models.

Matthias Deuschle, H., Kröplin, B.-H., 2012. Finite element implementation of Puck's failure theory for fibre-reinforced composites under three-dimensional stress. Journal of Composite Materials 46, 2485–2513. https://doi.org/10.1177/0021998312451480

Matzenmiller, A., Lubliner, J., Taylor, R.L., 1995. A constitutive model for anisotropic damage in fiber-composites. Mechanics of Materials 20, 125–152. https://doi.org/10.1016/0167-6636(94)00053-0

Mauersberger, M., Maurya, A., Markmiller, J.F.C., Rajan, S., 2024. Macro-mechanical Modeling of Aluminum Alloys Processed by Laser Powder-Bed Fusion. Submitted to Additive Manufacturing.

Maurya, A., Arumugam, D., Kiran, R., Rajan, S., 2024a. On point cloud failure criterion predictions. Journal of Composite Materials 58, 2851–2878. https://doi.org/10.1177/00219983241270964

Maurya, A., Pechetti, S., Chen, H., Rajan, S., Buenrostro, J., Pereira, J.M., Miller, S.G., 2025. Experimental Tests to Characterize the Behavior and Properties of HexPly Unidirectional Composite & TuFF Short Fiber Composite.

Maurya, A., Pechetti, S., Rajan, S., 2024b. An Improved Framework for Soft Body Armor Design. Submitted to Composites Part A.

Maurya, A., Raihan, M., Rajan, S., 2024c. Improving Delamination Modeling via Inverse Analysis. J. Aerosp. Eng. 37, 04024056. https://doi.org/10.1061/JAEEEZ.ASENG-5613

Maurya, A., Rajan, S.D., 2024. Incorporating point cloud failure criterion in an orthotropic visco-elastic-plastic material model. Journal of Composite Materials 58, 2169–2197. https://doi.org/10.1177/00219983241260882

Maurya, A., Tanneru, S.P., Rajan, S., Pereira, J.M., Miller, S.G., 2023. Experimental Tests to Characterize the Behavior and Properties of IM7-8552 Composite.

Mount, D.M., 2010. ANN Programming Manual, ANN Version 1.1.

Myers, R.H., Montgomery, D.C., 2002. Response Surface Methodology.

Nasirov, A., Gupta, A., Hasanov, S., Fidan, I., 2020. Three-scale asymptotic homogenization of short fiber reinforced additively manufactured polymer composites. Composites Part B: Engineering 202, 108269. https://doi.org/10.1016/j.compositesb.2020.108269

Nicholas, T., 1980. Dynamic Tensile Testing of Structural Materials Using a Split Hopkinson Bar Apparatus.

Ogasawara, T., Ishikawa, T., Yokozeki, T., Shiraishi, T., Watanabe, N., 2005. Effect of on-axis tensile loading on shear properties of an orthogonal 3D woven SiC/SiC composite. Composites Science and Technology 65, 2541–2549. https://doi.org/10.1016/j.compscitech.2005.06.003

Oliver, J., Caicedo, M., Huespe, A.E., Hernández, J.A., Roubin, E., 2017. Reduced order modeling strategies for computational multiscale fracture. Computer Methods in Applied Mechanics and Engineering 313, 560–595. https://doi.org/10.1016/j.cma.2016.09.039

Pai, A., Suri, R., Bhave, A.K., Verma, P., N H, P., 2023. Puck's Criterion for the tensile response of composite laminates: A numerical approach. Advances in Engineering Software 175, 103364. https://doi.org/10.1016/j.advengsoft.2022.103364

Parakhiya, Y., 2020. Framework for Generating Failure Surface through Virtual Testing of Unidirectional Polymeric Composites. Arizona State University.

Pechetti, S., 2024. A Framework for Soft Body Armor Design Using Solid Finite Elements. Arizona State University.

Pinho, S., Darvizeh, R., Robinson, P., Schuecker, C., Camanho, P., 2012. Material and structural response of polymer-matrix fibre-reinforced composites. Journal of Composite Materials 46, 2313–2341. https://doi.org/10.1177/0021998312454478

Pinho, S., Vyas, G., Robinson, P., 2013. Material and structural response of polymer-matrix fibre-reinforced composites: Part B. Journal of Composite Materials 47, 679–696. https://doi.org/10.1177/0021998313476523

Pinho, S.T., Robinson, P., Iannucci, L., 2006. Fracture toughness of the tensile and compressive fibre failure modes in laminated composites. Composites Science and Technology 66, 2069–2079. https://doi.org/10.1016/j.compscitech.2005.12.023

Pittie, T., Kartikeya, K., Bhatnagar, N., Anoop Krishnan, N., Senthil, T., Rajan, S.D., 2023. Building a predictive soft armor finite element model combining experiments, simulations, and machine learning. Journal of Composite Materials 57, 1599–1615. https://doi.org/10.1177/00219983231160497

Polla, A., Frulla, G., Cestino, E., Das, R., Marzocca, P., 2023. Coupled Thermo-Mechanical Numerical Modeling of CFRP Panel under High-Velocity Impact. Aerospace 10, 367. https://doi.org/10.3390/aerospace10040367

Puck, A., Schürmann, H., 2002. Failure analysis of FRP laminates by means of physically based phenomenological models. Composites Science and Technology 62, 1633–1662. https://doi.org/10.1016/S0266-3538(01)00208-1

Rajan, S., 2021. Object-Oriented Numerical Methods via C++.

Rajan, S., Dhandapani, K., Jain, R., 2023. Engineering Design Optimization (EDO) Workbench User's Manual.

Rajan, S., Khaled, B., Shyamsunder, L., 2021. Point Cloud Failure Criterion for Composites using k-Nearest Neighbor Classification. https://doi.org/10.48550/ARXIV.2106.02714

Robbins, J., 2019. On Building Blocks for Virtual Testing of Unidirectional Polymeric Composites. Arizona State University.

Salavatian, M., Smith, L.V., 2014. The effect of transverse damage on the shear response of fiber reinforced laminates. Composites Science and Technology 95, 44–49. https://doi.org/10.1016/j.compscitech.2014.02.012

Shanmugam, V., Penmetsa, R., Tuegel, E., Clay, S., 2013. Stochastic modeling of delamination growth in unidirectional composite DCB specimens using cohesive zone models. Composite Structures 102, 38–60. https://doi.org/10.1016/j.compstruct.2013.01.020

Shyamsunder, L., 2020. Failure Modeling in an Orthotropic Plastic Material Model under Static and Impact Loading. Arizona State University.

Shyamsunder, L., Khaled, B., Rajan, S.D., Blankenhorn, G., 2021. Improving failure sub-models in an orthotropic plasticity-based material model. Journal of Composite Materials 55, 2025–2042. https://doi.org/10.1177/0021998320982651

Shyamsunder, L., Khaled, B., Rajan, S.D., Goldberg, R.K., Carney, K.S., DuBois, P., Blankenhorn, G., 2020a. Implementing deformation, damage, and failure in an orthotropic plastic material model. Journal of Composite Materials 54, 463–484. https://doi.org/10.1177/0021998319865006

Shyamsunder, L., Khaled, B., Rajan, S.D., Goldberg, R.K., Carney, K.S., DuBois, P., Blankenhorn, G., 2020b. Implementing deformation, damage, and failure in an orthotropic plastic material model. Journal of Composite Materials 54, 463–484. https://doi.org/10.1177/0021998319865006

Shyamsunder, L., Khaled, B., Rajan, S.D., Pereira, J.M., DuBois, P., Blankenhorn, G., 2022a. Numerical validation of composite panel impact tests. International Journal of Impact Engineering 159, 104032. https://doi.org/10.1016/j.ijimpeng.2021.104032

Shyamsunder, L., Maurya, A., Rajan, S.D., Cordasco, D., Revilock, D., Blankenhorn, G., 2022b. Impact simulation of composite panels for aerospace applications. Composites Part B: Engineering 247, 110320. https://doi.org/10.1016/j.compositesb.2022.110320

Smith, D.L., Dow, M.B., 1991. Properties of three graphite/toughened resin composites.

Soghrati, S., 2021. Private communications.

Sun, Q., Meng, Z., Zhou, G., Lin, S.-P., Kang, H., Keten, S., Guo, H., Su, X., 2018. Multi-scale computational analysis of unidirectional carbon fiber reinforced polymer composites under various loading conditions. Composite Structures 196, 30–43. https://doi.org/10.1016/j.compstruct.2018.05.025

Sun, Q., Zhou, G., Meng, Z., Guo, H., Chen, Z., Liu, H., Kang, H., Keten, S., Su, X., 2019. Failure criteria of unidirectional carbon fiber reinforced polymer composites informed by a computational micromechanics model. Composites Science and Technology 172, 81–95. https://doi.org/10.1016/j.compscitech.2019.01.012

Talreja, R., 2016. Physical modelling of failure in composites. Phil. Trans. R. Soc. A. 374, 20150280. https://doi.org/10.1098/rsta.2015.0280

Toray, 2020. Toray Composite Materials America.

Totry, E., González, C., LLorca, J., 2008a. Failure locus of fiber-reinforced composites under transverse compression and out-of-plane shear. Composites Science and Technology 68, 829–839. https://doi.org/10.1016/j.compscitech.2007.08.023

Totry, E., González, C., LLorca, J., 2008b. Prediction of the failure locus of C/PEEK composites under transverse compression and longitudinal shear through computational micromechanics. Composites Science and Technology 68, 3128–3136. https://doi.org/10.1016/j.compscitech.2008.07.011

Tripathi, A., 2024. Print Technique and Material Modification In 3D Printing of Concrete (PhD Thesis).

Tripathi, A., Maurya, A., Rajan, S., Neithalath, N., 2024a. Understanding Properties and Behavior of 3D-Printed Concrete Specimens via Finite Element Modeling. under preparation.

Tripathi, A., Nair, S.A.O., Chauhan, H., Neithalath, N., 2024b. Print Geometry Alterations and Layer Staggering to Enhance Mechanical Properties of Plain and Fiber-Reinforced Three-Dimensional-Printed Concrete. MJ 121. https://doi.org/10.14359/51740262

Tsai, S.W., 1965. Strength characterstics of composite materials.

Tsai, S.W., Melo, J.D.D., 2016. A unit circle failure criterion for carbon fiber reinforced polymer composites. Composites Science and Technology 123, 71–78. https://doi.org/10.1016/j.compscitech.2015.12.011

Tsai, S.W., Wu, E.M., 1971. A General Theory of Strength for Anisotropic Materials. Journal of Composite Materials 5, 58–80. https://doi.org/10.1177/002199837100500106

Turon, A., Dávila, C.G., Camanho, P.P., Costa, J., 2007. An engineering solution for mesh size effects in the simulation of delamination using cohesive zone models. Engineering Fracture Mechanics 74, 1665–1682. https://doi.org/10.1016/j.engfracmech.2006.08.025

Upadhyay, R., Sinha, S., 2018. 3.6 GE-90 and Derivative Fan Blade Manufacturing Design, in: Comprehensive Composite Materials II. Elsevier, pp. 180–188. https://doi.org/10.1016/B978-0-12-803581-8.10075-X

Vadera, S., Ameen, S., 2020. Methods for Pruning Deep Neural Networks. https://doi.org/10.48550/ARXIV.2011.00241

Wan, L., Ismail, Y., Zhu, C., Zhu, P., Sheng, Y., Liu, J., Yang, D., 2020. Computational micromechanics-based prediction of the failure of unidirectional composite lamina subjected to transverse and in-plane shear stress states. Journal of Composite Materials 54, 3637–3654. https://doi.org/10.1177/0021998320918015

Wang, C.H., Duong, C.N., 2016. Failure criteria, in: Bonded Joints and Repairs to Composite Airframe Structures. Elsevier, pp. 21–45. https://doi.org/10.1016/B978-0-12-417153-4.00002-5

Wisnom, M.R., Khan, B., Hallett, S.R., 2008. Size effects in unnotched tensile strength of unidirectional and quasi-isotropic carbon/epoxy composites. Composite Structures 84, 21–28. https://doi.org/10.1016/j.compstruct.2007.06.002

Zand, B., Butalia, T.S., Wolfe, W.E., Schoeppner, G.A., 2012. A strain energy based failure criterion for nonlinear analysis of composite laminates subjected to triaxial loading. Journal of Composite Materials 46, 2515–2537. https://doi.org/10.1177/0021998312449891

Zhang, J., Zhou, L., Chen, Y., Zhao, L., Fei, B., 2016. A micromechanics-based degradation model for composite progressive damage analysis. Journal of Composite Materials 50, 2271–2287. https://doi.org/10.1177/0021998315602947

Zhou, J., Huang, Z.-M., 2022. Predicting delamination of hybrid laminate via stress modification on interlaminar matrix layer. Engineering Fracture Mechanics 264, 108333. https://doi.org/10.1016/j.engfracmech.2022.108333

Zhou, J., Huang, Z.-M., Xu, W., 2023. Prediction of laminate delamination from strength failure of interlaminar matrix-layer. Journal of Reinforced Plastics and Composites 42, 177–187. https://doi.org/10.1177/07316844221105289

Zhou, Y.-X., Huang, Z.-M., 2012. A bridging model prediction of the ultimate strength of composite laminates subjected to triaxial loads. Journal of Composite Materials 46, 2343–2378. https://doi.org/10.1177/0021998312449491